AD-767 570

ACTIVE NOSETIP EVALUATION STUDY

McDonnell Douglas Astronautics Company

Prepared for:

Space and Missile Systems Organization

November 1972

This Document Contains
Missing Page/s That Are
Unavailable In The
Original Document

DISTRIBUTED BY:

NTIS

National Technical Information Service
U. S. DEPARTMENT OF COMMERCE
5285 Port Royal Road, Springfield Va. 22151

Best Available Copy

20050203232

SAMSO-TR-73-74

ACTIVE NOSETIP EVALUATION STUDY

AD 767570

McDonnell Douglas Active Nosetip Evaluation Study Team

TECHNICAL REPORT SAMSO-TR-73-74

November 1972

Reproduced by
NATIONAL TECHNICAL
INFORMATION SERVICE
U S Department of Commerce
Springfield VA 22151

DDC
RECEIVED
SEP 13 1973
B

Approved for public release;
distribution unlimited

Space and Missile Systems Organization
Air Force Systems Command
Los Angeles Air Force Station, California

Best Available Copy

UNCLASSIFIED

Security Classification

DOCUMENT CONTROL DATA - R & D

(Security classification of title, body of abstract and indexing annotation must be entered when the overall report is classified)

1. ORIGINATING ACTIVITY (Corporate author)

McDonnell Douglas Astronautics Company
5301 Bolsa Avenue
Huntington Beach, California 92647

2a. REPORT SECURITY CLASSIFICATION

UNCLASSIFIED

2b. GROUP

3. REPORT TITLE

ACTIVE NOSETIP EVALUATION STUDY

4. DESCRIPTIVE NOTES *(Type of report and inclusive dates)*

Final Report

5. AUTHOR(S) *(First name, middle initial, last name)*

McDonnell Douglas Active Nosetip Evaluation Study Team

6. REPORT DATE	7a. TOTAL NO. OF PAGES	7b. NO. OF REFS
November 1972	314 330	21

8a. CONTRACT OR GRANT NO.	9a. ORIGINATOR'S REPORT NUMBER(S)
F04701-72-C-0233	MDC G4795
b. PROJECT NO.	
c.	9b. OTHER REPORT NO(S) *(Any other numbers that may be assigned this report)*
d.	SAMSO-TR-73-74

10. DISTRIBUTION STATEMENT

Approved for public release; distribution unlimited

11. SUPPLEMENTARY NOTES	12. SPONSORING MILITARY ACTIVITY
	USAF Space & Missile Systems Organization Los Angeles Air Force Station Los Angeles, California 90009

13. ABSTRACT

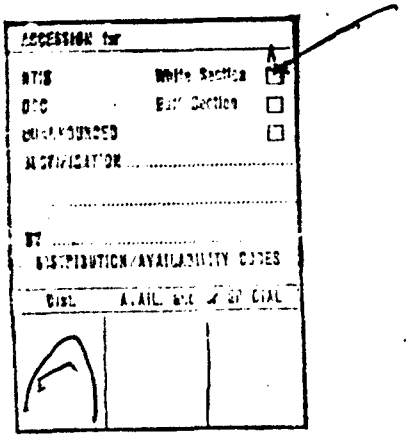
A compact, lightweight expulsion system for a transpiration-cooled nosetip has been designed. This system is sensitive to the environment and is capable of meeting the requirements of a wide variety of maneuvering reentry missions. An additional task was the completion of a nosetip test on a rocket sled that passed through a rain environment.

DD FORM 1473

UNCLASSIFIED

NOTICE

When Government drawings, specifications, or other data are used for any purpose other than in connection with a definitely related Government procurement operation, the United States Government thereby incurs no responsibility nor any obligation whatsoever; and the fact that the Government may have formulated, furnished, or in any way supplied the said drawings, specifications, or other data, is not to be regarded by implication or otherwise as in any manner licensing the holder or any other person or corporation, or conveying any rights or permission to manufacture, use, or sell any patented invention that may in any way be related thereto.



FOREWORD

This report was prepared by the McDonnell Douglas Astronautics Company, Huntington Beach, California, under U.S. Air Force Contract F04701-72-C-0233, entitled Active Nosetip Evaluation Study. The work was accomplished during the period 15 May through 15 December 1972. This effort was administered under the direction of the Space and Missile Systems Organization Project Officer, Capt. M. L. Anderson.

Program Manager for this study was T. G. Lee. The McDonnell Douglas study team consisted of the following personnel, listed according to their areas of expertise:

Thermodynamics - G. P. Johnson, T. G. Lee, J. R. Schuster

Mechanical Design - R. H. Bergloff, R. A. Glickman, J. T. Hollis

Gas Generator Analysis - L. E. Cothran, T. E. Ward

Materials - K. R. Wilson, R. G. Hocker

Electrical Circuitry - N. K. Yutani

Control System - J. J. Angelbeck

Nuclear Hardening - L. M. Langsam

14. KEY WORDS	LINK A		LINK B		LINK C	
	ROLE	WT	ROLE	WT	ROLE	WT
Transpiration						
Nosetips						
Expulsion						
Reentry Vehicles						
Rain Erosion						

CONTENTS

	NOMENCLATURE		xxi
Section 1	INTRODUCTION AND SUMMARY		1
Section 2	NOSETIP DESIGN		9
	2.1	Ideal Coolant Flow	10
	2.2	Nosetip External Geometry	14
	2.3	Nosetip Internal Configuration	14
		2.3.1 Ideal Inner Contours	36
		2.3.2 Final Inner Contour	38
	2.4	Design Coolant Requirements	40
		2.4.1 Coolant Weights, Pressures, and Distributions	40
		2.4.2 Effect of Coolant Supply Pressure	49
		2.4.3 Effect of Coolant Temperature	49
		2.4.4 Effect of Nosetip Attachment	51
	2.5	Alternate Nosetip Configurations	51
Section 3	FLOW CONTROL CONCEPTS		61
	3.1	Flow Control Parameters	61
	3.2	Mechanical Valve Concepts	63
		3.2.1 Square-Root-of-g Valve	70
		3.2.2 Dual-Slope Valve	71
		3.2.3 Mark II Valve	73
		3.2.4 Volume Compensation	74
		3.2.5 Pressure Control	78
		3.2.6 Partitioned Nosetip Flow Control	81
	3.3	Electromechanical Valve Flow Control	81
		3.3.1 Utilization of Free-Stream Parameters	84
		3.3.2 Electrical Generation of Free-Stream Parameters	87
		3.3.3 Nosetip Performance Sensors	95
		3.3.4 Closed-Loop Coolant Flow Control Analysis	115
		3.3.5 Electromechanical Valve Designs	122

ABSTRACT

This document describes the results of an investigation to reduce the volume and weight requirements of a transpiration-cooled nosetip expulsion system. Efficient expulsion system designs were investigated to minimize the volume and weight requirements for a transpiration-cooled nosetip. Coolant requirements were reduced through efficient design of the nosetip and heat shield. All parts of the expulsion system were optimized to minimize coolant wastage and volume. The critical component was found to be the coolant control valve. Many types of control were investigated, each sensitive to some environmental or vehicular parameters. Two methods were found to be quite attractive. The first was a deceleration-sensing device coupled with an expelled coolant volume compensator. The second utilized an electromechanical valve which used the free-stream velocity and density and the vehicle angle of attack to regulate flow. A conical reservoir was found to be mandatory from a volumetric efficiency viewpoint. In order to take full advantage of this type of design, a bladder expulsion technique must be used. Both metallic and elastomeric bladders were considered. Warm- and cold-gas pressurization systems were investigated. Hot-gas techniques were found to be considerably more efficient. A multiple-grain solid propellant approach was selected for use in this study. The combination of the selected components resulted in a highly efficient and compact design which could meet the requirements of a wide variety of missions.

An additional task performed during this contract was the successful completion of a rocket sled test through a rain environment. A test model was obtained from another Air Force program, modified to fit within the sled, and tested. Results of other Air Force sled tests with transpiration materials are also included in this report.

Section 4	EXPULSION CONCEPTS		129
	4.1	Piston	129
	4.2	Bladder	129
		4.2.1 Nonmetallic Bladder	129
		4.2.2 Rolling Bladder (Nonmetallic)	132
		4.2.3 Metallic Bladders	132
Section 5	PRESSURIZATION		137
	5.1	Cold-Gas Pressurization	137
	5.2	Warm-Gas Pressurization	140
		5.2.1 Solid-Propellant Pressurization Concepts	142
		5.2.2 Monopropellant Pressurization Systems	161
		5.2.3 Compatibility With Expulsion Concepts	170
Section 6	INITIATION CONCEPTS		177
Section 7	SYSTEM DESIGN CONSIDERATIONS		181
	7.1	Packaging	181
		7.1.1 Layout	181
		7.1.2 Materials	181
		7.1.3 Assembly	186
		7.1.4 Comparison With Contract Envelope	188
		7.1.5 Interface Requirements	188
	7.2	Structural Evaluation	188
		7.2.1 Critical Load Definition	188
		7.2.2 Component Analysis	197
	7.3	Mass Properties	197
		7.3.1 Detailed Breakdown	197
		7.3.2 Possible Improvements	197
	7.4	Nuclear Hardening	200
	7.5	Environmental Performance	201
	7.6	Reliability and Safety	203
	7.7	Manufacturing	203
Section 8	CONCEPT DEFINITION		207
	8.1	Ranking System	207
	8.2	Concept Ranking	208
		8.2.1 Flow Control	208
		8.2.2 Expulsion	210
		8.2.3 Pressurization System	211
	8.3	Selected Designs	213

Section 9	ROCKET SLED TEST		219
	9.1	Facility Description	220
		9.1.1 Rocket Sled Configuration	220
		9.1.2 Environment	220
		9.1.3 Data Acquisition and Instrumentation	220
	9.2	Test Model	224
	9.3	Post-Test Analysis and Data Reduction	224
		9.3.1 Environment	229
		9.3.2 Coolant Flow Margins	235
		9.3.3 Nosetip Temperatures	236
		9.3.4 Physical Damage	240
	9.4	Results of Related Tests	240
		9.4.1 Holloman Sled Tests of Dry, Porous, 316L Stainless Steel	240
		9.4.2 Test Environment, Matrix, and Models	240
		9.4.3 Test Configuration and Propulsion System	240
		9.4.4 Procedures	246
		9.4.5 Results and Discussion	246
		9.4.6 Significance of Results	257
Section 10	REFERENCES		259
Appendix A	CALCULATION OF THERMALLY IDEAL COOLANT FLUX		261
Appendix B	HEAT SHIELD ANALYIS METHODOLOGY		265
Appendix C	APPROXIMATION OF COOLANT FLOW REQUIREMENTS WITH FREE-STREAM PARAMETERS		269
Appendix D	TRANSPIRATION NOSETIP TRANSIENT THERMAL ANALYSIS		285
Appendix E	STRESS ANALYSIS		297

FIGURES

1-1	Reentry Parameter Histories, Trajectory L-6	2
1-2	Reentry Parameter Histories, Trajectory S-3	2
1-3	Reentry Parameter Histories, Trajectory 606	3
1-4	Reentry Parameter Histories, Trajectory L-1(a)	3
1-5	Reentry Parameter Histories, Trajectory L-12	4
2-1	Coolant Flow Comparison	12
2-2	Ground Test Coolant Margins	13
2-3	Nose Radius Effect on Coolant Requirement	15
2-4	Ideal Coolant Histories	16
2-5	Material Properties for 5055A Carbon-Phenolic	19
2-6	5055A Carbon-Phenolic Char Conductivity	20
2-7	Thermogravimetric Analysis and Properties of EPON 934	23
2-8	Temperature and Pressure at Bond Surface	24
2-9	Heat Shield Requirement	26
2-10	Fiberflake Insulation Thermal Properties	28
2-11	Coolant Temperature Histories, L-6	29
2-12	Required Heat Shield Thickness	30
2-13	Surface Recession Histories, L-6, $S/R_N = 1.67$	31
2-14	Heat Shield Temperature Profile at Impact, L-6	31
2-15	Recession History, Trajectory 606, $S/R_N = 5.76$, Windward	32

2-16	Temperature Profile at Impact, Trajectory 606, $S/R_N = 5.76$, Windward	32
2-17	Heat Transfer Downstream of Aft Facing Step	34
2-18	Recession Profiles, Test 35, $\alpha = 10$, Camphor	35
2-19	Heat Shield Requirements	36
2-20	Optimized Nosetip Contours	39
2-21	Nosetip Contour and Permeability	41
2-22	Design Coolant Flow Histories	42
2-23	Design Coolant Pressure Histories	43
2-24	Coolant Distribution at Peak Flow, L-6	44
2-25	Coolant Distribution at Peak Flow, 606	45
2-26	Coolant Distribution at Peak Flow, S-3	46
2-27	Coolant Distribution at Peak Flow, L-12	47
2-28	Coolant Distribution at Peak Flow, L-1(a)	48
2-29	Effect of Coolant Pressure on Design Coolant Weight, L-6 Trajectory	50
2-30	Effect of Coolant Temperature on Design Coolant Weight, L-6 Trajectory	52
2-31	Actual Coolant Temperature, L-6 Trajectory	52
2-32	Nosetip Weld Attachment	53
2-33	Effect of Attachment on Coolant Distribution	54
2-34	High-Pressure Nosetip	57
2-35	Partitioned Nosetip	58
2-36	Miniskirted Nosetip, Dual-K	60
3-1	L-6 and S-3 Single Parameter Correlation	62
3-2	Excess Coolant Rate Histories	64
3-3	Excess Coolant Rate Histories	65
3-4	Excess Coolant Flow Rate vs Parameters Valve Sensing Stagnation Pressure (Gain = 0.000221 Lb/Sec/Psi)	66

3-5	Excess Coolant Flow Rate vs Parameters Valve Sensing $\sqrt{\text{Stagnation Pressure}}$ (Gain = 0.007165 Lb/Sec/ $\sqrt{\text{Psi}}$)	67
3-6	Excess Coolant Flow Rate vs Parameters Valve Sensing Axial g's (Gain = 0.010625 Lb/Sec/g's)	68
3-7	Excess Coolant Flow Rate vs Parameters Valve Sensing $\sqrt{\text{Axial g's}}$ (Gain = 0.045772 Lb/Sec/$\sqrt{\text{g's}}$)	69
3-8	Square-Root-of-g Valve	71
3-9	Deceleration Functions	72
3-10	Dual-Slope g Valve	73
3-11	Mark II Flow Control Valve Schematic	74
3-12	Dual-Slope Valve Coolant Excess	75
3-13	Preprogrammed Control	77
3-14	Pressure Valve	79
3-15	Flow Rate Dependence of Chamber Pressure	80
3-16	Design Flow vs Stagnation Pressure	82
3-17	Flow Diverter	83
3-18	Effect of Angle of Attack on Design Coolant Flow Rate	86
3-19	Electromagnetic Valve Flow Histories, L-6 and 606	89
3-20	Electromagnetic Valve Flow History, S-3	90
3-21	Electromagnetic Valve Flow Histories, L-1(a) and L-12	91
3-22	Analog System	93
3-23	Free-Stream Parameter Digital Converter	94
3-24	Use of Thermocouples	96
3-25	Heat Shield Surface Temperatures	97
3-26	Thermocouple Voltage Characteristics	100
3-27	One-Wire Thermocouples	101

3-28	Two-Wire Thermocouple With Optional One-Wire Thermocouple in Stainless Steel Sheath	102
3-29	Use of Gamma Ray Detection	103
3-30	Signal-to-Noise Ratio for Gamma Ray Detection	107
3-31	Use of Optical Detection	109
3-32	Signal-to-Noise Ratio Between 3 and 4 Microns	111
3-33	Signal-to-Noise Ratio Between 0.46 and 0.48 Microns	111
3-34	Use of Acoustic Detection	113
3-35	Closed-Loop Flow Control Concept	116
3-36	Nosetip Temperature Response to Step in Heat Input for (0.015 + t_D)-Sec Response Valve	118
3-37	Coolant Flow Response to Step in Heat Input for (0.015 + t_D)-Sec Response Valve	118
3-38	Nosetip Temperature Response to Step in Heat Input for (0.020 + t_D)-Sec Response Valve	119
3-39	Coolant Flow Response to Step in Heat Input for (0.020 + t_D)-Sec Response Valve	119
3-40	System Response to 80-Percent Step Increase to Nosetip Heating, Valve Response = 15 msec + t_D	120
3-41	System Response to 80-Percent Step Increase to Nosetip Heating, Valve Response = 20 msec + t_D	121
3-42	Single-Stage Leakage Flux Proportional Flow Control Valve	123
3-43	Electromagnet Force Motor Optimization	124
3-44	Two-Stage Pulse-Width-Modulated Flow Control Valve	126
3-45	Pulsed Valve Schematic	127
4-1	Double-Piston Expulsion	130
4-2	Nonmetallic Bladder	131
4-3	Rolling Bladder	133

5-1	Helium Gas Bottle Volume and Weight	139
5-2	Transpiration Coolant Expulsion System	141
5-3	Burning Rate for D-198 Propellant	145
5-4	Pressurization Igniter Circuit	147
5-5	Pressure History, S-3 Trajectory	148
5-6	Pressure History, L-6 Trajectory	149
5-7	Pressure History, L-1(a) Trajectory	150
5-8	Three-Grain Gas Generator	152
5-9	Burning Surface for Circumferential Burning Grain	154
5-10	Required and Delivered Pressure, S-3 Trajectory	155
5-11	Required and Delivered Pressure, L-6 Trajectory	156
5-12	Required and Delivered Pressure, L-1(a) Trajectory	157
5-13	Required and Delivered Pressure, L-12 Trajectory	158
5-14	Required and Delivered Pressure, 606 Trajectory	159
5-15	Blowdown Monopropellant Concept	162
5-16	Bootstrap Monopropellant Concept	162
5-17	Required and Delivered Pressure, S-3 Trajectory	164
5-18	Required and Delivered Pressure, L-6 Trajectory	165
5-19	Monopropellant Burned, L-6 Trajectory	166
5-20	Percent Ammonia Dissociated, L-6 Trajectory	168
5-21	Monopropellant Concept	169
5-22	Average Surface Temperature of the Bladder	171

5-23	Average Surface Temperature of the Bladder, S-3 Trajectory	172
5-24	Temperature Distribution Through the Bladder, L-6 Trajectory	174
5-25	Temperature of Well-Mixed Coolant, L-6 Trajectory	175
5-26	Temperature of Well-Mixed Coolant	176
6-1	Initiation System Concepts	178
7-1	Baseline System Layout	183
7-2	System Interface	189
7-3	Force and Moment Histories, L-6	190
7-4	Force and Moment Histories, 606	190
7-5	Force and Moment Histories, L-1(a)	191
7-6	Force and Moment Histories, L-1(a), 60,000-Ft Blast Encounter	191
7-7	Force and Moment Histories, S-3	192
7-8	Force and Moment Histories, L-12	192
7-9	Critical Load Summary	193
7-10	Nosetip Pressure Distributions, L-1(a) With Blast, Flight Time = 24.5 Sec	194
7-11	Nosetip Pressure Distributions, S-3, 19.7 Sec	194
7-12	Nosetip Pressure Distributions, L-6, 45.4 Sec	195
7-13	Heat Shield Temperature Profiles, L-1(a), 24.5 Sec	195
7-14	Heat Shield Temperature Profiles, S-3, 19.7 Sec	196
7-15	Heat Shield Temperature Profiles, L-6, 45.4 Sec	196
7-16	Critical Stress Areas	198

8-1	Mark II Flow Control Valve Schematic	214
8-2	Mark II Valve Flow History—L12 and L-1(a) Trajectories	215
8-3	Mark II Valve Flow History—606 and L-6 Trajectories	216
8-4	Mark II Valve Flow History—S-3 Trajectory	217
9-1	Photograph of Holloman Sled Track	221
9-2	Rocket Sled Test Configuration	222
9-3	Sled Test Transpiration System Schematic	225
9-4	Rocket Sled Test Model	227
9-5	Nosetip Flow Rate vs Pressure for Tip No. 538-5	229
9-6	Sled Velocity History	230
9-7	Stagnation Point Heat Transfer and Pressure Histories	231
9-8	Particle-Induced Flow Separation	232
9-9	Heat Transfer Histories at Location of Minimum Coolant Margin	234
9-10	Flow Rate History	235
9-11	Coolant Flow Margins for Sled Test	237
9-12	Predicted Sled Test Stagnation Point Temperature Histories	238
9-13	Predicted Sled Test Temperature Histories at Peak Heating Location (33 Deg)	239
9-14	Sample	242
9-15	AFML 13.5-Deg Half-Angle Cone Schematic	243
9-16	AFML 30-Deg Half-Angle Cone Schematic	244
9-17	Mach 4.0 Schematic and Shock Wave Pattern for Small Wedge	245
9-18	Rain Erosion Specimens	248

9-19	Effect of Exposure Angle on Surface Appearance and Percent Gas Flow Time Increase	249
9-20	Time Increase for Nitrogen Gas Flow as a Function of Exposure Angle and Velocity	251
9-21	Surface Roughness as a Function of Exposure Angle and Velocity	252
9-22	Weight Change as a Function of Exposure Angle and Velocity	254
9-23	Scanning Electron Micrographs of Surface Damage	255
9-24	Typical Cross-Section View of Sample 259-4	256

TABLES

2-1	Coolant Flow Design Uncertainties	14
2-2	Preliminary Heat Shield Requirements	17
2-3	Conductivity Effect on Heat Shield Requirements	21
2-4	Effect of Bond Temperature on Heat Shield Requirements	22
2-5	Allowable Pressure	25
2-6	Skirt Length and Ideal Coolant Requirement Summary	27
2-7	Final Ideal Coolant Requirements	33
2-8	Nosetip Design Coolant Summary	49
2-9	Design Coolant Requirements for Alternate Nosetips	56
3-1	Correlation of Parameters	70
3-2	Electromagnetic Flow Control Valve Parametric Equations	88
3-3	Possible Isotopes	105
5-1	D-198 Propellant Exhaust Gas and Ballistic Characteristics	144
5-2	Three-Grain Propellant Design Summary	153
5-3	Summary of Pressurization With Solid Propellants	160
5-4	Considerations for Monopropellant Studies	167
5-5	Variation in Coolant Temperature (L-6 Trajectory)	173
7-1	Material Selection	186

7-2	**Critical Stress Results**	199
7-3	**Mass Properties**	200
7-4	Environmental Performance Considerations	201
7-5	Failure Modes and Effects	204
8-1	Ranking System	208
8-2	Flow Control Ranking	209
8-3	Coolant Requirements	209
8-4	Expulsion System Ranking	211
8-5	Pressurization Ranking	211
9-1	Sled Test Environment	223
9-2	Matrix of Holloman Sled Tests of Dry, Porous Samples	241
9-3	Vehicle Test Configuration	246
9-4	Rain Erosion Specimen Damage Evaluation Data	250

NOMENCLATURE

A	area or Arrhenius constant
Δb_j	lamina thickness of j lamina
C	drag constants
C_p	specific heat
D	diameter
E^*	activation energy
F	force
F_B	char fraction
F_T	total force
F_{tu}	ultimate tensile stress
G	gravity
h	enthalpy
H	altitude or enthalpy including heats of formation
I	moment of inertia
J	conversion factor
k	thermal conductivity
K	permeability or constant
K_j	specie mass fraction of j specie
m	mass
$\dot{m}$	mass flux
M	moment

N_c	enthalpy-based heat transfer coefficient
P	pressure
Pr	Prandtl number
q	heat flux
ΔQ	combustion term
r	recovery factor
R	body radius or gas constant
R_N	nose radius
Re	Reynolds number
$\dot{s}$	ablation rate
S	running length
SCF	stress concentration factor
SH	step height
t	time or thickness
T	temperature
u	velocity
V	volume
x	distance
Z	compressibility
α	angle of attack or viscous pressure-drop constant
β	inertial pressure-drop constant
γ	void fraction
γ'	resin fraction
Γ	porous matrix tortuosity
ϵ	emissivity or thread efficiency
η	acceleration
θ	angle from stagnation point

μ	viscosity
ξ	damping ratio, or Equation 3-10
ρ	density
σ	stress or Stefan-Boltzman constant
ω	natural frequency

Subscripts

A	axial
B	base
be	bending
c	char or tip chamber
co	coolant
com	compressive
e	boundary layer edge or effective
g	gas
i	initial
in	inner
m	matrix
N	normal
o	unmodified or initial
out	outer
r	recovery
R	radial
s	stagnation
th	thread
v	coolant vapor
vi	virgin
w	wall

x	pitch direction
y	yaw direction
Z	axial direction
θ	at angle θ
∞	free stream

Section 1
INTRODUCTION AND SUMMARY

Transpiration cooling is a proven thermal protection concept capable of withstanding extremely high heat transfer rates. In fact, the porous matrix concept used during this study is capable of surviving any reentry environment currently envisioned. This capability results in several important advantages over other types of nosetip thermal protection. Some of the more significant are retention of the nose shape, increased mission flexibility, and all-weather operational capability.

Unfortunately, transpiration is not a complete nosetip panacea. The coolant storage and explusion system requires a significant volume and weight. It is to this problem that the effort expended on this contract was addressed.

The primary objective was to generate a preliminary design of a flightweight expulsion concept which minimizes the volume or length required to house the system. This was accomplished by minimizing the coolant requirements and by generating expulsion system concepts which result in very little wasted space or coolant. Since the design of this system is somewhat dependent upon the vehicle and missions being considered, several ground rules were required. A water-cooled stainless steel tip with a carbon-phenolic heat shield formed the basic thermal protection system. Nose radius was considered variable, and three radii were considered (0.5, 0.75, and 1.0 in.). The cone angle was fixed at 7 deg. Five trajectories, covering a wide range of missions, were studied. These trajectories are shown in Figures 1-1 through 1-5. The aerothermodynamic environments for these trajectories were supplied at the start of the contract.

Coolant requirement minimization was accomplished in two ways. First, the nosetip external geometry was selected by minimizing the ideal coolant requirement. A 1.0-in.-radius tip without a skirt resulted from this study.

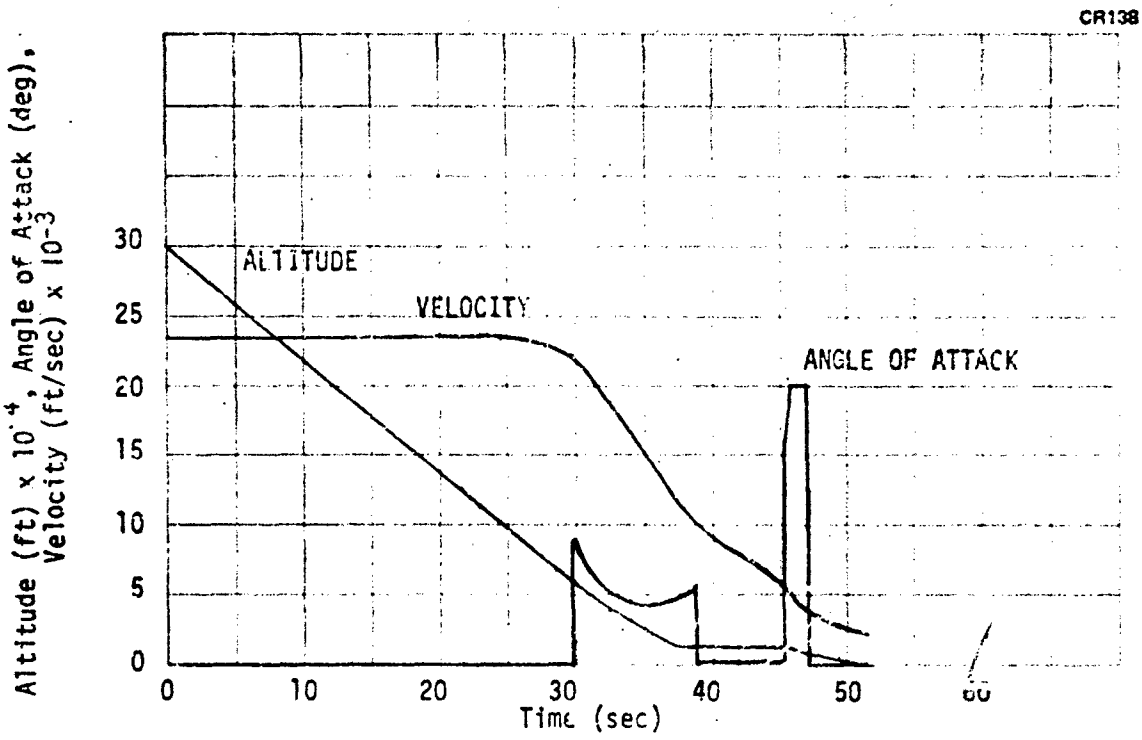


Figure 1-1. Reentry Parameter Histories, Trajectory L-6

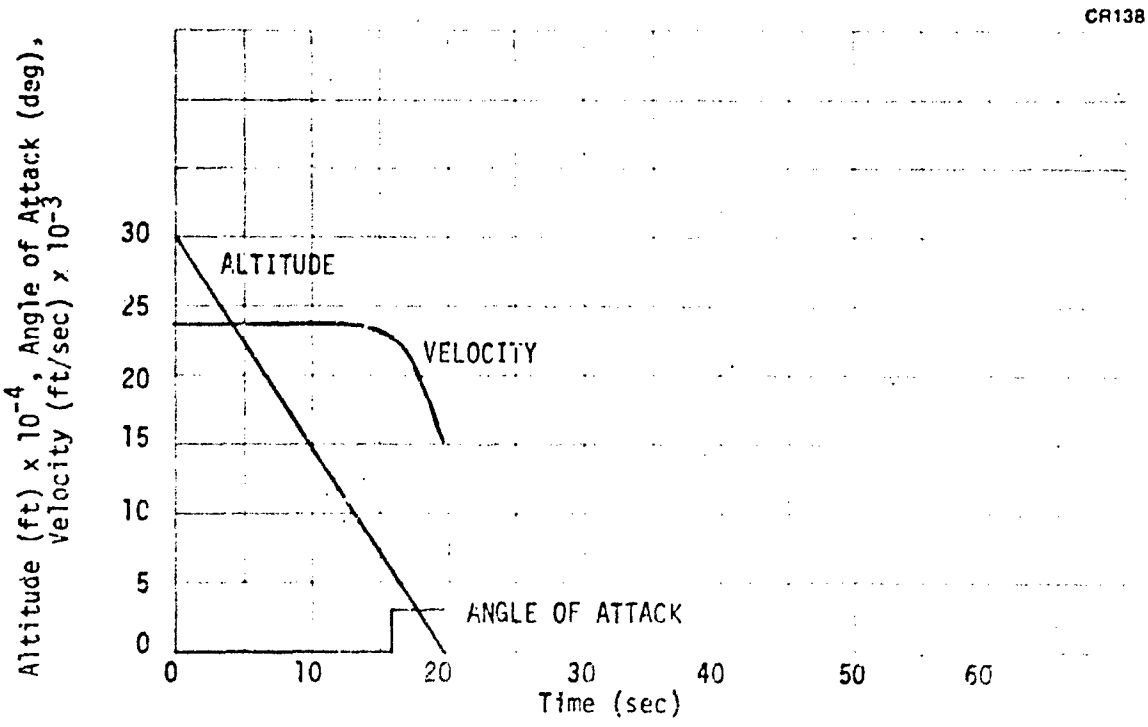


Figure 1-2. Reentry Parameter Histories, Trajectory S-3

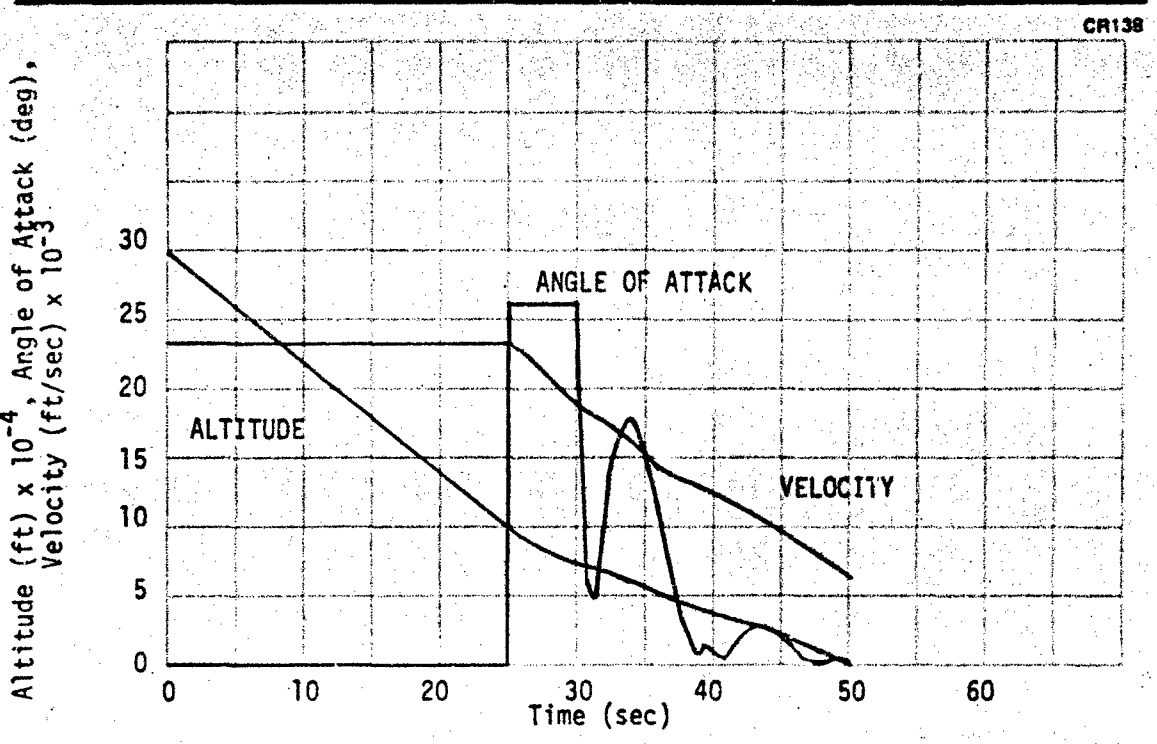


Figure 1-3. Reentry Parameter Histories, Trajectory 606

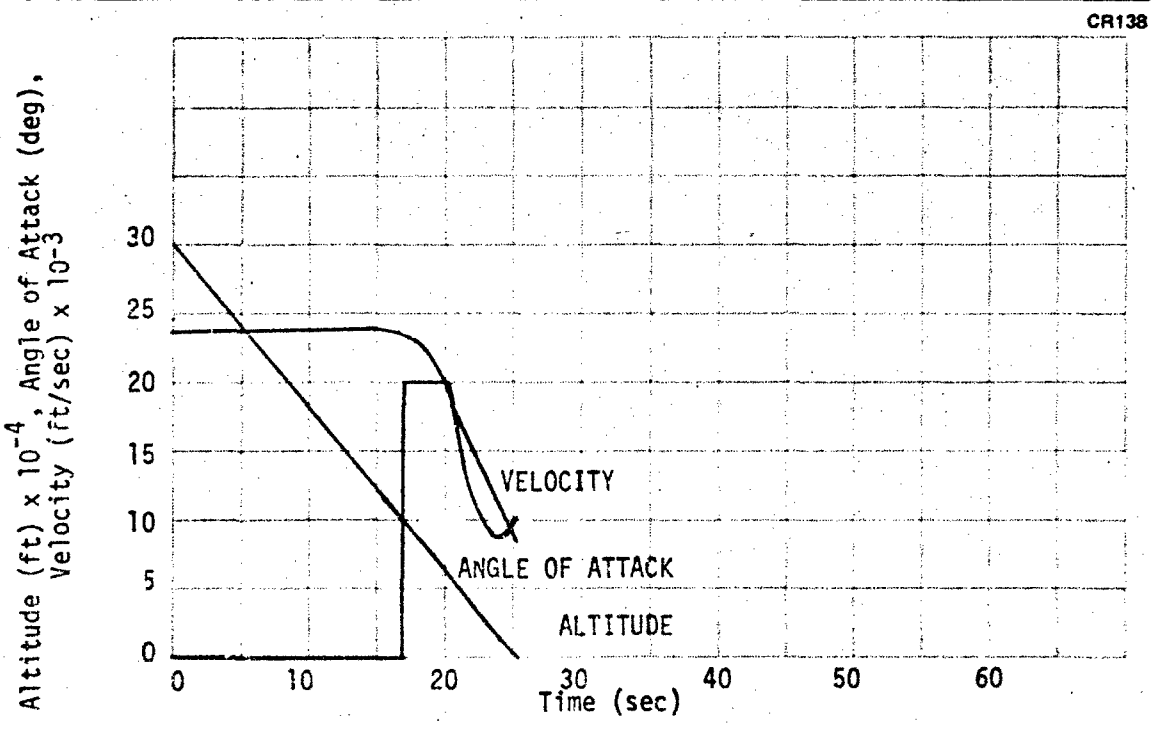


Figure 1-4. Reentry Parameter Histories, Trajectory L-1(a)

pressure, nosetip cavity pressure, deceleration, coolant flow, velocity, altitude, angle of attack, and nosetip response. Depending upon the type of parameter, either a mechanical or an electromechanical valve was designed.

Two flow control concepts are considered acceptable. The recommended concept is a purely mechanical deceleration-sensing valve whose flow characteristics are changed according to the integrated coolant flow. This type of valve results in only 5 percent coolant excess for the trajectories being considered and can be developed within the one-year schedule. The other concept requires an electromechanical valve. This valve requires considerably more development and could be made available within 12 to 18 months. Free-stream velocity and density and the vehicle angle of attack are used to compute flow rates. A small digital electronic network was designed to convert vehicle accelerations into these parameters and then compute flow rates using simplified aeroheating relationships. Although this valve requires slightly more coolant (11 percent over design) than the recommended design, it may be capable of being more generally applied to a variety of trajectories. A considerable effort was expended toward the development of a nosetip response sensor. A control concept of this type would be truly closed-loop. Two approaches may be possible: surface thermocouples and optical sensing of nosetip melt. It is anticipated that no excess coolant would be required; however, a very large development program would be required to ensure reliability and verify predictions of nosetip response with in-depth vaporization.

Bladder and piston reservoirs were the only concepts considered during this contract. Pistons, both single and double, are considerably less efficient than are bladders. Both metallic and nonmetallic bladder designs were studied. It is felt there is little to choose between these two types. The metallic bladder is being developed on a concurrent AFRPL contract; however, insufficient data was available to adequately evaluate its performance. This type of bladder has the disadvantages of requiring an ullage bubble to prevent thermal expansion and may permit considerably more heat transfer into the coolant. The nonmetallic bladder is being developed at McDonnell Douglas Astronautics Company (MDAC), but very little data has been generated. The most serious drawback of this design appears to be long-term storage with elastomeric materials.

Both cold- and warm-gas pressurization concepts were studied. Cold-gas systems (consisting of high-pressure helium) require more volume and are heavier than the warm-gas systems. Warm-gas designs considered both monopropellants and solid propellants. Monopropellant gas generators are slightly larger and may require more development to achieve the high-pressure (7,000 psi) requirement. The major difficulty in designing a solid propellant gas generator is the need to supply sufficient pressure for all trajectories and still not exceed the peak design pressure for the worst case. In order to accomplish this, it is necessary to use multiple propellant grains. Two- and three-grain designs were investigated, both of which will perform adequately for the trajectories being considered. The three-grain configuration is recommanded, as it will provide more flexibility.

A considerable number of other investigations have been performed to ensure that the conceptual design will meet all requirements for an operational vehicle. These studies include: (1) initiation of the transpiration system, (2) evaluation of mass properties, (3) power and instrumentation requirements, (4) response to a nuclear encounter, (5) performance under environmental conditions, (6) reliability, (7) safety, (8) long-term storage, and (9) manufacturing. No unresolved problem areas were discovered during any of the above investigations. For this reason, it is felt that no major design changes will be required during the development phase.

Some of the more important results from these studies are the following. System initiation will be obtained using a combination of timers and acceleration switches, depending upon the type of control system contained within the vehicle. Materials were selected to provide maximum strength and resistance to corrosion, and to minimize weight. A stainless steel, 17-4 PH, was chosen for all metallic parts in contact with water. The system design resulted in a total weight of 16.88 lb, including 3 lb of water, and was packaged in less than 25 in., measured with the nosetip. Protection from a nuclear encounter was provided by applying a shield between the substructure and expulsion system.

A ranking system was developed to aid in the selection of a preferred design. The results obtained with this system indicate that the best design for the

current ground rules, including a development schedule of one year or less, consists of a volume-compensated, deceleration-sensing flow-control valve, a flexible nonmetallic bladder, and a three-grain solid propellant gas generator. Development test plans have been generated for these concepts as well as several alternates for extended development schedules. These plans are included in a separate report.

A rocket sled test was performed to gather information on the response of a porous nosetip to a very heavy rain environment. The sled passed through 2,400 ft of rain with a water content of 6.87 gm/m^3 at an average velocity of about 5,180 ft/sec. Some damage did occur; however, it is very difficult to translate these results to a flight situation because of the extreme differences in environment.

Section 2
NOSETIP DESIGN

In order to arrive at a final nosetip design, several analytical tasks were accomplished in sequence. The specified nose radii cover the range of interest from the standpoint of vehicle performance and design. Aerodynamic heating distributions were received for these hemisphere-cone configurations for the specified set of reentry trajectories. A boundary layer blocking analysis was performed to determine the thermally ideal coolant distributions that are required. These distributions were integrated over time to yield, for each trajectory, the thermally ideal coolant weight as a function of nose radius and conical skirt length. For each nose radius, the space available for heat shield was evaluated as a function of cone length. This evaluation is simply based on geometric relationships and takes into account the required space for the substructure and the coolant supply tube. Then, by conducting a heat shield ablation analysis, the required heat shield thickness on the cone was evaluated as a function of distance from the hemisphere-cone junction. After applying the necessary design margin, this required thickness distribution was compared with the geometrically available distribution to define the required nosetip conical skirt length for each nose radius.

These skirt length requirements were used in conjunction with the thermally ideal coolant weights related to the nose radius and skirt length to define the thermally ideal coolant weight for each nose radius. The minimum weight value defined the optimum nose radius-skirt length combination.

It was then necessary to conduct the hydraulic design of the nosetip to define the inner contour, the material permeability, and the coolant pressure requirements. The objective was to closely match the design coolant distribution at the nosetip surface with the thermally ideal distribution increased by the desired margin of safety. The nosetip inner contour was approximated by first conducting one-dimensional analyses for various ratios of coolant

Preceding page blank

pressure to stagnation pressure. After selecting a value for the design pressure ratio, a three-dimensional porous flow analysis was conducted to refine the inner contour and select the required nosetip permeability to obtain the desired coolant distribution.

The reentry conditions selected for the point design of the nosetip were from the L-6 trajectory at the time of peak coolant flow, which was 34 sec after reentry at 300,000 ft altitude. In selecting the conditions that required peak coolant flow, coolant wastage was minimized for the trajectory.

2.1 IDEAL COOLANT FLOW

Ideal coolant flows were computed for the five trajectories and the three nose radii. This was accomplished by solving an energy balance, as described in Appendix A. Although it would be theoretically possible for the tip to perform adequately with these flow rates, there are a number of uncertainties which cannot be easily included in the basic analysis. For this reason, a design safety margin was determined using the following parameters: nosetip permeability variation and measurement accuracy, porous flow prediction, external pressure and heat transfer, and coolant effectiveness.

The primary source of information for evaluation of this margin was the ongoing vehicle test program currently being accomplished at MDAC. The reasons for emphasizing this program over past efforts are that improvements have been made in (1) the techniques of obtaining permeability data, (2) the porous flow analysis methods, and (3) the method of regulating flow rates in the nosetip environmental tests.

Errors in permeability measurement are among the most difficult to determine. It is estimated that it is possible to measure permeability within 10 percent. Permeability variations within the porous material can be measured in a gross sense. It has been found that material can be made which has variations of less than 10 percent.

The accuracy of the coolant flow prediction is also difficult to determine because it is not possible, using current techniques, to precisely measure the point-to-point flow. However, the total flow through the tip can be

measured and compared to that predicted. While it may be argued that matching total flows is not valid, it does seem to be a reasonable approach. This is particularly true when one considers that deviations from the actual distribution would be most important at the stagnation point and that margins have been experimentally obtained at this point to verify the flow. These margins will be discussed in subsequent paragraphs. A comparison for total flow rate for an actual flight test using the latest analytic techniques is shown in Figure 2-1. As can be seen, the worst error is about 5 percent. This type of error has also been observed in comparisons of analysis to probe data. However, the accuracy of the probe has not been determined.

Uncertainties in the aerothermodynamic environment to be considered during this study were defined by the contract. A 5-percent variation in pressure and a 15-percent variation in heat transfer were specified.

The uncertainty in the coolant effectiveness was evaluated using the results of the recent series of tests performed at MALTA and at Philco-Ford. A summary of the results obtained at the stagnation point for these tests is shown in Figure 2-2. A more detailed description of these tests and a complete comparison to predictions is available in Reference 2-1. Only the stagnation-point results were used in order to eliminate the influence of upstream injection. If this phenomenon were included, the coolant requirement could be drastically reduced. For the MALTA test series, two points at zero angle of attack are of the most interest. One of these shows that melting of the tip occurred with a margin of -4 percent. The other indicates that a liquid layer still existed with a margin of +9 percent.

The ADP data are not quite as definitive as those obtained at MALTA. This is due to the facts that film coverage was not as good and that the films themselves were more difficult to read. This is particularly true in defining the point at which the liquid film disappears and oxidation begins. However, the onset of melting was easier to define. Two points are of interest. One test with an angle of attack of 0 deg indicated that melting did not occur until the margin dropped below -5 percent. The other test, with an angle of attack of 7.5 deg, showed that melting occurred at a margin of +2 percent.

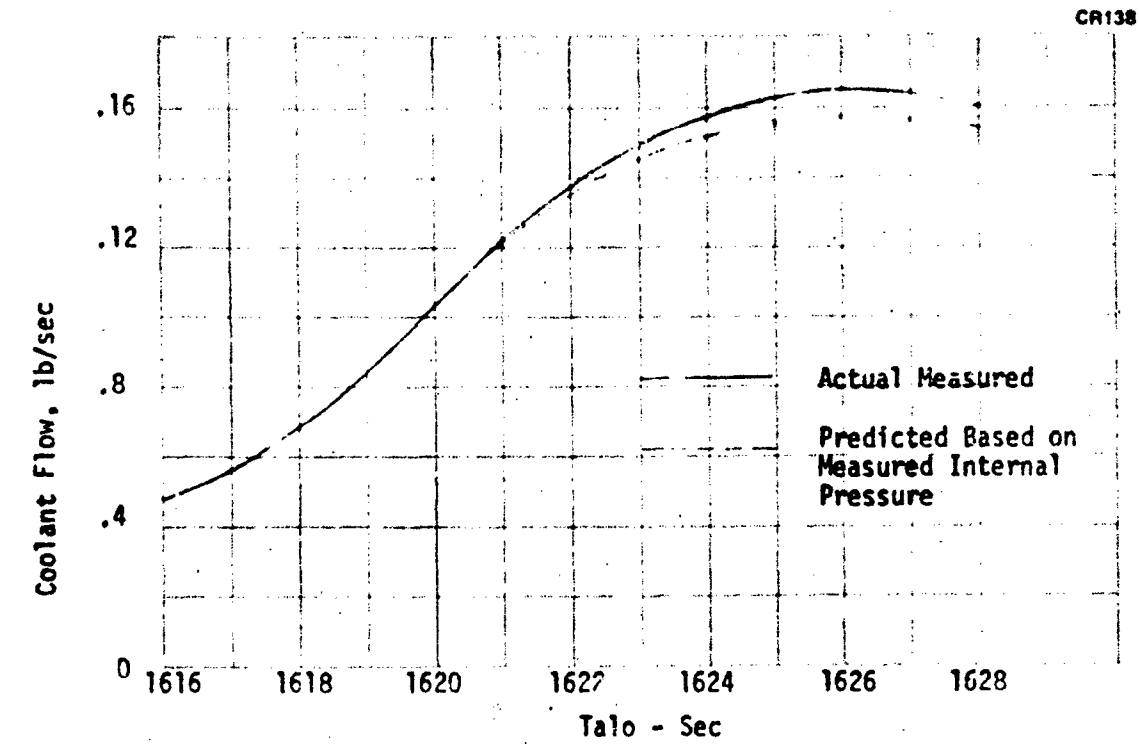


Figure 2-1. Coolant Flow Comparison

Based on the results of these two test series, the point at which the nosetip will melt occurs between a margin of 8 percent to 9 percent and 2 percent. With this as a guideline, an uncertainty in the coolant effectiveness calculation of 10 percent has been assigned.

The overall design factor of safety is obtained by combining the effects of all these parameters. Table 2-1 summarizes the uncertainties assigned to each of the parameters. When these uncertainties are combined using a root sum squaring (RSS) procedure, the resulting safety factor is 1.24. This factor will be used in the calculation of the design and actual coolant flow requirements.

Ideal coolant flows have been obtained for all trajectories and all nose radii. In order to estimate the effect of nose radii on coolant requirements, Figure 2-3 was constructed. In order to account for heat shield requirements just aft of the tip, a constant diameter of the nosetip base was assumed for

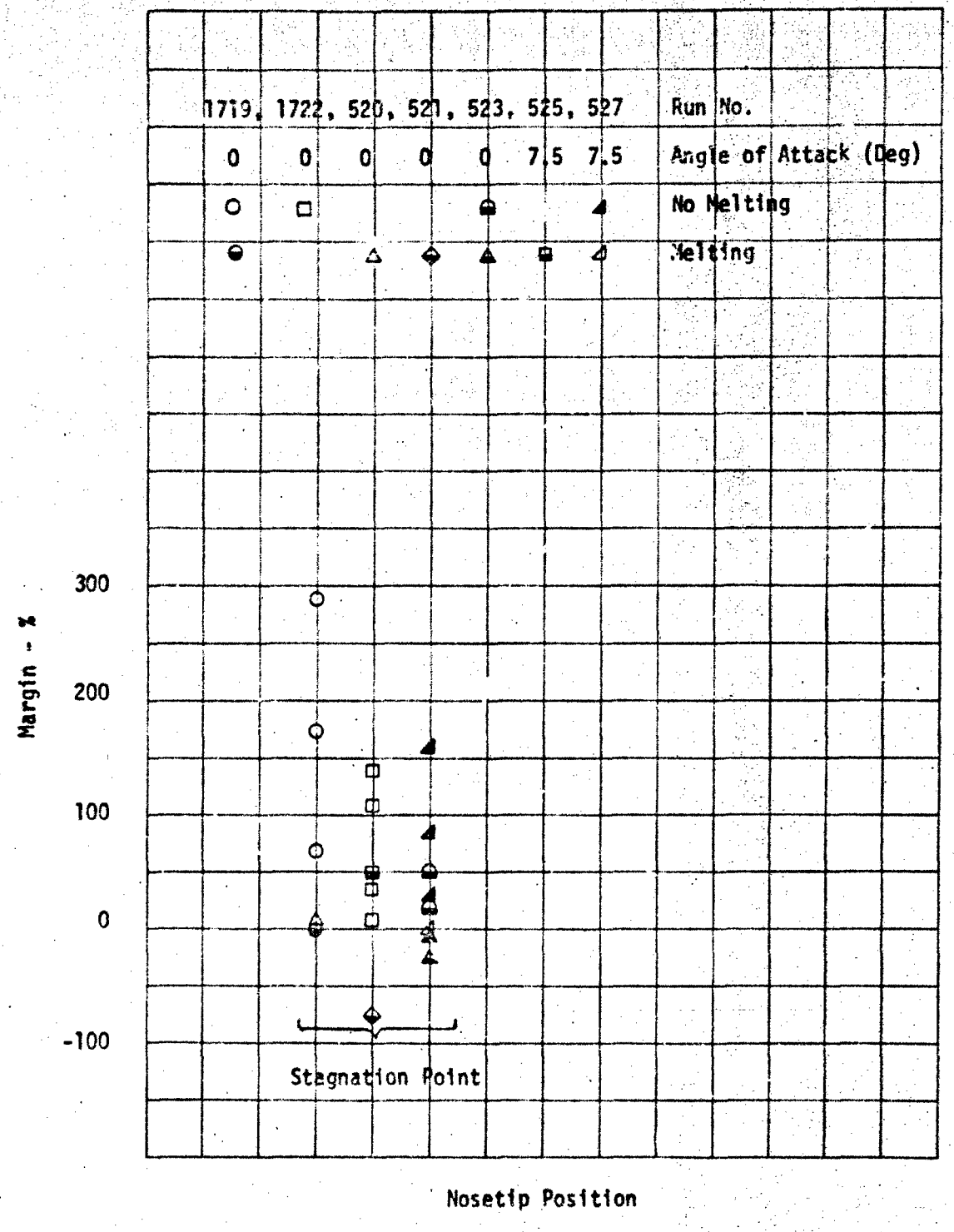


Figure 2-2. Ground Test Coolant Margins

Table 2-1
COOLANT FLOW DESIGN UNCERTAINTIES

Parameter	Uncertainty (percent)
Permeability variation	10
Permeability measurement	10
Porous flow prediction	5
Pressure	5
Heat transfer	15
Coolant effectiveness	10
RSS total	24

each configuration. This diameter is that corresponding to an S/R_N of 1.67 for the 1-in. nose radius configuration. As can be seen, the 1-in. radius results in the least coolant for each trajectory. By comparing trajectories, it can be seen that L-6 defines the total coolant requirement. Additional coolant flow requirements for specific geometries will be presented in the following section.

Figure 2-4 shows the total ideal coolant requirement histories for all trajectories considering a 1.0-in. radius and flow out the hemisphere portion only. Maximum coolant flow rate is required for the S-3 mission.

2.2 NOSETIP EXTERNAL GEOMETRY

The nosetip external configuration was selected to minimize coolant requirements. The first step was to obtain heat shield requirements for vehicles with all three nose radii. These then allowed the required skirt lengths to be computed. Knowing the skirt length enabled the total ideal coolant to be determined for each configuration. The optimum geometry, or that resulting in minimum coolant, was then selected.

Heat shield ablation calculations were performed for the five specified trajectories and the three nose radii using the supplied environments. These calculations were begun at 125,000 ft altitude and were continued until impact.

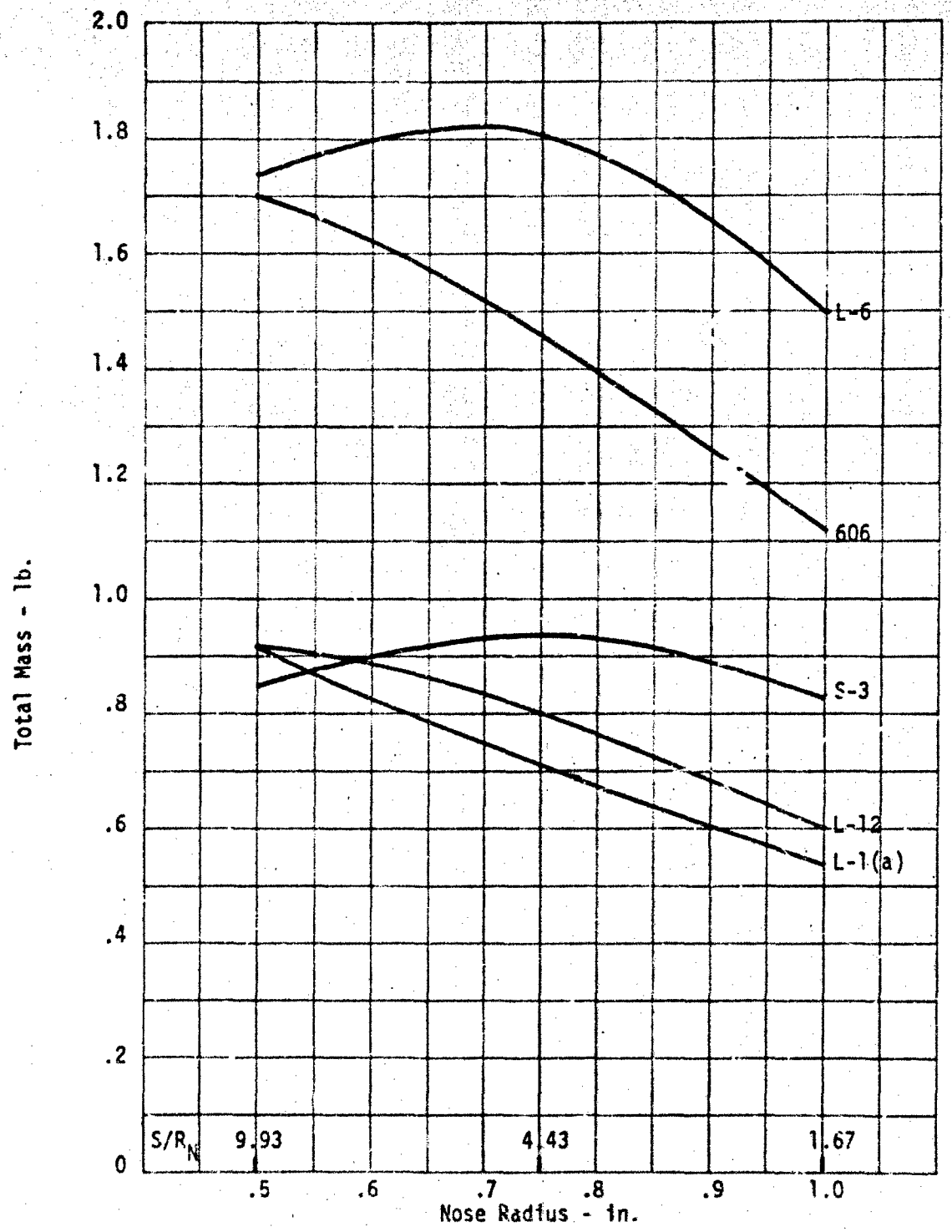


Figure 2-3. Nose Radius Effect on Coolant Requirement

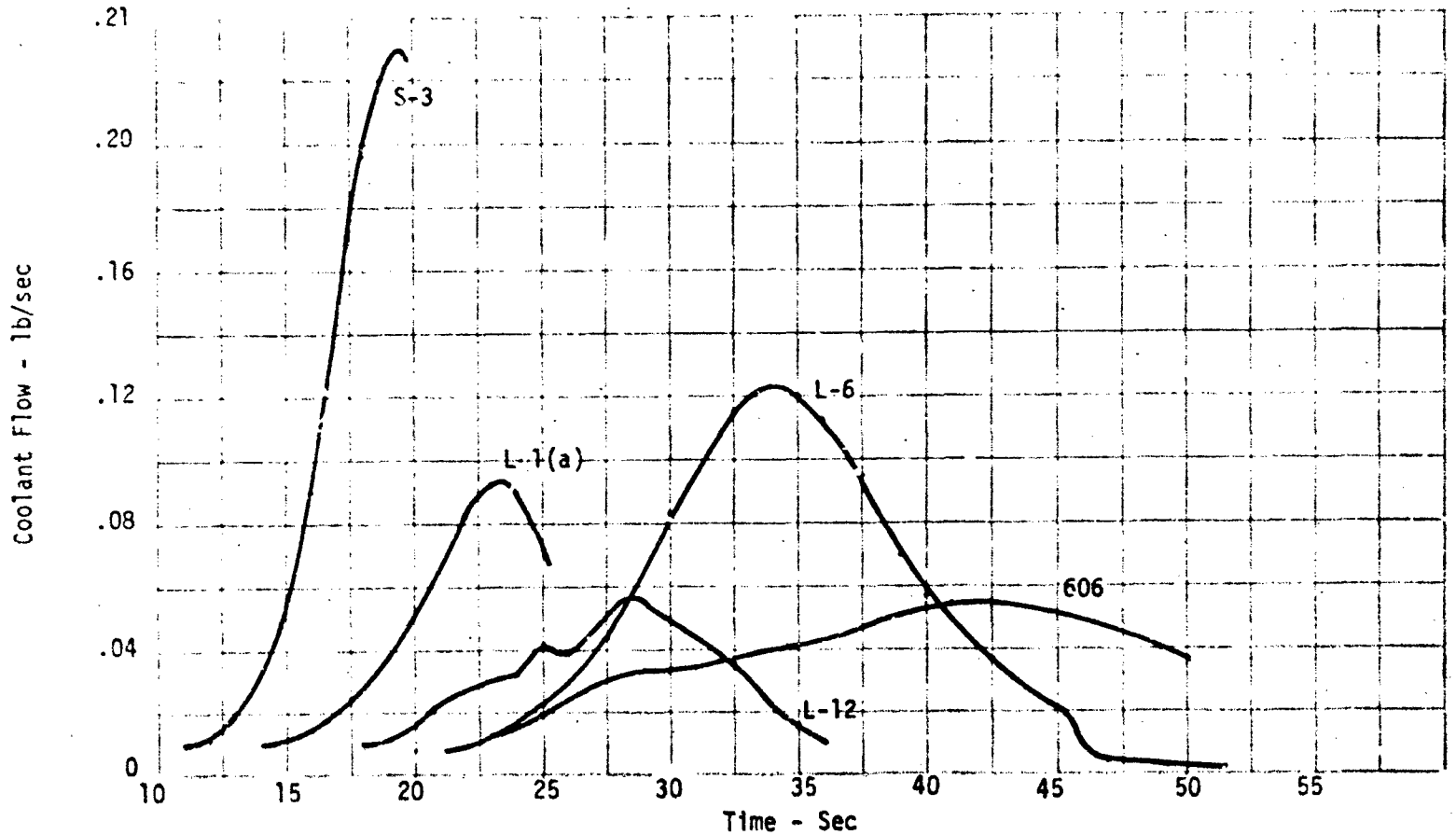


Figure 2-4. Ideal Coolant Histories

Environmental ground rules constrained transition to occur at 125,000 ft and precluded the influence of heat transfer reduction due to downstream cooling and the generation of an aft facing step. Heat shield material was restricted to 5055A carbon-phenolic. All computations were performed using the MDAC F678 computer program (see Appendix B) using cylindrical coordinates. The heat shield thicknesses obtained with these calculations were multiplied by a 1.3 safety factor to account for uncertainties in environment predictions and material properties.

Screening analyses to determine design trajectories and the effect of nose radius were accomplished first. These calculations were performed allowing the substructure to reach a maximum temperature of 400°F. As will be shown later, this condition may result in heat shield failure due to bond outgassing. The results of this screening analysis were not altered by changing this ground rule. Heat shield thicknesses at the tangent point and at the 1.0-ft running length location were obtained for all trajectories and the 0.75-in. radius configuration. Calculations were performed for both the windward and leeward rays. Similar analyses were accomplished for the tangency point on the L-6 trajectory with the 0.5- and 1.0- in. radii. The results obtained are given in Table 2-2.

Table 2-2
PRELIMINARY HEAT SHIELD REQUIREMENTS

Location	Ray	Trajectory						
		L-6	606	L-1(a)	L-12	S-3	L-6 R_N=0.5 in.	L-6 R_N=1.0 in.
Tangent point	0	0.958	0.756	0.442	0.468	0.474	0.988	0.930
	180	0.770	0.405	0.388	0.435	0.410	0.803	0.740
1.0-ft running length	0	0.775	0.984	0.839	0.543	0.364		
	180	0.463	0.424	0.260	0.388	0.312		

Based on the results presented in this table, the heat shield design trajectories are the L-6 for all leeside analyses and the near-nose windward, while the 606 is required for windward ray calculations further aft. As can be seen, there is not a large influence of nose radius on heat shield requirement.

Before presenting complete heat shield requirements, it is necessary to discuss the effect of material properties and bondline temperature limit. Figure 2-5 gives the thermodynamic properties of 5055A carbon-phenolic which were used for the initial analyses. The char conductivity did not agree with available experimental data, so a sensitivity study was accomplished to determine the effect.

In general, the effect of char thermal conductivity on heat shield requirements is fairly small. However, for long missions, such as those being studied here, where a thick char layer is built up and the heat can soak into the material, the effect is significant. A survey of char thermal conductivity information has been accomplished (see Figure 2-6). Very little experimental data is available, and the data that has been generated is not for the exact material being used on this study due to variations in manufacturing technique and cloth layup angle.

The General Electric correlation (References 2-2 and 2-3) and the original MDAC correlation were obtained from flight and ground test data reduction and have been used to correlate this type of data. The Boeing curve (Reference 2-4) was obtained using a theoretical approach. The rapid increase at higher temperatures is due to radiation through the char.

Another correlation was generated and is shown in Figure 2-6 as the final curve. This is essentially the original relationship with a T^3 term to account for radiation effects. These values have been used for all heat shield sizing presented in this report.

To illustrate the effect of conductivity, Table 2-3 has been constructed. Three locations were compared for three conductivity correlations. There is only a small difference in heat shield requirements using the original and

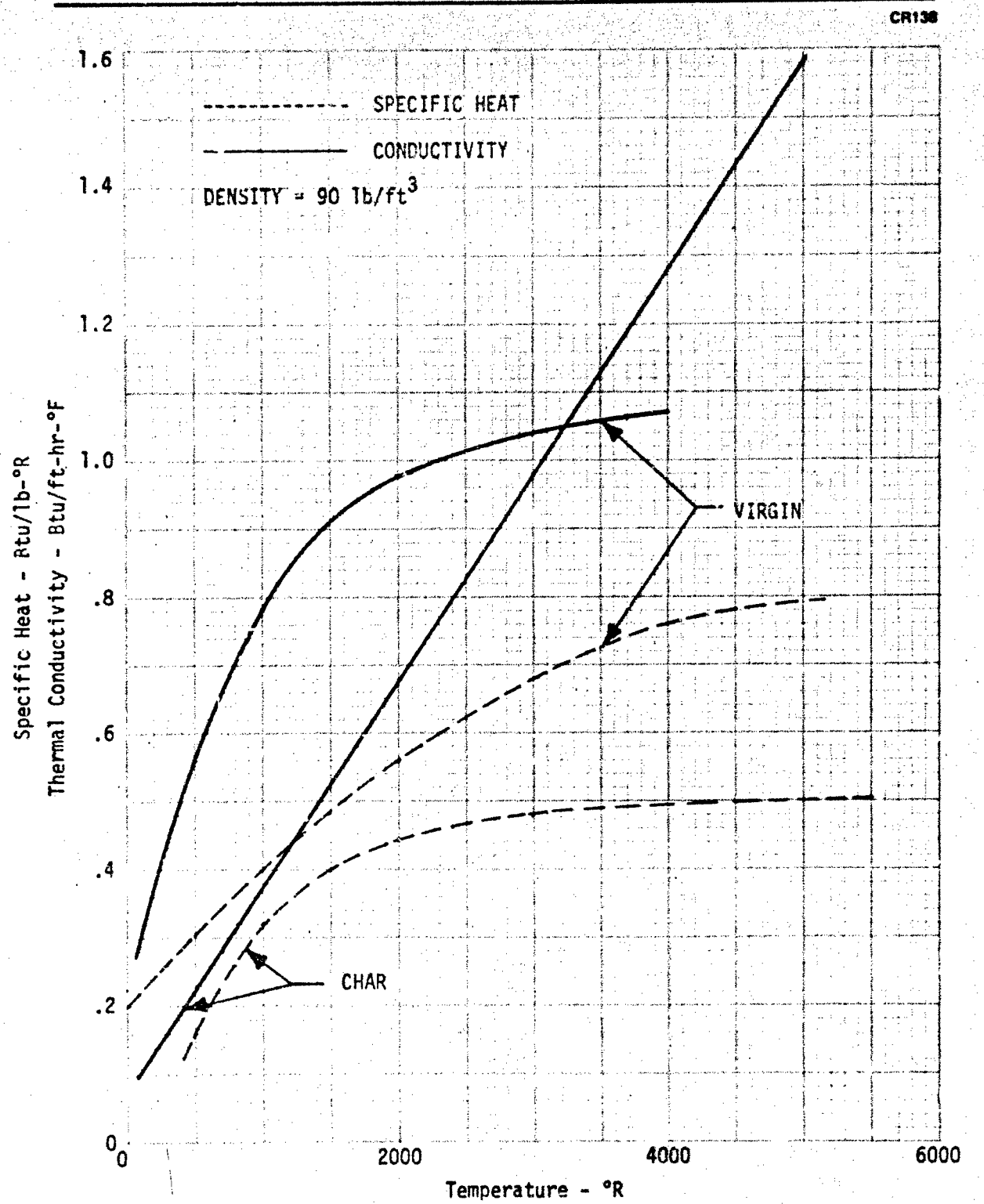


Figure 2-5. Material Properties for 5055A Carbon-Phenolic

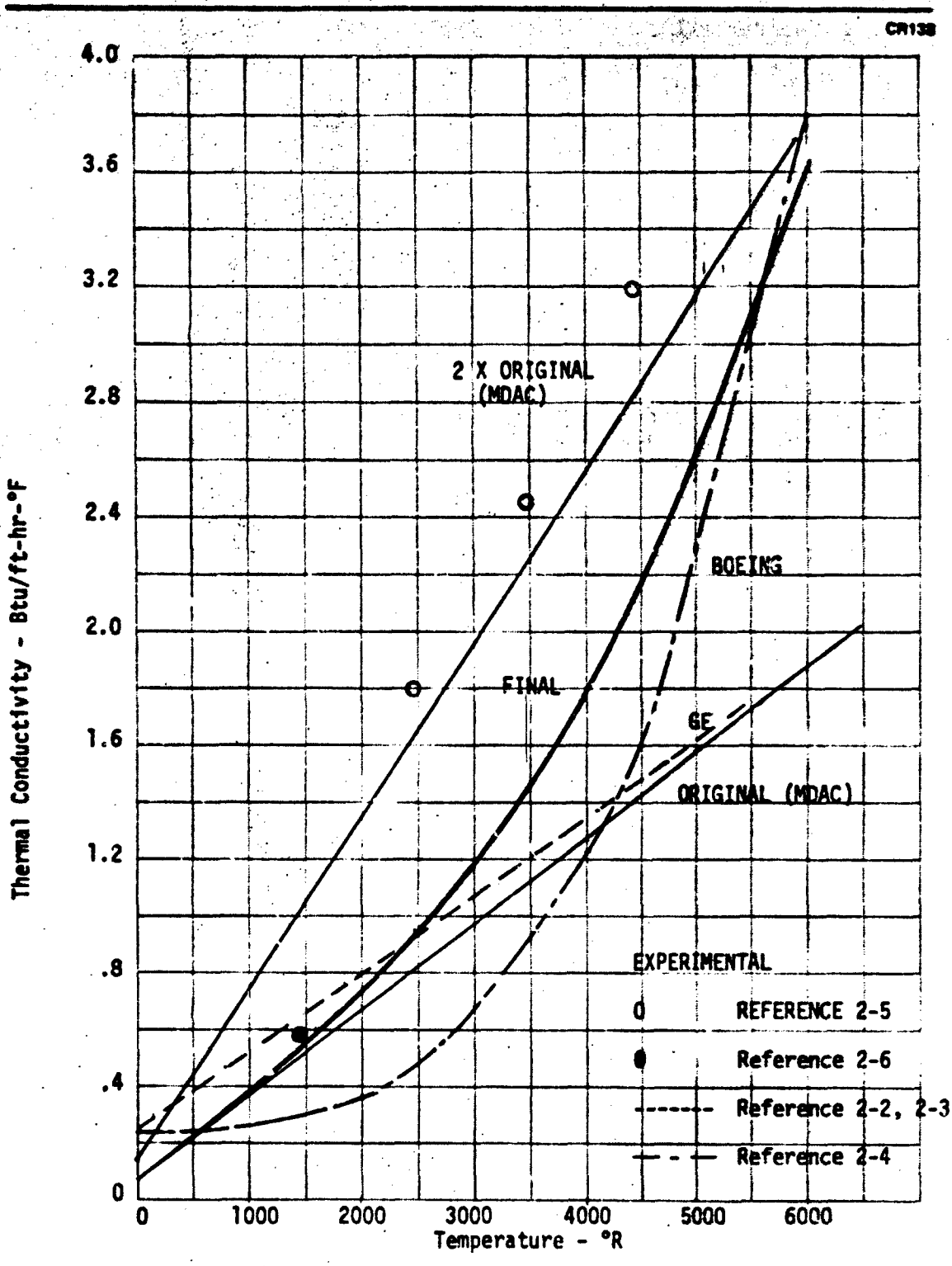


Figure 2-6. 5055A Carbon Phenolic Char Conductivity

final correlation. This is due to the fact that at lower temperatures, the values at which most of the char layer exists, there is only a small difference in conductivity. For the twice original correlation, there is a large difference at these temperatures which translates into much larger heat shield requirements.

Table 2-3

CONDUCTIVITY EFFECT ON HEAT SHIELD REQUIREMENTS

Location	Conductivity		
	Original	2 X Original	Final
$S/R_N = 1.67$, $R_N = 1.0$, Trajectory L-6, windward	0.95	1.04	0.975
$S/R_N = 1.67$, $R_N = 1.0$, Trajectory L-6, leeside	0.79	0.95	0.82
$S/R_N = 5.76$, $R_N = 1.0$, Trajectory 606, windward	1.12	1.22	1.14

As previously mentioned, during the calculation of the original heat shield requirements it was assumed that the bond layer could act as an insulator and could achieve high temperatures. While this assumption allows smaller heat shields (Table 2-4), it may also result in failure of the heat shield due to pressure buildup. Computations were performed to determine internal pressures and allowable pressures for the heat shield.

A short literature survey was accomplished to obtain carbon-phenolic permeability data and decomposition data for EPON 934 bond. Very little permeability data was available, so a parametric investigation was accomplished. Two values, 0.4×10^{-10} and 0.5×10^{-9} in.^{2}, were considered. Available data indicated that fully charred permeability was about 0.3 to 0.7×10^{-10}, so the values assumed are probably optimistic. For this reason, only the results of the lower permeability are presented. Decomposition information was obtained for EPON 934 in the form of TGA data and is presented in Figure 2-7. Calculations were performed at the point of maximum heat shield requirement for a 1.0-in. nose radius configuration.

Table 2-4

EFFECT OF BOND TEMPERATURE ON HEAT SHIELD REQUIREMENTS

Location	High-Temperature Bond (Bond/Substructure =400°F)	Low-Temperature Bond (Bond/Heat Shield=400°F)
$S/R_N = 1.67$, $R_N = 1.0$, Trajectory L-6, windward	0.93	1.04
$S/R_N = 1.67$, $R_N = 1.0$, Trajectory L-6, windward	0.85	0.95
$S/R_N = 5.76$, $R_N = 1.0$, Trajectory 606, windward	1.09	1.22

Figure 2-8 gives the temperature and pressure at the bond-heat shield interface as a function of time for two values of char thermal conductivity. The results for the final conductivity, as previously discussed, would lie between these two but would be closer to the original curve. The critical point, or point of peak pressure, occurs for an interface temperature of about 700°F for both conductivities. At this temperature, the bond is outgassing at a high rate while phenolic decomposition has only begun. Maximum pressures are 235 psi and 150 psi for the high- and low-conductivity values, respectively.

Stress calculations were performed to determine the pressures which the heat shield could withstand without failure. These calculations were performed at the peak pressure point. The amount of heat shield material still having strength is of great importance; however, there is very little strength data for 5055A above 500°F and none above 1,000°F.

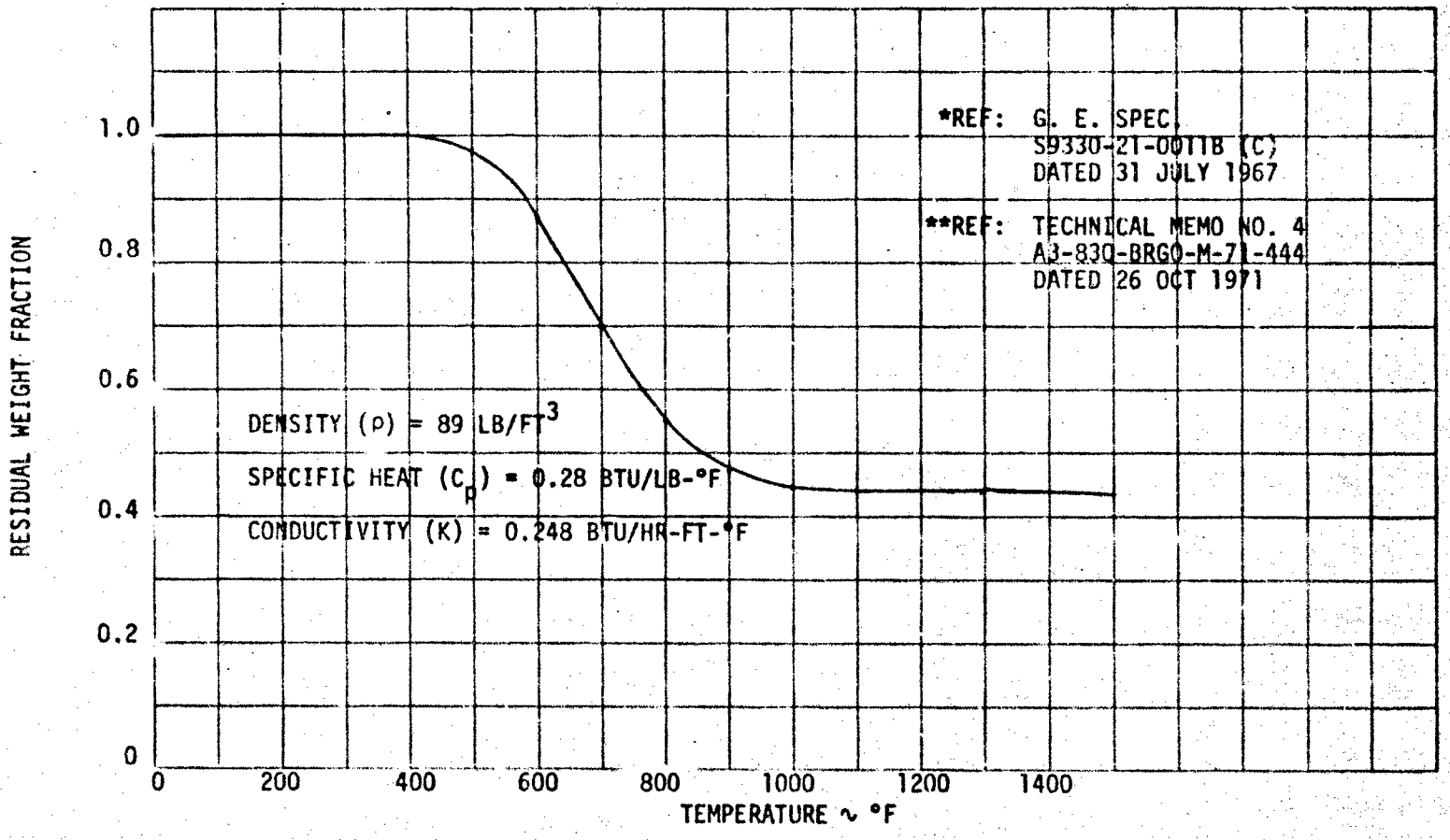


Figure 2-7. Thermogravimetric Analysis* and Properties** of EPON 934

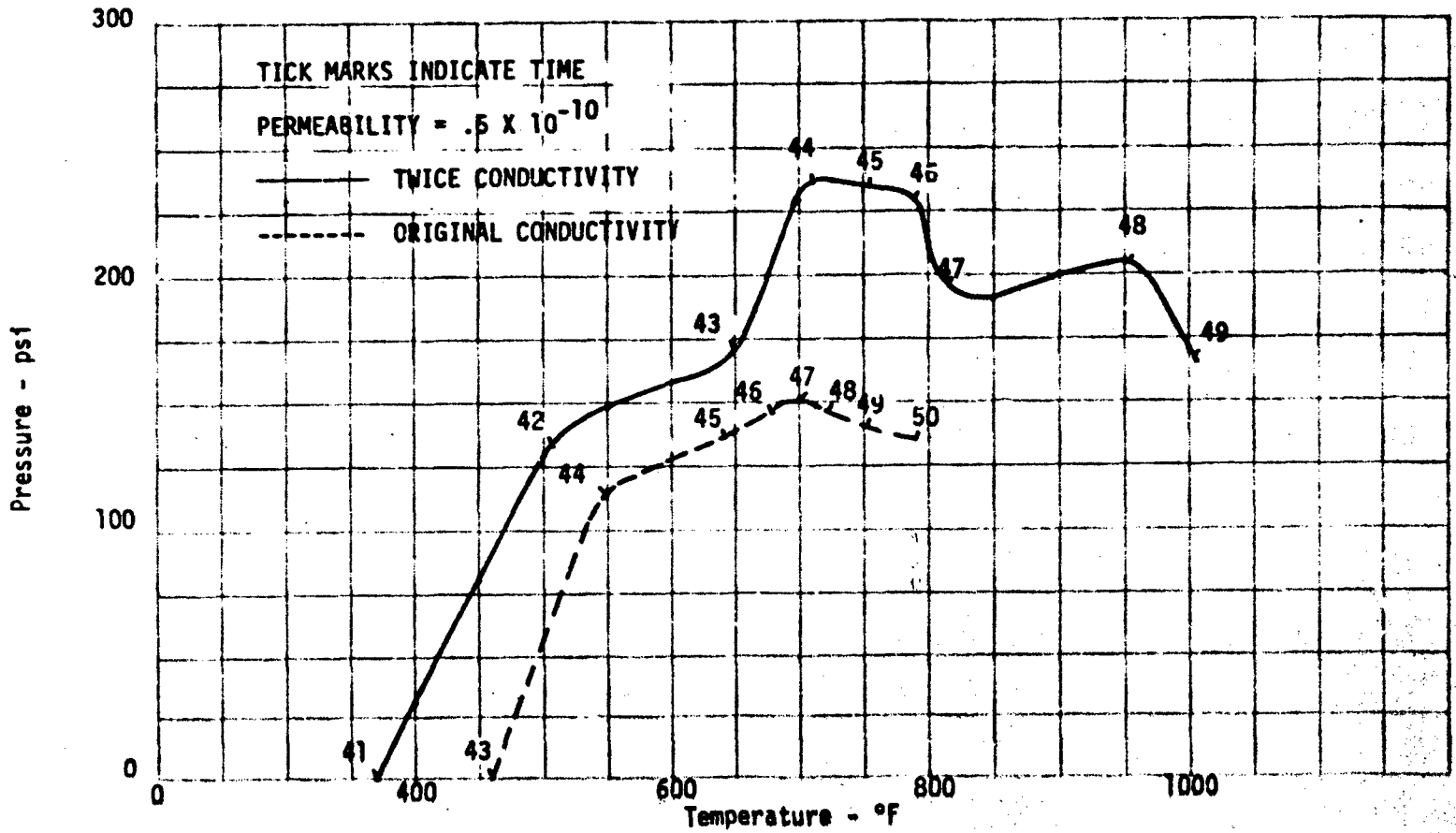


Figure 2-8. Temperature and Pressure at Bond Surface

Allowable pressures were computed assuming that char had strength up to temperatures of 1,000 and 2,000°F and are presented in Table 2-5. As can be seen, the lower temperature limit results in an allowable pressure considerably below those predicted, while the upper temperature yields a value roughly equivalent to those calculated.

Table 2-5
ALOWABLE PRESSURE

Maximum Char Temperature (°F)	Pres re (psia)
1,000	46
2,000	206

This analysis has shown that through the use of fairly optimistic assumptions, the allowable pressures are about equal to those predicted. This does not result in a high-confidence design. In addition, a time point later in the flight, although having a lower pressure, may have much less strength in the char layer. Therefore, the use of the bond as an insulating material will not be used during this study.

Using the final correlation of char conductivity and limiting the temperature at the back face of the carbon-phenolic to 400°F, heat shield requirements were computed. Most calculations were performed for the 1.0-in. radius configuration, since it was indicated in Section 2.1 that coolant requirements would be less with this geometry. Enough points were analyzed for the other radii to verify this. The results of this investigation are given in Figure 2-9.

These heat shield thicknesses were translated into skirt lengths and ideal coolant requirements. Skirt lengths were obtained by defining the smallest nosetip base diameter which will contain the heat shield, a 0.04-in. bond layer, and the coolant supply wand. Two wand diameters, 0.125 and 0.25 in., were considered. A 0.06-in. substructure was included with the larger wand. Skirt lengths are summarized for all three nose radius configurations in Table 2-6.

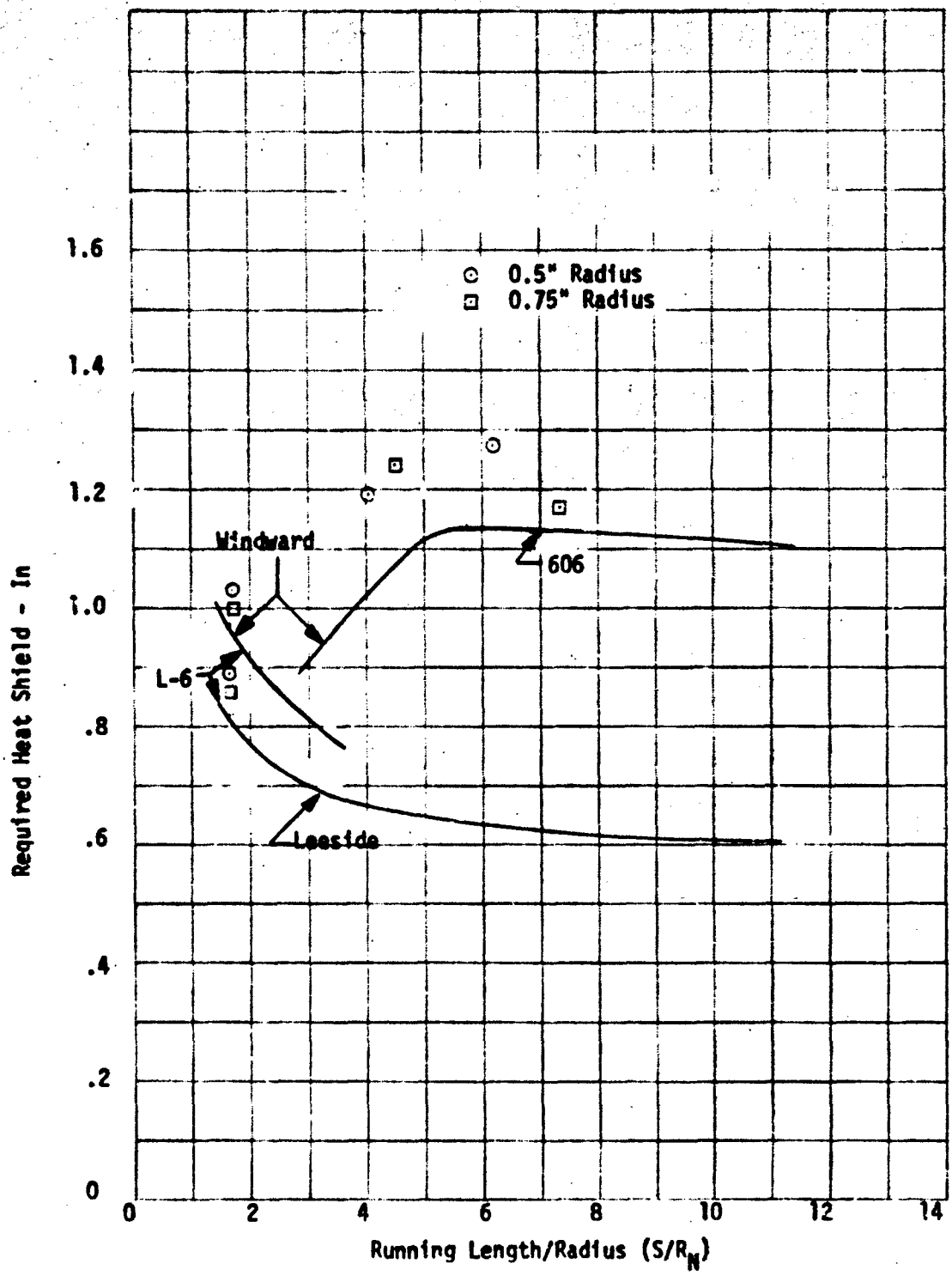


Figure 2-9. Heat Shield Requirements

Table 2-6

SKIRT LENGTH AND IDEAL COOLANT REQUIREMENT SUMMARY

Nose Radius (in.)	Wand Outside Diameter (in.)	Skirt Length (in.)	Coolant Requirements (lb)
1.0	0.125	0.15	1.46
	0.25	0.62	1.75
0.75	0.125	2.25	1.82
	0.25	3.40	2.26
0.5	0.125	4.75	1.95
	0.25	5.65	2.33*

*Denotes 606 trajectory; all others L-6.

For each skirt length, total ideal coolant requirements were found for each trajectory. Maximum requirements are given in Table 2-6. Trajectory L-6 was found to be sizing for all but one case. It is evident that a 1.0-in. nose radius will result in the minimum coolant requirement regardless of the wand diameter. This radius will therefore be used for all further analyses presented in this report. The larger radius also minimizes skirt length, which makes it easier to match actual flow rates to the ideal. This is such an important factor that additional efforts were expended to reduce skirt length to zero.

The primary task was to determine the effect of replacing a portion of the carbon-phenolic immediately aft of the tip with a high-temperature insulator. An optimization to determine the best design was not accomplished. The thickness of the insulation was selected to allow use of a 0.30-in.-diameter wand and to leave several mils of charred carbon-phenolic at impact. This resulted in a 0.13-in. thick layer. A total insulation length of 1.0 in. was assumed. The material selected was Fiberflake (Figure 2-10), manufactured by the Atomic Energy Commission. This material will not be bonded on either side.

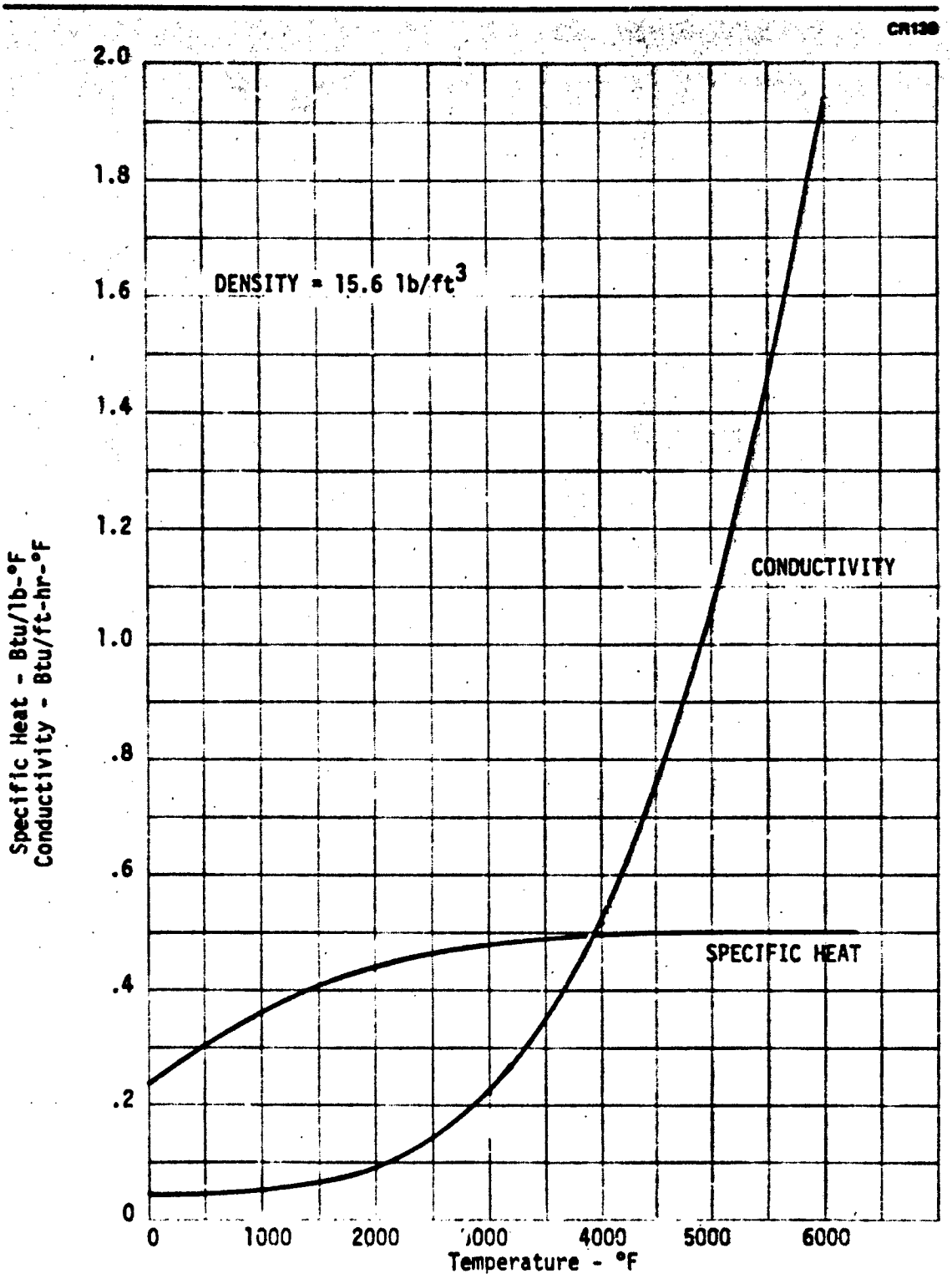


Figure 2-10. Fiberflake Insulation Thermal Properties

The real question in this case is how much heat will be transferred to the coolant through the insulation. Temperature histories of the coolant for the L-6 mission are shown in Figure 2-11. Two cases, one considering a constant coolant inlet temperature of 70°F and the other using a time-dependent temperature from gas generator heating, were analyzed. For this latter case, the peak inlet temperature was 80°F. As can be seen, there is slightly less than a 4°F rise in coolant temperature for both cases. Another analysis indicated that there was essentially no difference in the final temperature if the coolant wand was initially at 100°F rather than 70°F.

Final heat shield design included this insulation layer for the first 1.0 in. aft of the tip. The heat shield requirement distribution for the selected design is given in Figure 2-12. Recession histories and temperature profiles at impact for three important conditions are presented in Figures 2-13 through 2-16.

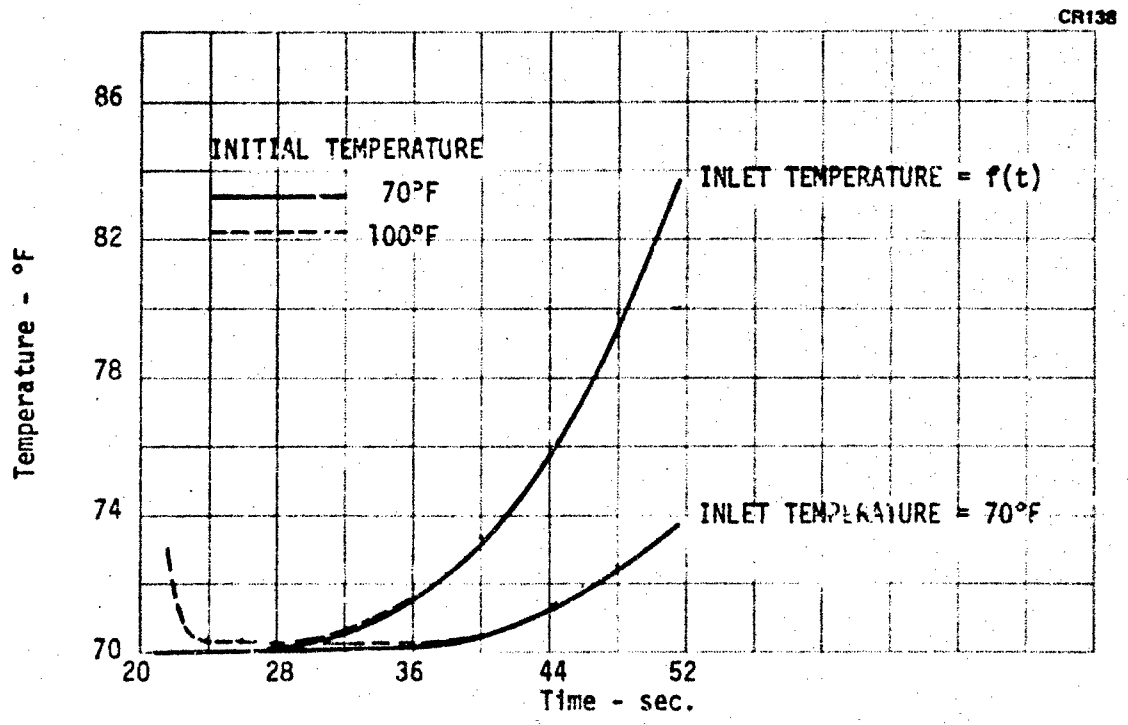


Figure 2-11. Coolant Temperature Histories, L-6

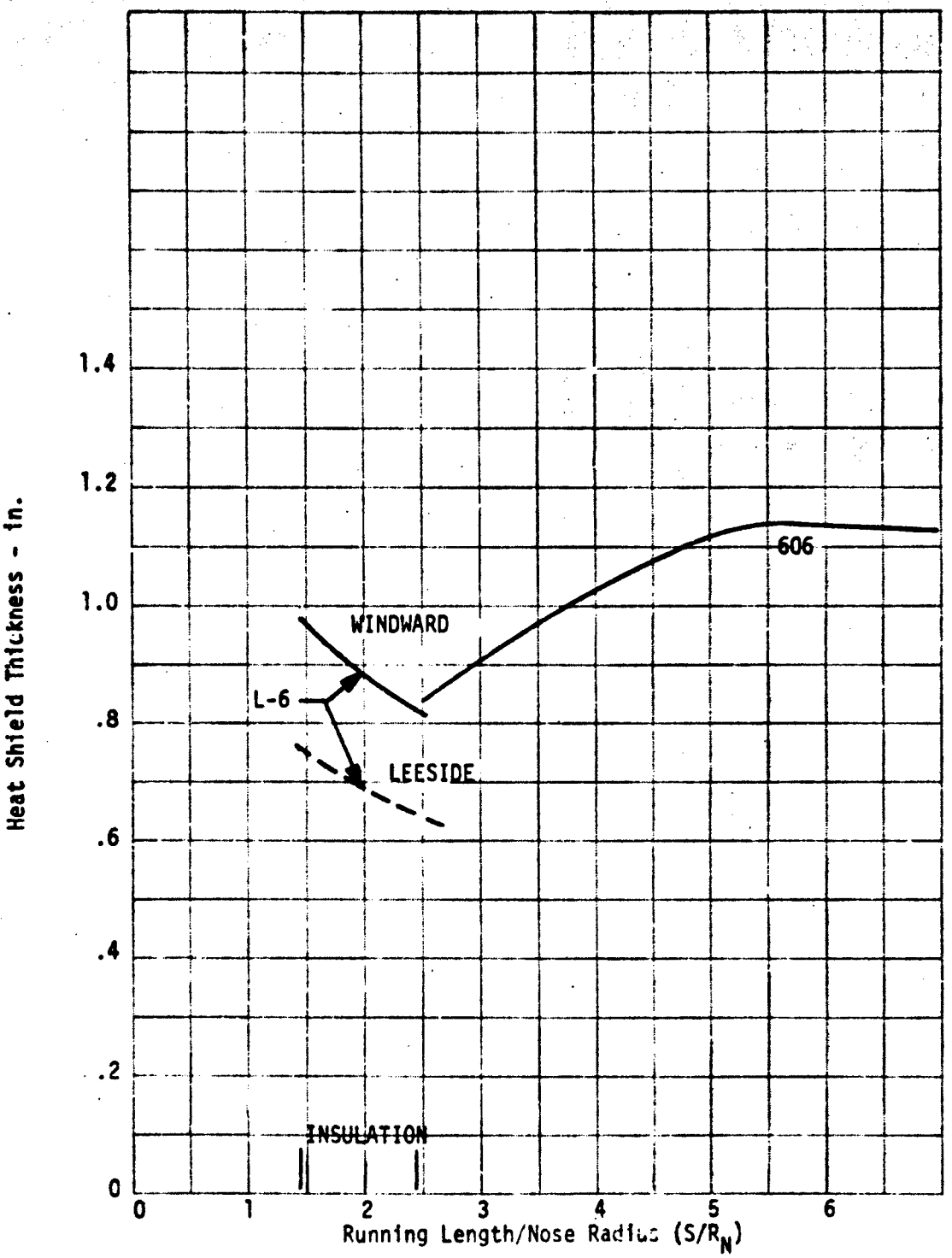


Figure 2-12. Required Heat Shield Thickness

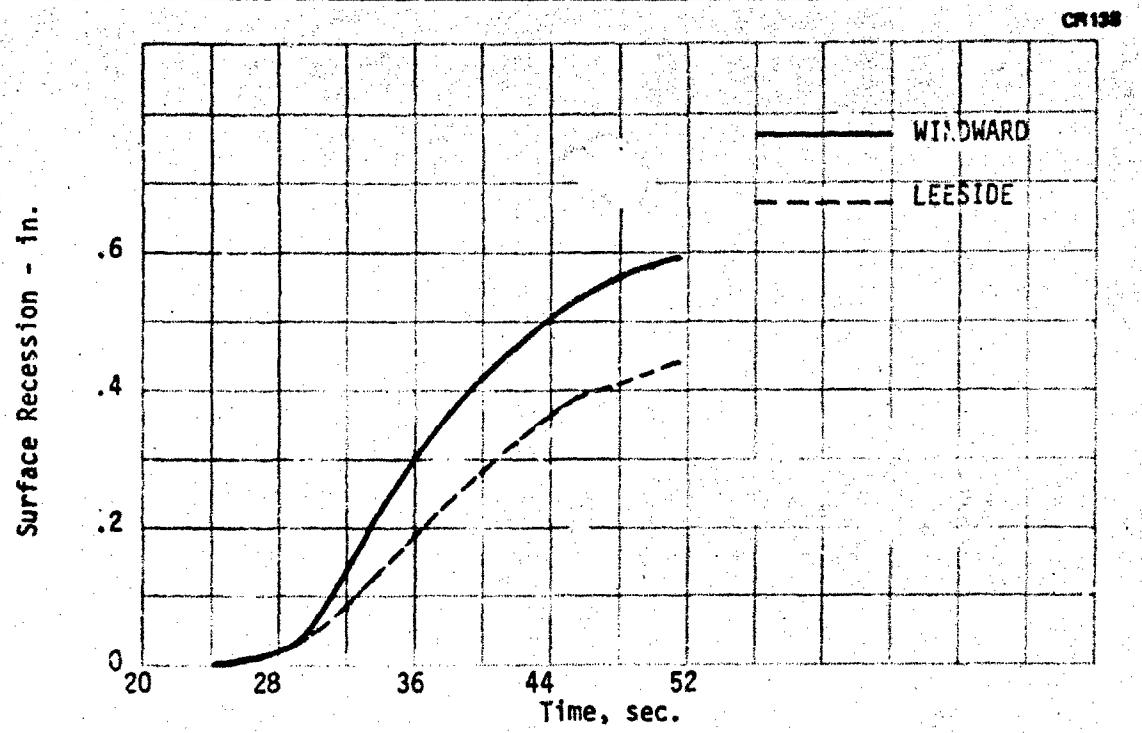


Figure 2-13. Surface Recession Histories, L-6, $S/R_N = 1.67$

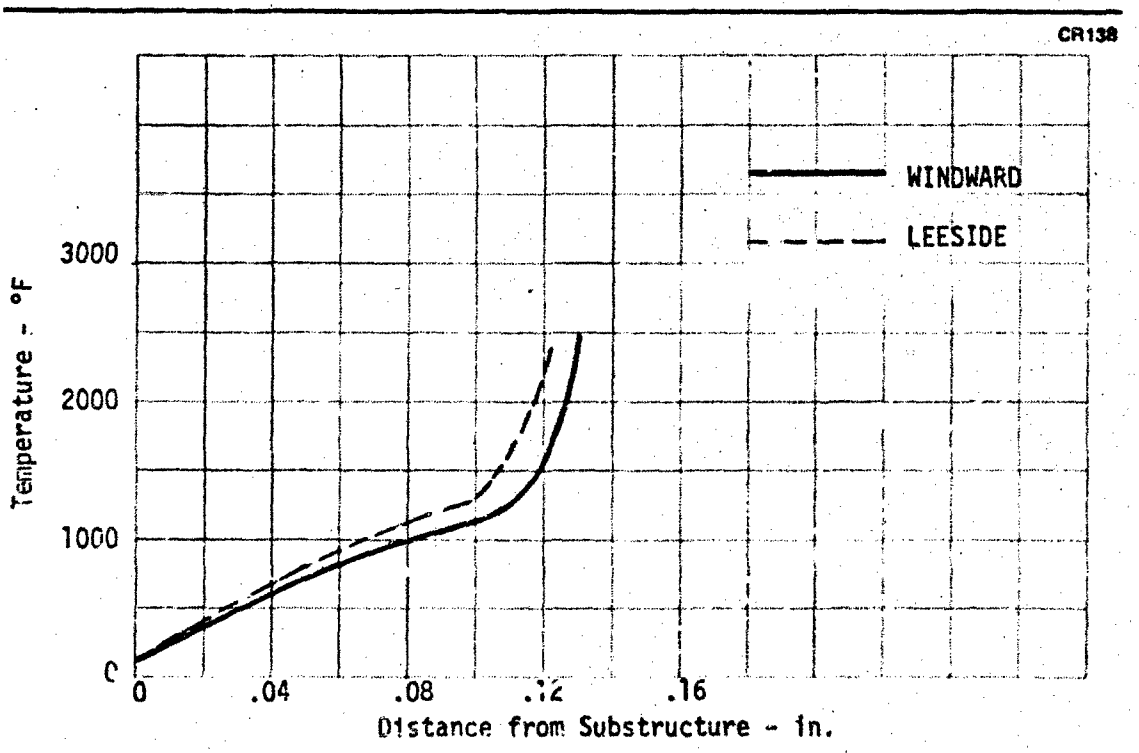


Figure 2-14. Heat Shield Temperature Profile at Impact, L-6

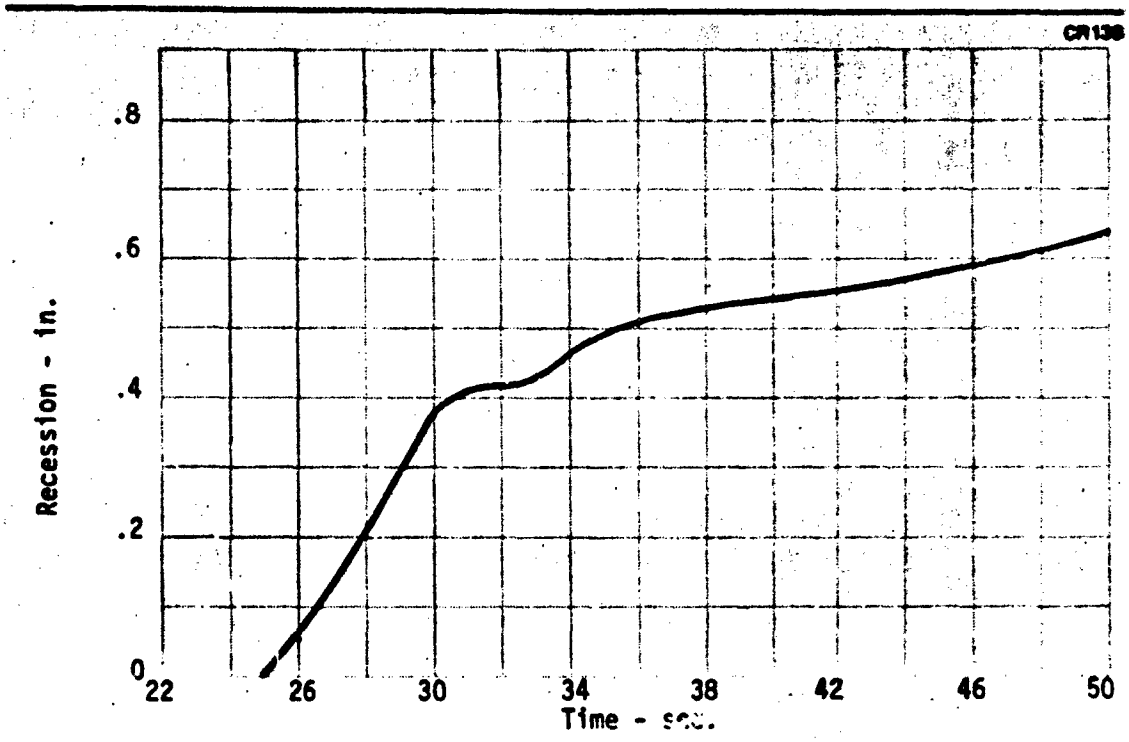


Figure 2-15. Recession History, Trajectory 606, S/R_N = 5.76, Windward

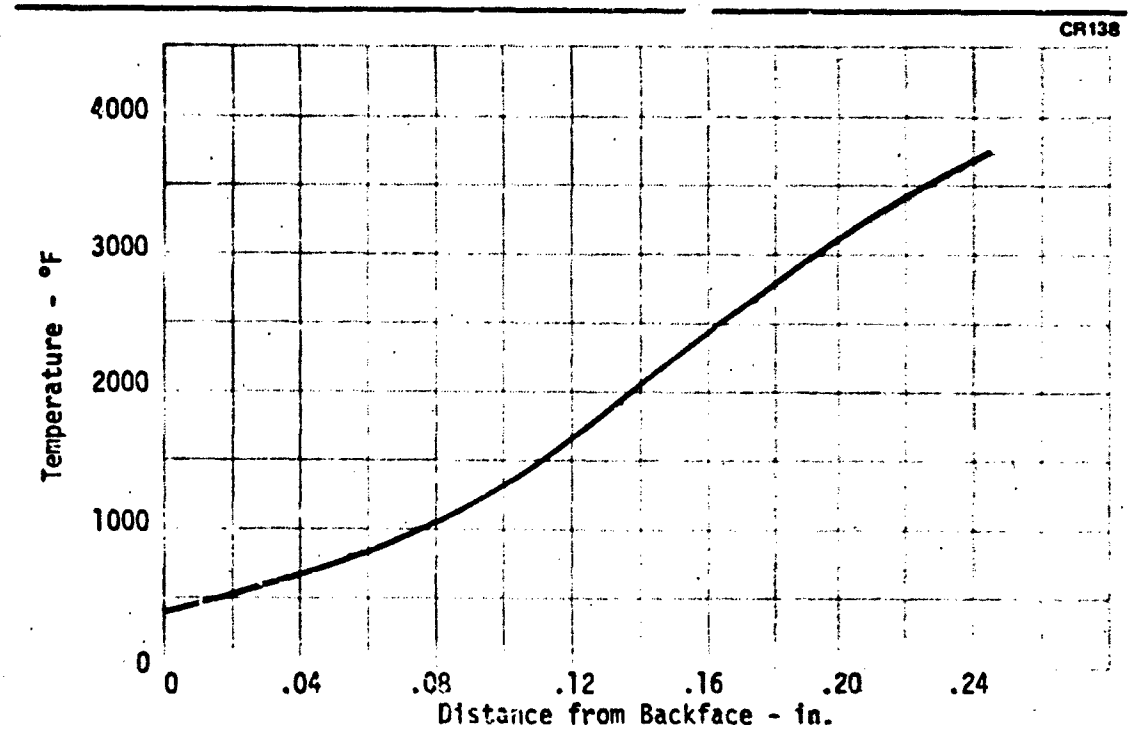


Figure 2-16. Temperature Profile at Impact, Trajectory 606, S/R_N = 5.76, Windward

Ideal coolant requirements with the 1-in.-radius, no-skirt configuration have been evaluated and are presented in Table 2-7. These quantities were used to obtain the final design discussed in the following sections.

Table 2-7
FINAL IDEAL COOLANT REQUIREMENTS

Trajectory	L-6	606	S-3	L-12	L-1(a)
Coolant weight (lb)	1.35	0.99	0.76	0.53	0.48

Although not a part of the original contract, the effect of forming an aft facing step immediately behind the nosetip was evaluated. This step is created by the recession of the heat shield and causes separation of the boundary layer and subsequent reattachment downstream. Convective heating along the surface aft of the step is reduced where the boundary layer is separated and increases during reattachment. A rigorous analysis would require very complex and time-consuming procedures. Since only an estimation of the effect was desired, a simple empirical procedure (Reference 2-7) was followed. This technique essentially modifies the recession rates according to an experimentally defined change in heat transfer coefficient. The correlation used for the current analysis is shown in Figure 2-17.

To verify this analysis technique, comparisons to some experimental data obtained with a low-temperature subliming material (Reference 2-8) were performed. Several cases were analyzed, but only the one for 10 deg angle of attack is included (Figure 2-18). As can be seen, the agreement is extremely good. Although this data was obtained for a low-energy flow (wind tunnel) and not precisely the configuration recommended in this study, it appears that this analysis technique could result in reasonably accurate predictions.

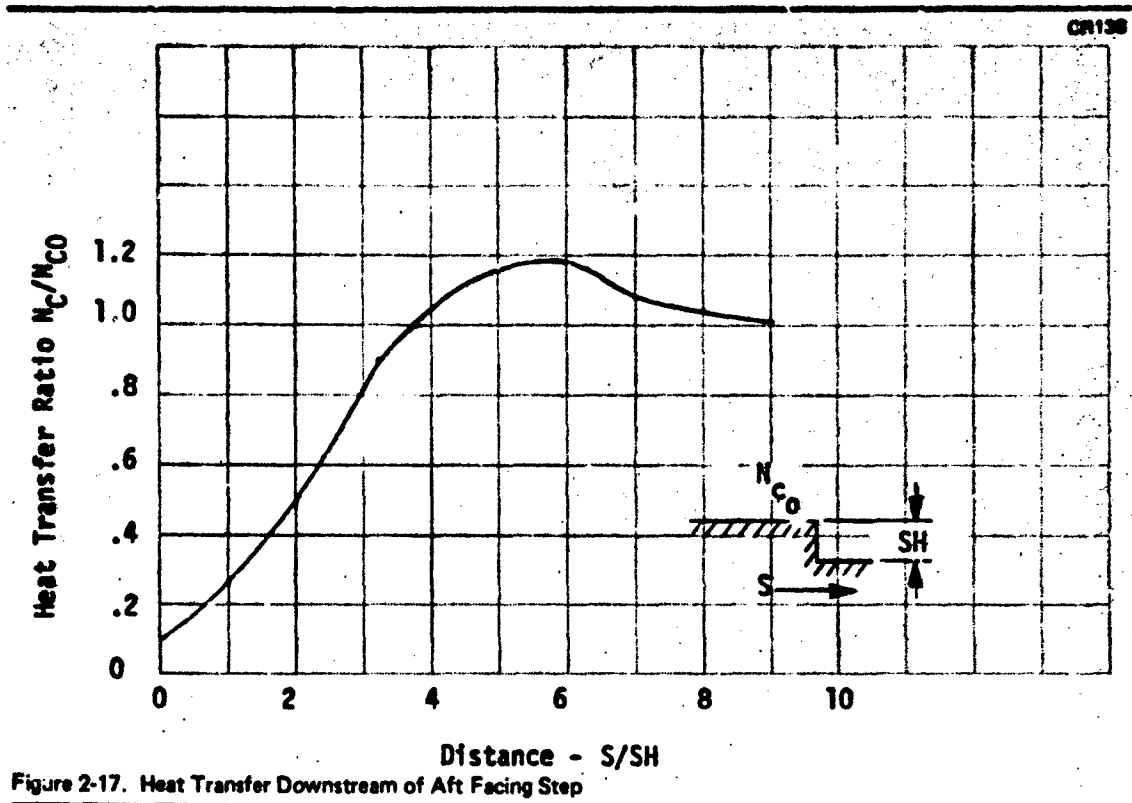


Figure 2-17. Heat Transfer Downstream of Aft Facing Step

The effect of this phenomenon on design requirements has been evaluated for the baseline configuration. The reduction in heat shield thickness is shown in Figure 2-19. This reduction is sufficient to allow operation without a skirt or an insulation layer. It is recommended that this phenomenon be further evaluated in the development phase and that full advantage be taken of this method of reducing skirt length.

2.3 NOSETIP INTERNAL CONFIGURATION

Selection of the nosetip inner contour is accomplished by minimizing the mismatch between the actual and thermally ideal coolant distributions at the nosetip external surface. A good match is obtained by selecting the proper combination of nosetip permeability and inner contour. Due to the large pressure and heating gradients over the surface of the hemisphere, it is this portion of the nosetip that is difficult to design, while the inner contour of a conical skirt can be readily selected to provide an excellent match between

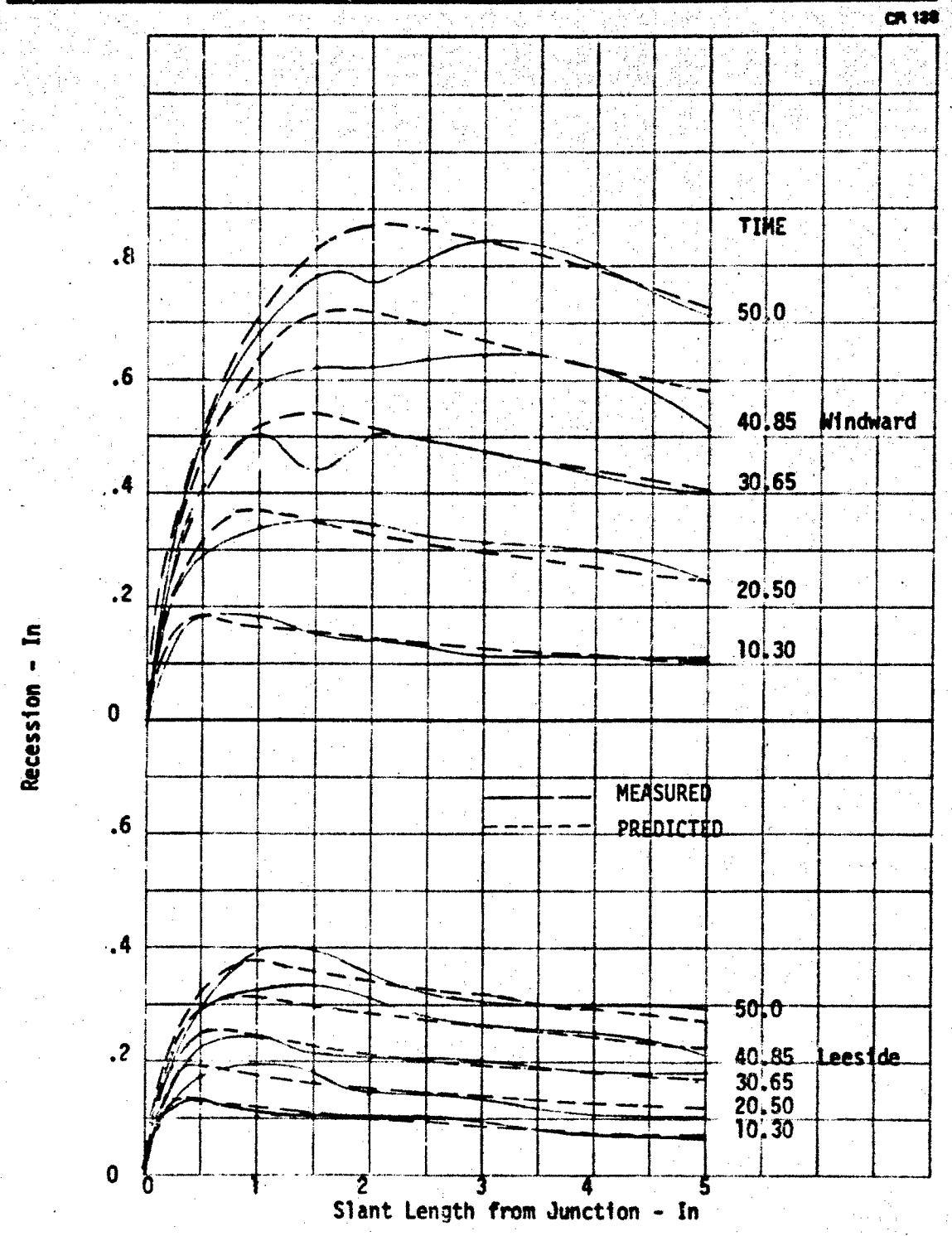


Figure 2-18. Recession Profiles, Test 35, μ = 10, Camphor

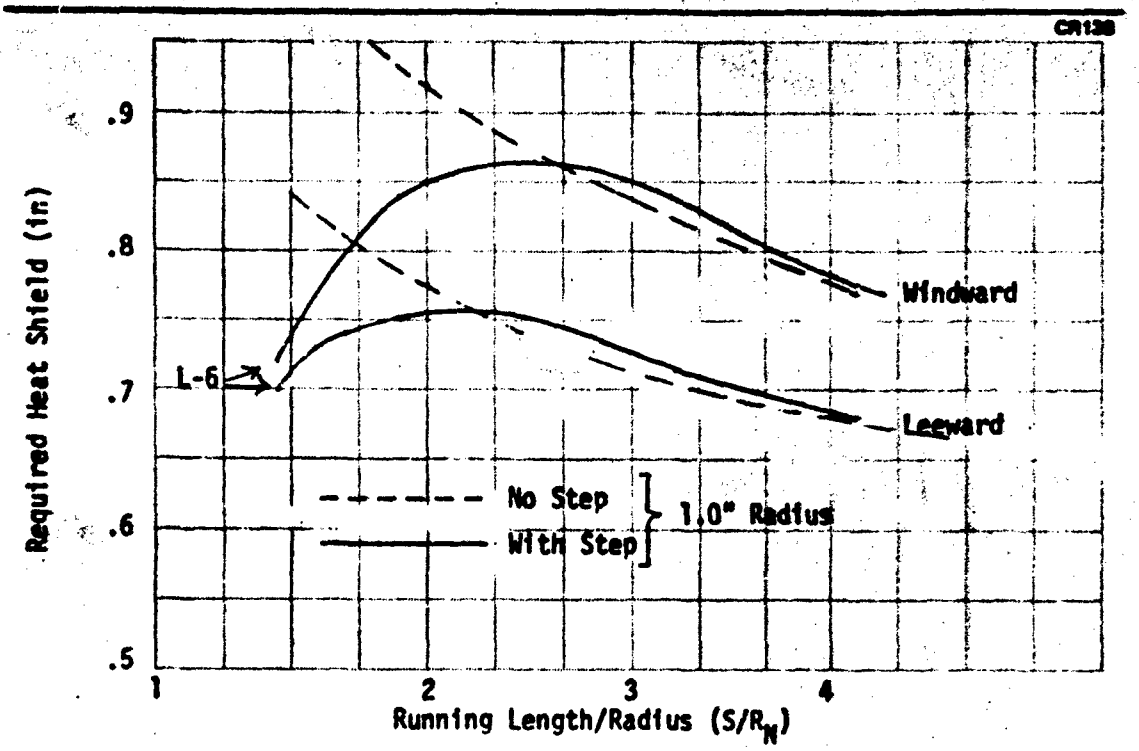


Figure 2-19. Heat Shield Requirements

ideal and actual coolant flux. The inner contour was first approximated using ideal one-dimensional relationships and then refined using a three-dimensional, porous-flow computer program.

2.3.1 Ideal Inner Contours

If it is assumed that the heating on the hemisphere is essentially turbulent, then the equations in Appendix C can be utilized as a basis for approximating the inner contour. It is pointed out in Appendix C that peak turbulent heating occurs about 34 deg from the stagnation point. Referring to Equation C-19, it can therefore be deduced that the desired coolant distribution is approximated by

$$\frac{\dot{m}_\theta}{\dot{m}_{34}} = \frac{1.88\,\theta^{0.6}\,(0.275)^{0.8\theta^2}}{(1.0 - 0.1667\theta^2)^{0.7}} \qquad (2\text{-}1)$$

The inertial component of the porous flow pressure gradient is generally much smaller than the viscous component. Therefore Equation C-24 can be reduced to

$$P_{in} - P_{out_\theta} = \frac{\mu R_{out}}{K\rho G} \left\{\frac{R_{out}-R_{in}}{R_{in}}\right\}_\theta \dot{m}_\theta \qquad (2\text{-}2)$$

or

$$\left.\frac{R_{out}-R_{in}}{R_{in}}\right|_\theta = \frac{P_{in} - P_{out}\big|_\theta}{\frac{\mu R_{out}}{K\rho G}\dot{m}_\theta} \qquad (2\text{-}3)$$

where K is the porous material permeability.

From past experience, it is known that regardless of what type of contour is selected, a perfect match between ideal and actual coolant distribution cannot be achieved due to the varying stagnation pressure. The amount of coolant wastage is minimized, however, if the tip permeability and contour are selected to yield a good match at the point of peak stagnation heating, which usually occurs close to the point in time of peak stagnation pressure.

Utilizing Equation C-5, Equation 2-3 becomes

$$\left.\frac{R_{out}-R_{in}}{R_{in}}\right|_\theta = \frac{P_{in} - 0.275\theta^2 P_s}{\frac{\mu R_{out}}{K_\rho G}\dot{m}_\theta} \qquad (2\text{-}4)$$

and considering the location of peak heating on the hemisphere,

$$\frac{\left.\frac{R_{out}-R_{in}}{R_{in}}\right|_\theta}{\left.\frac{R_{out}-R_{in}}{R_{in}}\right|_{34}} = \left(\frac{P_{in} - 0.275\theta^2 P_s}{P_{in} - 0.634 P_s}\right) \frac{(1.0 - 0.1667\theta^2)^{0.7}}{[1.88\theta^{0.6}(0.275)^{0.8\theta^2}]} \qquad (2\text{-}5)$$

If, at this design point in the trajectory, the nosetip internal pressure is related to the stagnation pressure by a factor K, i.e.,

$$P_{in} = K P_s \tag{2-6}$$

then Equation 2-5 can be rearranged to yield

$$\left.\frac{R_{out}}{R_{in}}\right|_{\theta} = 1.0 + \left[\left.\frac{R_{out}}{R_{in}}\right|_{34} - 1.0\right] \frac{[K-0.275\theta^2]\,[1.0-0.1667\theta^2]^{0.7}}{[K-0.634]\,[1.888\cdot 6(0.275)^{0.8}\theta^2]} \tag{2-7}$$

The analytical contour is therefore a function of local angle, the ratio K, and the ratio between the outer and inner radii at the location of maximum heating (34 deg.). The thinnest portion of the hemisphere occurs at the angle of maximum heating, as this is where the greatest flux of coolant is desired. The radius ratio at this angle should be chosen based on consideration of permeability, structural, and fabrication requirements. Typically, this ratio has been about 1.25.

Figure 2-20 presents a family of nosetip inner contours generated using Equation 2-7 over a range of internal to stagnation pressure ratio, K. The wall thickness has been held constant below an angle of 34 deg. In addition, due to the small radial distance from the nosetip centerline, coolant wastage in this region is relatively unimportant from the standpoint of nosetip total flow requirement.

2.3.2 Final Inner Contour

A three-dimensional porous-flow analysis of the nosetip coolant distribution was conducted using the MDAC H859 computer program. The program treats a nosetip as a nodal system and accounts for both viscous and inertial pressure drop, angle-of-attack effects, and viscous heating in the porous flow. The environment selected for the analysis was that occuring at 34 sec for the L-6 trajectory. The thermally ideal coolant flow for this trajectory is a maximum at this time.

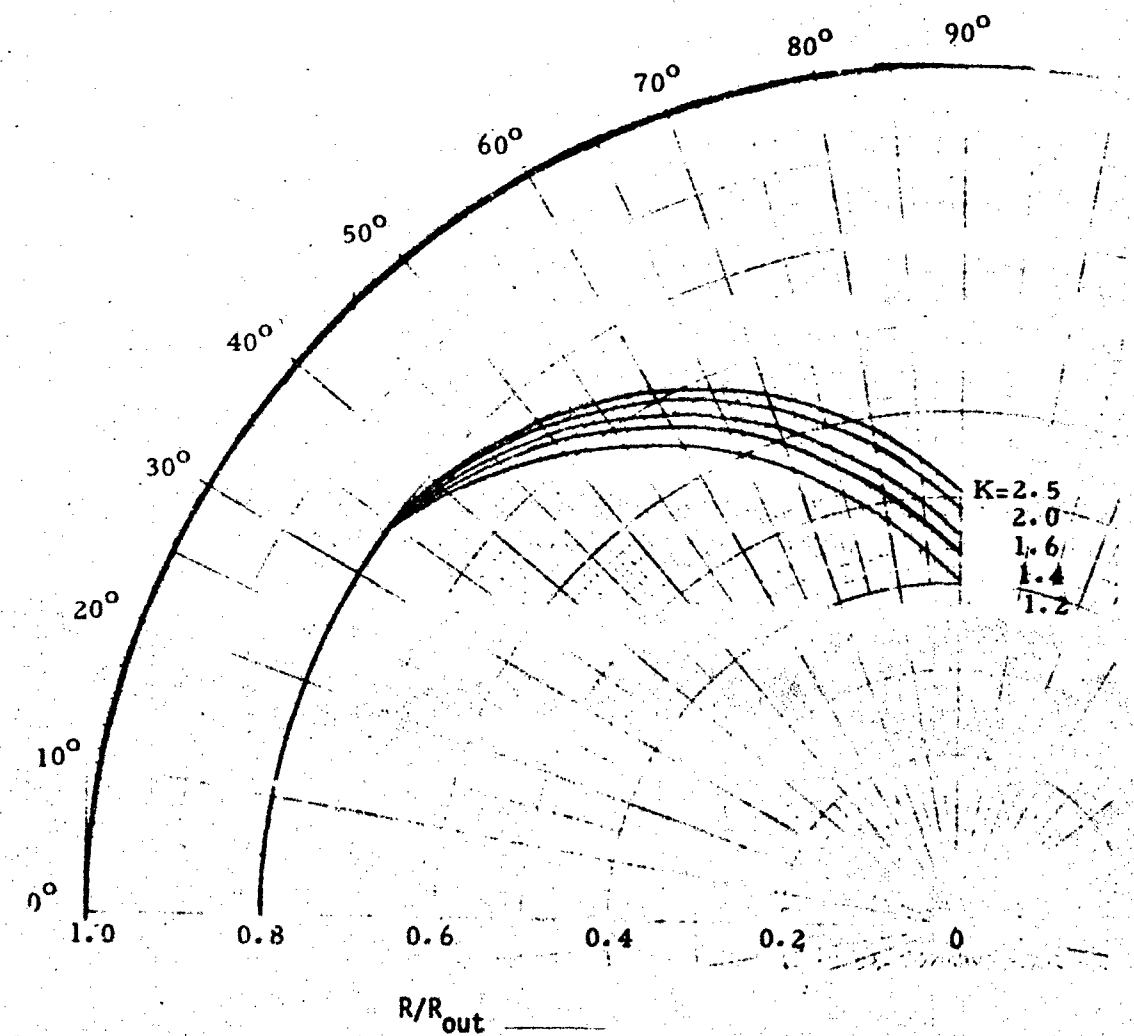


Figure 2-20. Optimized Nosetip Contours

Based on past experience and the desire to maintain required coolant pressure within a reasonable limit, a value of 2.0 was chosen for the ratio of coolant pressure to stagnation pressure. It was anticipated that this would also be a near-optimum value from the standpoint of coolant expulsion system weight and volume.

The ideal contours of Figure 2-20 were each investigated. It was found that the best match to the ideal coolant distribution could be obtained using the ideal contour labeled with a K value of 1.2. In addition, the contour forward of the 34-deg location was gradually thickened toward the stagnation point in order to reduce coolant wastage in this region. Figure 2-21 presents the final contour that was evolved. The design permeability of the porous material is 3.06×10^{-11} in.^{2}.

2.4 DESIGN COOLANT REQUIREMENTS

The basic design coolant requirements were evaluated by determining the flow conditions necessary to maintain at least a 24-percent margin over the thermally ideal coolant flux everywhere on the nosetip surface. As a perfect match could not be obtained between the design distribution and the augmented ideal distribution, some excess coolant is required. The coolant temperature assumed was 530°R, the nosetip goemetry and permeability of Figure 2-21 were used, and the geometric effect of the nosetip attachment was not taken into account. As will be demonstrated later, the effects of variable coolant temperature and an attachment are offsetting for the current design.

2.4.1 Coolant Weights, Pressures, and Distributions

Table 2-8 presents a summary of the design coolant requirements for the five study trajectories. The maximum amount of coolant is required for Trajectory L-6 and is 2.31 lb. The peak rate of coolant expenditure and peak coolant pressure are required for Trajectory S-3 and are 0.378 lb/sec and 6,317 psia, respectively. Figure 2-22 presents the design coolant flow history for each trajectory, and Figure 2-23 presents the coolant pressure histories. Figures 2-24 through 2-28 present the design coolant distribution for each trajectory at the time of peak coolant flow.

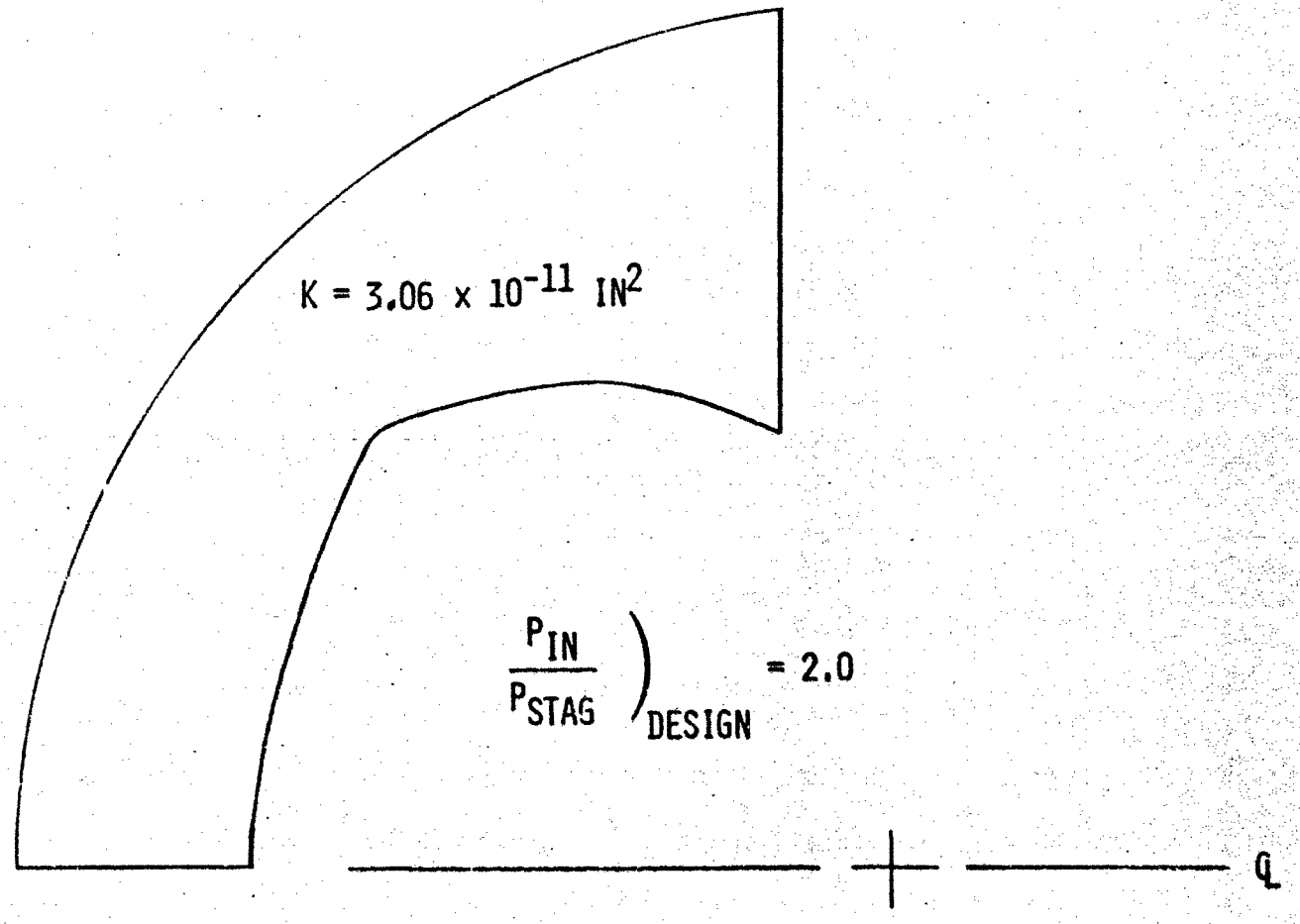


Figure 2-21.) Contour and Permeability

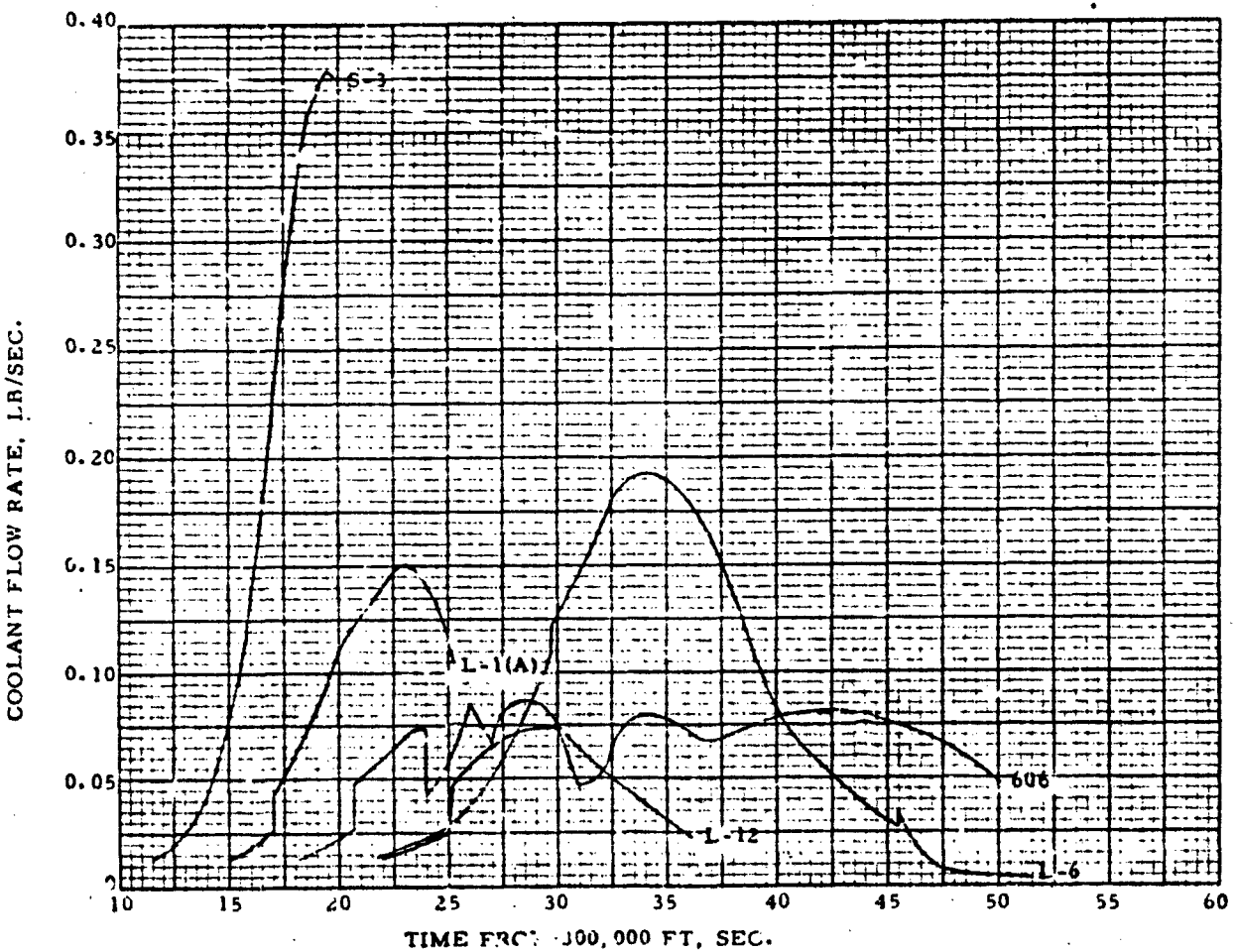


Figure 2-22. Design Coolant Flow Histories

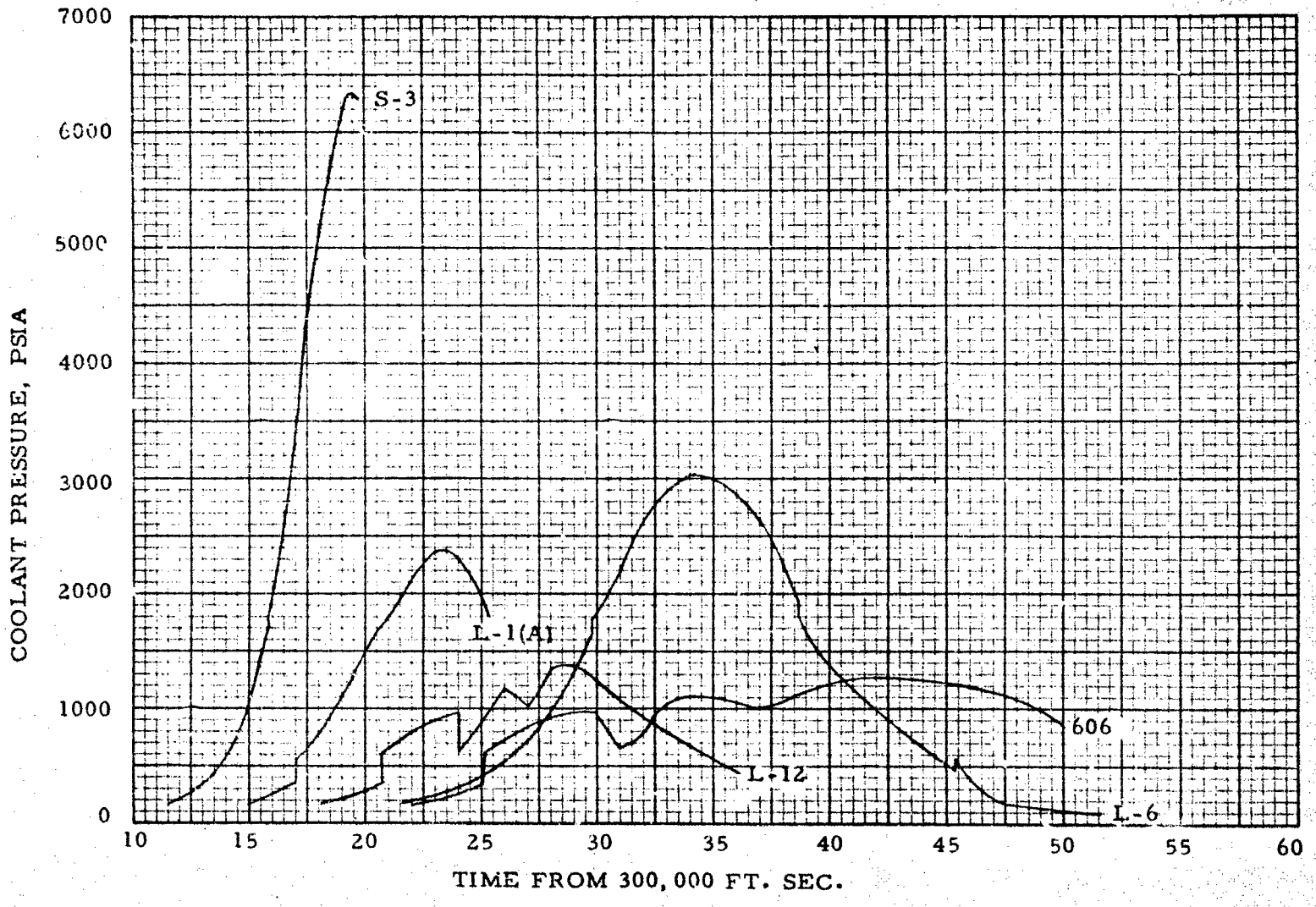


Figure 2-23. Design Coolant Pressure Histories

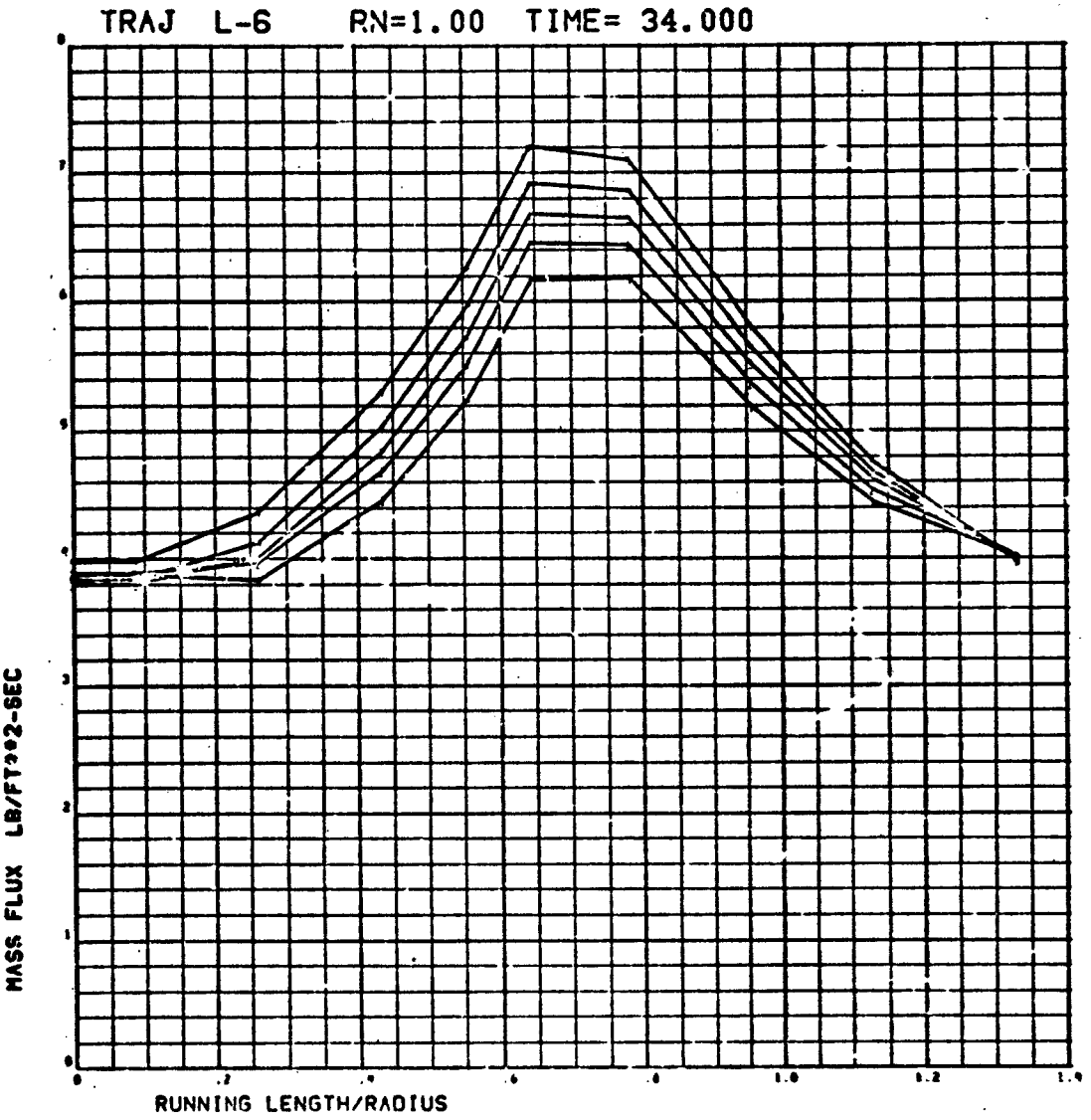


Figure 2-24. Coolant Distribution at Peak Flow, L-6

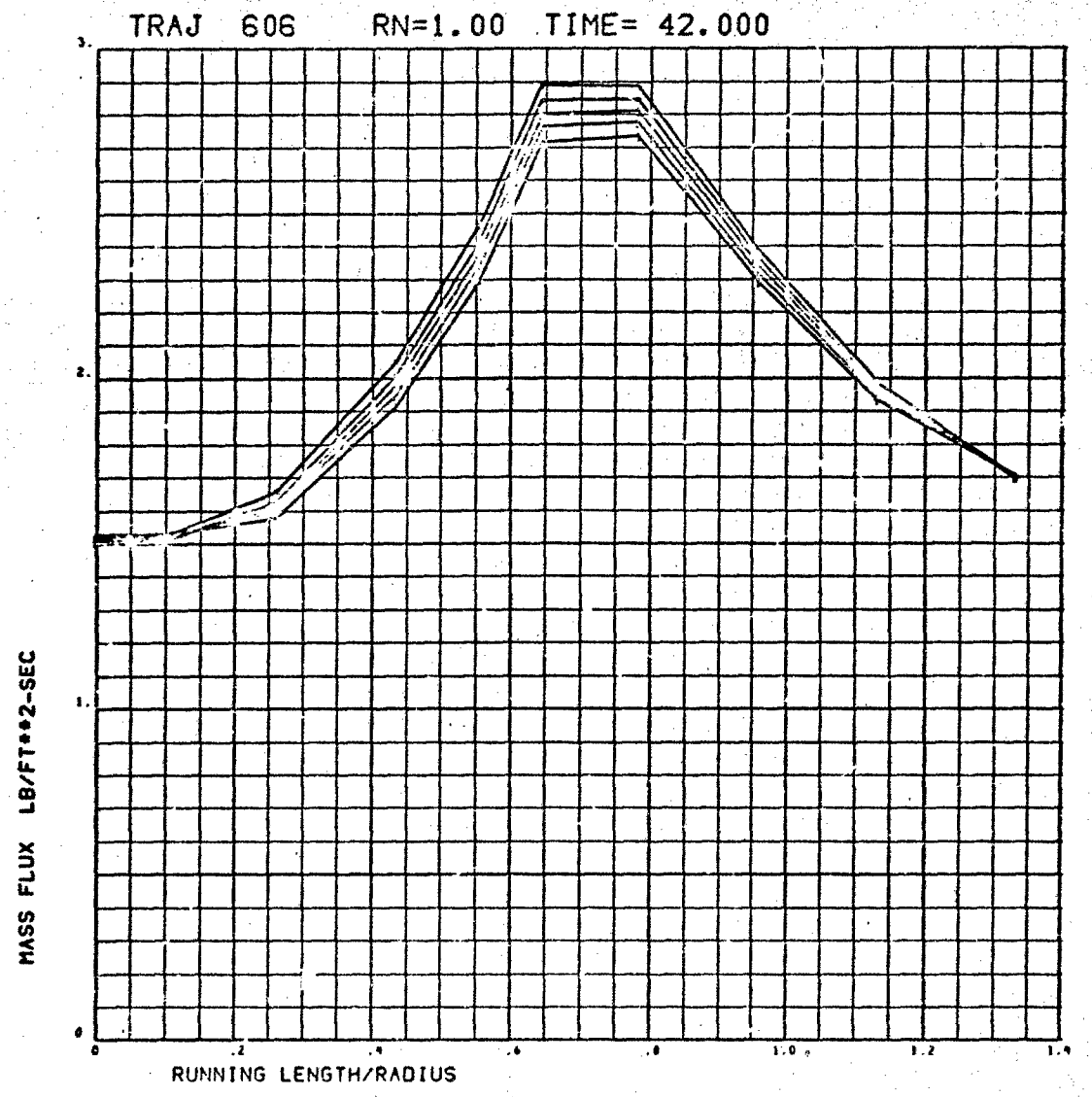


Figure 2-25. Coolant Distribution at Peak Flow, 606

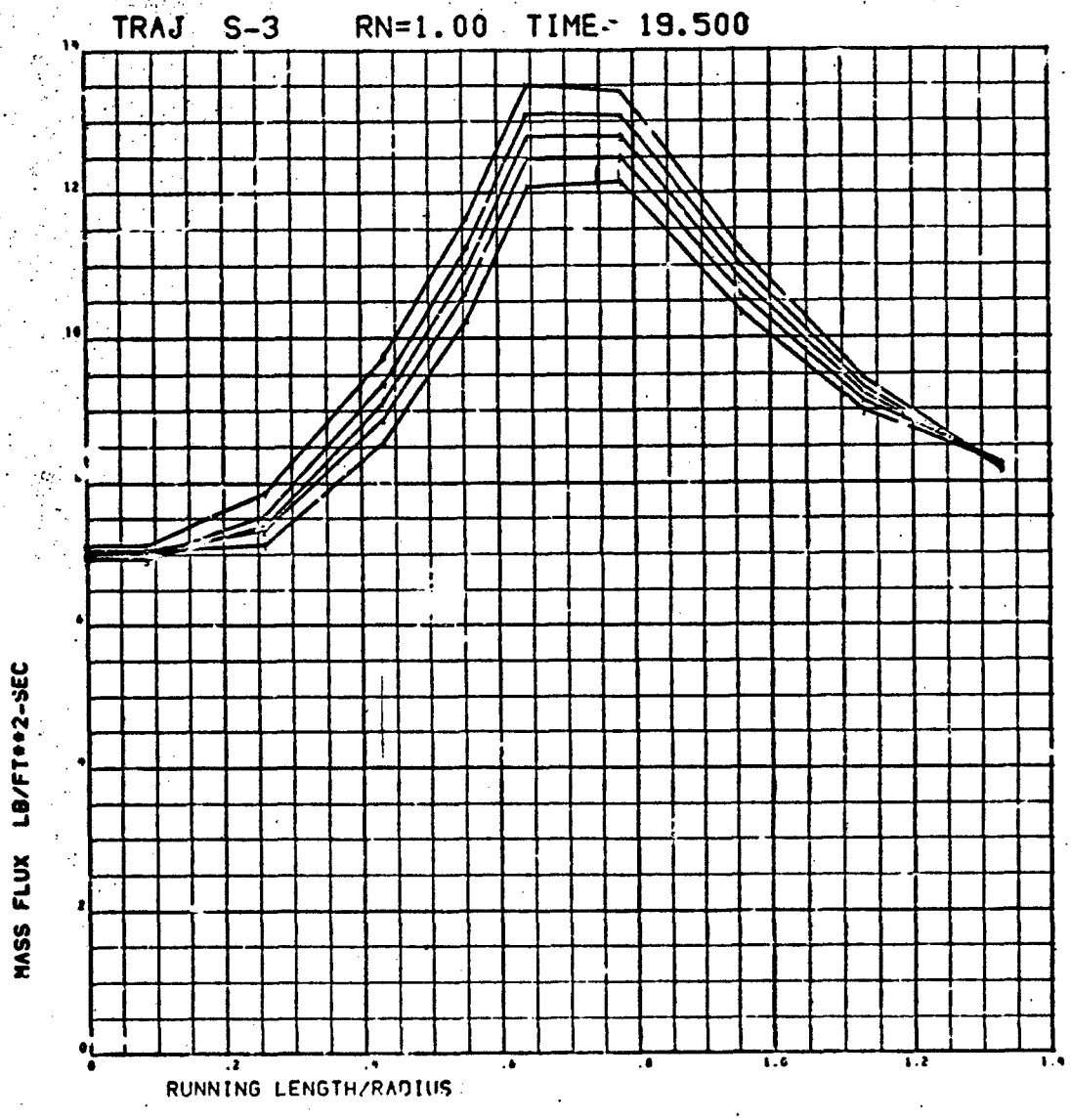


Figure 2-26. Coolant Distribution at Peak Flow, S-3

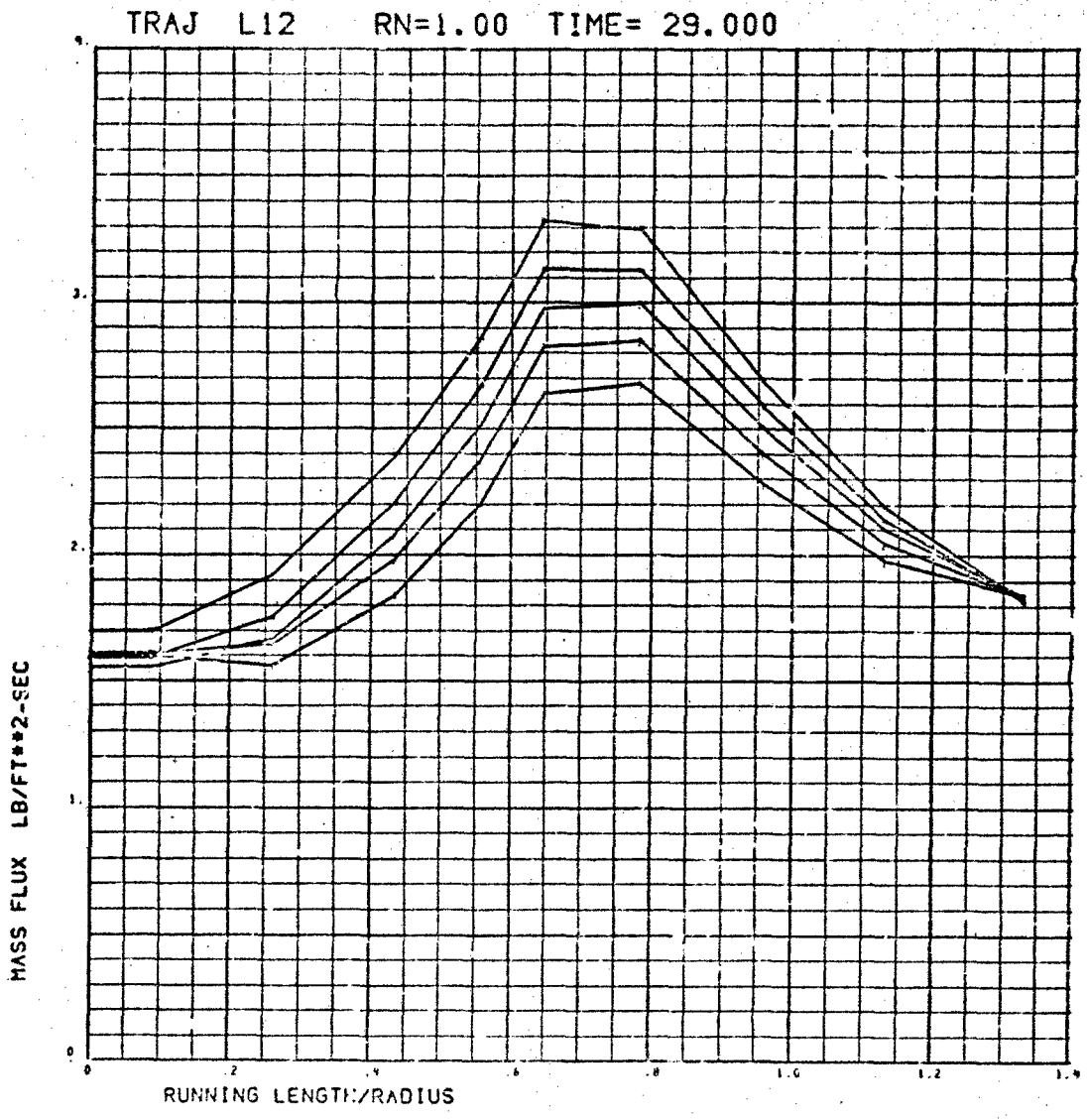


Figure 2-27. Coolant Distribution at Peak Flow, L-12

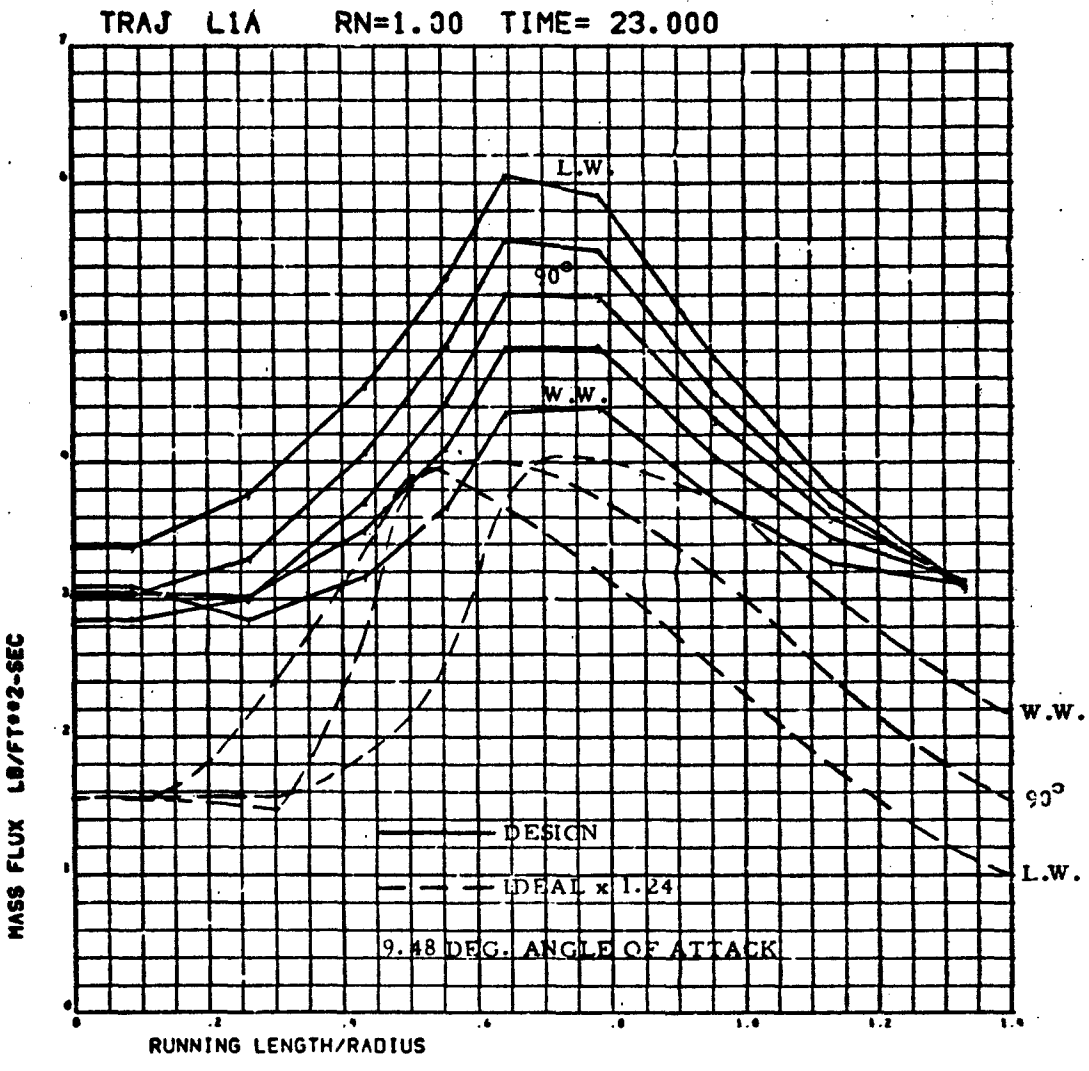


Figure 2-28. Coolant Distribution at Peak Flow, L-1(a)

Table 2-8

NOSETIP DESIGN COOLANT SUMMARY

Trajectory	Design Coolant Weight (lb)	Peak Design Flow (lb/sec)	Peak Design Pressure (psia)
L-6	2.31	0.193	3,036
606	1.81	0.0813	1,280
S-3	1.30	0.378	6,317
L-12	0.982	0.0867	1,378
L-1(a)	0.962	0.150	2,375

2.4.2 Effect of Coolant Supply Pressure

As indicated previously, the nosetip inner contour was defined assuming a design value of 2.0 for the ratio of coolant pressure to stagnation pressure. In order to investigate the effect of this pressure ratio, the nosetip contour of Figure 2-21 was analyzed for the L-6 trajectory to find optimum permeabilities and the associated design coolant weights. Figure 2-29 presents the design coolant weight as a function of this pressure ratio.

The weight approaches an asymptote of about 2.17 lb at a value of 3.0 for the pressure ratio. At the design pressure ratio of 2.0, the coolant weight is 6 percent higher. As will be seen in a later section, however, the coolant weight savings at higher pressure are offset by increased thickness requirements for the walls of the coolant reservoir and gas generator, and a value of 2.0 for the pressure ratio is essentially optimum for the overall system weight.

2.4.3 Effect of Coolant Temperature

The temperature assumed for the coolant in the nosetip inner cavity has a direct bearing on the design coolant weight. In essence, this is due to the effect of temperature on coolant viscosity. Because the nosetip material is isotropic in structure, the coolant flow distribution is affected by the tangential pressure gradient at the nosetip outer surface. This pressure gradient combines with the viscous-flow-induced radial pressure gradient to

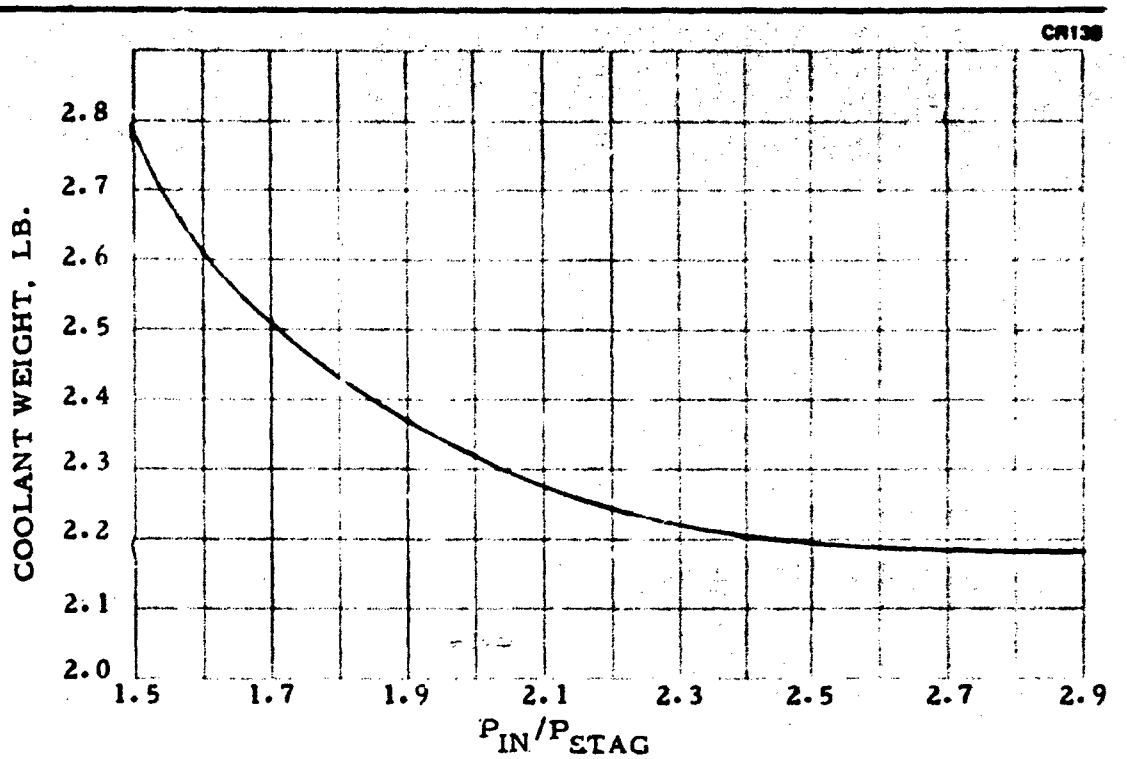


Figure 2-29. Effect of Coolant Pressure Design on Coolant Weight, L-6 Trajectory

define the coolant streamlines in the porous material. As the coolant viscosity decreases due to increasing coolant temperature, the radial pressure gradient decreases, allowing the tangential gradient at the surface to cause greater bending of the coolant streamlines in the aft direction. This decreases the amount of coolant flowing to the nosetip surface in regions of high pressure, while allowing excess coolant to flow out of regions of lower pressure.

Figure 2-30 presents the design coolant weight for the L-6 trajectory as a function of coolant temperature. Over the assumed temperature range, the relationship is nearly linear.

The coolant supply temperature can vary for several reasons: (1) the value at liftoff can be different than the assumed value of 530° R, (2) the value can be raised due to a nuclear encounter, (3) the value can be raised due to heating of the coolant through the bladder material, or (4) the value can be

raised due to heating of the coolant supply tube by conduction through the heat shield material. Since no specification of coolant launch temperature was made, this effect can be inferred from Figure 2-30. The other three sources of temperature change have been investigated and are discussed in other parts of this report. Figure 2-31 presents an estimate of the coolant combined temperature history inside the nosetip.

The design coolant flow for this temperature history was evaluated and found to result in a total coolant weight of 2.404 lb, an increase of 3.5 percent over the amount required for a constant coolant temperature of 530°R.

2.4.4 Effect of Nosetip Attachment

The preferred method of attaching the nosetip to the coolant supply tube will require that an electron beam weld be made similar to that illustrated in Figure 2-32. The weld will present an impermeable barrier to coolant flow. In order to determine the effect of the weld on coolant flow distribution, the H859 three-dimensional porous flow program was used to analyze the nosetip with the attachment lip shown in dashed lines in Figure 2-32. The inner surface of the lip was assumed impermeable.

Figure 2-33 presents a typical windward ray coolant distribution, both with and without the attachment. Also shown is the thermally ideal distribution augmented by the 24-percent margin of safety. As can be seen, the attachment reduces the coolant flux in regions aft of about 40 deg from the nosetip symmetry point.

There is a net saving in coolant weight amounting to 3.5 percent and offsetting the coolant weight increase due to the effect of a variable coolant temperature.

2.5 ALTERNATE NOSETIP CONFIGURATIONS

Elimination of a conical skirt for the baseline nosetip configuration was made possible by leaving out the substructure in the near-nose region and providing additional thermal insulation to protect the 0.30-in.-diameter coolant supply tube from high heating.

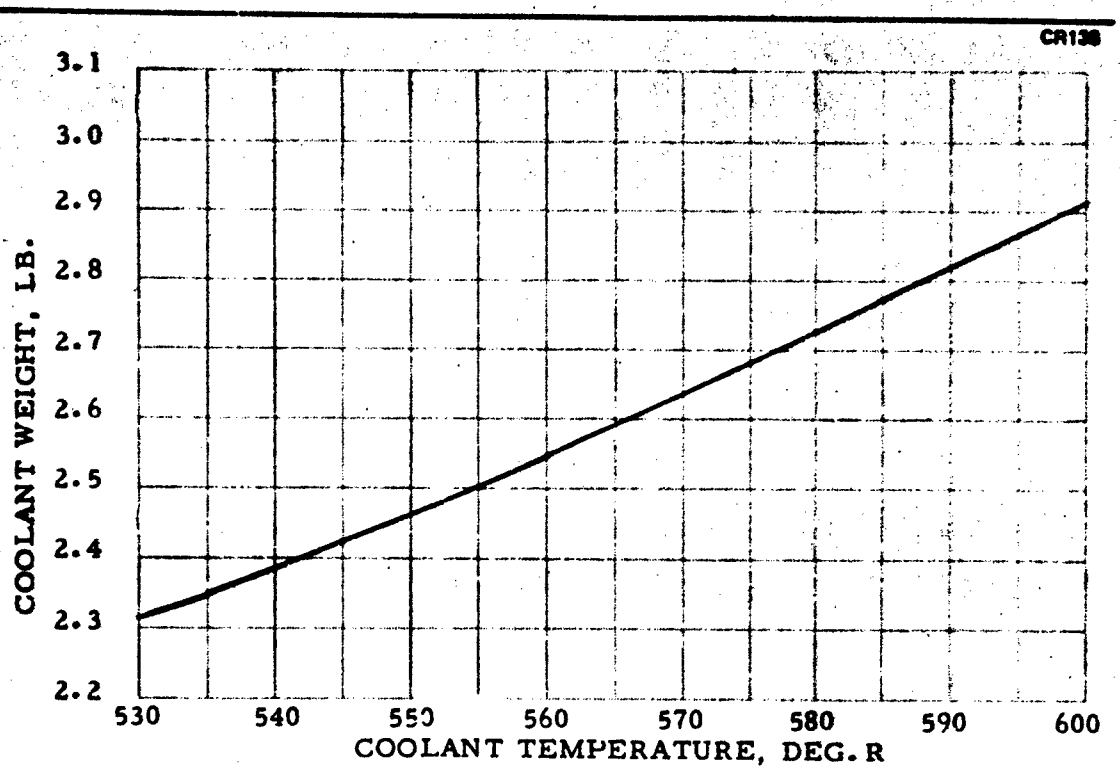


Figure 2-30. Effect of Coolant Temperature on Design Coolant Weight, L-6 Trajectory

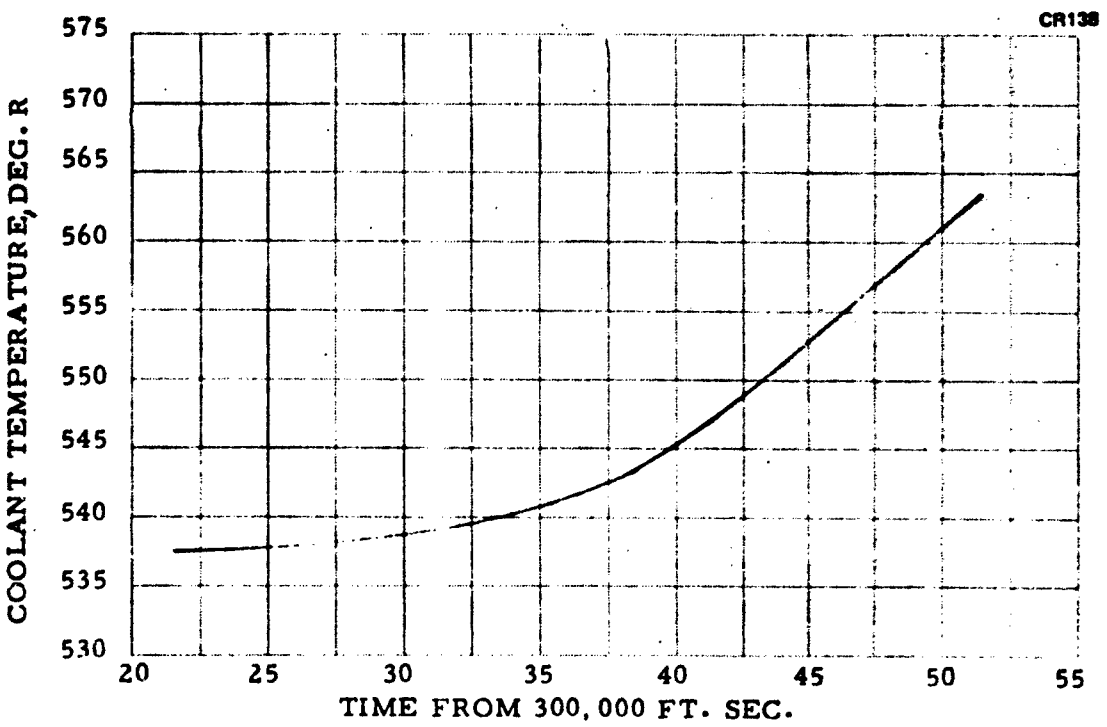


Figure 2-31. Actual Coolant Temperature, L-6 Trajectory

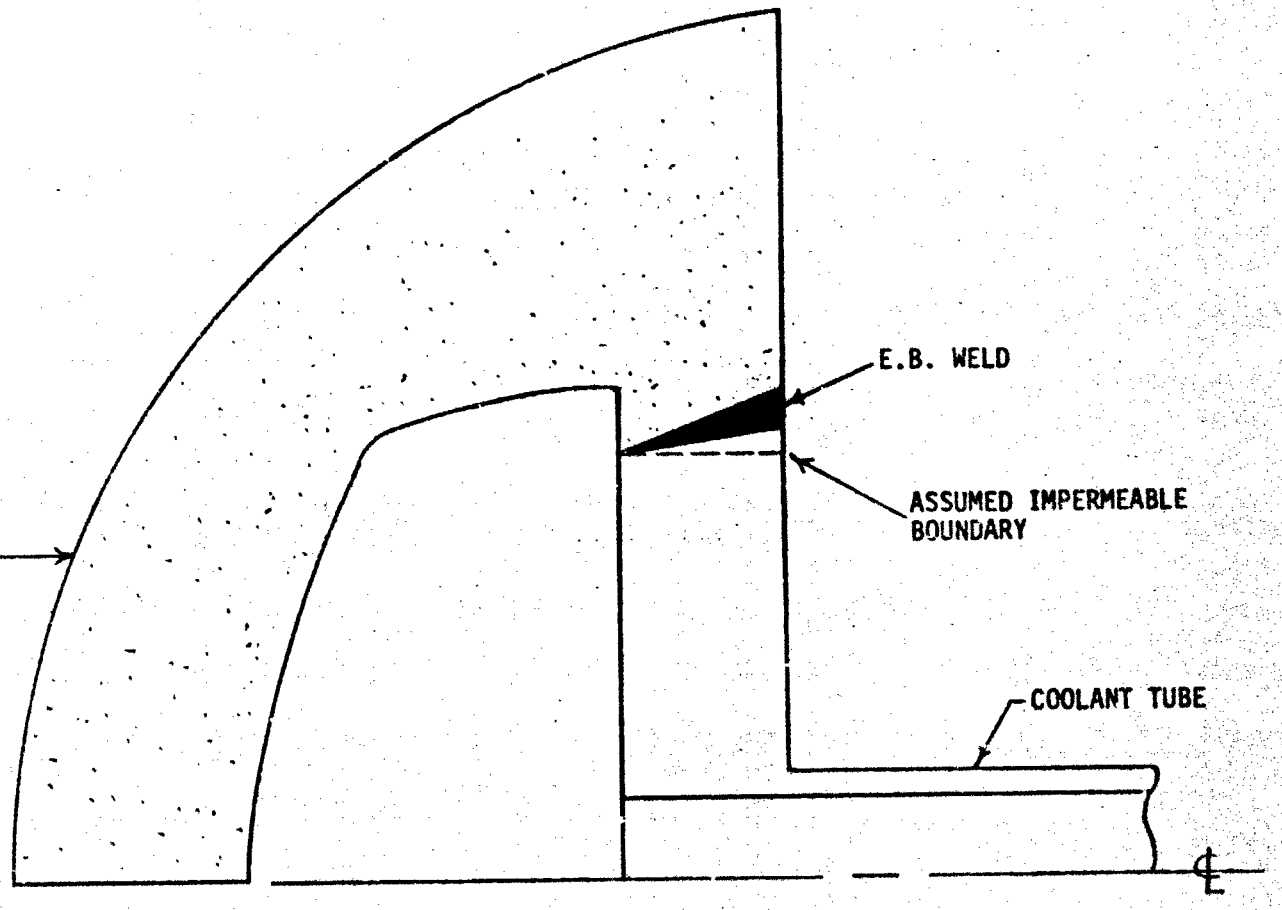


Figure 2-32. Nosetip Weld Attachment

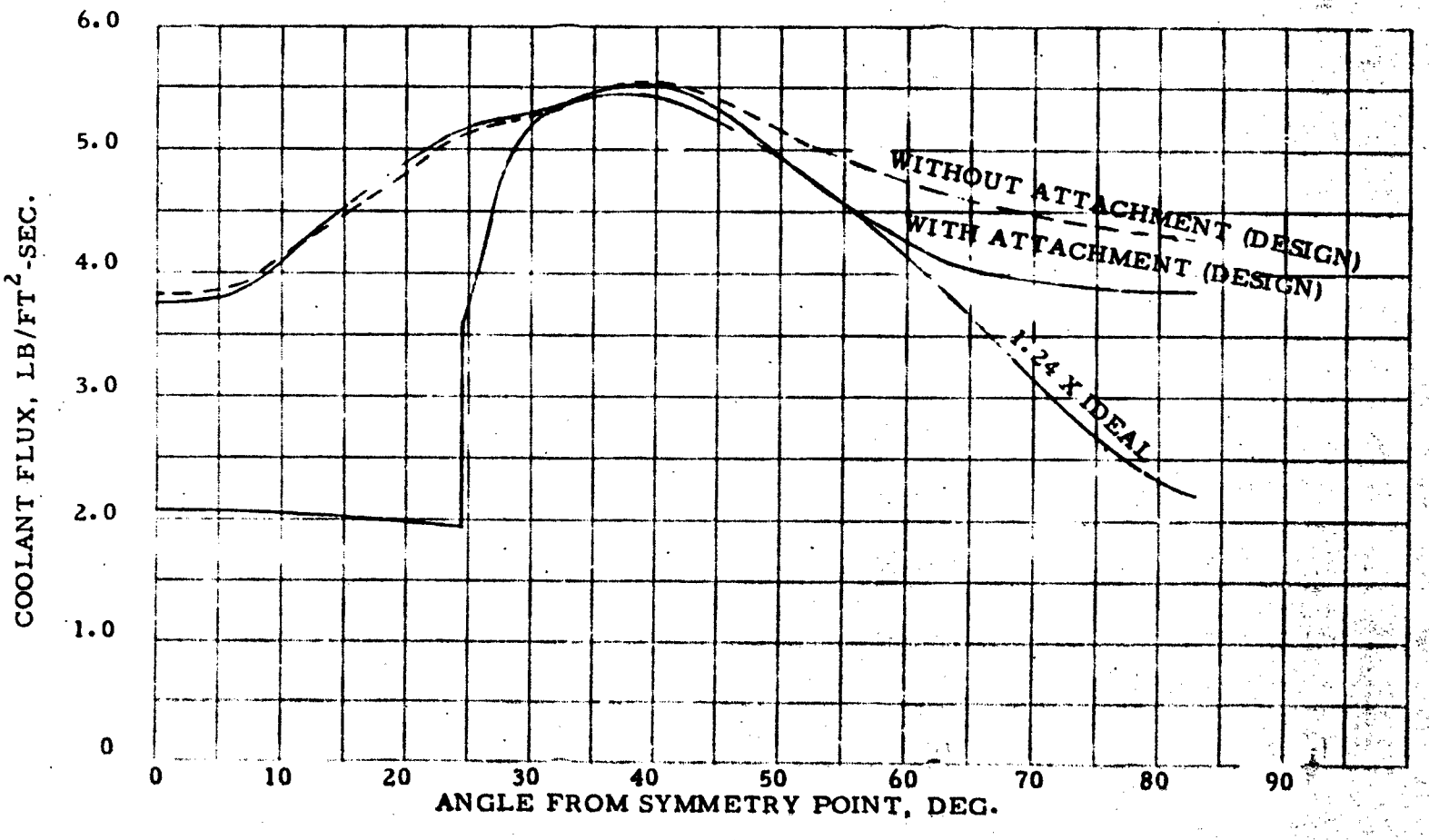


Figure 2-33. Effect of Attachment on Coolant Distribution

Three alternate configurations, employing substructure but without additional insulation were investigated. The coolant requirements of each are summarized in Table 2-9. None of these designs are recommended, and none were used for definition of the total system.

If a 0.25-in.-diameter coolant tube without insulation is retained, then a 0.62-in.-long conical porous skirt must be incorporated into the nosetip. This is to provide a large enough body diameter at the nosetip-heat shield junction to accommodate the heat shield, heat shield bond, substructure, and coolant tube. To meet these requirements, two alternate nosetip configurations were studied.

Figure 2-34 presents the geometry and permeabilities for a dual-permeability nosetip with a 0.62-in. skirt and a design value of 2.5 for the ratio of maximum coolant cavity pressure to maximum stagnation pressure. The relationship between coolant pressure and coolant usage for a hemisphere is discussed in Section 2.4.2, and a value of 2.5 for the pressure ratio is shown to reduce the required coolant. The internal geometry of the hemispherical portion has been slightly modified from the baseline design, and the internal cone angle of the skirt is -14 deg. The permeability of the hemisphere is 1.80×10^{-11} in.^{2}, and the permeability of the skirt is 1.12×10^{-11} in.^{2}. The permeability junction occurs at the tangency point.

Figure 2-35 presents the geometry and permeabilities for a skirted nosetip that has been partitioned circumferentially in order to permit two pressure levels to be established in the nosetip coolant cavity. This approach yields coolant savings because at angle of attack the leeside portion coolant pressure can be maintained lower than for the windward side, thus resulting in a lower rate of coolant expenditure.

With respect to inner contour and hemisphere permeability, the partitioned nosetip is identical to the baseline tip. The permeability of the skirt is 1.45×10^{-11} in.^{2}. The partition shown in Figure 2-35 results in an included angle of 135 deg for the windward portion. This is not necessarily the optimum angle. Therefore, if partitioning were to be incorporated as a design feature, it would be advisable to study the effect of partition-included angle on coolant requirement.

Table 2-9
DESIGN COOLANT REQUIREMENTS FOR ALTERNATE NOSETIPS

Requirement	High-Pressure Nosetip Trajectory					Partitioned Nosetip Trajectory					Miniskirt Nosetip Trajectory				
	L-6	606	S-3	L-12	L-1(a)	L-6	606	S-3	L-12	L-1(a)	L-6	606	S-3	L-12	L-1(a)
Peak flow, lb/sec	0.231	0.192	0.463	0.179	0.233	0.236	0.105	0.471	0.130	0.197	0.212	0.1361	0.423	0.142	0.200
Peak pressure, psia	4,013	2,913	8,297	2,729	3,862	3,095	2,245	6,430	2,097	2,972	3,075	1,605	6,463	1,744	2,752
Total flow, lb	2.93	3.02	1.58	1.63	1.68	2.97	2.41	1.62	1.36	1.26	2.61	2.45	1.44	1.31	1.38

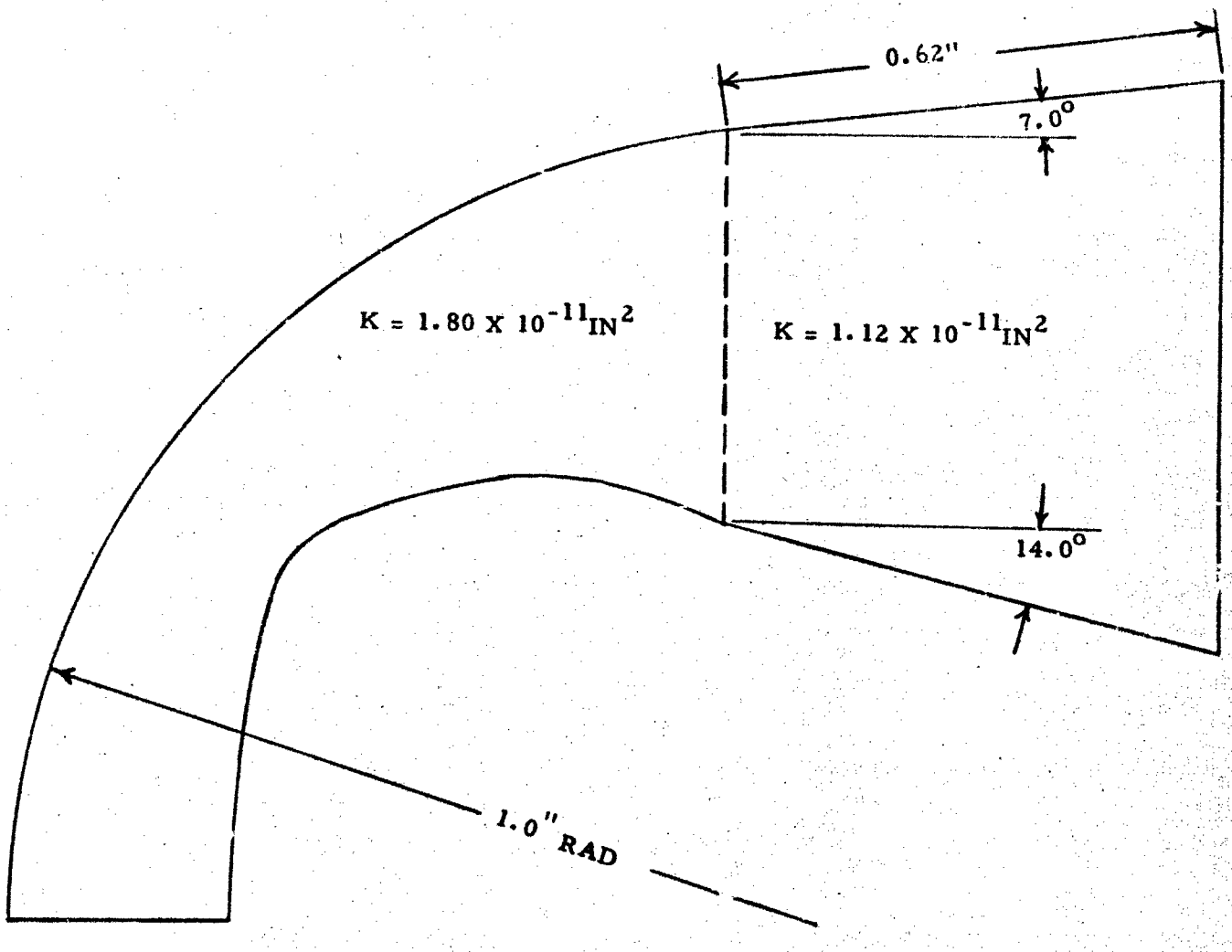


Figure 2-34. High-Pressure Nosetip ($P_{:N}/P_{STAG} \approx 2.5$)

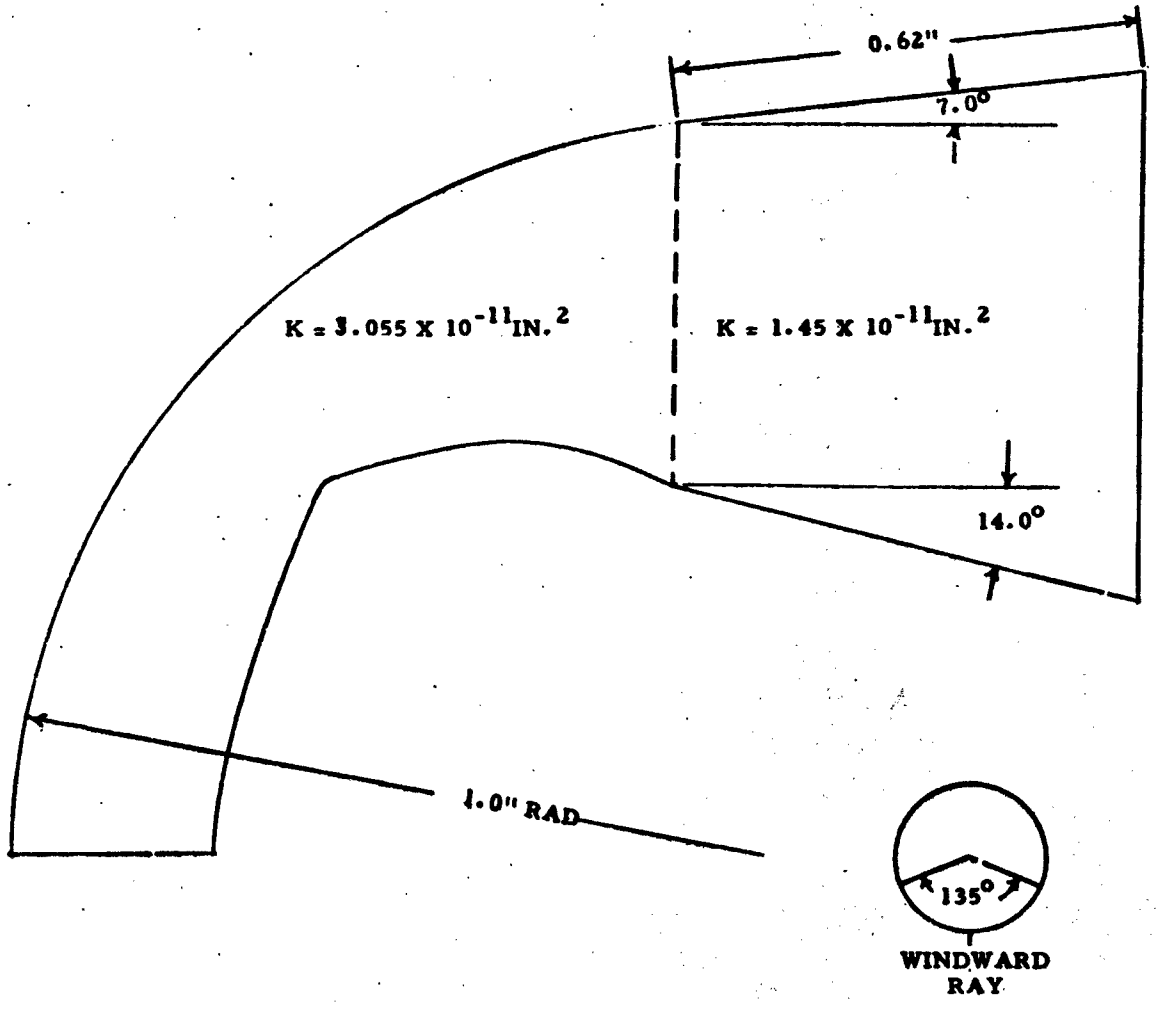


Figure 2-35. Partitioned Nosetip

In order to reduce coolant requirements, it is desirable to utilize the shortest skirt possible. Based on a temperature limit of 400°F for the bond-heat shield interface, and a minimum coolant wand outside diameter of 0.125 in., a skirt length of 0.15 in. is permissible. Figure 2-36 presents the geometry and permeabilities for a dual-permeability nosetip with a 0.15-in. skirt. The internal contour for the hemispherical portion is identical to that for the high-pressure nosetip, but the internal angle of the skirt is -21 deg. The permeability of the hemisphere is 2.79×10^{-11} in.^{2}, and the permeability of the skirt is 1.44×10^{-11} in.^{2}. The permeability junction occurs at the tangency point. The design ratio for maximum coolant cavity pressure to maximum stagnation pressure is 2.0.

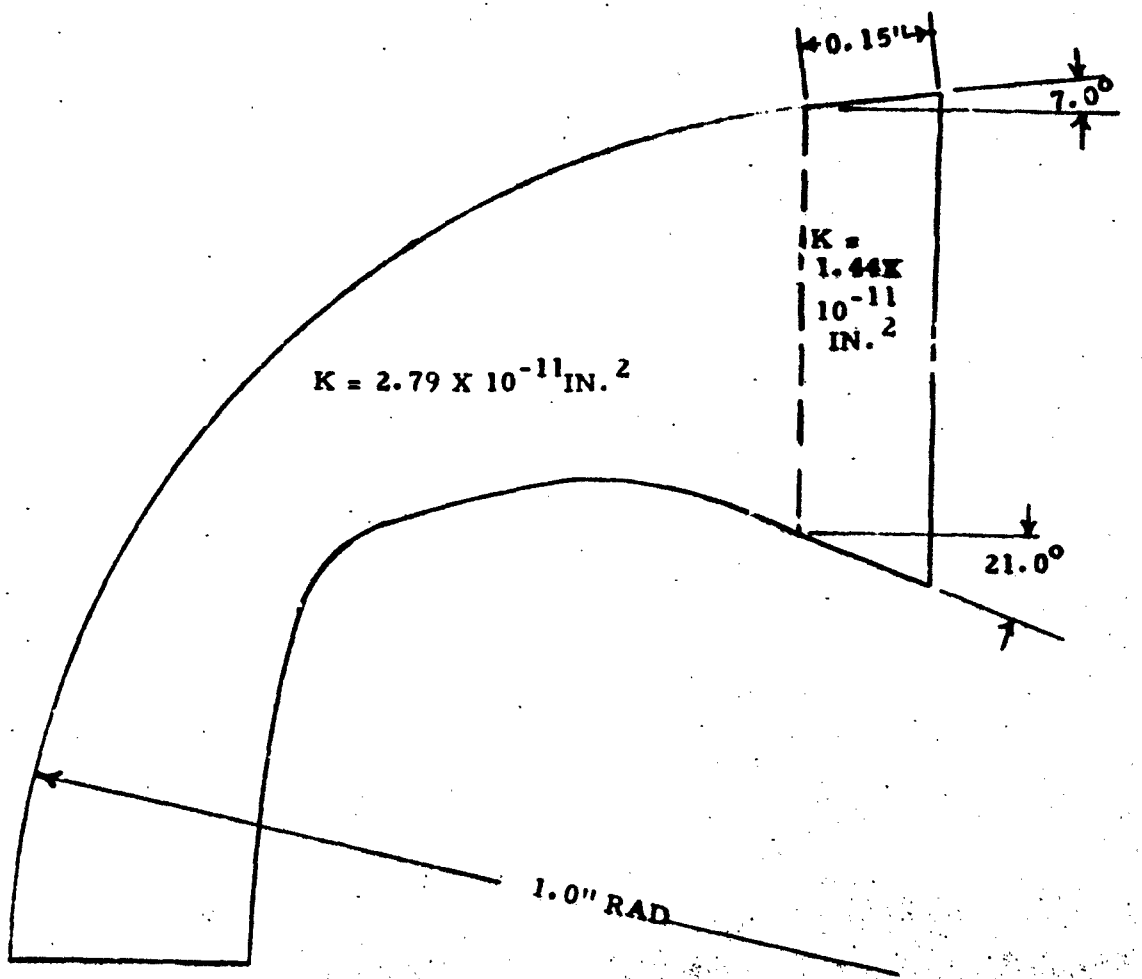


Figure 2-38. Miniskirted Nosetip, Dual-K

Section 3
FLOW CONTROL CONCEPTS

Investigation of flow control concepts was accomplished through a two-phase effort. First, a survey of available parameters for flow control was made. These parameters were then applied to the design flows in a search for correlations. Secondly, those parameters which exhibited good correlation were investigated to determine if means for mechanizing the relationships were feasible. Several control units were designed and applied to the spectrum of trajectories, and comparative performance was determined.

Two types of valves, mechanical and electromechanical, were considered during the study. The mechanical valves were entirely self-contained and required no input from outside sources. The electromechanical valves required an electrical signal to regulate flow. This signal could be obtained from a nosetip sensor network or from a control system designed to compute vehicle trajectory parameters.

3.1 FLOW CONTROL PARAMETERS

Eight parameters were selected for investigation as possible flow control parameters. They were: (1) axial acceleration, (2) lateral acceleration, (3) stagnation pressure, (4) tip internal or chamber pressure, (5) velocity, (6) altitude, (7) angle of attack, and (8) time.

Two trajectories were used, the L-6 and S-3. These trajectories size the system for total volume and maximum flow rate. It was assumed that any system which would meet the requirements of these trajectories would be adequate for the other three. This assumption was verified for each flow control concept.

To investigate the correlation of each of these parameters with required flow rates, Figure 3-1 was constructed to show the influence of the selected parameter on design flow for both the S-3 and L-6 trajectories.

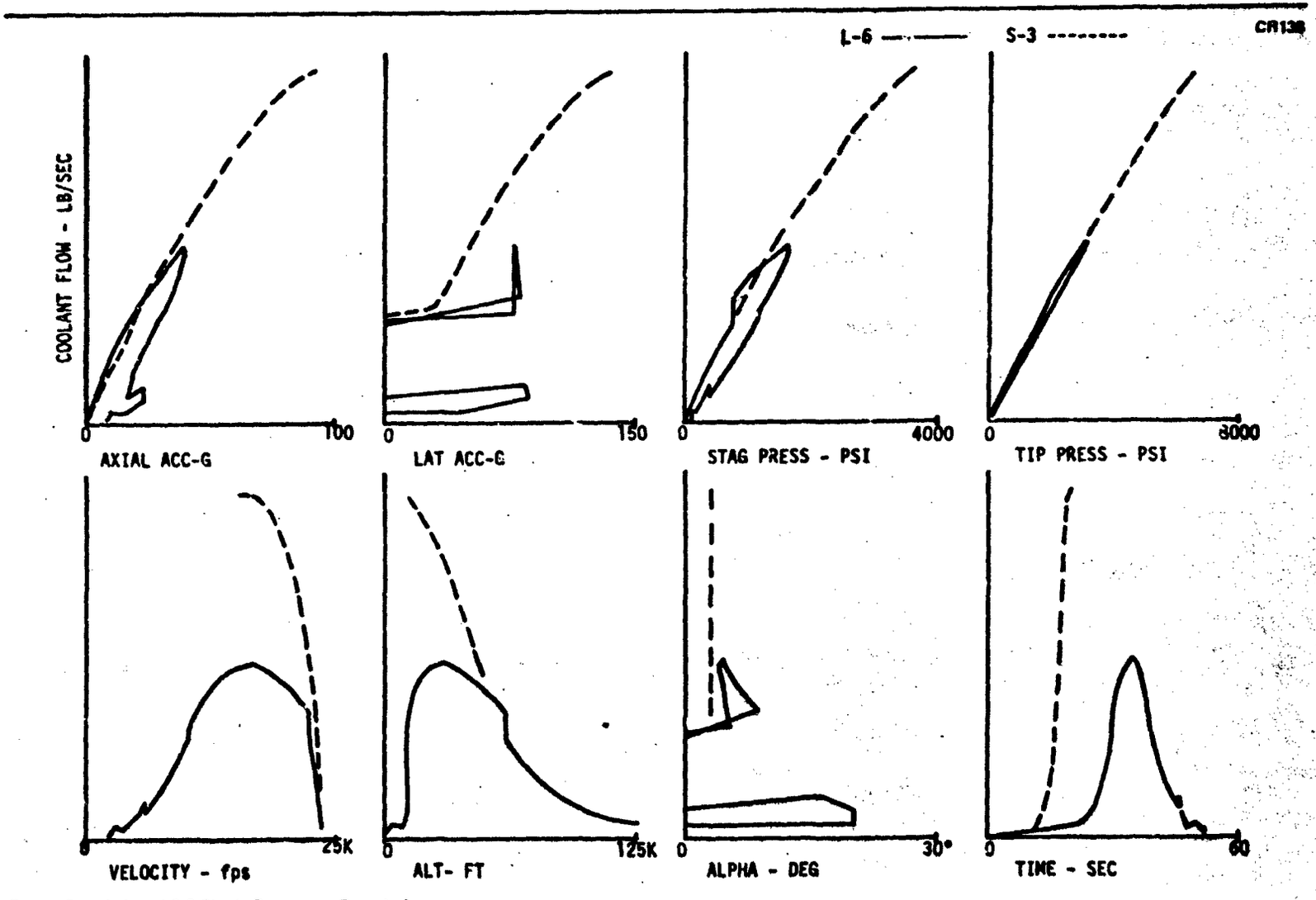


Figure 3-1. L-6 and S-3 Single Parameter Correlation

The criteria for a good, mechanizable parameter would be a curve, single-valued in flow, which could be approximated by a simple function such as a linear or square root. From the figure, tip pressure seems to meet these criteria well, and axial acceleration and stagnation pressure moderately well. The other parameters, by themselves, have a poor correlation.

The next step was to investigate the possibility of using two of the parameters in combination. This was accomplished in the following sequence: (1) select a function of the first parameter, (2) calculate actual flows based on that parameter, (3) calculate difference between design and actual flow, and (4) plot this difference against each of the other parameters.

The parameters and functions selected for the first iteration were: (1) axial acceleration, (2) square root of axial acceleration, (3) stagnation pressure, and (4) square root of stagnation pressure.

Plots of the excess flow obtained with the initial parameter are shown as a function of time in Figures 3-2 and 3-3. The relationships these parameters have with other parameters are given in Figures 3-4 through 3-7. Again, a good criterion for the combination is a single-valued function. The correlations obtained using this approach are summarized in Table 3-1. As can be seen, there were practically no good correlations obtained. For this reason, a purely analytical approach to generate correlating functions was abandoned. Further investigations of these parameters and how they may be implemented for flow control will be discussed in the following sections on valve design.

3.2 MECHANICAL VALVE CONCEPTS

The following systems were investigated for direct parametric control of coolant flow: (1) square-root-of-g valve, (2) dual-slope g valve, (3) Mark II g valve, (4) volume compensation, (5) pressure control, and (6) partitioned tip. These concepts are each discussed in the following sections.

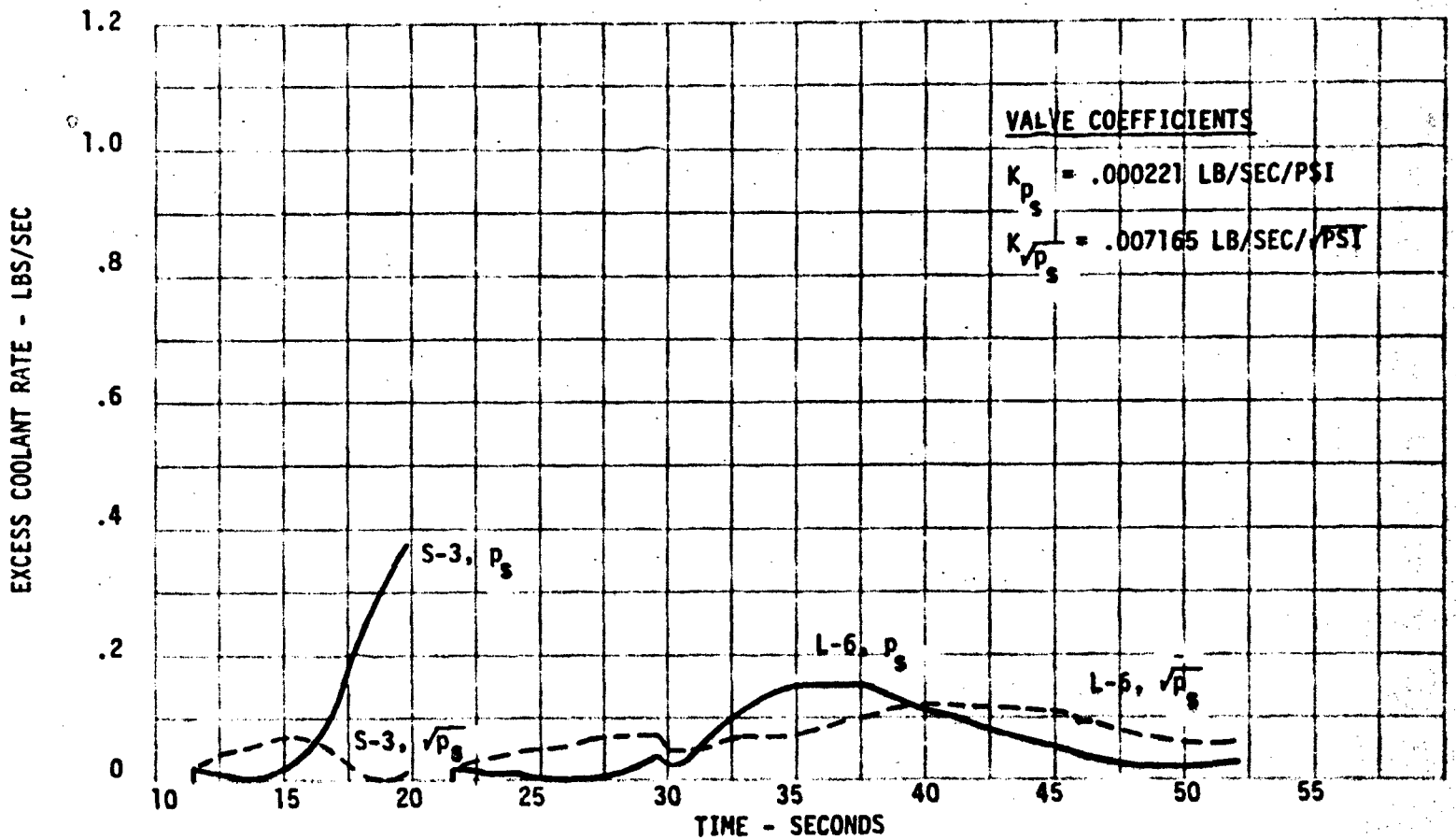


Figure 3-2. Excess Coolant Rate Histories

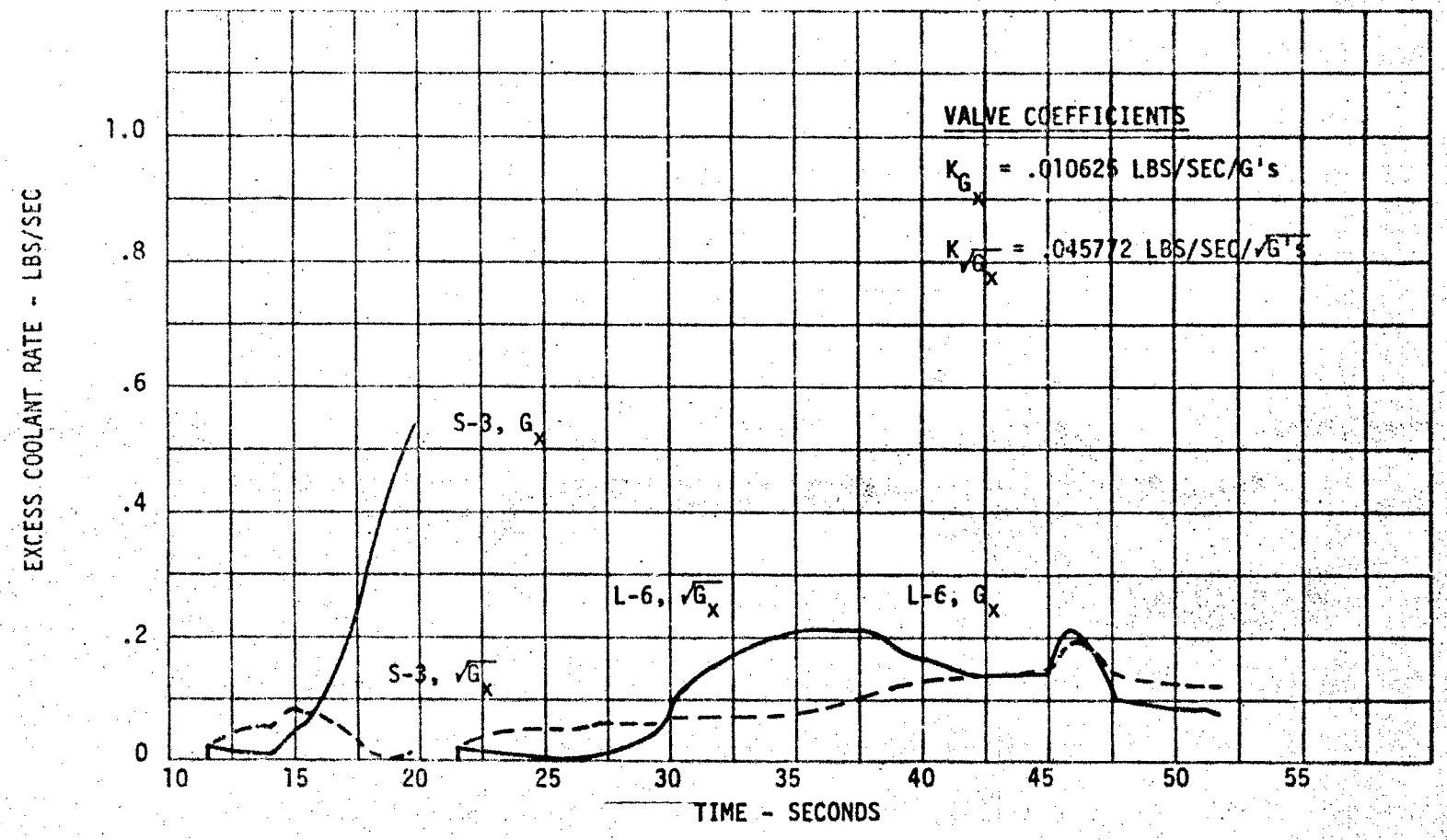


Figure 3-3. Excess Coolant Rate Histories

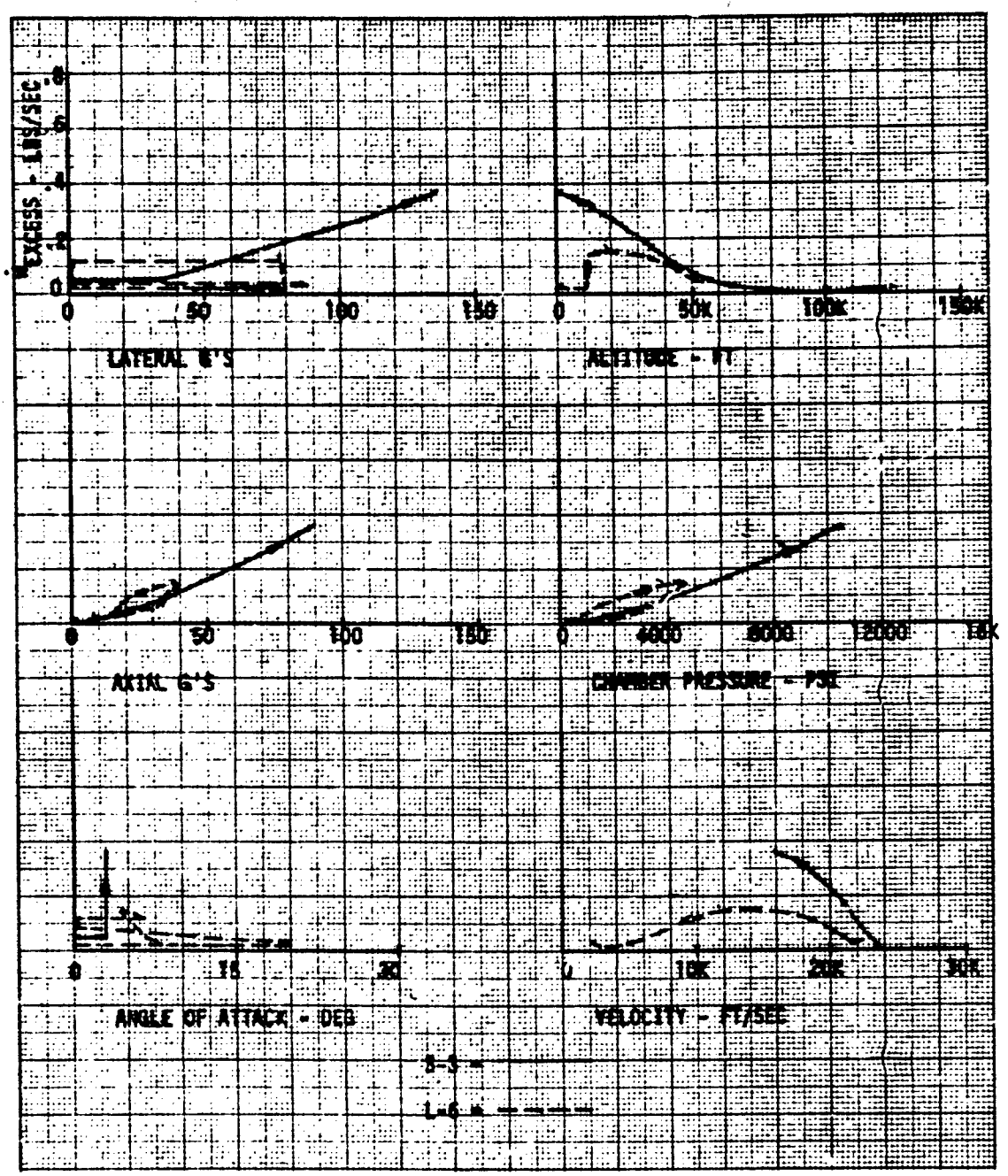


Figure 3-4. Excess Coolant Flow Rate vs Parameters Valve Sensing Stagnation Pressure (Gain = 0.00022 Lb/Sec/Psi)

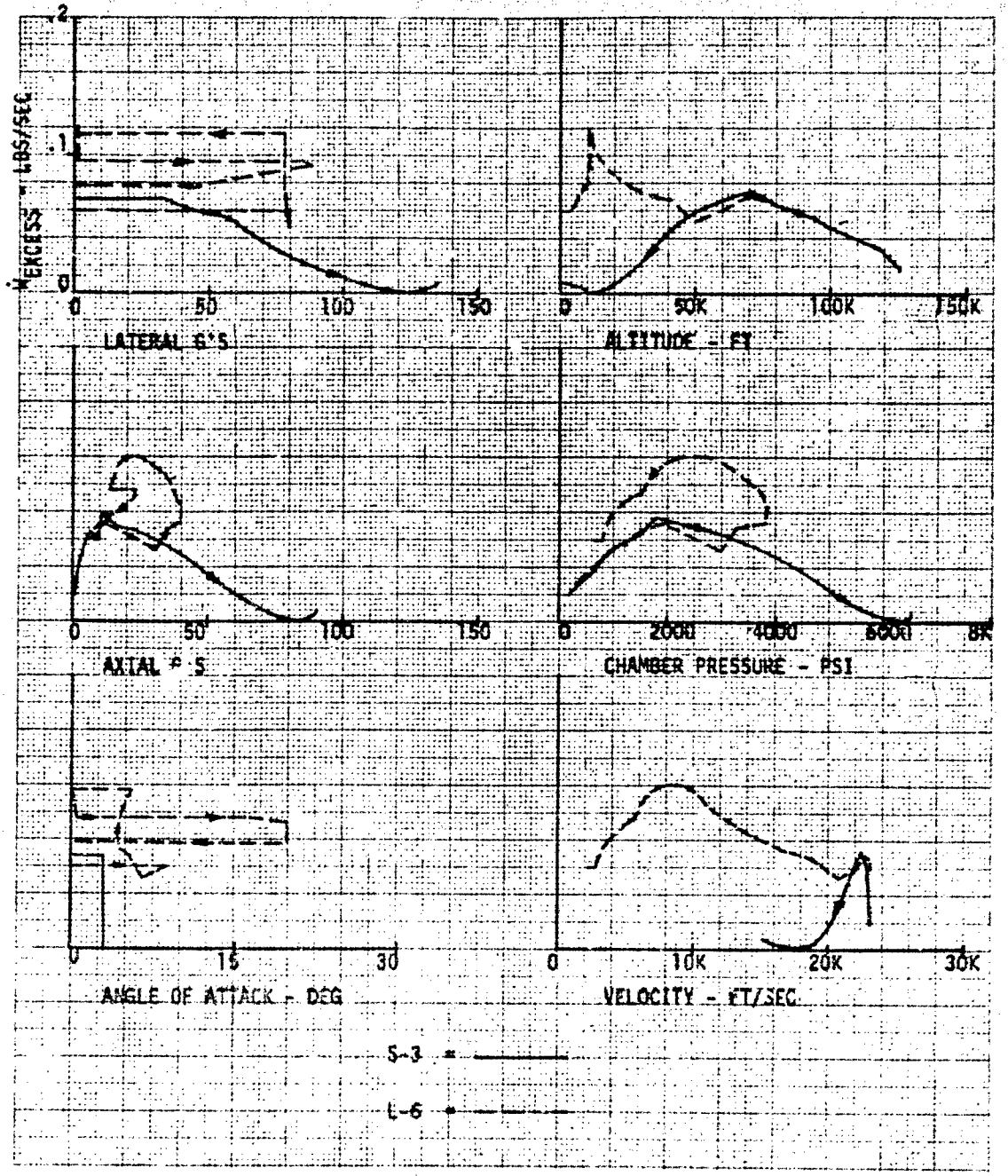


Figure 3-5. Excess Coolant Flow Rate vs Parameters Valve Sensing $\sqrt{\text{Stagnation Pressure}}$
(Gain = 0.007165 Lb/Sec $\sqrt{\text{Psi}}$)

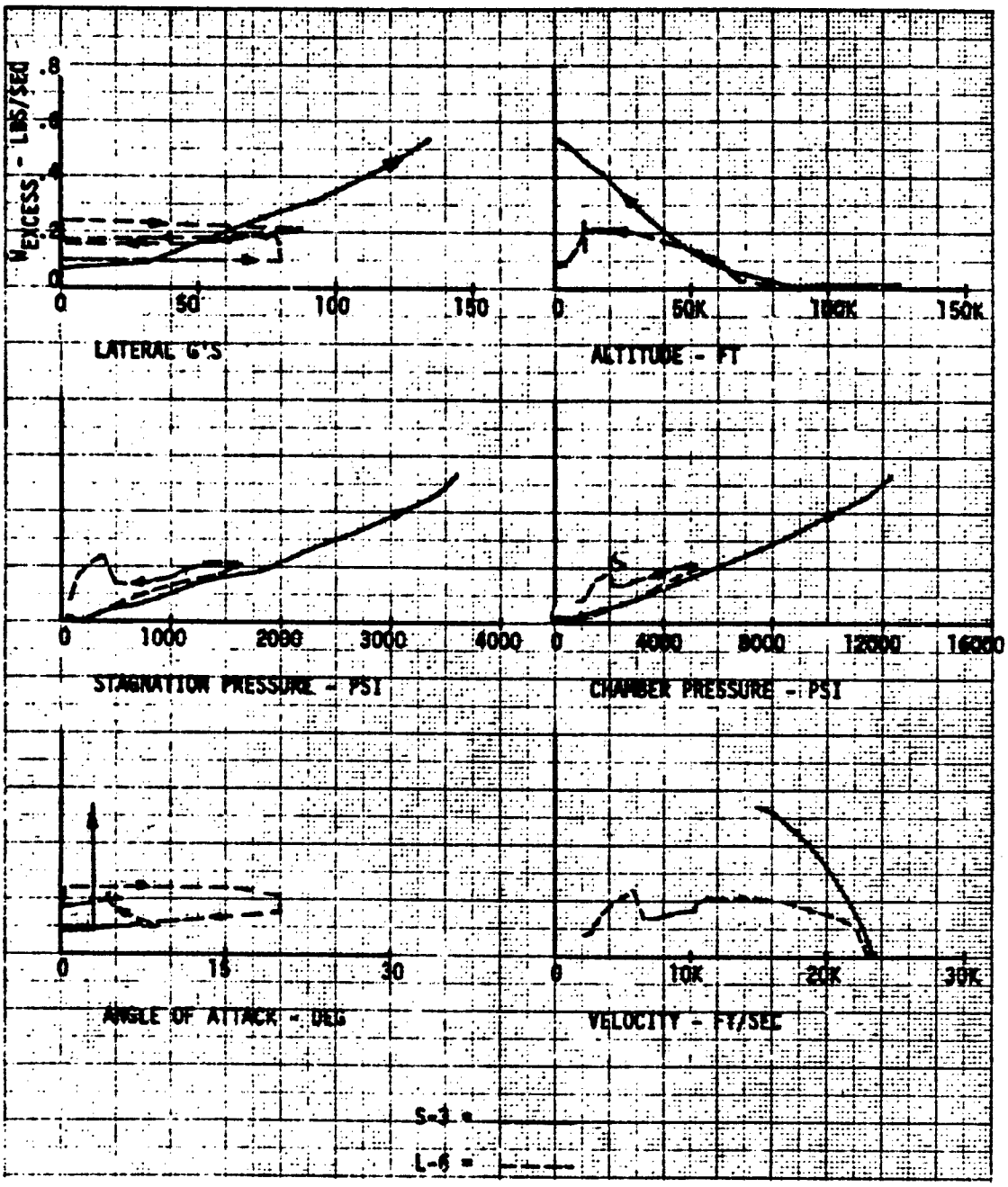


Figure 3-6. Excess Coolant Flow Rate vs Parameters Valve Sensing Axial g's
(Gain = 0.010625 Lb/Sec/g's)

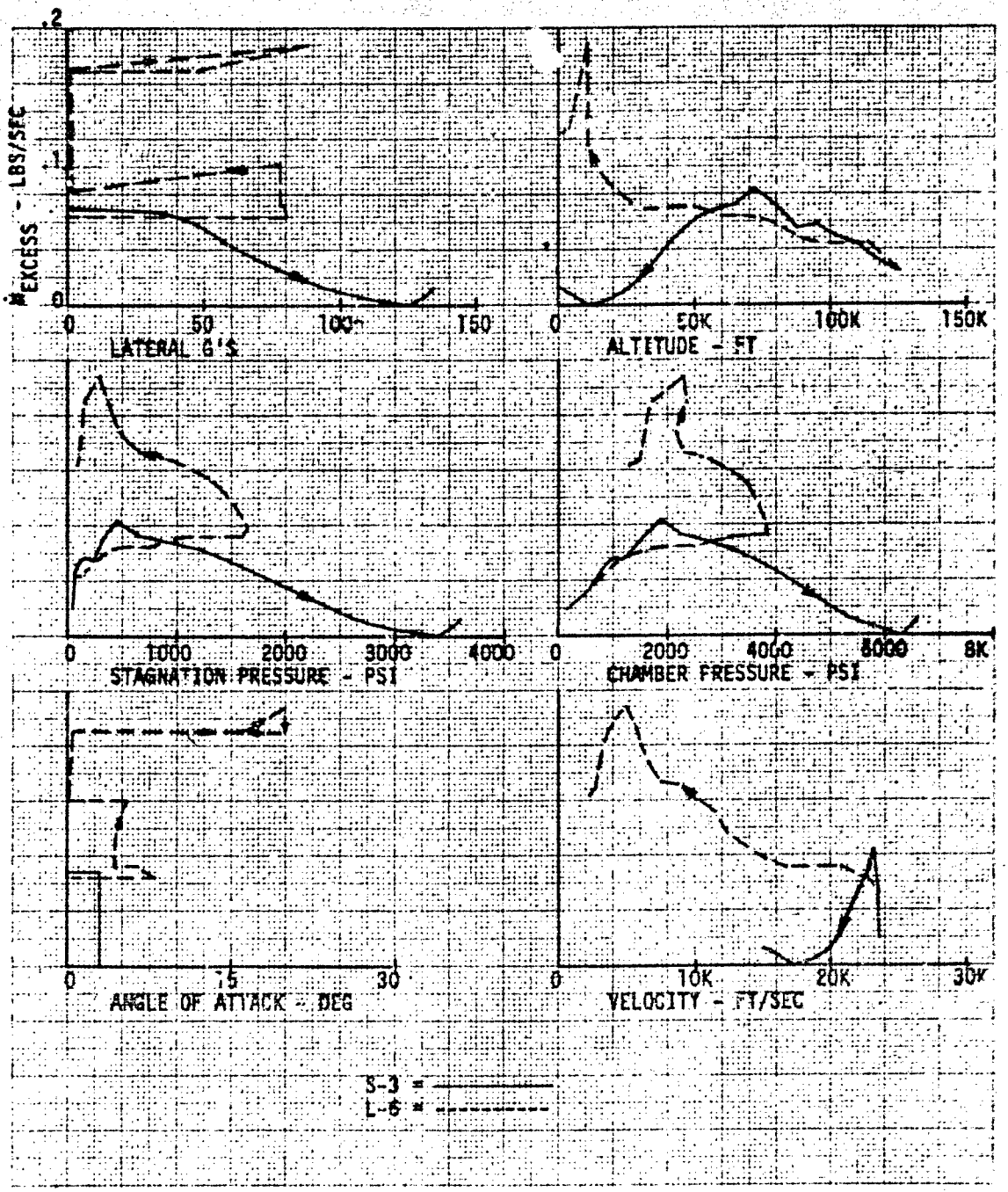


Figure 3-7. Excess Coolant Flow Rate vs Parameters Valve Sensing $\sqrt{\text{Axial g's}}$
(Gain = 0.045772 Lb/Sec/ $\sqrt{\text{g's}}$)

Table 3-1

CORRELATION OF PARAMETERS

	Primary Parameter			
	Axial Acceleration		Stagnation Pressure	
Secondary Parameter	Linear	Sq Rt	Linear	Sq Rt
Axial acceleration	--	--	G	P
Lateral acceleration	P	P	P	P
Stagnation pressure	F	P	--	--
Tip chamber pressure	F	P	G	P
Angle of attack	P	P	P	P
Altitude	P	P	P	P
Velocity	P	P	P	P

P = Poor

F = Fair

G = Good

3.2.1 Square-Root-of-g Valve

The square-root-of-acceleration (g) valve, such as that used in the RVTO-1A, -2A, and ACE vehicles, is included for comparison purposes. The valve is shown schematically in Figure 3-8.

The valve holds a differential pressure, which is a function of acceleration, across a fixed orifice. The force due to acceleration of the mass is opposed by a pressure force across the spool. This force is generated by pressures upstream and downstream of the fixed orifice acting on the spool area. A force unbalance on the spool causes the variable orifice size to change, thereby changing flow rate to maintain the desired pressure drop. In this way, the valve compensates for changes in upstream and downstream pressures and produces a flow proportional to the square root of the acceleration.

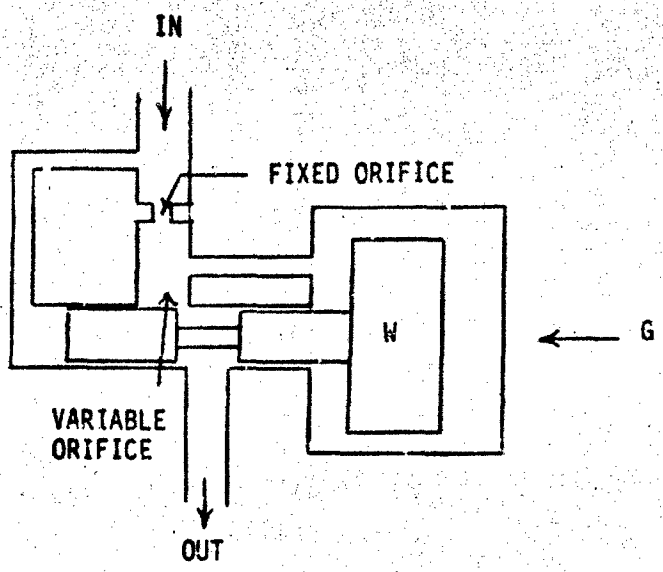


Figure 3-8. Square-Root-of-g Valve

A curve of flow versus acceleration for this valve is shown in Figure 3-9. While the valve meets the requirements of the S-3 and L-6 trajectories, the total coolant required will be large due to excessive flow margins.

3.2.2 Dual-Slope Valve

Examination of Figure 3-9 shows that a single square root of acceleration, enveloping all curves, results in an excess of coolant for the lower-g portions of the curve. This excess can be reduced by modification of the g valve so that it operates on one curve to cover the lower g levels and switches to another curve for the higher g's. This effect can readily be accomplished using the design shown in Figure 3-10. A secondary mass, preloaded by a spring, is included. Below the g level determined by the mass and the preload, the primary mass operates the g valve. Above this critical g level, the spring is overcome and allows the secondary mass to contact the primary mass and so that the two act effectively as one larger mass to produce a new relationship between acceleration and flow. For the design being considered

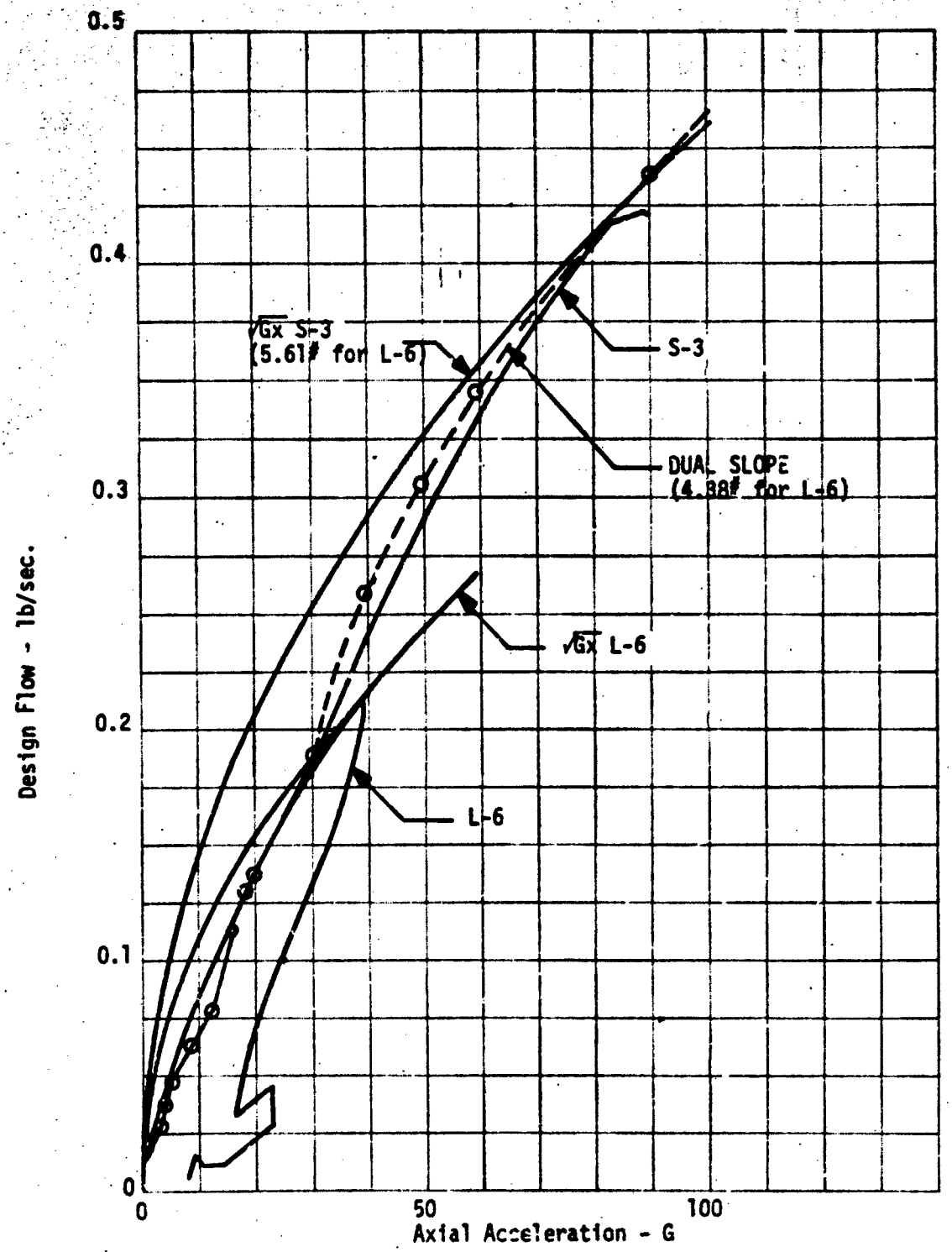


Figure 3-9. Deceleration Functions

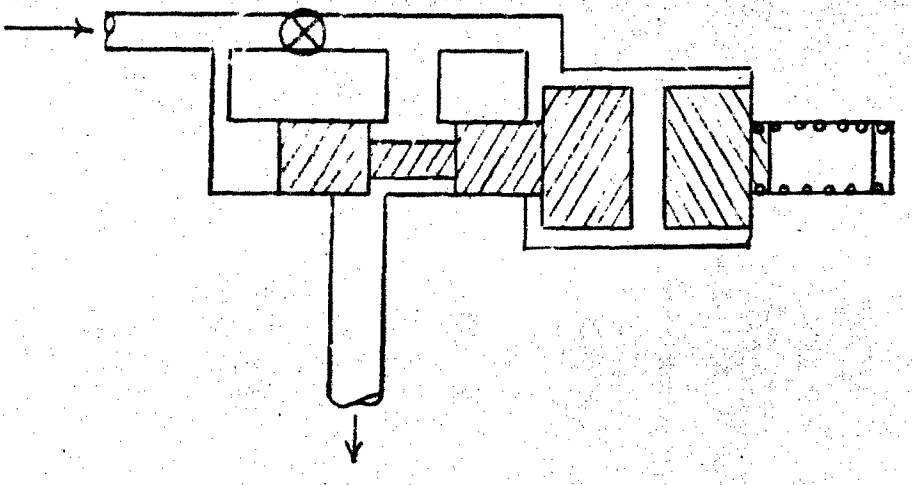


Figure 3-10. Dual-Slope g Valve

here, this valve will essentially follow the L-6 requirements at low g levels and the S-3 requirements at high g levels.

3.2.3 Mark II Valve

The Mark II g valve is an adaptation of the original g valve which allows the flow rate to be almost any single-value function of g instead of just the square root of g. Limitations with this valve are that only one flow rate is available for a value of acceleration, and extremely abrupt changes in flow requirement with g will be faired in slightly due to mechanical constraints. As was the case with the original valve, the flow is independent of changes in upstream or downstream pressure.

A schematic of the valve is shown in Figure 3-11. Acceleration forces act on the mass, moving it to a position where the acceleration force is balanced by a spring force. This position represents a flow area generated by the pin in the orifice. A differential pressure regulator holds the pressure across

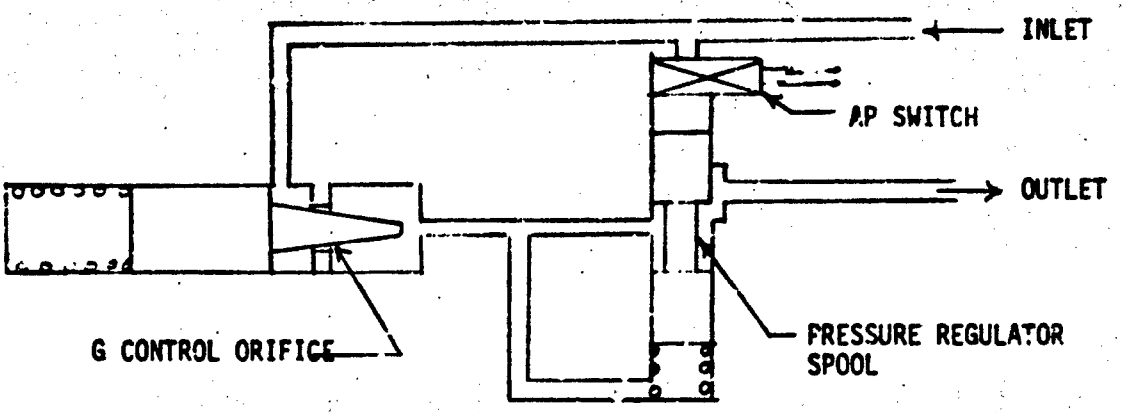


Figure 3-11. Mark II Flow Control Valve Schematic

this orifice constant, so the flow rate is a function of the flow area. Thus, the flow will follow the relationship with acceleration into the pin. Since the pressure regulator spool can be made small and light, and since flow is a function of the square root of the differential pressure, vehicle accelerations will have a negligible effect on this part of the valve.

3.2.4 Volume Compensation

Although a good fit may be obtained by either the dual-slope or Mark II valves for the first part of the flow-g curve (see Figure 3-9) for the L-6 trajectory, there is another part of the curve which requires a different function. No valve giving a single value of flow as a function of acceleration can be expected to improve this situation. If we determine the excess flow from a g valve as a function of volume, we find there is a correlation (see Figure 3-12). Therefore, if the gain of the g valve can be varied as a function of volume of coolant used, a better fit to design flow can be obtained.

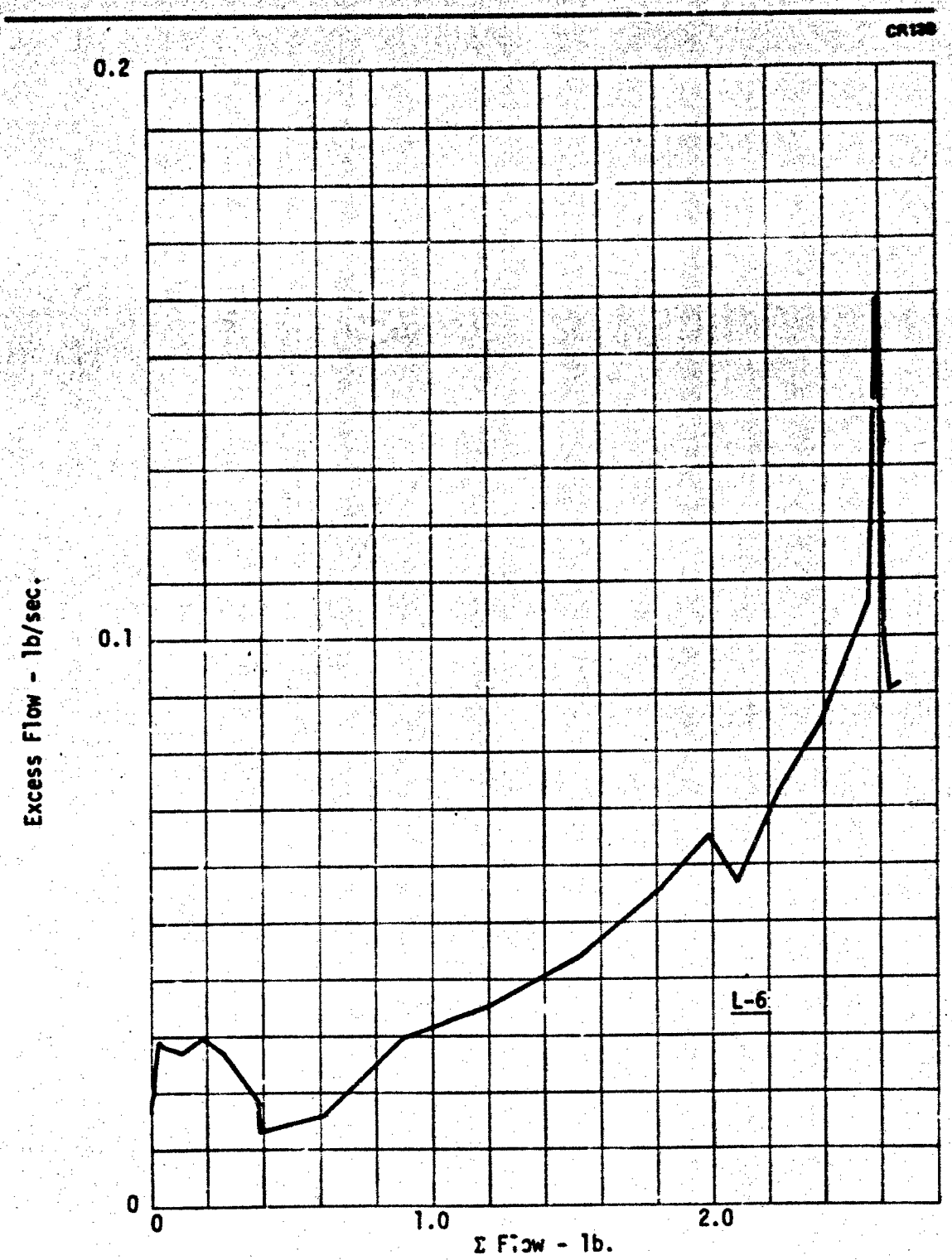


Figure 3-12. Dual-Slope Valve Coolant Excess

The gain of the g valve is a function of the effective area of the calibrating orifice. Although this area could be varied directly, it is preferable to add a series orifice, variation of which has the same effect but decreases the sensitivity of the system to tolerances, etc.

Orifice area variation can be easily accomplished with a piston-type reservoir. One merely attaches a pin with the required shape to the piston and allows this pin to enter an orifice at the forward end of the reservoir. Orifice area will now be a function of pin shape and position, with the latter controlled by the coolant volume in the reservoir.

For a bladder or diaphragm reservoir, another scheme must be used. A flow divider consisting of two orifices is placed in the coolant flow path. The ratio of flow in each path is a function of the orifice diameters. One branch carries only a small percentage of the flow and contains a free-sliding piston with the metering rod attached. The other branch flows through the orifice being regulated by the metering pin. The displacement of the piston is a percentage of the total flow, and the metering pin may be calibrated accordingly to give the desired flow function.

Other means of volume measurement such as a gear or vane-type fluid motors are feasible and could be adopted if warranted.

The real advantage of this scheme is that it can be used with either the dual-slope g valve or the Mark II valve. Considerable improvement in the performance of these valves is possible through the use of volume compensation. This will be discussed further in Section 8. A preprogrammed valve (Figure 3-13) using this basic concept has been designed and is included for comparison. The valve consists of a pressure regulator which holds a constant pressure across a pair of series orifices. One of the series orifices is varied by the metering pin. The other orifice is fixed but may be bypassed by opening a squib valve to produce a different flow characteristic. This will allow prelaunch selection to satisfy whatever trajectories are to be flown.

1. $\dot{m} = f(m)$
2. PRESSURE COMPENSATED
3. PRE-LAUNCH SELECTION

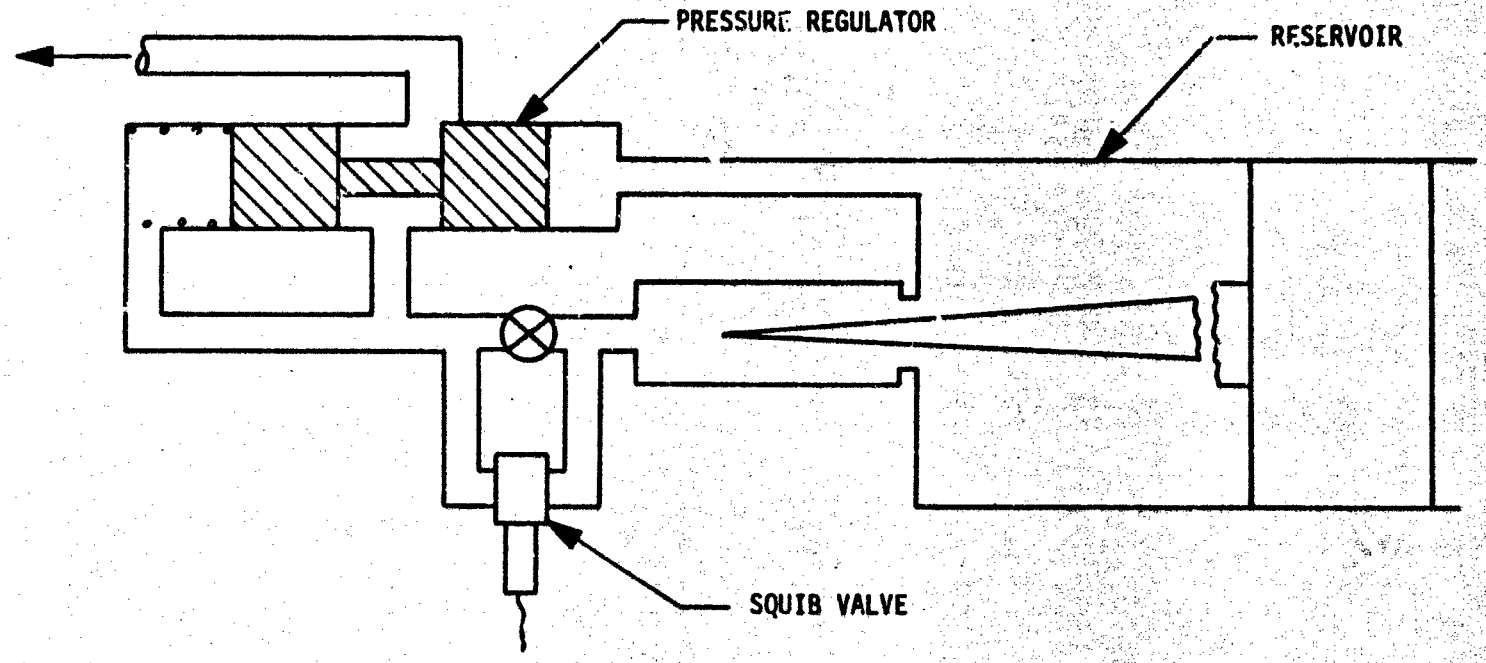


Figure 3-13. Preprogrammed Control

3.2.5 Pressure Control

Although there appeared to be a good correlation between required flow and tip or chamber pressure in the single-parameter study, there are several obstacles to its implementation.

Chamber pressure is the sum of the stagnation pressure and an average pressure drop through the tip. Since the latter is a function of flow rate, a part of the apparent good correlation is illusion.

A simple valve for implementing this control is shown in Figure 3-14. The flow through this valve design is proportional to the square root of chamber pressure. When applied to a system, however, the resultant flow becomes a function of valve and tip characteristics and does not meet design requirements well. Figure 3-15 shows the actual and required flows with this valve.

From Figure 3-15, it can be seen that a valve with a linear flow characteristic might give a better correlation. By combining the steady-state equations of flow for a linear valve (Equation 3-1) and for flow through the tip (Equation 3-2),

$$\dot{m} = K_2 P_c \tag{3-1}$$

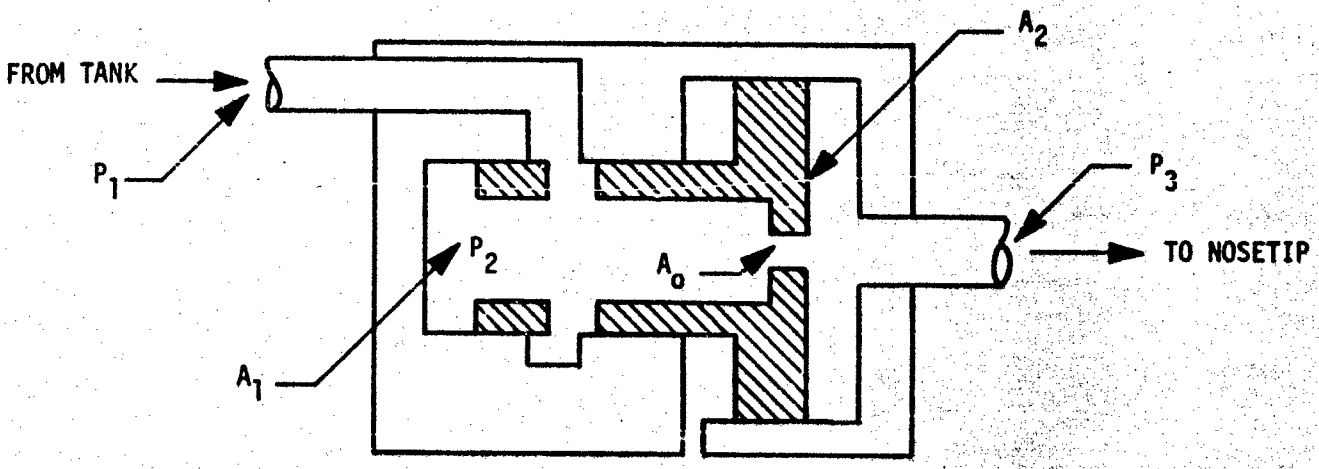
$$\dot{m} \simeq K_1 (P_c - 0.5 P_s) \tag{3-2}$$

where

$\dot{m}$ = flow of coolant.
P_c = chamber pressure.
P_s = stagnation pressure.

the following relationship is obtained:

$$\dot{m} = \frac{K_1 K_2 P_s}{2 (K_1 - K_2)} \tag{3-3}$$



$$q = K\sqrt{P_3}$$

INSENSITIVE TO P_1

Figure 3-14. Pressure Valve

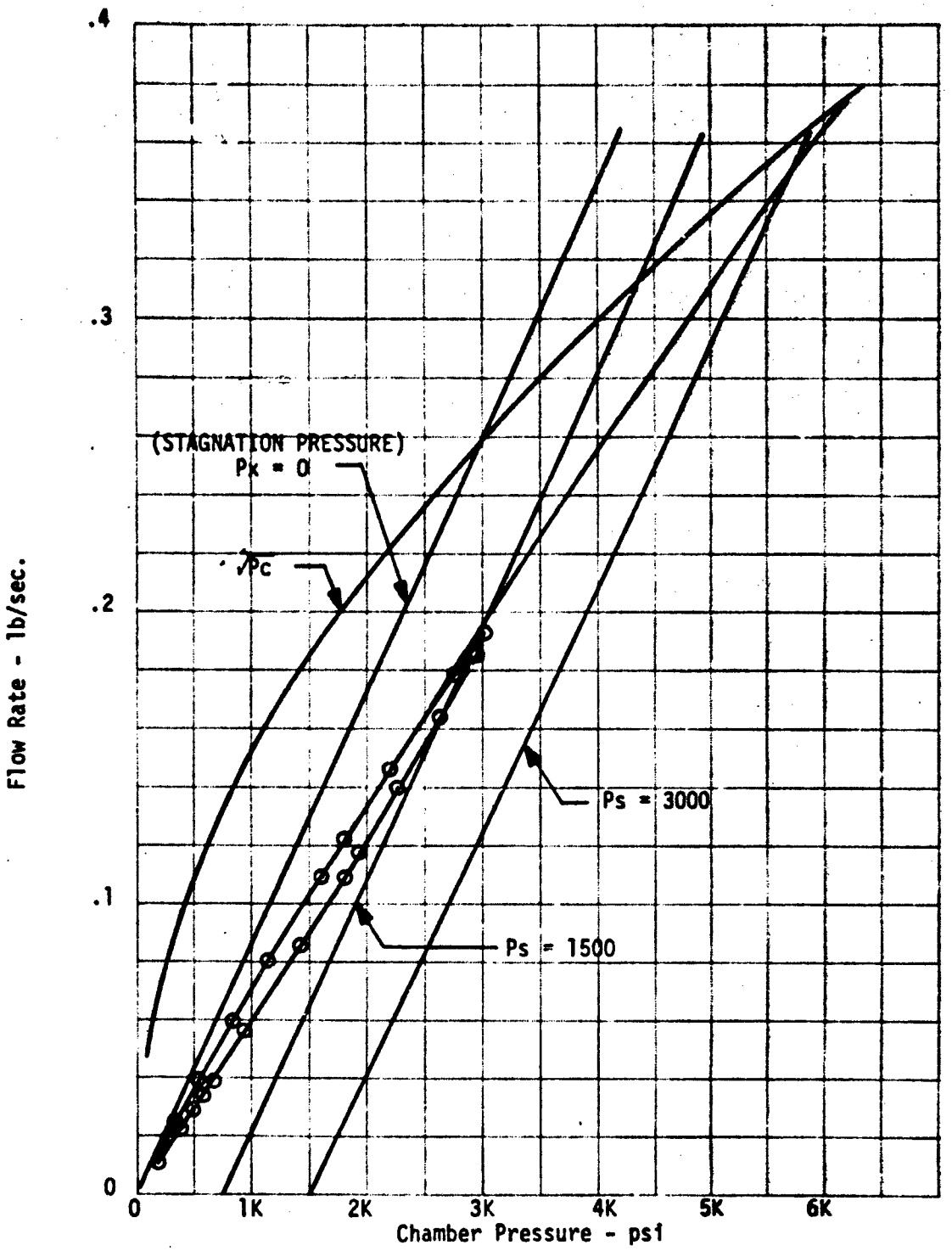


Figure 3-15. Flow Rate Dependence on Chamber Pressure

Therefore, flow will be a linear function of stagnation pressure. Looking at Figure 3-16, which shows the relationship of design flow to stagnation pressure, it is obvious that a linear relationship is not a good fit to the curves, and excessive coolant margins will be required.

Another pitfall of the pressure control system is the stability margin. A valve is required which gives increased flow rate as chamber pressure increases. Since the chamber pressure also increases as flow increases, there is a limit to valve gain.

3.2.6 Partitioned Nosetip Flow Control

In order to deliver coolant flow to a partitioned nosetip, it is necessary to split the main flow such that each section of the nosetip receives the proper amount of coolant to reflect angle-of-attack effects. Figure 3-17 illustrates a flow diverter used to proportion coolant flow as a function of lateral acceleration. The lateral forces operating on the spring-loaded dumbbell piston cause it to shift, reducing coolant flow to one portion and increasing it to the other. This concept would be used in conjunction with another primary flow control device such as a g valve.

Unfortunately, the amount of coolant which can be saved by partitioning the tip is quite small for the current nosetip designs. For a tip with a long skirt, this concept could be very attractive.

3.3 ELECTROMECHANICAL VALVE FLOW CONTROL

Electromechanical flow control valves are very attractive from the standpoint of mission adaptability. This type of valve has quick response and can make use of environmental feedback to reduce excessive coolant usage. Electromechanical valves can be used in either closed-loop, open-loop, or functional flow control systems.

Two types of electromechanical flow control concepts were investigated. The first of these utilizes free-stream parameters as input to a flow control system. The second takes inputs from a nosetip response sensor.

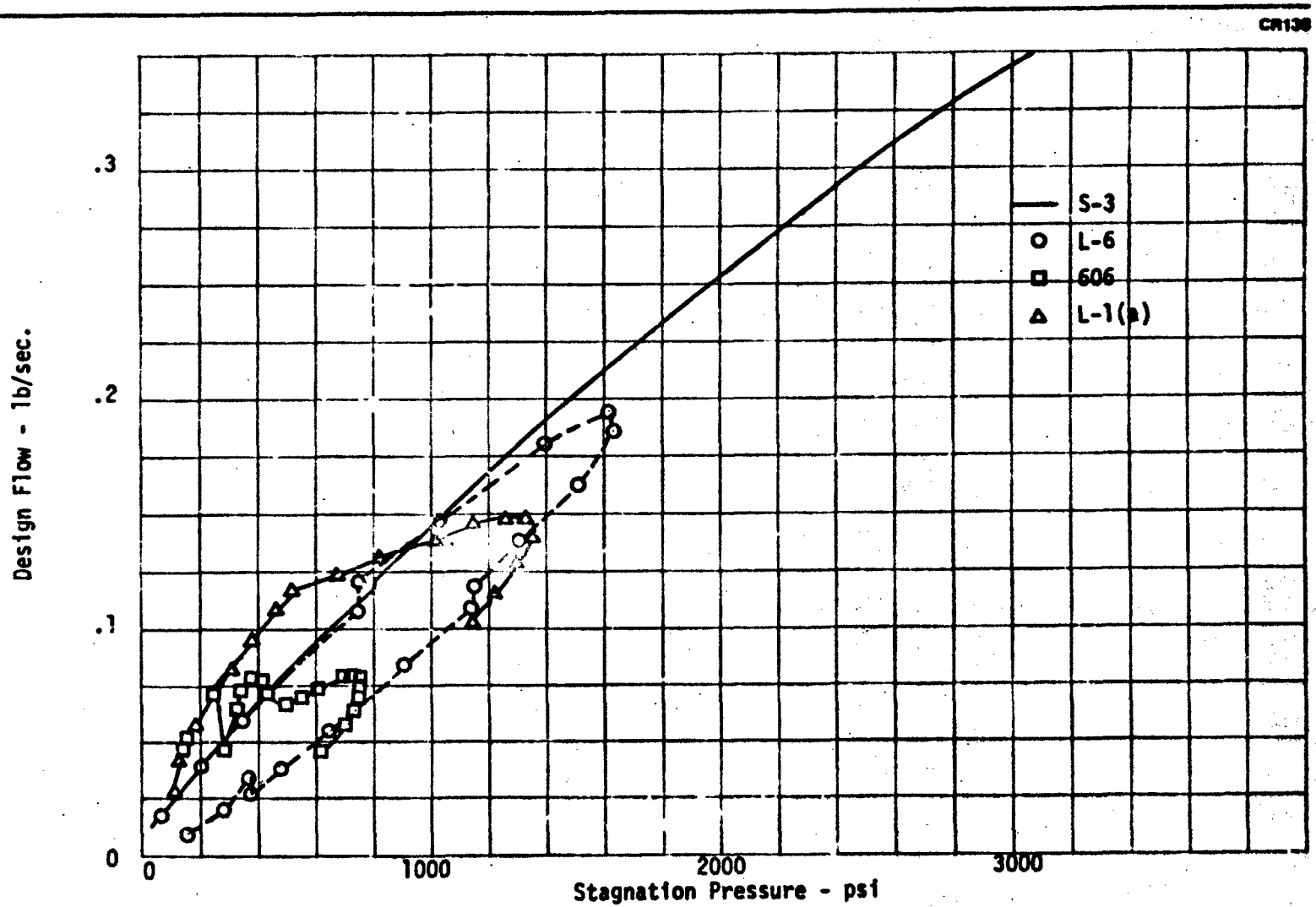


Figure 3-16. Design Flow vs Stagnation Pressure

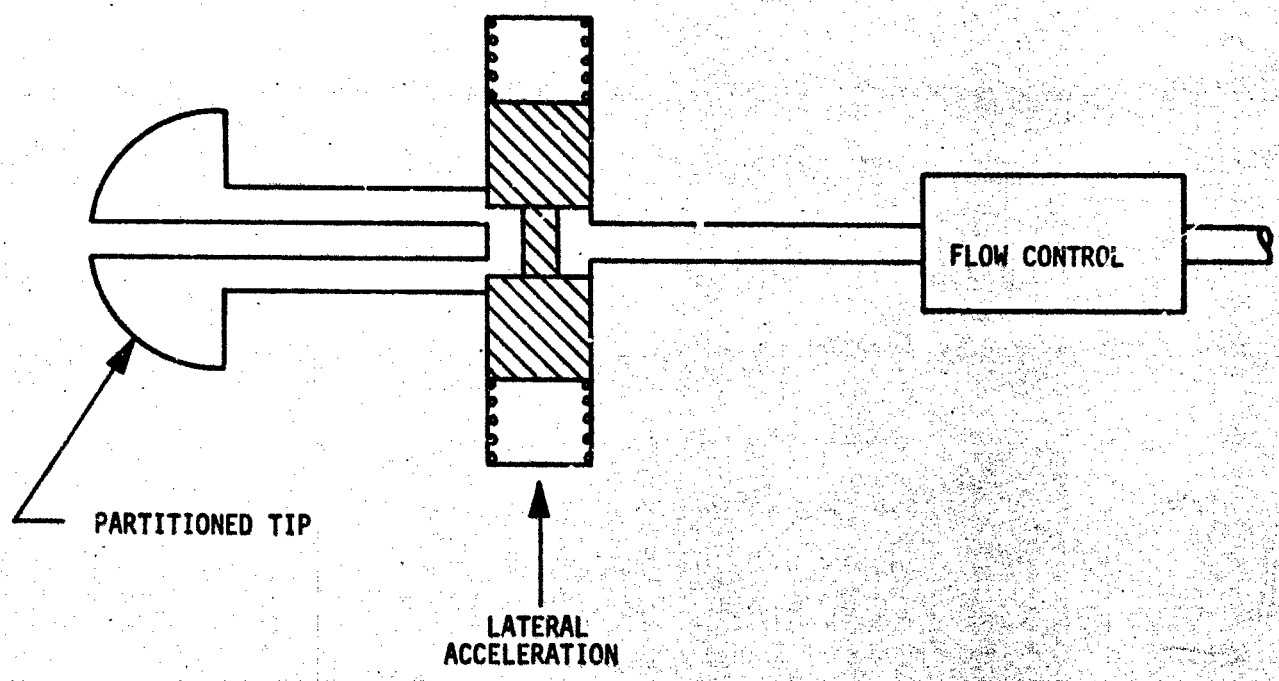


Figure 3-17. Flow Diverter

3.3.1 Utilization of Free-Stream Parameters

The flow control concept utilizing free-stream velocity, density, and angle of attack (u, ρ, and α) is an open-loop, environment-sensitive system which appears to be adaptable to a wide range of trajectory requirements without resulting in excessive flow margins. These parameters are related to coolant requirements for a porous hemispherical nosetip by a set of relationships that are essentially fixed. Theoretically, coolant flow can be modulated through environmental feedback, resulting in a control system which would be second in abaptability only to a closed-loop, direct-feedback system utilizing nosetip sensors. Disadvantages of the u, ρ, α system are the development time and the complexity and uncertainty of the computer and electrical components necessary to drive the valve. In addition, since the system operates essentially open-loop, flow feedback may be required due to variations in upstream and downstream pressures.

The thermally ideal coolant flow rate for a 7-deg cone angle and zero angle of attack is approximated in Equation 3-4 (derived in Appendix C, Equation C-21):

$$\dot{m} = 1.584 \times 10^{-2} \frac{R_N^{1.8} u^{1.29} \rho^{0.8}}{Pr^{2/3}} \left[(1.0 + 3.03 \times 10^{-8} u^2)^{1/4} - 1.0\right] \quad (3\text{-}4)$$

The bracketed term accounts for turbulent mass transfer blocking on the nosetip surface.

Ignoring the mass transfer blocking term, there is a more simplified control equation of the form:

$$\dot{m}_{actual} = K_v u^a \rho^b \quad (3\text{-}5)$$

Using Equation 3-5, a computer simulation found the optimum values of a and b that minimized the excess coolant flow for every time point on the L-6 trajectory. L-6 was chosen because it has the highest design coolant weight. The valve gain, K_v, was adjusted to form an envelope around the coolant requirements for all five trajectories.

Poor results were achieved with this equation, as 43.8 percent excess coolant was required. The excess coolant flow is defined as

$$\text{Percent excess flow} = 100 \left[\frac{\int_{t_o}^{t} \dot{m}_{actual}\, dt}{\int_{t_o}^{t} \dot{m}_{design}\, dt} - 1 \right] \tag{3-6}$$

The mass transfer blocking effect was then taken into account by expressing Equation 3-4 as

$$\dot{m}_{actual} = K_v\, u^a\, \rho^b \left[(1.0 + 3.03 \times 10^{-8}\, u^2)^{1/4} - 1.0 \right] \tag{3-7}$$

and using the same procedure to find new values of a, b, and K_v. This time, 32.6 percent excess coolant resulted. It was obvious that an additional correlation still needed to be made.

Figure 3-18 shows the effect of angle of attack on design coolant flow rate. By fitting the relationship with a quadratic, Equation 3-7 can be extended to

$$\dot{m}_{actual} = K_v\, u^a\, \rho^b \left[(1.0 + 3.03 \times 10^{-8} u^2)^{1/4} - 1.0 \right] \cdot \left[1.0 + 0.0036 |\alpha| + 0.00115 \alpha^2 \right] \tag{3-8}$$

After optimizing the a and b constants, 11.3 percent excess coolant flow resulted for the L-6 trajectory.

For some types of vehicle control, the altitude rather than the density may be available. Density must then be computed. Equation C-39 is an approximation to air density in the form of an exponential of a cubic in geometric altitude. When this function is used to provide the air-density term in

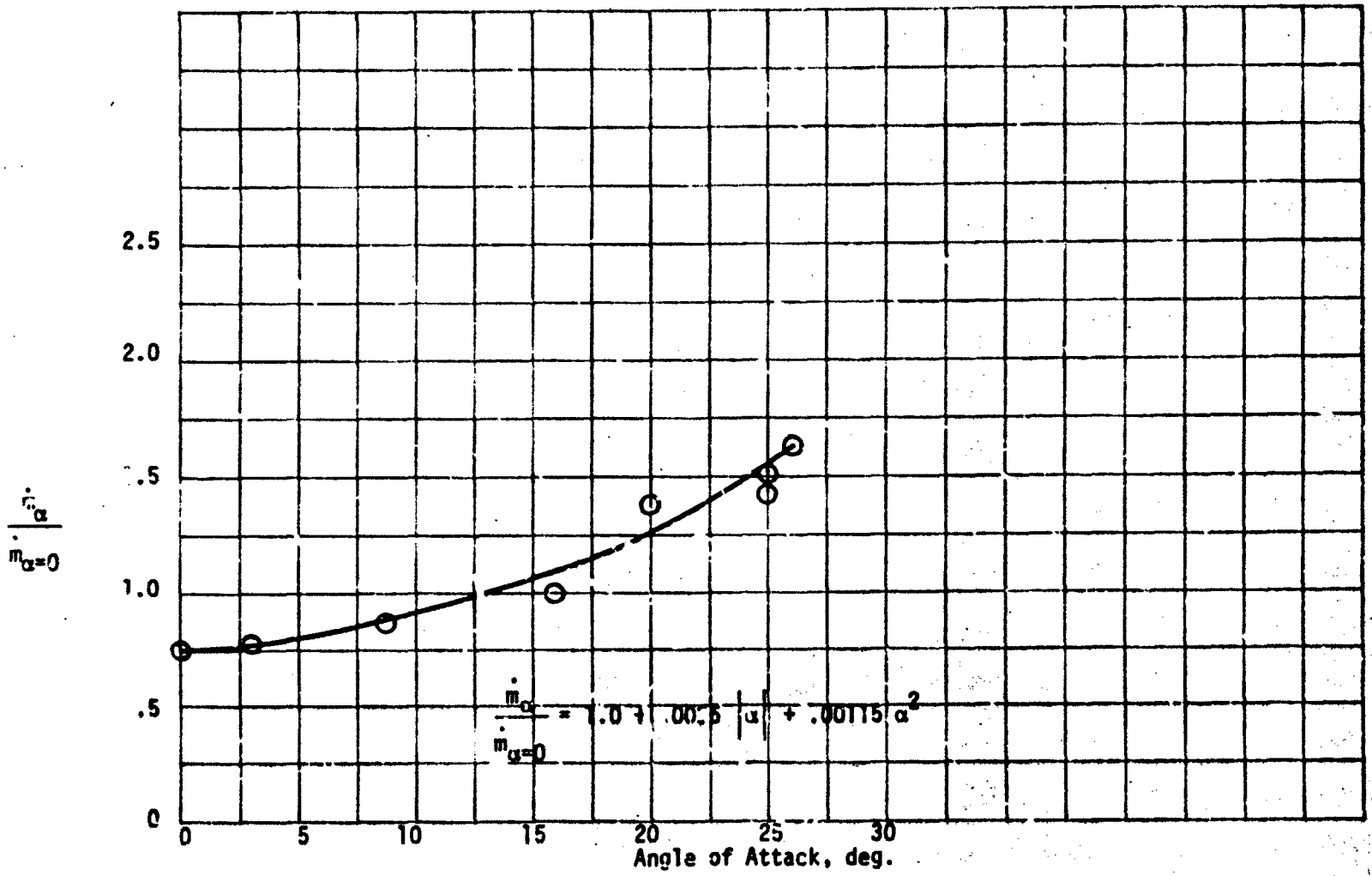


Figure 3-18. Effect of Angle of Attack on Design Coolant Flow Rate

Equation 3-8, the excess coolant is reduced to 10.9 percent. Apparently the small errors in the density function are in the right direction to improve coolant utilization.

Table 3-2 summarizes the parametric equations for actual coolant flow and the resulting excess coolant. It is interesting to note that the final exponents for the velocity and density terms are very close to those of Equation 3-4, which were estimated analytically in Appendix C. As further evidence of the validity of the approach, Figures 3-19 through 3-21 present actual and design coolant flow histories using Equation 3-8.

3.3.2 Electrical Generation of Free-Stream Parameters

The free-stream parameters required to determine actual coolant flow must be obtained or generated from outputs available from the vehicle autopilot. Two types of autopilot have been specified for this study (Reference 3-1). In the Type A autopilot, only pitch, yaw, and axial accelerations (η_x, η_y and η_z) are available for signal conditioning. In the Type B autopilot, it is assumed that u, ρ, and α are available. Therefore, this type will not be investigated further.

Both analog and digital signal conditioning devices were considered for the Type A autopilot. In both systems, η_x, η_y, and η_z are inputs, and a signal representing Equation 3-8 is relayed to the electromagnetic flow control valve. As shown in Appendix C, angle of attack, α, is obtained from the normal acceleration, η_N, and the axial acceleration, η_Z (Equation 3-9)

$$|\alpha| = 1/2\left(\frac{C_2}{\xi_N} - C_1\right) \pm \sqrt{\left(C_1 - \frac{C_2}{\xi_N}\right)^2 \Big/ 4 - C_3} \qquad (3\text{-}9)$$

where the C's are constants describing the drag characteristics of the vehicle, and ξ_N is the ratio of vehicle normal and axial accelerations.

$$\xi_N = \frac{\eta_N}{\eta_Z} \qquad (3\text{-}10)$$

Table 3-2

ELECTROMAGNETIC FLOW CONTROL VALVE PARAMETRIC EQUATIONS

1. $\dot{m} = K_v u^{2.13} \rho^{0.8}$

2. $\dot{m} = K_v u^{0.875} \rho^{0.661} \left[(1.0 + 3.03 \times 10^{-8} u^2)^{1/4} - 1.0 \right]$

3. $\dot{m} = K_v u^{1.0} \rho^{0.810} \left[(1.0 + 3.03 \times 10^{-8} u^2)^{1/4} - 1.0 \right] \left[1.0 + 0.0036 |\alpha| + 0.00115 \alpha^2 \right]$

4. $$\begin{cases} \dot{m} = K_v u^{1.0} \rho_*^{0.810} \left[(1.0 + 3.03 \times 10^{-8} u^2)^{1/4} - 1.0 \right] \left[1.0 + 0.0036 |\alpha| + 0.00115 \alpha^2 \right] \\ \rho_* = 0.002377\, e^{(0.0419 - 3.05 \times 10^{-5} H - 1.96 \times 10^{-10} H^2 + 7.15 \times 10^{-16} H^3)} \end{cases}$$

Coolant Use, L-6 Trajectory (m_{design} = 2.312 lb)

Equation	Lb of Coolant	Excess (percent)
1	3.325	43.8
2	3.068	32.6
3	2.574	11.3
4	2.565	10.9

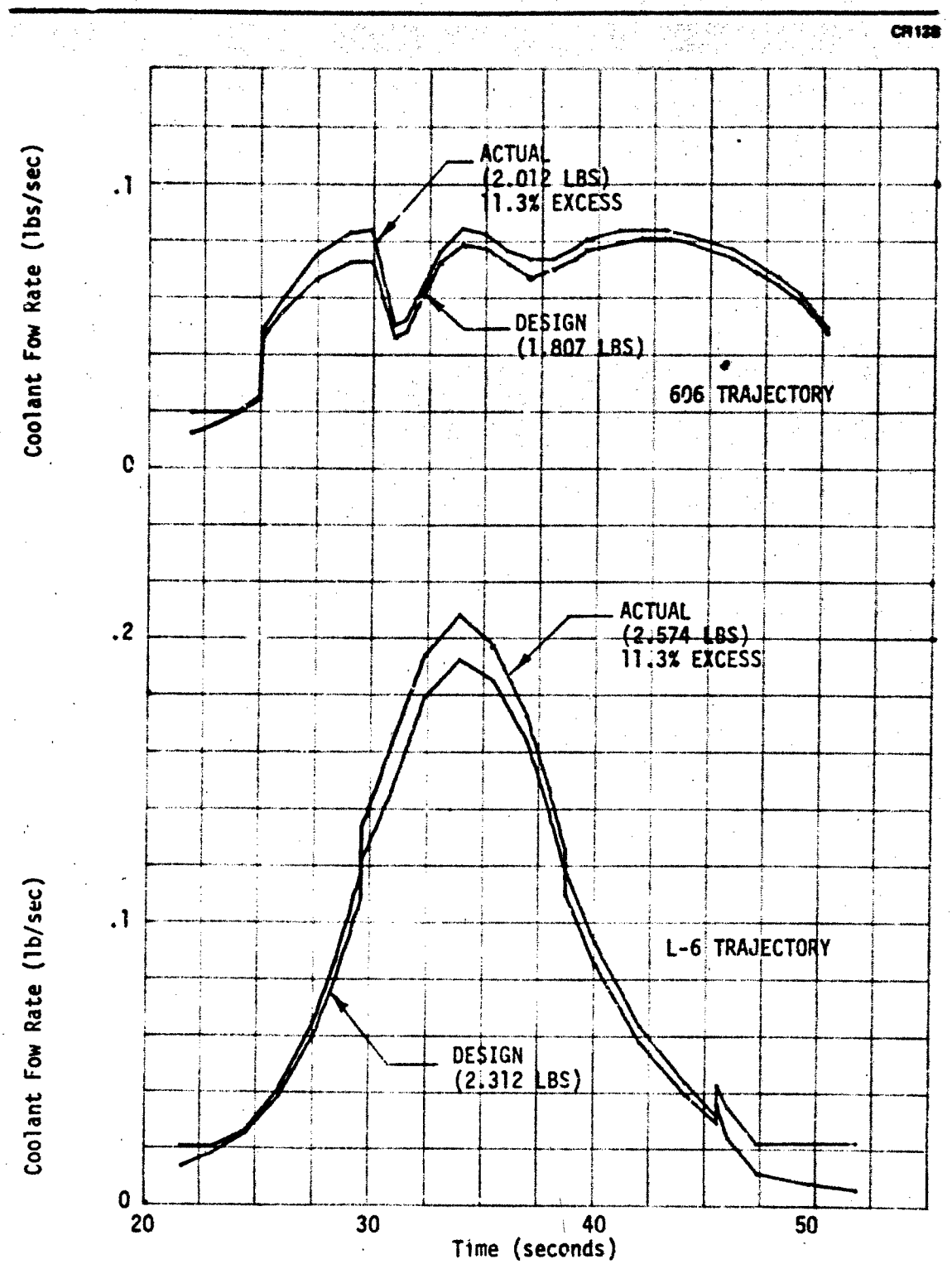


Figure 3-19. Electromagnetic Valve Flow Histories, L6 and 606

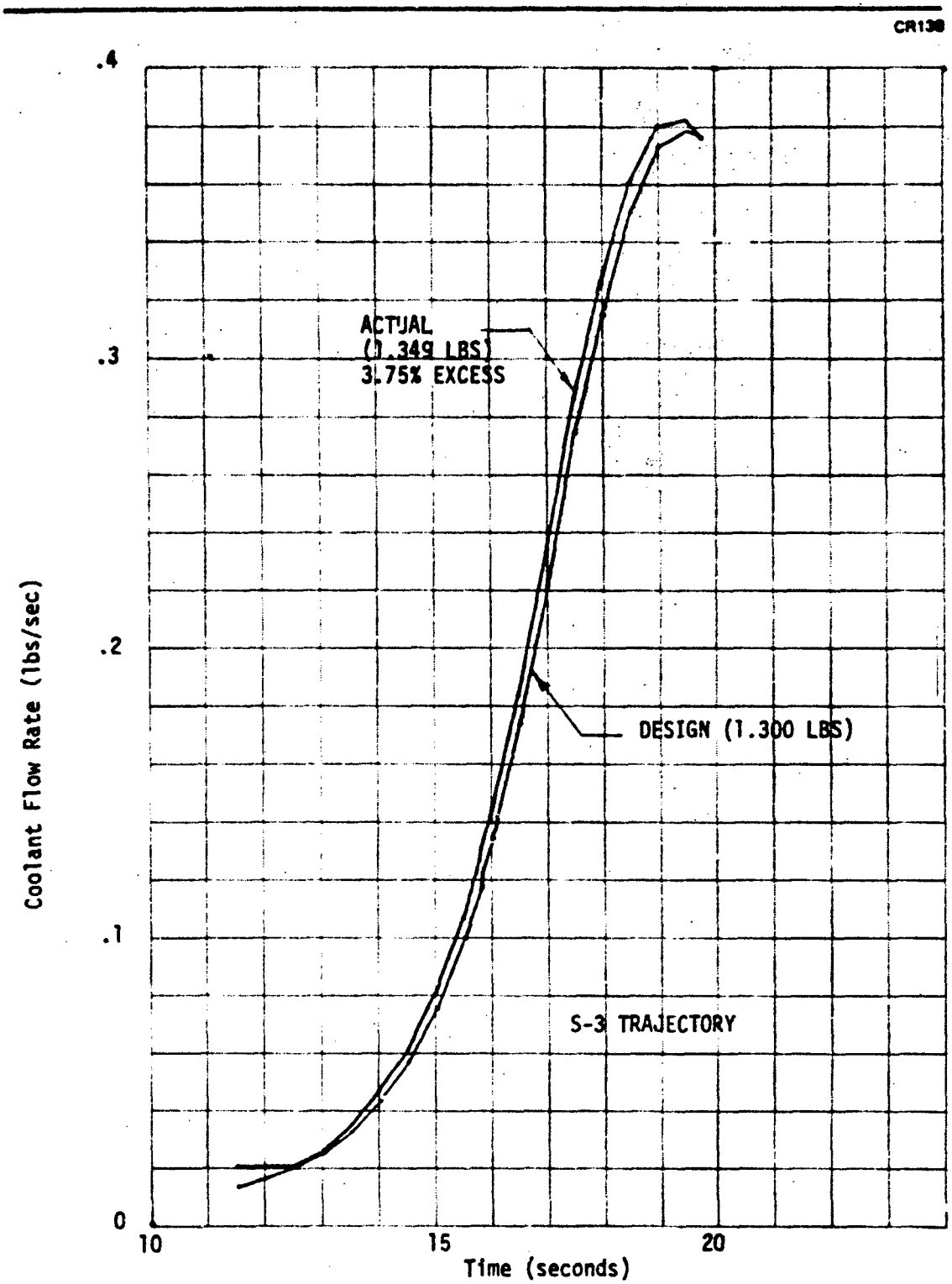


Figure 3-20. Electromagnetic Valve Flow History, S-3

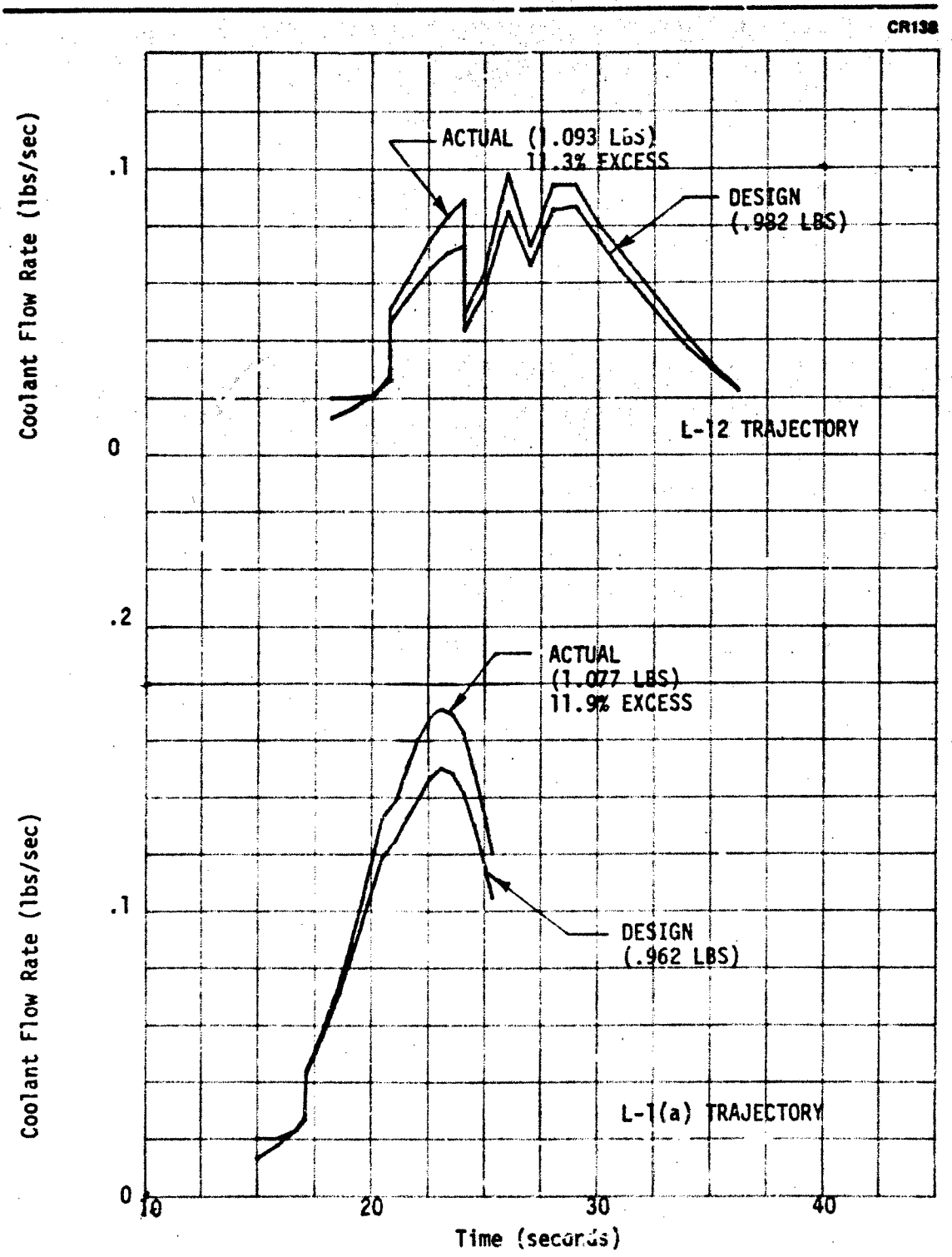


Figure 3-21. Electromagnetic Valve Flow Histories, L-1(a) and L-12

Velocity is obtained by integrating resultant accelerations according to Equation 3-11.

$$u_\infty = u_o + \int_{t_o}^{t} (\eta_Z \cos \alpha + \eta_N \sin \alpha)\, dt \qquad (3\text{-}11)$$

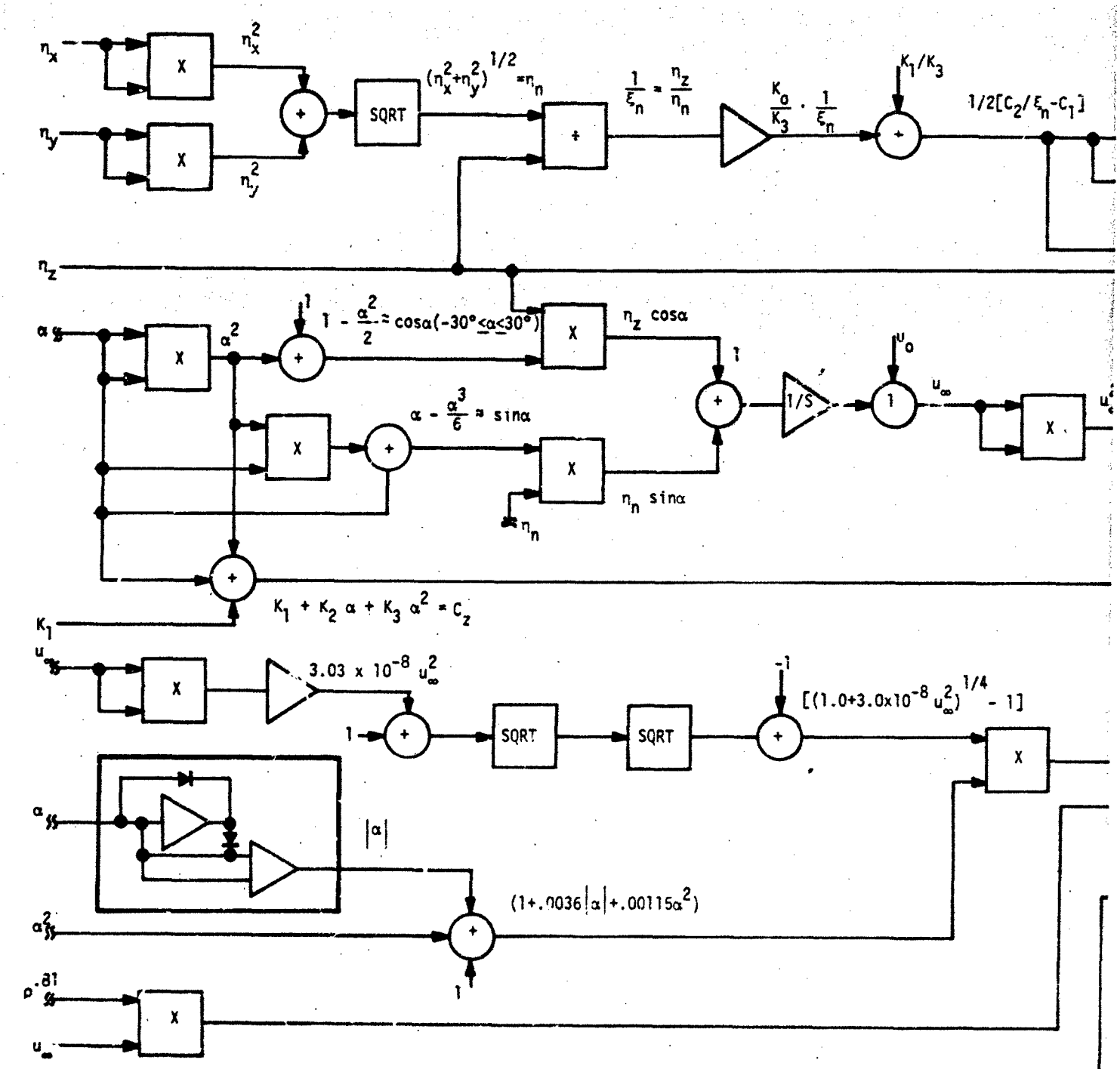
Since altitude cannot be determined with sufficient accuracy using only vehicle accelerations, an atmosphere density model cannot be used. Therefore, free-stream density must be derived from the axial drag equation as shown in Appendix C:

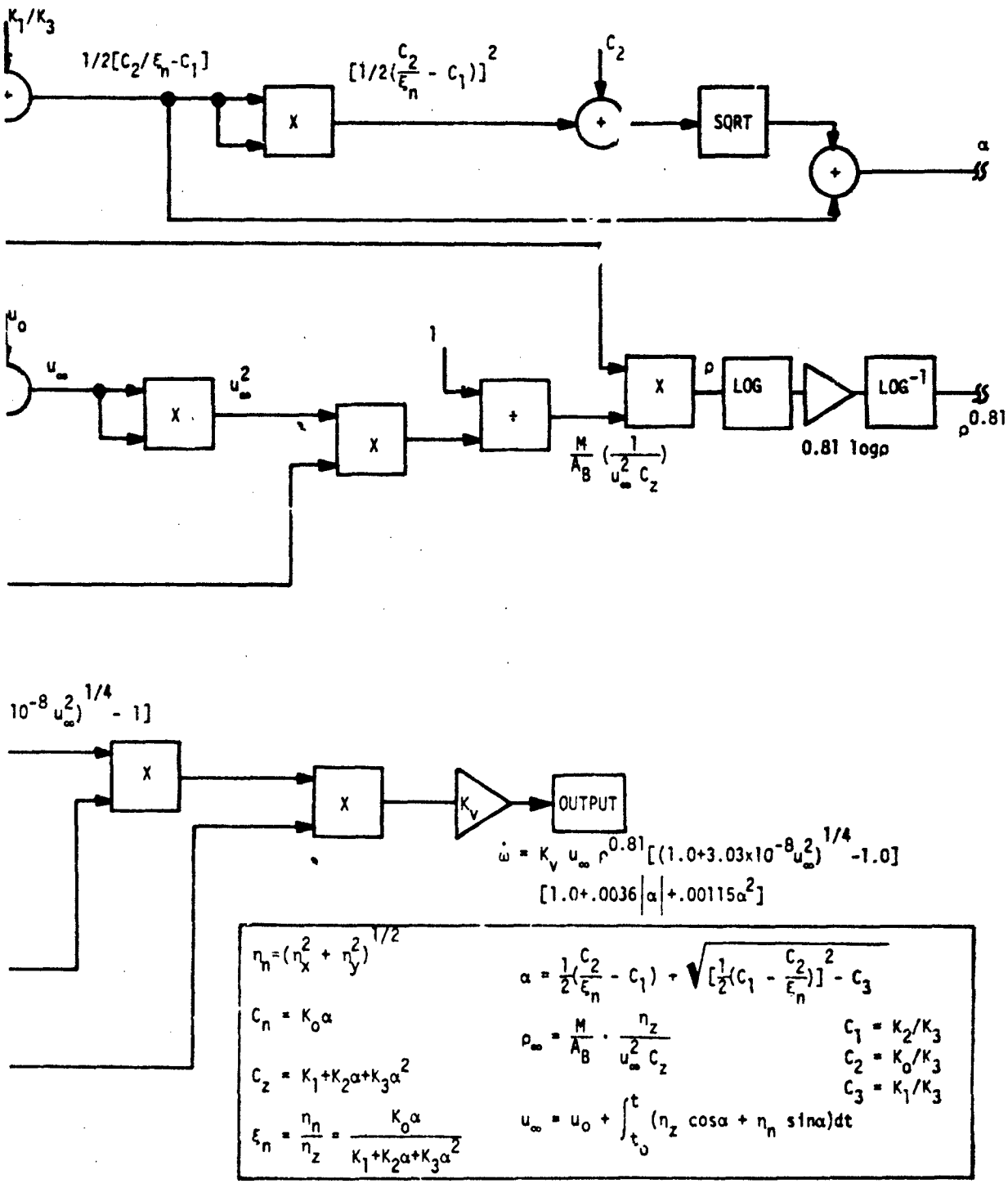
$$\rho_\infty = \frac{C\,\eta_Z}{u_\infty^2\, C_Z} \qquad (3\text{-}12)$$

where $C = \frac{m}{A_B}$, m is the vehicle mass, A_B is the vehicle base area, and C_Z is the axial drag coefficient, defined in Equation C-29.

Figure 3-22 is the schematic of the analog valve signal conditioner valve driver. This system uses approximately 20 analog multipliers and 40 operational amplifiers. In addition to that shown, circuitry would be necessary in the form of limiters to prevent division by numbers approaching zero and also to prohibit the possibility of negative square roots. A low-pass filter is also required to eliminate high-frequency noise. This type of network would contain signal errors exceeding the 10-percent target value due to its complexity, and would not be practical for the Type A autopilot vehicle.

The digital system, which would be within the 10-percent accuracy range, would basically consist of the circuitry shown in Figure 3-23. This system consists of a multiplexer to process the incoming accelerometer data, and a digital-to-analog converter to interface the accelerometer data with the digital processor. The processor will contain the software and hardware necessary to solve the flow rate equation. An 8-bit system with a 10-μsec processor cycle time would allow 10^4 instructions to be processed and still remain within a 10-msec execution time for determining a solution to the


n_x
X
n_x^2
n_y
X
n_y^2
+
SQRT
$(n_x^2+n_y^2)^{1/2}=n_n$
÷
$\frac{1}{\xi_n}=\frac{n_z}{n_n}$
$\frac{K_a}{K_3}\cdot\frac{1}{\xi_n}$
K_1/K_3
+
$1/2[C_2/\xi_n-C_1]$
n_z
α
X
α^2
1
$1-\frac{\alpha^2}{2}\approx\cos\alpha(-30°\leq\alpha\leq30°)$
X
$n_z\cos\alpha$
1
+
1/S
u_o
1
u_∞
X
$\alpha-\frac{\alpha^3}{6}\approx\sin\alpha$
X
$n_n\sin\alpha$
n_n
+
$K_1+K_2\alpha+K_3\alpha^2=C_z$
K_1
u_∞
X
$3.03\times10^{-8}u_\infty^2$
1
+
SQRT
SQRT
-1
$[(1.0+3.0\times10^{-8}u_\infty^2)^{1/4}-1]$
X
α
$|\alpha|$
α^2
$(1+.0036|\alpha|+.00115\alpha^2)$
+
1
ρ
.81
X
u_∞



$$\dot{\omega} = K_v\, u_\infty\, \rho^{0.81}[(1.0+3.03\times10^{-8}u_\infty^2)^{1/4}-1.0]\,[1.0+.0036|\alpha|+.00115\alpha^2]$$

$$\eta_n=(\eta_x^2+\eta_y^2)^{1/2} \qquad \alpha = \frac{1}{2}(\frac{C_2}{\xi_n} - C_1) + \sqrt{[\frac{1}{2}(C_1 - \frac{C_2}{\xi_n})]^2 - C_3}$$

$$C_n = K_o\alpha \qquad \rho_\infty = \frac{M}{A_B}\cdot\frac{n_z}{u_\infty^2 C_z} \qquad C_1 = K_2/K_3,\ C_2 = K_o/K_3,\ C_3 = K_1/K_3$$

$$C_z = K_1+K_2\alpha+K_3\alpha^2 \qquad u_\infty = u_o + \int_{t_o}^{t}(n_z\cos\alpha + n_n\sin\alpha)dt$$

$$\xi_n = \frac{n_n}{n_z} = \frac{K_o\alpha}{K_1+K_2\alpha+K_3\alpha^2}$$

Figure 3-22. Analog System

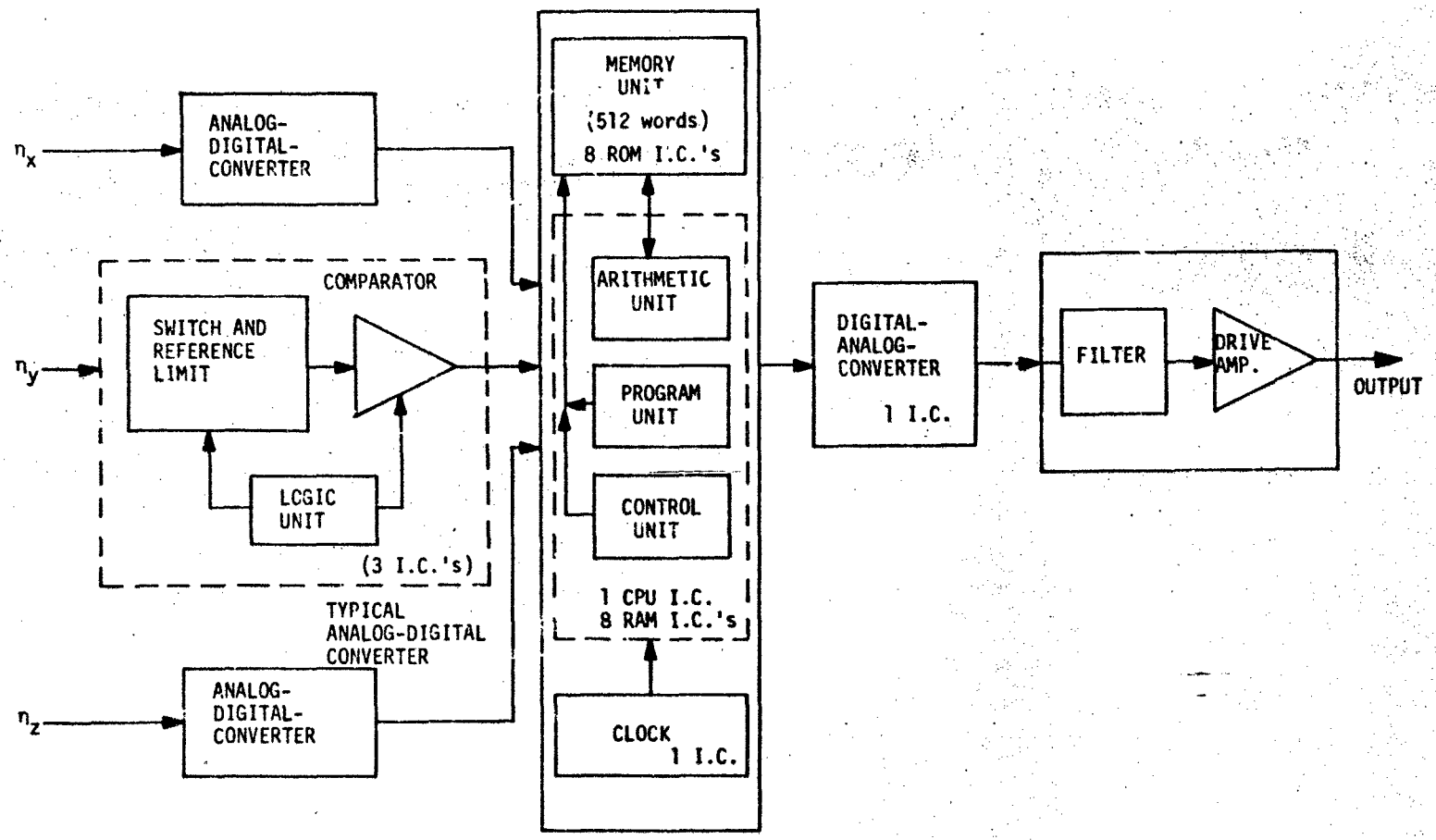


Figure 3-23. Free-Stream Parameter Digital Converter

flow control equation with three-axis acceleration input data. A digital-to-analog converter would then convert the processor solution to an analog signal, which would be conditioned to drive the valve. Using the beam lead packaging technique, this system could be packaged within a 15-in.^{3} volume, and the power requirements would be within 15 w.

3.3.3 Nosetip Performance Sensors

The ultimate in flow control concepts would be to sense the response of the nosetip to the aerothermodynamic environment and meter the flow in a manner which allowed the tip to operate right on the threshold of failure. The critical factor in this system is the response sensor. A fairly extensive survey of sensor concepts which may be usable for this application has been accomplished.

Five basic approaches have been considered for providing nosetip performance sensory data that can be utilized for controlling coolant flow rate. These approaches include the use of thermocouples, gamma ray detection, acoustic detection, optical detection, and electromagnetic detection. Two of the five approaches appear feasible. These are utilization of thermocouples in the porous nosetip to sense nosetip surface temperature, and utilization of an optical sensor embedded in the heat shield to sense nosetip melt particles in the surface boundary layer. Each of the five approaches is analyzed in detail in the following subsections.

3.3.3.1 Thermocouples

In order to permit quick response to changes in the nosetip environment, it is desirable to place thermal sensors as close to the heated surface as possible. Figure 3-24 illustrates approaches that might be used to provide surface temperature measurement in three areas: on the porous nose, at the back edge of the porous nose, and in the heat shield at the nosetip-heat shield junction. The latter approach utilizes a sheathed thermocouple in order to facilitate installation and avoid any shunting that might occur, both due to contact with the metallic nosetip and charring of the heat shield. Figure 3-25 illustrates temperature histories recorded with this method during a recent

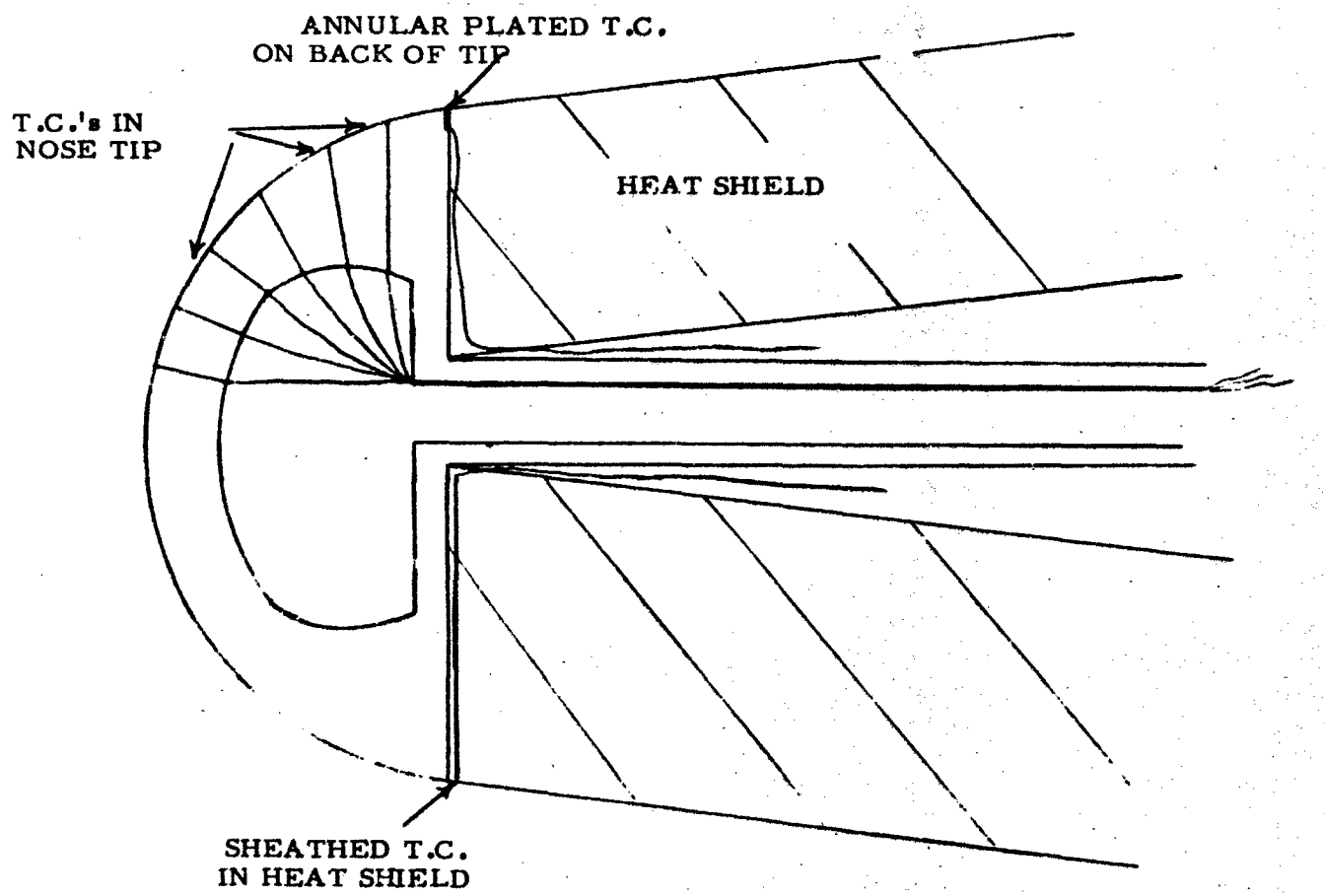


Figure 3-24. Use of Thermocouples

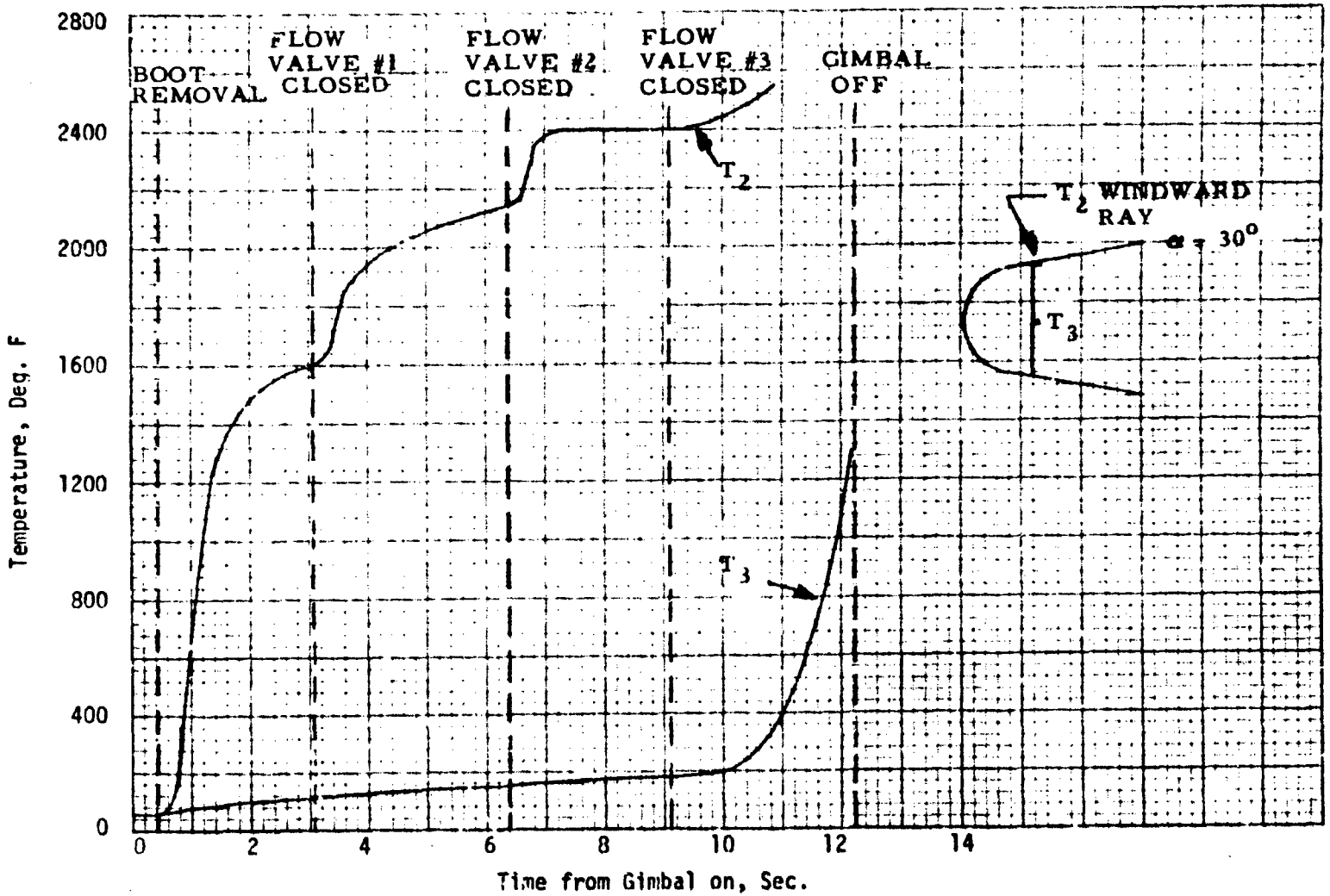


Figure 3-25. Heat Shield Surface Temperatures

ground test conducted at 30 deg angle of attack with step reductions in coolant flow. Considerable response to coolant flow change is apparent, particularly on the windward ray. However, as can be seen, the time to steady state for this type of instrumentation is relatively long. In addition, this is a heat shield temperature measurement and does not necessarily reflect conditions everywhere on the nosetip surface; that is, melting could be occurring somewhere on the tip due to local coolant starvation while excess coolant is being ejected aft of this region, yielding a low temperature measurement on the heat shield. For these reasons, heat shield thermocouples are not recommended.

A continuous thermocouple junction can be formed at the back face of the nosetip by plating, flame spraying, or vacuum-depositing one side of the junction on the surface or back edge of the nosetip, relying on the nosetip material to form the second side of the junction. Extreme care would have to be exercised in attaching the lead wires, and each wire would have to be of the same material as the corresponding side of the junction. Although this technique should provide rapid response, like heat shield thermocouples it could indicate low surface temperature while at some forward point a high surface temperature existed. Therefore, this approach is not recommended.

The installation and hot-flow ground test of 0.020-in.-diameter sheathed thermocouples in porous nose material has been attempted in the past. The tests indicated that a hot spot forms around the thermocouple, apparently due to local blockage of coolant flow, and the nosetip eventually fails due to melting in this region. By reducing the size of the thermocouple, however, the disturbance created may be correspondingly reduced to an acceptable effect.

Sheathed thermocouples are available in diameters down to 0.008 in. However, it is felt that further reductions in size are possible if thermocouples can be custom made, starting with bare wire, which is available in diameters down to 0.0003 in. The minimum couple size appears to be limited by the ability to produce holes in the nosetip material. A minimum hole diameter of 0.002 in. may be achievable by EDM (electrical discharge machining) or by laser drilling. However, the best which has been achieved to date is 0.0039 in.

Single-wire systems can be produced by utilizing the nosetip material in conjunction with the wire material to form the junction at the wire attachment point. If a conventional, ceramic-insulated, two-wire couple were used, there could be some difficulty associated with obtaining a thermocouple bead in good contact with the nosetip material. Attachment of the bead to the nosetip surface could be accomplished by peening or by hot or cold welding. The technique of hot-spot welding is well developed and appears to be the best choice.

Two-wire systems can also be made by utilizing a pair of holes, closely spaced, and attaching each wire to the nosetip surface. The electrical path created by the nosetip material between the two wires completes the couple. By utilizing only a single wire for each hole, more reliable contact with the tip surface is possible, and larger-diameter wire can be used, which is appealing from the standpoint of thermocouple durability.

The selection of wire materials for producing nosetip thermocouples is based primarily on two considerations: operating temperature and couple voltage. Figure 3-26 presents electromotive force (EMF) curves for several couples as a function of temperature. The maximum expected use temperature would be the melting temperature of the nosetip material, while the liquid film temperature on the surface could be as low as a few hundred degrees at low surface pressure. For two-wire couples, it appears that chromel-alumel would be a good selection. Possible single-wire couples could be formed with stainless steel and platinum, chromel and stainless steel, and beryllium and platinum.

Figures 3-27 and 3-28 present possible design approaches for one- and two-wire thermocouple systems in porous stainless steel. The one-wire systems require a 0.002-in.-diameter hole, and the two-wire system requires a 0.003-in.-diameter hole.

3.3.3.2 Gamma Ray

Figure 3-29 illustrates the use of a basic concept that is being developed for the purpose of sensing graphite nosetip shape change on a flight test vehicle. For application to a transpiration nosetip, a radioactive source

CR138

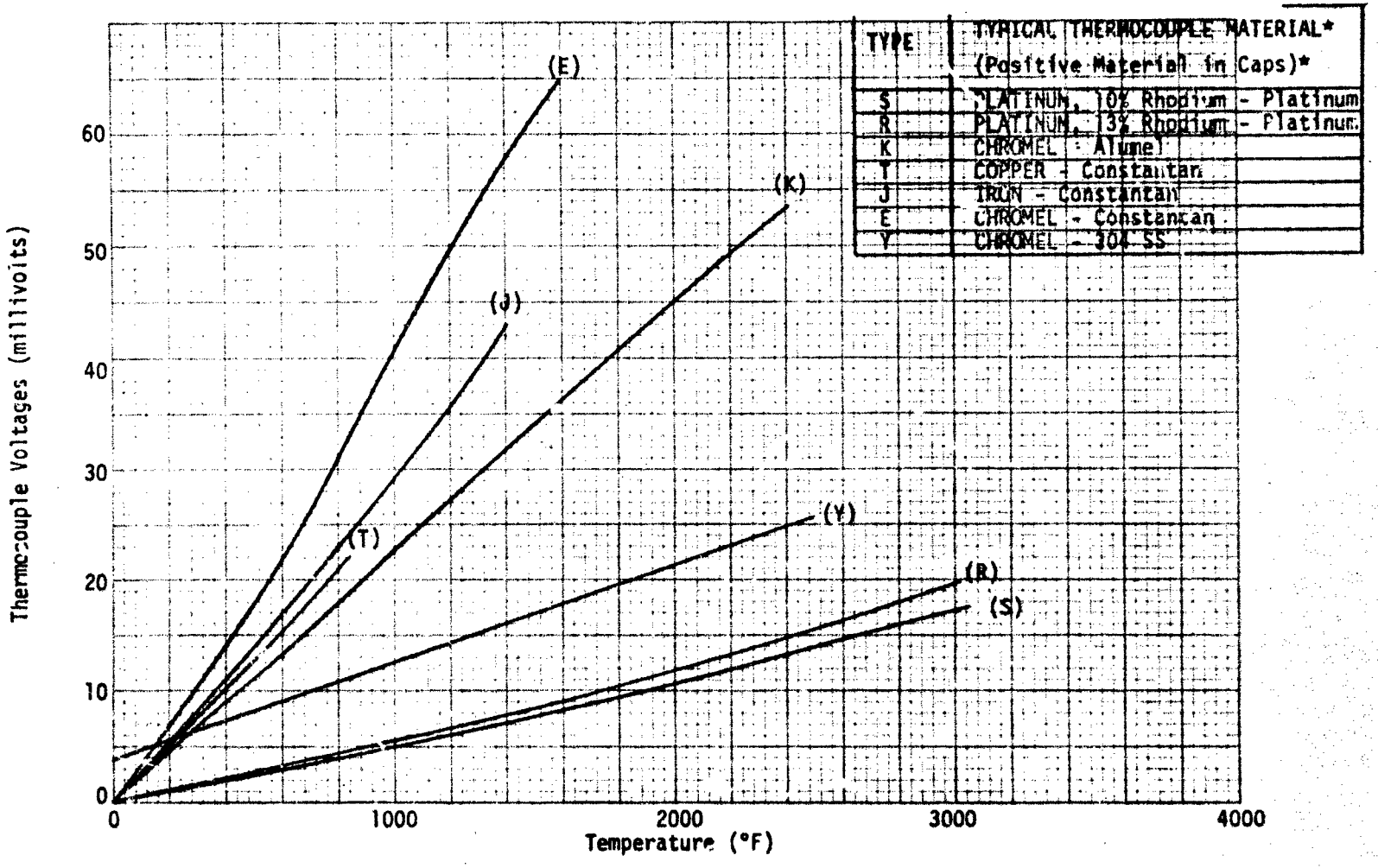


Figure 3-26. Thermocouple Voltage Characteristics

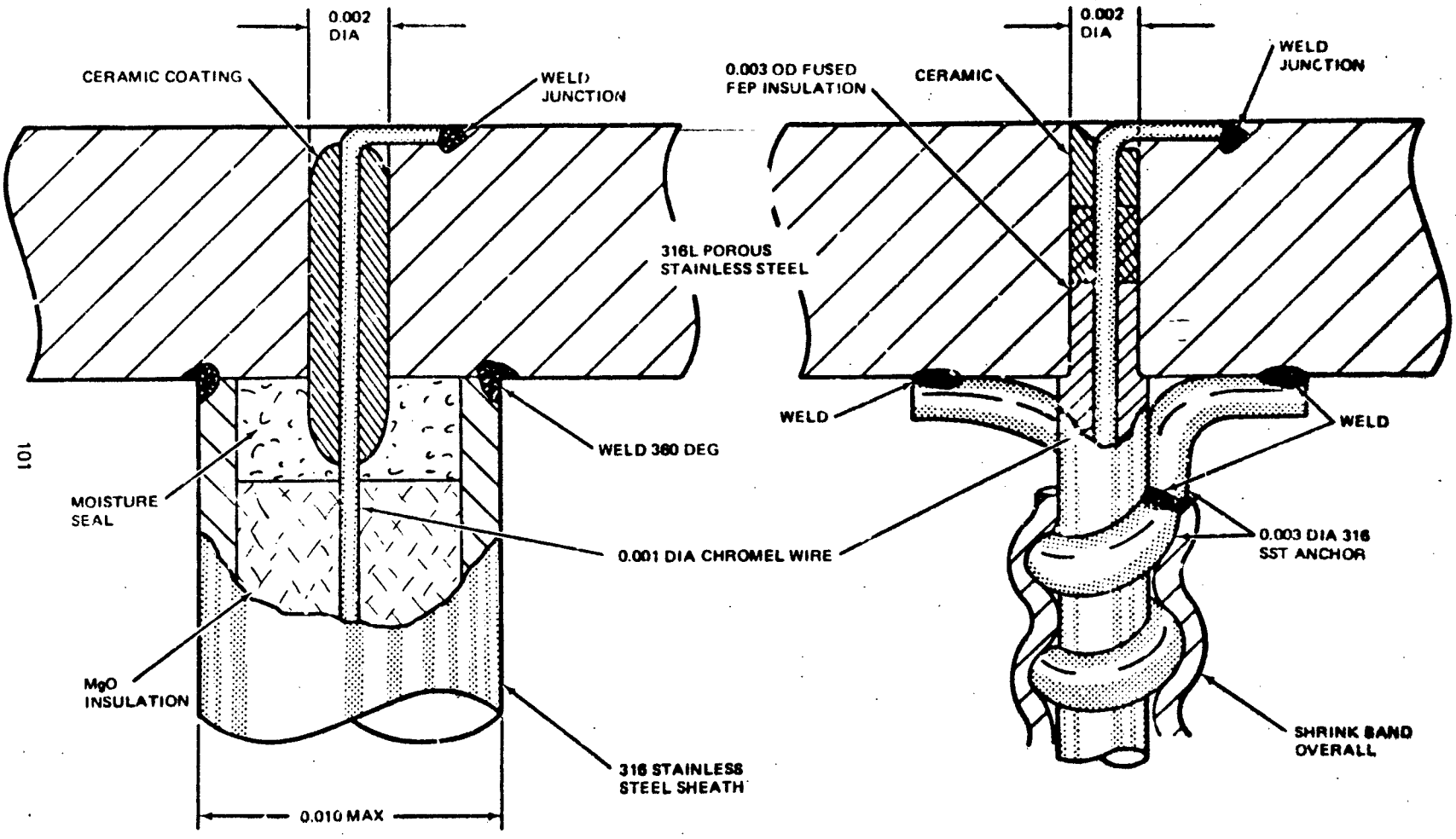


Figure 3-27. One-Wire Thermocouples

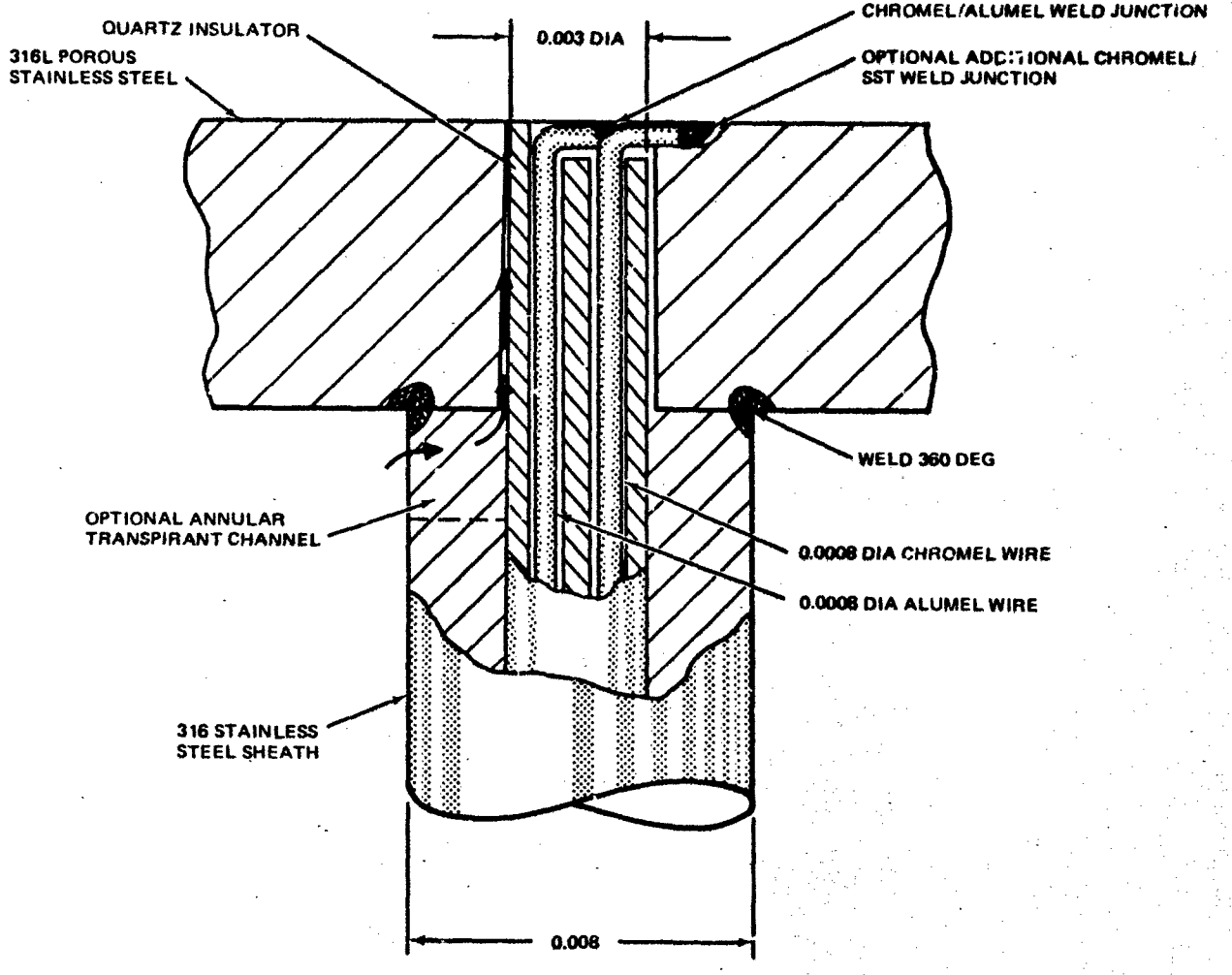


Figure 3-28. Two-Wire Thermocouple With Optional One-Wire Thermocouple in Stainless Steel Sheath

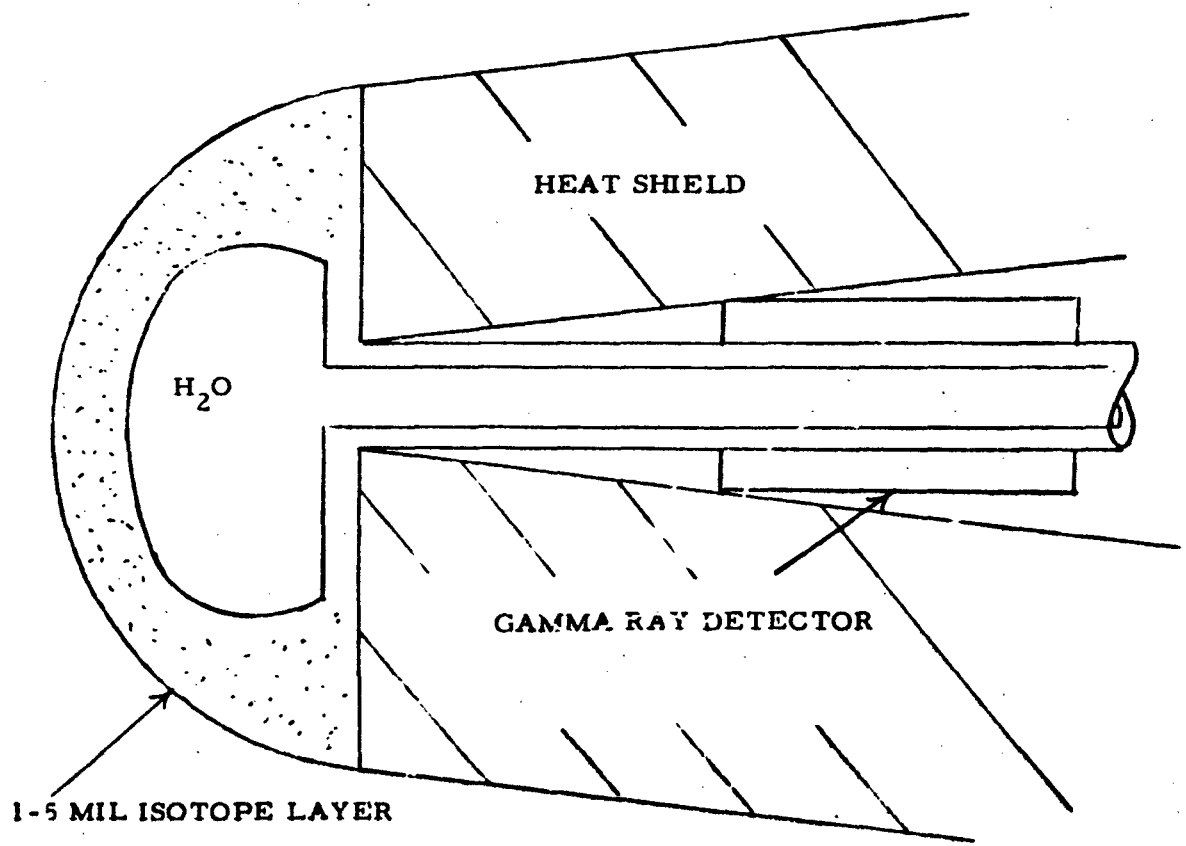


Figure 3-29. Use of Gamma Ray Detection

is distributed over the external surface of the tip. A detector located behind the nosetip senses the level of radiation and, in conjunction with an electronic package, produces a signal when a change in activity is observed. The change in activity is caused by a loss of a small amount of the radioactive material. A desirable feature of this approach is that with a single sensor, a change could be detected regardless of where it occurred on the tip.

Several important considerations impact possible designs for this type of sensor:

A. The source must be a gamma-ray emitter.
B. The gamma rays need to be of sufficient energy to penetrate to the detector.
C. The half-life should be on the order of several years to allow for an adequate shelf life.
D. The material must be compatible with the nosetip and unaffected by the coolant (i. e., must not react with or dissolve in the coolant at elevated temperatures)
E. The properties of the material should not degrade in storage (e. g., oxidation or corrosion).
F. The source should be easily activated, with no competing reactions within the primary nosetip porous material.
G. The isotope should be porous and not seriously degrade the nosetip performance.
H. The overall design should minimize radiation hazards to ground personnel.
I. The continually changing environment during reentry requires that the isotope layer be reusable several times.

Possible candidates for an isotope are listed in Table 3-3. From these, it appears that $Eu^{152, 154}$ and Bi^{207} are the prime candidates.

The isotope coating must be porous to permit coolant flow. It would thus have to be either flame-sprayed onto the surface of the nosetip or infiltrated into the pore structure near the surface.

Table 3-3

POSSIBLE ISOTOPES

Source	Half-Life (yr)	Activation	Melting Point (°C)	Comments
Na^{22}	2.6	Na^{23} (p, d)	98	Forms soluble hydroxide.
Co^{60}	5.3	Co^{59} (n, γ)	1,495	Melting point suitable only for ablation.
Sb^{125}	2.7	Te^{129} (p, α)	631	Hard to activate.
Cs^{134}	2.1	Cs^{133} (n, γ)	29	Forms soluble hydroxide.
Eu^{152}	13	Eu^{151} (n, γ)	826	
Eu^{154}	7.8	Eu^{153} (n, γ)	826	
Bi^{207}	30	Pb^{207} (p, n)	271	

Two major design problems exist using the radioactive isotope technique. One is the hazard to personnel at the required activity levels. The second is the problem of providing sufficient sensitivity. The former difficulty can, in principle, be minimized by providing suitable lead shielding around the nosetip during storage. Such shielding would probably have to be removed prior to launching. Obviously, there is no restriction on the location of the shielding as long as it lies between personnel and the nosetip.

The second problem is of a more serious nature in that it involves inherent limitations due to the radiation detector. Typically, it is difficult to reliably operate a gamma ray detector at counting rates above 5×10^6 counts per second. Usually, 10^6 counts/sec or less is the normal operating limit. The statistical error in a given counting sample is the square root of the number of counts in the sample. The sample time length is given by the desired response time of the system. This implies the following relation to determine the absolute sensitivity limitation based on detector properties only:

$$\frac{\sqrt{N}}{N} = \frac{F_{area}\ \sqrt{Time}}{N_{reuse} \cdot N_{sigma}} \qquad (3\text{-}13)$$

where

N = maximum counts/sec in the detector x 10^6.

F_{area} = fraction of the total area that has melted.

Time = sample time (i. e., response time).

N_{reuse} = number of times the system can respond to a melt at a single point.

N_{sigma} = signal-to-noise ratio

All but one of the quantities on the right of the expression must be set to either typical or limiting values to determine the last variable. Obviously, both variables in the denominator should be no smaller than 2. Since a typical spot of overheating on the surface is about 2 mm in diameter, this fact will limit the total area permitted to have a radioactive coating. The response time should be less than 100 msec. Inserting these numbers, it rapidly becomes clear that the entire surface cannot be covered with activity. The small activity change in a 2-mm spot could never be observed within a reasonable response time. However, if the activity is confined to a band on one side of the nosetip, e. g., the windward ray, which extends from the stagnation point to the heat shield, then a decrease in response time is achieved. This special configuration of activity is practical for flight with angle of attack.

If the diameter of the hot spot is assumed to be equal to the width of the radioactive band, then signal-to-noise ratio can be determined as a function of response time and the ratio of bandwidth to number of reuse times for a particular spot. Figure 3-30 presents signal-to-noise ratio for a range of these parameters. Assuming a bandwidth-to-reuse ratio of 0.02 in., a response time of 0.01 sec yields a signal-to-noise ratio of about 1.1, which would be marginal at best. As will be seen in the discussion of nosetip thermal transients, the reuse cycle time for this approach would probably be on the order of 10 to 100 msec, more or less, making this approach impractical.

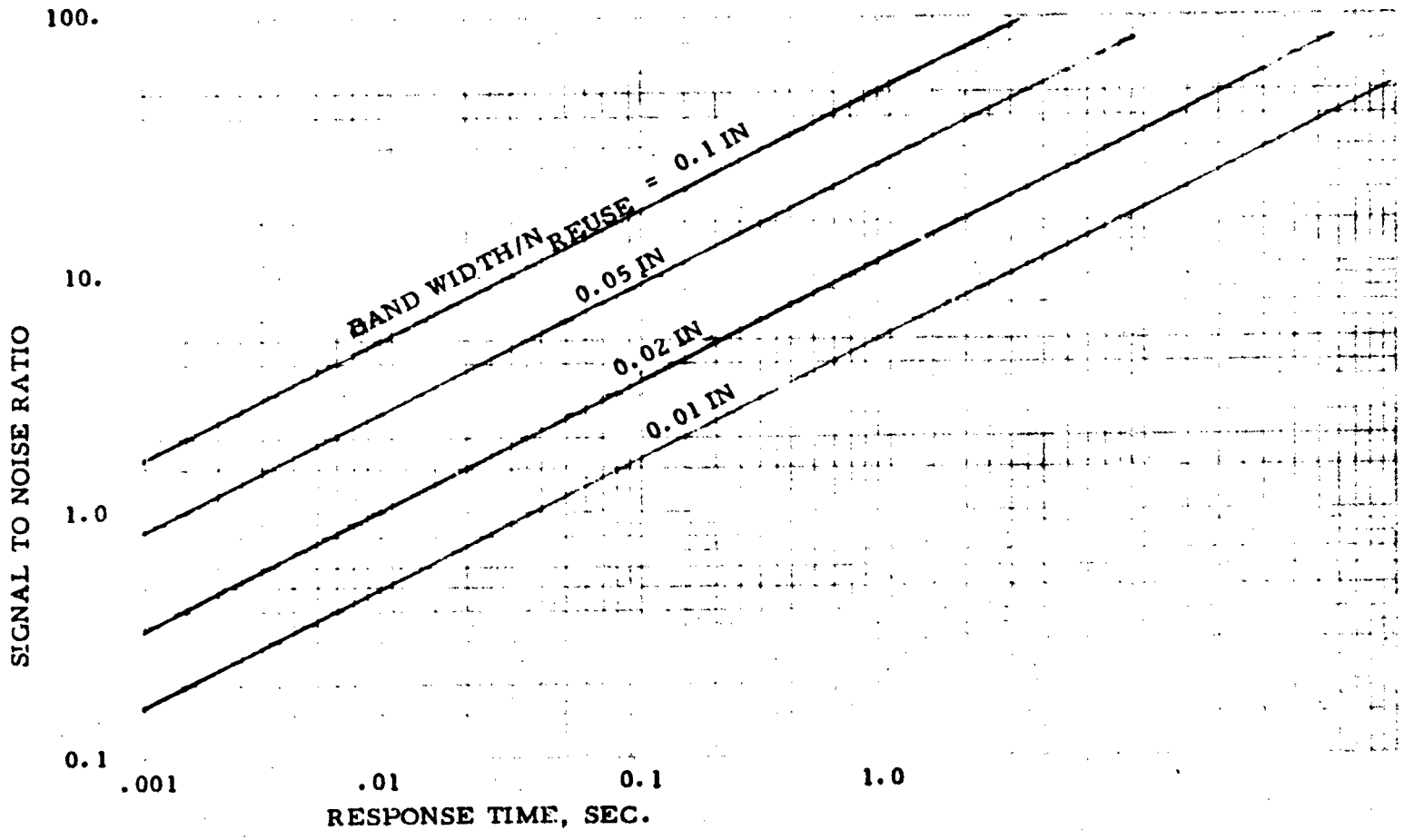


Figure 3-30. Signal-to-Noise Ratio for Gamma Ray Detection

3. 3. 3. 3. Optical

Figure 3-31 illustrates the use of optical techniques for determining the existence of high temperature on the surface of the nosetip. An optical sensor is located on the windward ray within the heat shield at the nosetip junction and senses the electromagnetic radiation from particles or combustion products that are produced on the nosetip and carried aft. This technique can sense high surface temperature over a fairly large portion of the tip.

Two spectral regions appear attractive from the standpoint of discriminating a signal. The infrared wavelength range between 3 and 4 μm is a minimum in the reflected and radiated solar and sky spectrum, thus permitting discrimination against earth, sun, and sky background radiation. The next window begins between 0. 5 and 0. 4 microns, the upper end of the solar spectrum, and bordering between visible light and ultraviolet.

A suitable detector for the 3- to 4-μm band is lead selenide (PbSe) operating at ambient temperature (20°C). Typical PbSe detectors with a 1- by 1-mm sensitive area are manufactured by Santa Barbara Research Center. An interference filter, designed to pass the 3- to 4-μm band, is mounted just in front of the detector in a well about 1/4 in. in diameter. The size of the well can be reduced if necessary and made rectangular. A plug of synthetic sapphire with optically polished faces is mounted in the well in front of the filter and serves as a window which is refractory and transparent to 3- to 4-μm radiation. The melting temperature of the sapphire is 5,000°R, and the sapphire could easily survive with a minimal amount of downstream cooling from the transpiration tip. The production of particles in front of the window may be facilitated by mounting the window back from the surface in a reentrant position, which may also prevent the premature covering of the window by the molten material. If aerodynamic requirements prevail, however, the window can be mounted flush with the surface.

A suitable detector of radiation in the 0. 5- to 0. 4-μm range is the silicon avalanche photodiode. A typical unit with preamplifier (General Electric Company) has a noise-equivalent power figure at this wavelength of about 3.7×10^{-13} wHz$^{-1/2}$. The same arrangement shown in Figure 3-31 can be used, with the Si detector substituted for the PbSe infrared detector.

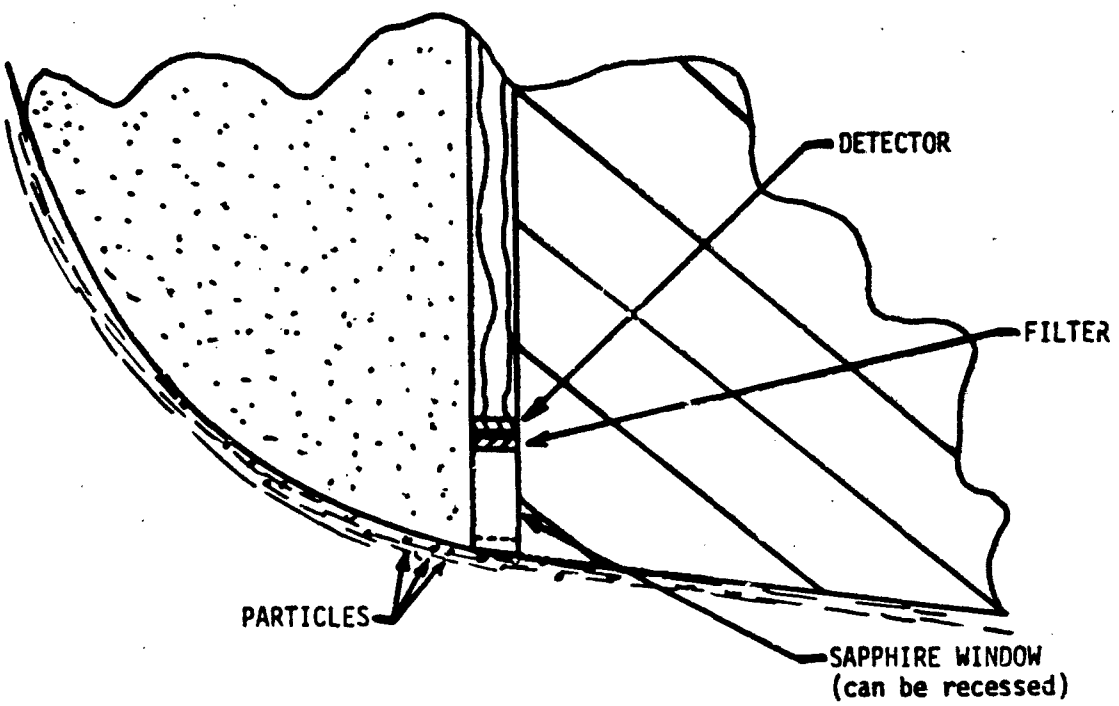


Figure 3-31. Use of Optical Detection

Liu and Steinberg (Reference 3-2) conducted a series of experiments in an attempt to resolve spectra from laboratory-simulated reentry models. They determined that the molecular band system of CH molecules consisted of strong infrared, while BeO had a very strong emission at 0.47 μm. Other materials might also qualify.

To illustrate the feasibility of discriminating boundary layer particles, calculations were performed in two spectral bands: 3 to 4 μm and 0.46 to 0.48 μm. It can be shown that the signal-to-noise ratio is given by

$$S/N = \frac{2\eta_w d_p^2 \epsilon_p d_w^{\frac{1}{2}} A_c^{\frac{1}{2}} D^*}{4 x_p \nu_p^{\frac{1}{2}}} \int_{\lambda_1}^{\lambda_2} H_\lambda (T_p)\, d\lambda \qquad (3\text{-}14)$$

where

n_w = effective transmission of window and filter.
d_p = diameter of particle (cm).
ϵ_p = emittance of particle.
d_w = diameter of window (cm).
A_c = sensitive area of detector (cm^2).
D* = specific detectivity of detector (cm $Hz^{1/2}$ w^{-1}).
x_p = distance from particle to detector (cm).
$H_\lambda (T_p)$ = spectral emittance of black body (w cm^{-2}).
T_p = temperature of particle (K).
$\lambda_1 \lambda_2$ = wavelength limits of spectral passband (cm).
v_p = velocity of particle past window (cm sec^{-1}).

Figure 3-32 shows this relation for the 3- to 4-μm band, and Figure 3-33 for the 0.46- to 0.48-μm band, plotted as S/N versus T_d, for several values of the particle velocity past the window. Assumed values of the other parameters, which are representative, are listed on the figures. It can be readily seen that the signal-to-noise ratio expected should provide for adequate discrimination against background radiation. These calculations are for the detection of a single particle. It should be noted that greater sensitivity can be obtained by integrating the signals from several particles as they pass by for a convenient period, in order to reduce the probability of false alarm further. The curves may be scaled up or down, depending on whether larger or smaller values are taken for the parameters in the equation. For example, it can be noted that S/N is proportional to the square of the particle diameter, but only to the square root of the window diameter.

If particles are not formed, but a continuous film of molten material passes over the window, this event can be detected by the same arrangement by making use of the step-function signal produced in the detector by the hot emitting material. The sensitivity requirements are considerably less for this situation than for the detection of small particles passing at high speed in front of the window.

CR138

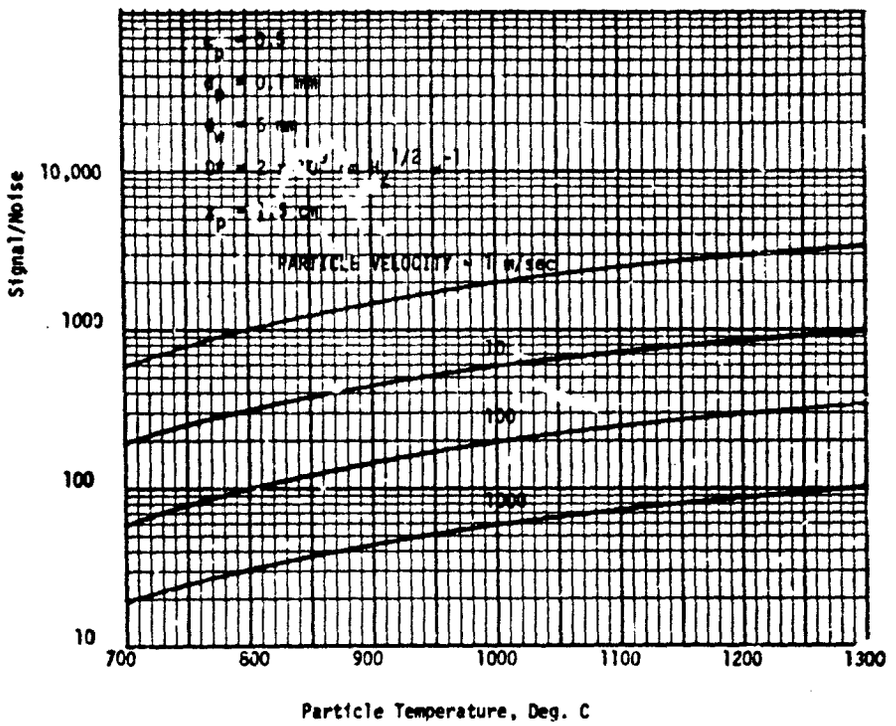


Figure 3-32. Signal-to-Noise Ratio Between 3 and 4 Microns

CR138

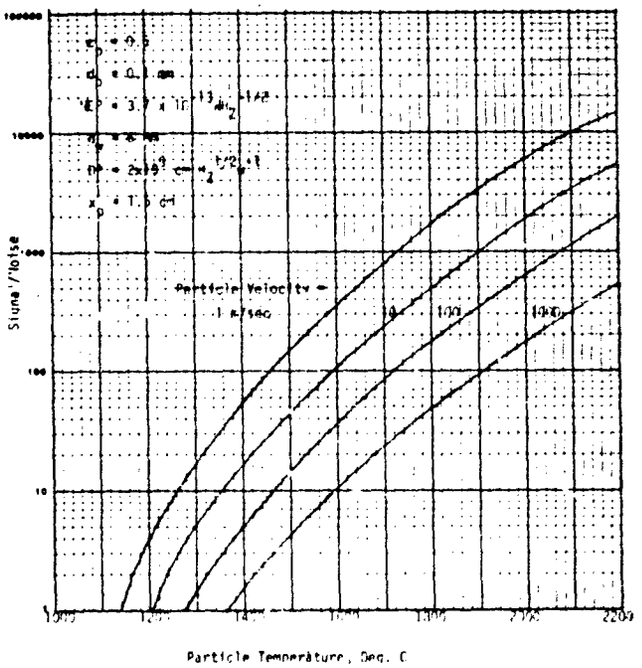


Figure 3-33. Signal-to-Noise Ratio Between 0.46 and 0.48 Microns

The observable material used to provide the emissions would be applied in a thin layer, a few mils thick, to the surface of the tip. Hydrocarbons, like plastics or epoxy, should provide a good source of CH for production of radiation in the infrared region. The problem would be in obtaining a porous coating to permit coolant flow. BeO would be a natural product from a melting beryllium nosetip. If it were plasma-sprayed to the surface of a stainless steel tip, a porous layer could be obtained.

3.3.3.4 Acoustic

Figure 3-34 illustrates the use of acoustic sensors to determine temperature change at the surface of the nosetip. The method involves the evaluation of surface wave velocity, which is affected by temperature. This is done by placing a piezoelectric transducer on the aft face of the nosetip and propagating a wave around the surface of the tip. The wave would be picked up by either a second receiving transducer or by the first transducer using a pulse echo technique (the transducer alternately transmits and receives). By measuring the time between transmission and receiving, wave velocity is determined. Changes in wave velocity (due to changes in nosetip temperature) would be monitored. By selecting a wave frequency in the ultrasonic region, wave propagation would be confined to a surface layer a few thousandths of an inch deep.

As it was not clear how to set up an analytical model of the acoustic technique, some simple laboratory tests were conducted to determine feasibility. An acoustic wave was propagated along the surface of a (3 by 3 by 0.1 in.) piece of 304 stainless steel that was heated by a hot air gun. A 5-MHz transducer was used as a transmitter. A 10-MHz transducer positioned 1-9/16 in. from the transmitter was used as the receiver. Changes in transit time through the stainless steel due to temperature were measured with the time delay multiplier on an oscilloscope.

At 73°F, the received signal was referenced to a delay time of 0.0 μsec with a signal amplitude of 4 cm peak-to-peak with a low gain setting on the amplifier. The temperature was slowly increased from 73°F to 204°F. As the temperature increased, the delay time increased while the amplitude of the received signal decreased, requiring a higher gain setting on the amplifier

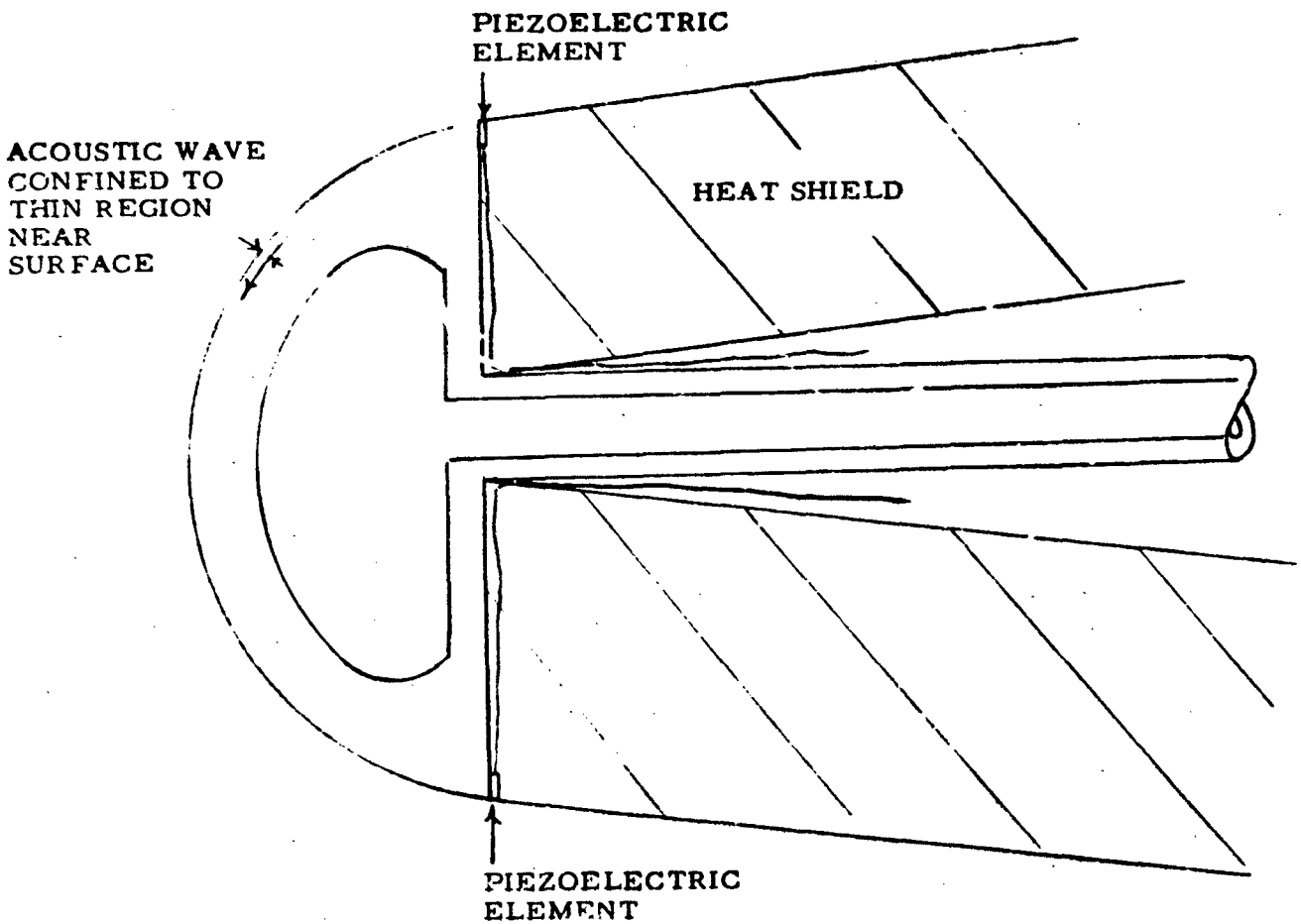


Figure 3-34. Use of Acoustic Detection

to bring the signal back to the 4-cm peak-to-peak reference point. At 204°F, the delay time had increased to 0.85 μsec, but the amplitude of the received signal was reduced to almost the level of the electrical noise. The thermal expansion of the stainless steel was determined and found to account for only 0.007 μsec increase in the delay time, therefore having a negligible effect.

To apply the technique to a nosetip, a quartz element (because of its high ultrasonic energy characteristics) would transmit the surface wave around the outside surface, and the wave would be picked up by a lithium sulfate element (because of its high resolution characteristics) positioned on the opposite side. There are three obvious problems. First of all, as indicated from the tests, the signal-to-noise ratio is low. Secondly, since the test results were obtained on a specimen that was subjected to a temperature rise over its entire length, the signal-to-noise ratio should be much lower for a nosetip that is experiencing hot spots over small portions of its surface. Finally, suitable insulation techniques would be required to keep the piezoelectric elements from going higher than 165°F. At temperatures higher than 165°F, piezoelectric elements show a definite loss in sensitivity and output power. From the practical standpoint, this technique does not appear feasible for use with a transpiration nosetip.

3.3.3.5 Eddy Current

An electromagnetic technique might be applied by locating an eddy current sensing coil in the coolant cavity near the forward wall of the nosetip. The excited coil would generate a magnetic field which would induce eddy currents into the nosetip. A change in surface temperature would cause a change in the electrical conductivity of the nosetip. This change in electrical conductivity would affect the induced eddy current, which would alter the electrical impedance of the sensing coil. Changes in the resistance and reactive components of the sensing coil would be monitored to determine surface temperature.

As for the acoustic method, it was not clear how to set up an analytical model. Therefore, a laboratory test was performed. An eddy-current-sensing coil was placed on the top surface of a 3 by 3 by 0.1 in. piece of

stainless steel. A Nortec Model NDT-3 eddy current instrument was used to excite and generate a magnetic field which induced eddy current into the stainless steel test sample. Temperature applied to the bottom of the stainless steel caused a change in the electrical conductivity of the stainless steel. Information was obtained by taking meter readings (μamp) from the NDT-3. Operating frequency was 20 kHz, and at this frequency, the depth of penetration was 0.081 in.

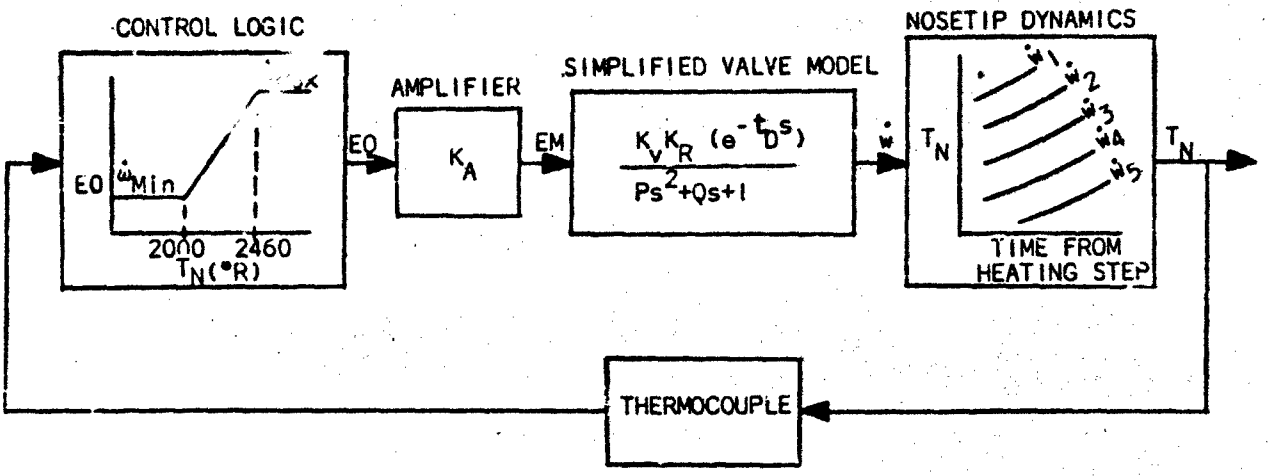
A hot air gun connected to an adjustable voltage source provided a variable temperature. Temperature was recorded with a chromel-alumel thermocouple adapted to a digital voltmeter. The temperature was increased from 73°F to 199°F. At 73°F, the μamp meter setting was referenced at zero. As the temperature increased, the μamp readings increased. At 199°F, the μamp reading had increased to 450. At this point, the temperature was decreased to 73°F. As the temperature decreased, the μamp readings decreased to the original zero reference point.

The drawback with this approach when it is applied to a nosetip is sensitivity. The sensitivity is proportional to the fraction of the mass of the nosetip that is at elevated temperature. Since hot spots are initially small in size and restricted to an extremely thin layer near the surface, the surface condition would be masked by the major part of the nosetip that was at low temperature.

3.3.4 Closed-Loop Coolant Flow Control Analysis

The temperature-feedback, closed-loop control system has been simulated on the digital computer. The system control block diagram is shown in Figure 3-35. For simplicity, the control logic was assumed to be a simple ramp control function sized to provide a minimum coolant flow below the first set point (2,000°R) and a maximum flow at the saturation set point (2,460°F). The control valve was assumed to respond as a second-order function with a response time (t_R) and a time delay (t_D). The time delay was 10 percent to 30 percent of the total time response. This represents the response characteristics of a typical control valve. Values of 15 and 20 msec were assigned to t_R, and the system was simulated with alternate delay times. Valve natural frequencies and damping ratios were calculated to give the optimum response.

CLOSED LOOP FLOW CONTROL BLOCK DIAGRAHM



VALVE MODEL PARAMETER VALUES

t_R(MSEC)	ω_n(RAD/SEC)	$P = \frac{1}{\omega_n 2}$	$Q = \frac{2\xi}{\omega_n}$
15	159	$.398 \times 10^{-4}$	.0088
20	120	$.695 \times 10^{-4}$	.0165

$\omega_n = 2\pi(\frac{.38}{t_R})$ FOR $\xi = .7$

EO = Control Logic Output Signal

EM = Amplified Signal

K_A = Amplifier Gain

T_N = Measured Nosetip Temperature

t_D = Valve and Thermocouple Time Delay

t_R = Valve Response

$t_R + t_D$ = System Response

ω_n = Natural Frequency

ξ = Damping Ratio

Figure 3-35. Closed-Loop Flow Control Concept

A forcing function was obtained from thermodynamic calculations for the closed-loop simulation. A table of values of coolant flow rate represented the nosetip dynamics for a step change in heat input versus time. This table was then used to drive the system. The step input was 80 percent higher than the assumed nominal heating value of 14 000 Btu/ft^2-sec. This table represented only one operating condition which may not have been the worst case. If the temperature feedback control system is to be optimized, extensive nosetip heating analysis would be necessary to completely define the nosetip response. Transient nosetip temperature response to step heating has been computed, as discussed in Appendix D, and is shown in Figures D-1 and D-2. Typical nosetip temperature transients and coolant flow transients are shown in Figures 3-36 and 3-37 for t_R = 15 msec. Similar curves for t_R = 20 msec are shown in Figures 3-38 and 3-39.

In order to obtain a measure of valve response efficiency, the coolant flow margin was defined as the increment of flow rate above the steady-state flow rate associated with a constant nosetip temperature of 2,460°R. This increment was calculated at the maximum flow transient and is about 30 percent lower than the ideal requirements presented in Section 2. The values of 2,000°R and 2,460°R for minimum and maximum tip temperature were chosen arbitrarily and would be redefined if the control system were to be optimized.

Typical gain and phase were obtained from linear analysis (i.e., for a fixed point in time, representative gains were determined for the nonlinearities). Figures 3-40 and 3-41 are plots of the summarized computer output information. Gain margin, phase margin, and flow margin are plotted against time delay. In Figure 3-40, the valve response is 15 msec plus time delay. In Figure 3-41, valve response is 20 msec plus time delay. These responses were estimates of the actual valve characteristics that would be required.

Figures 3-38 and 3-39 indicate that the system will be stable up to 4 msec pure delay with a 24-msec total response (20 msec second-order response and 4 msec delay). However, at this response, the flow margin is very high, so that a faster-response valve is desired. A 17- to 20-msec total response

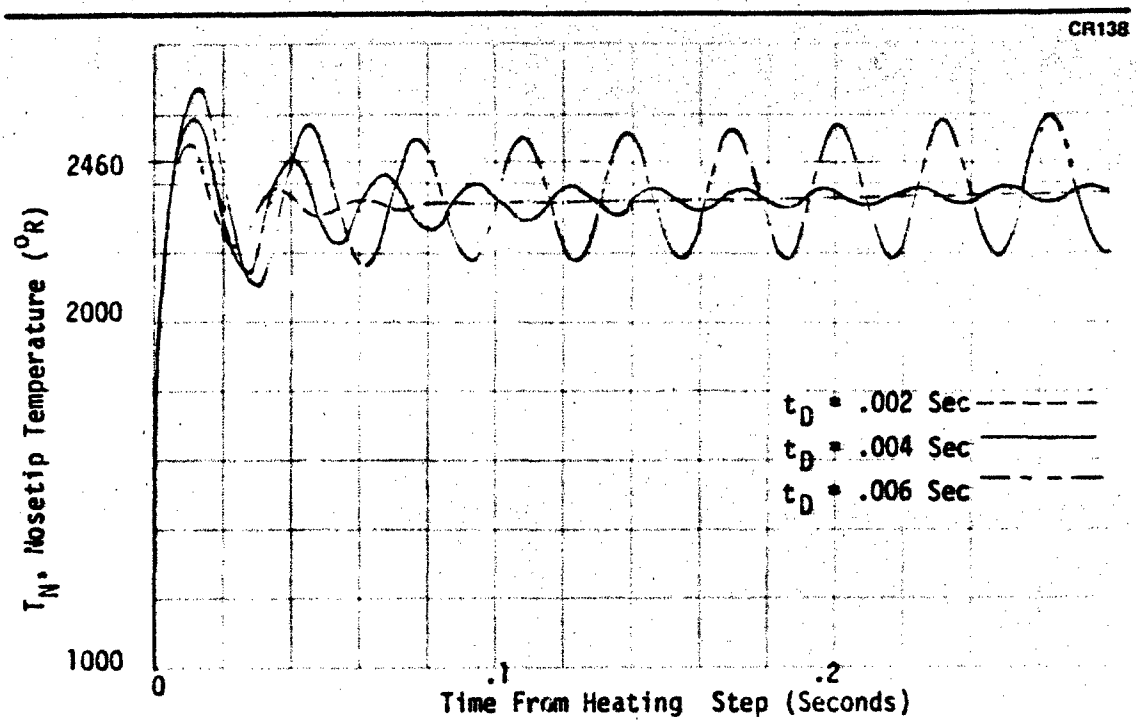


Figure 3-36. Nosetip Temperature Response to Step in Heat Input for (0.015 + t_D) - Sec Response Valve

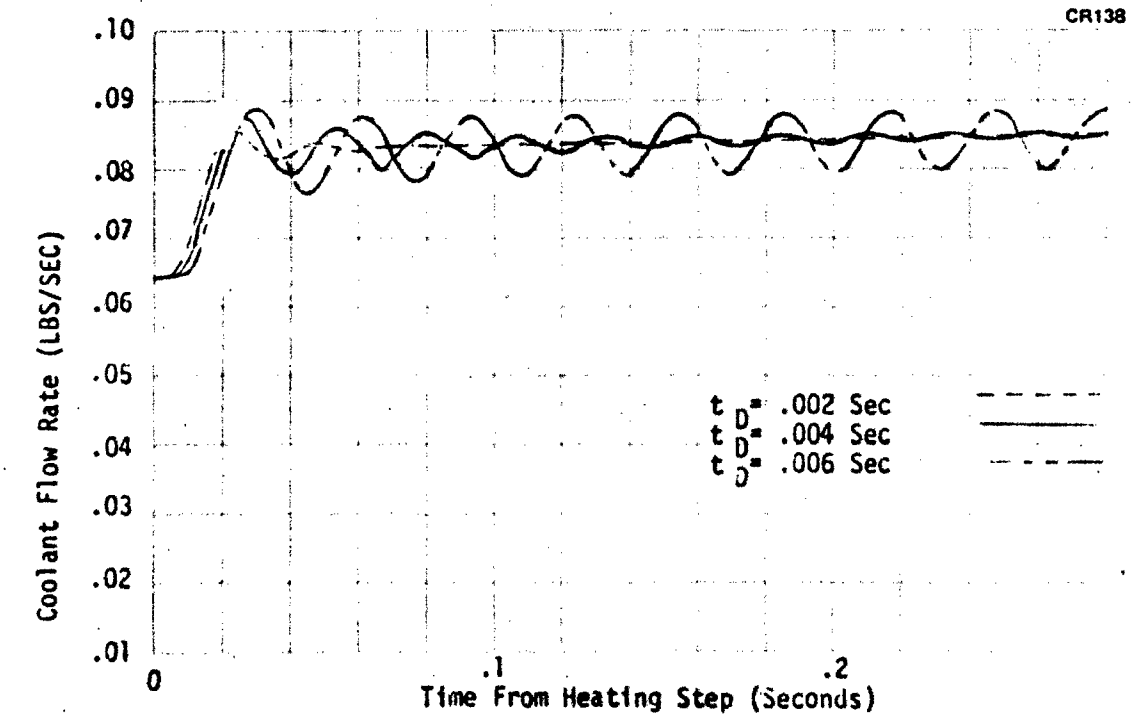


Figure 3-37. Coolant Flow Response to Step in Heat Input for (0.015 + t_D) - Sec Response Valve

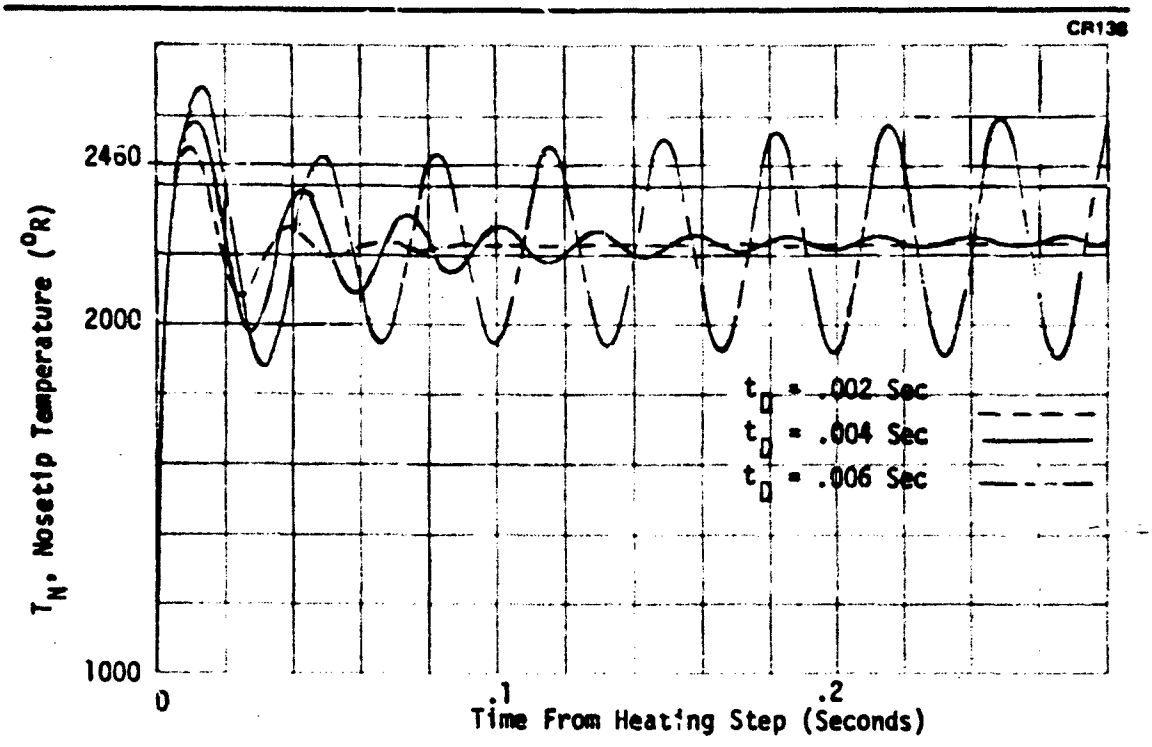


Figure 3-38. Nosetip Temperature Response to Step in Heat Input for (0.020 + t_D) - Sec Response Valve

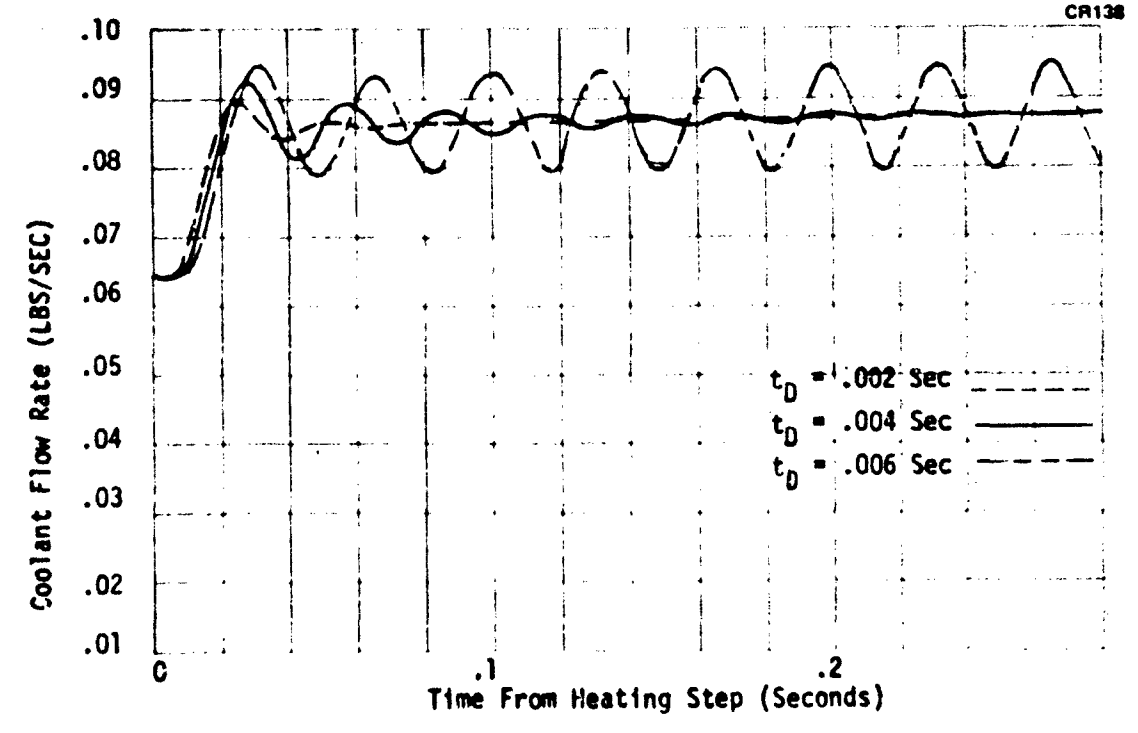


Figure 3-39. Coolant Flow Response to Step in Heat Input for (0.020 + t_D) - Sec Response Valve

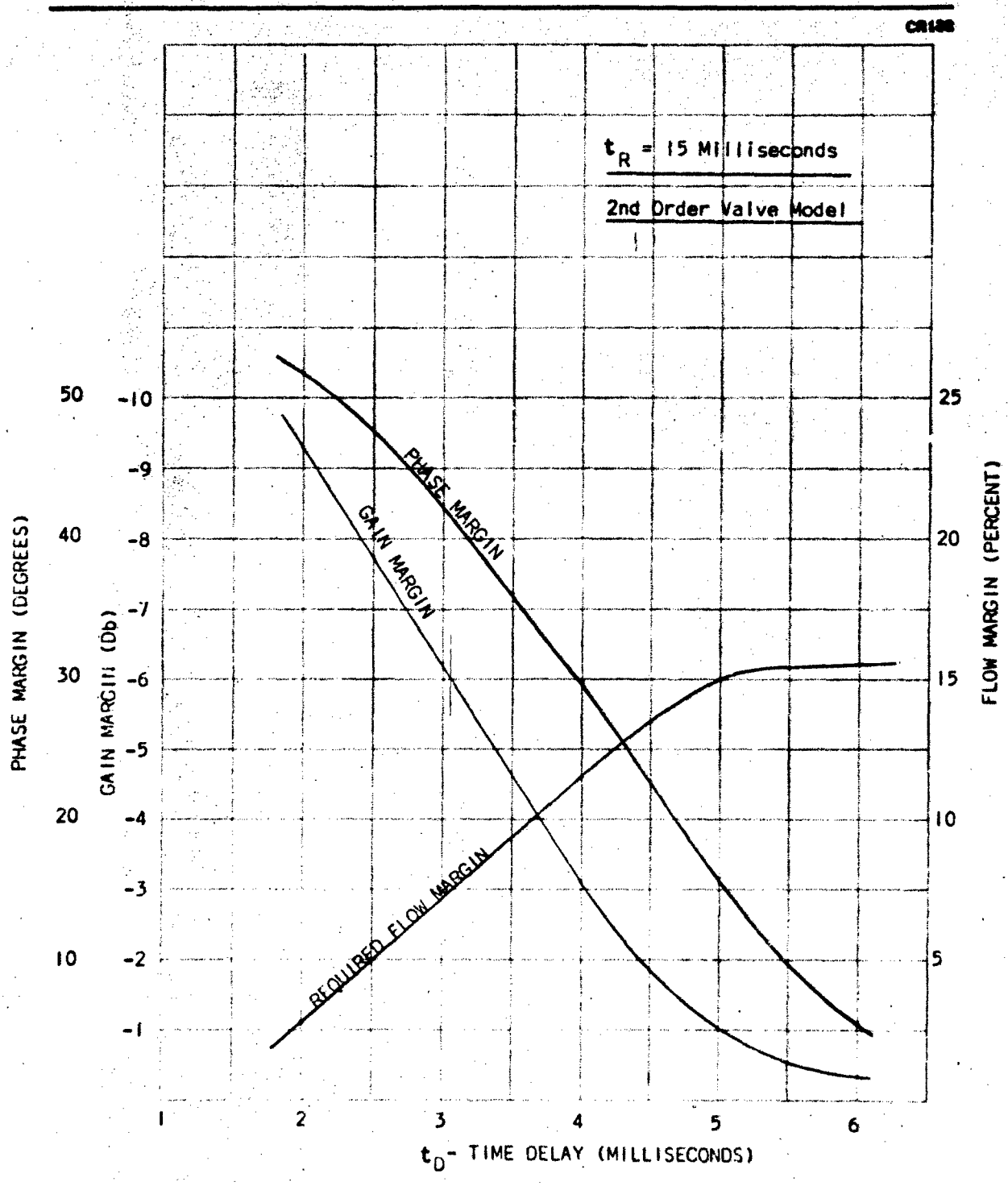


Figure 3-40. System Response to 80-Percent Step Increase to Nosetip Heating, Valve Response = 15msec + t_D

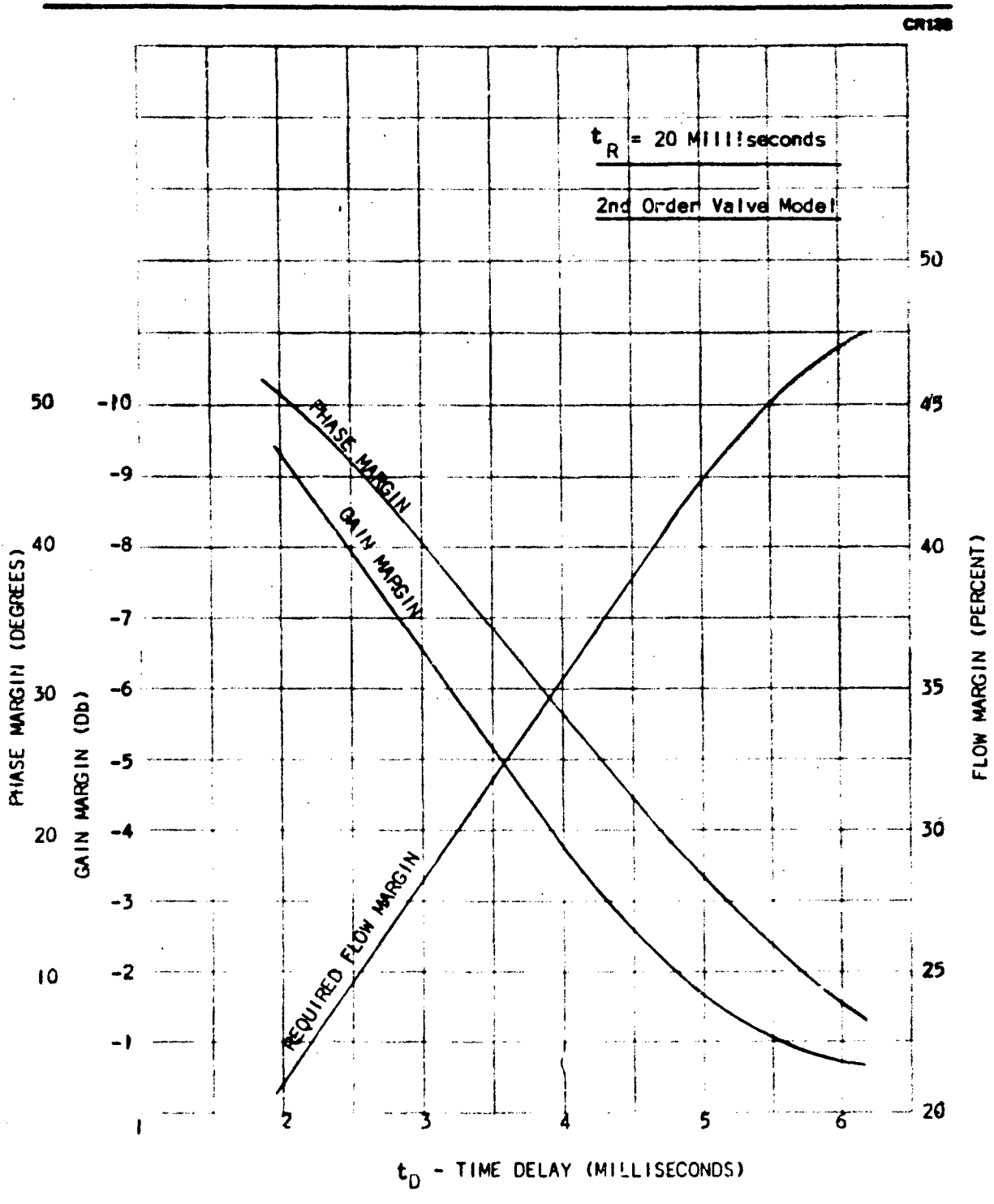


Figure 3-41. System Response to 80-Percent Step Increase to Nosetip Heating, Valve Response = 20 msec + t_D

valve appears adequate for this system and would require less than 15 percent margin on the high surface temperature design flow rate at this heating level. Time delays greater than 4 msec have exhibited oscillations in the response which may limit delays to less than this value.

3.3.5 Electromechanical Valve Designs

The electromechanical valve designs discussed in this section are applicable to either the closed-loop sensor feedback system or to the open-loop u, ρ, α systems. Valve development time must be scheduled for this type of control valve concept because all past vendor surveys have indicated that no high-pressure water flow control valves are available which can withstand a five-year storage. Two types of valves are currently being considered; however, configuration changes may occur during development.

Figure 3-42 is a schematic of a typical single-stage proportional flow control valve. The flow is modulated by a pressure-balanced spool and is driven by a leakage flux magnet. The leakage flux magnet force is independent of plunger position over a large portion of its stroke. This permits the metering orifice and flow to be proportional to electrical current or voltage. Moving part weight makes the valve somewhat sensitive to axial acceleration (which may improve coolant usage) and to lateral acceleration (which causes hysteresis in valve response). The high length-to-diameter (L/D) ratio of the leakage flux magnet makes it suitable to the shallow cone-angle envelope shown in Figure 3-42.

A similar-type electromagnetic driver which has a slightly lower L/D ratio is the plunger solenoid. This driver has more force potential, but its sensitivity to plunger position is more pronounced than the leakage flux magnet.

Figure 3-43 illustrates six types of magnets which have widely varying force-stroke characteristics. One or more of these types may be optimized to give the required force-stroke characteristics using return springs and/or limited stroke range. For example, a flat-faced armature has a magnet force which is proportional to the reciprocal of the square of the air gap. By limiting the

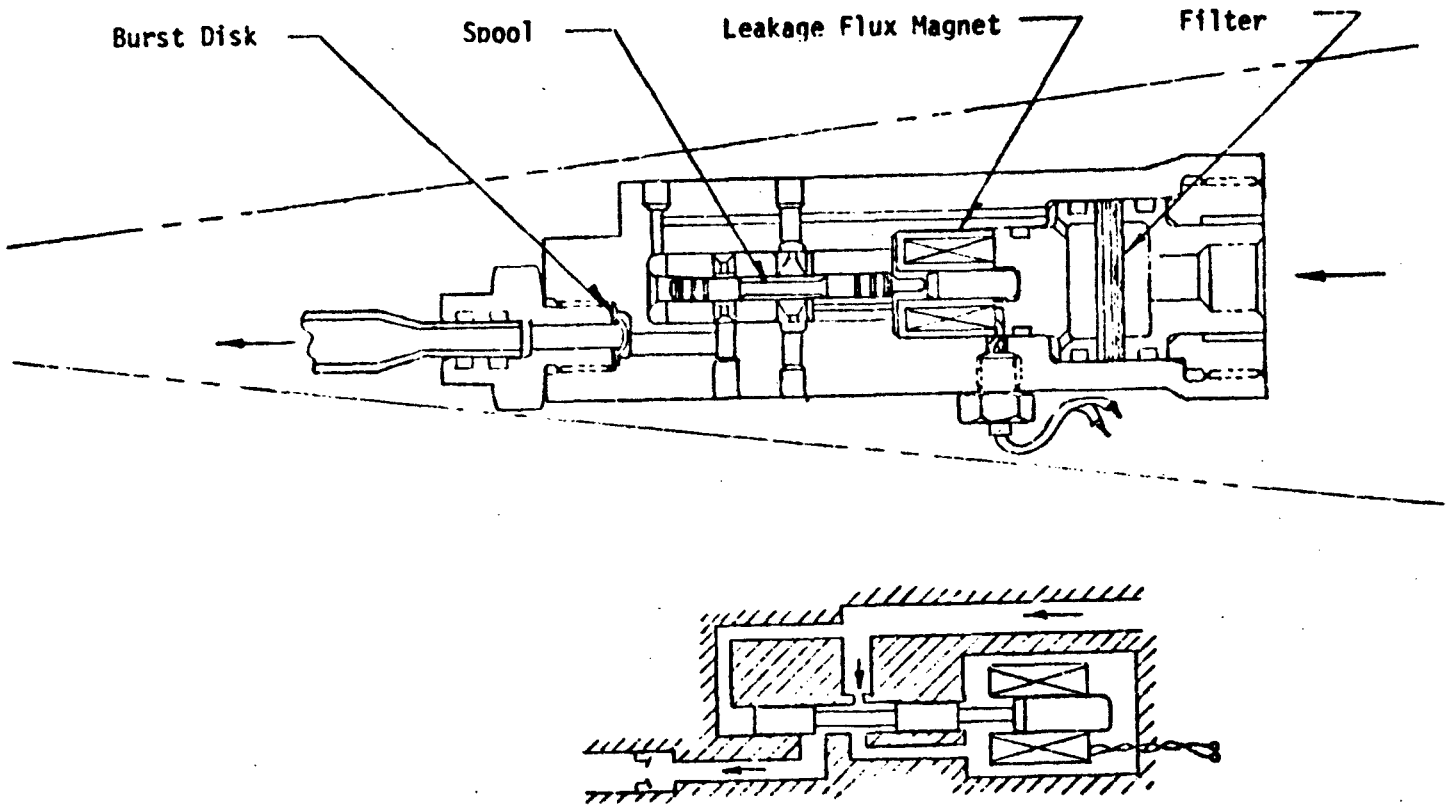
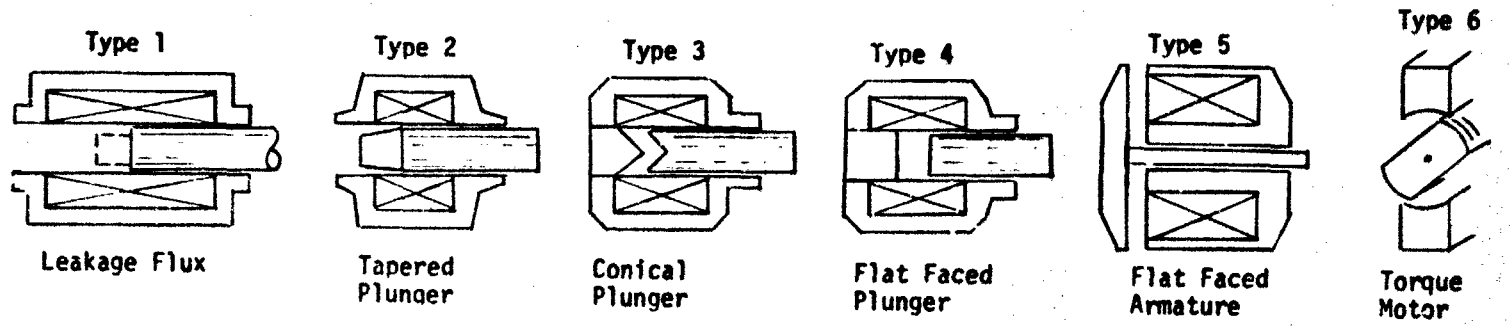
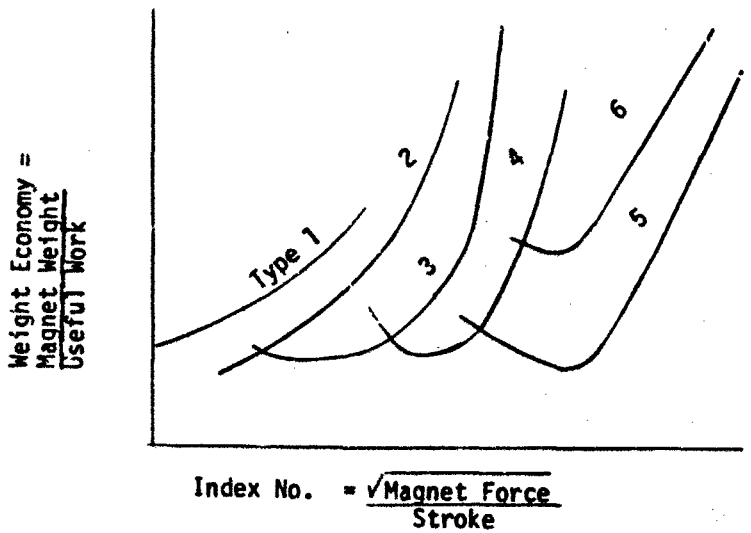


Figure 3-42. Single-Stage Leakage Flux Proportional Flow Control Valve



ELECTROMAGNET ACTUATOR CONFIGURATIONS



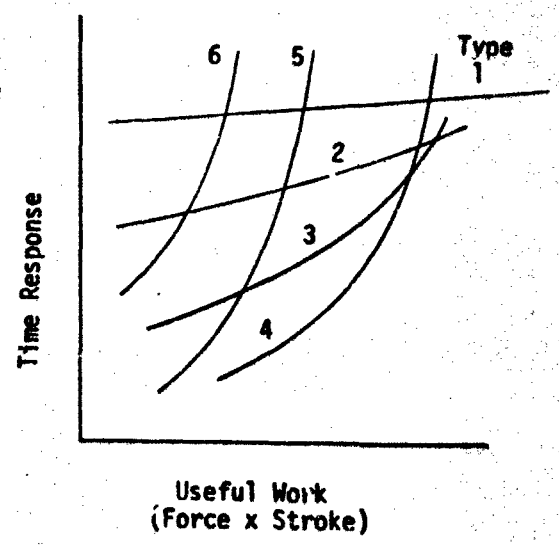


Figure 3-43. Electromagnet Force Motor Optimization

stroke, a linear force-to-stroke characteristic may be approximated. Trade-offs of weight economy and a parameter such as index number (defined in Figure 3-43) would be conducted during development tests. Three-dimensional mapping of flux paths would also be investigated to minimize the required amount of magnet material. Response time of the closed-loop system valve must be optimized using the valve driver electrical network.

The effect of axial and lateral acceleration will be reduced by using the smallest possible spool diameter. Spool valves have been built and tested with diameters of 0.125 in. If some mechanical axial deceleration feedback is desired, the spool can be made deliberately heavy.

The single-stage flow control valve requires an analog or digital-analog simulator signal to operate proportionally. A single-stage valve will require approximately 10 w of continuous power. A two-stage valve such as the one illustrated in Figure 3-44 can be operated with a pulse-width-modulated signal and requires slightly less power. Figure 3-45 is an enlargement of the pulsed valve. The g-balanced armature of this valve opens and closes a flapper as a pulsed signal is relayed to the magnet. This has the effect of modulating the pressure on the right-hand side of the main-stage poppet. The ratio of on-to-off electrical signal operating a square-wave function of fixed frequency determines the amount of opening of the main-stage outlet. The pilot-stage outlet is returned into the low-pressure throat area of the main stage. The valve also has zero leakage with no input signal, unlike many two-stage designs. A restricting orifice on the right side of the main-stage poppet reduces pilot losses. Output flow would be slightly oscillatory due to the pulsed pilot flow.

Response of a breadboard prototype valve of this design was determined for the on-off mode. The response of signal to full-on and no signal to full-off was less than 3 msec. Eighty-five-percent pressure recovery was measured across the valve during this test. Pressure recovery can be improved with design changes.

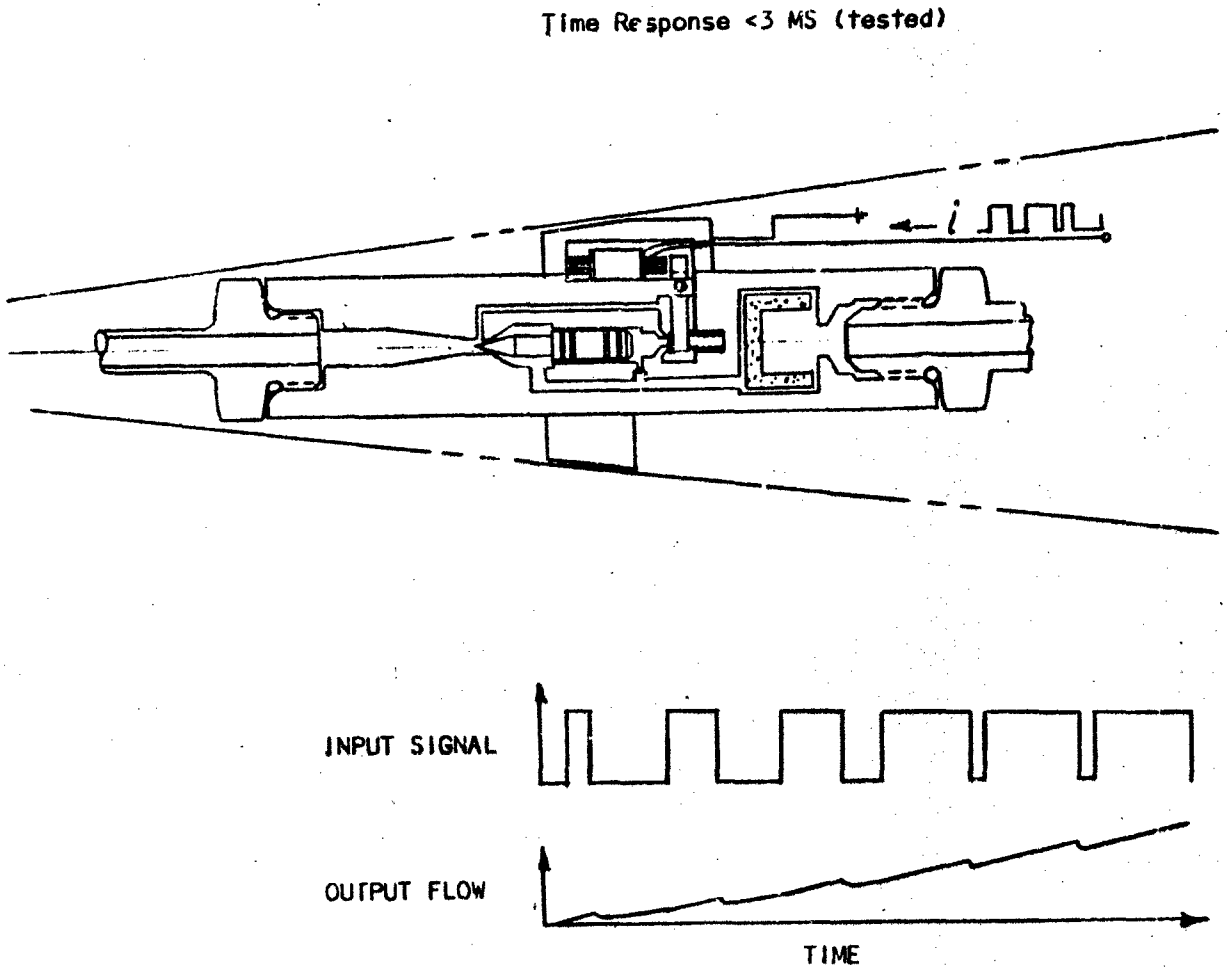
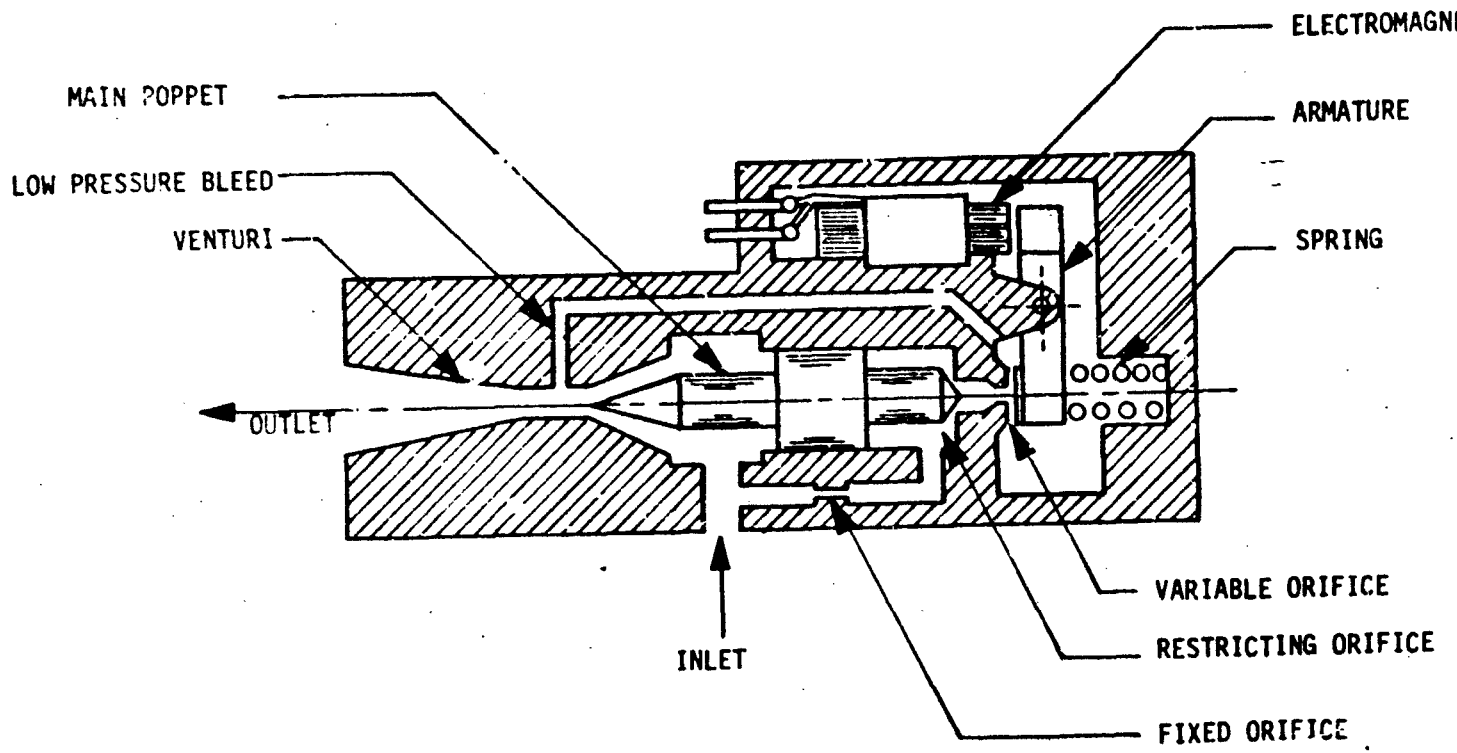


Figure 3-44. Two-Stage Pulse-Width-Modulated Flow Control Valve



DESIGN CONCEPT

- VENTURI TYPE MAINSTAGE - SMALL SIZE, LOW PRESSURE DROP, SMALL FLUID FORCES ON POPPET FACE
- LARGE ACTUATION FORCES ON MAIN STAGE POPPET
- "G" BALANCED ARMATURE
- PILOT VALVE FLOW EXHAUSTED TO VENTURI THROAT
- RESTRICTING ORIFICE - REDUCES PILOT FLOW AND IMPROVES RESPONSE

Figure 3-45. Pulsed Valve Schematic

Valve component configurations may be optimized using a computer analysis method currently under development. This method minimizes the value of a nonlinear polynomial expression by determining the optimum values of the variables in the equation. For example, valve weight can be minimized by varying dimensions, which in turn are functions of flow and pressure constraints.

Section 4
EXPULSION CONCEPTS

Expulsion concepts seriously considered during this study were limited to two: piston and bladder. These were selected on the basis of possible development and reliability.

4.1 PISTON

Two types of improved-efficiency piston expulsion systems were considered, a single-piston type and a double-piston arrangement. Both of these operate within a stepped cylindrical bore. The double piston arrangement (Figure 4-1) consisted of an external stepped piston with a second piston located internal to the small step of the external piston. The single piston looks very similar, except that a single stepped piston is used instead of the double piston. As expected, a better utilization of the allocated volume was achieved by use of the double-piston arrangement. However, neither one of the piston concepts is competitive on either a weight or volume basis with the bladder configurations described in the following paragraphs. Advantages of using a piston expulsion system include the high level of confidence and reliability gained from past usage and performance, straightforward method of manufacture, and low development risk.

4.2 BLADDER

Three types of bladders (nonmetallic, rolling, and metallic) were investigated. None of these concepts are completely developed. Therefore, insufficient design information is available to accurately define their relative merits. However, best estimates were used in order to arrive at a selected design.

4.2.1 Nonmetallic Bladder

The nonmetallic bladder concept, shown in Figure 4-2, consists of a reservoir like the frustrum of a cone. The conical shape of the reservoir most efficiently utilizes the available space specified in the contract. The

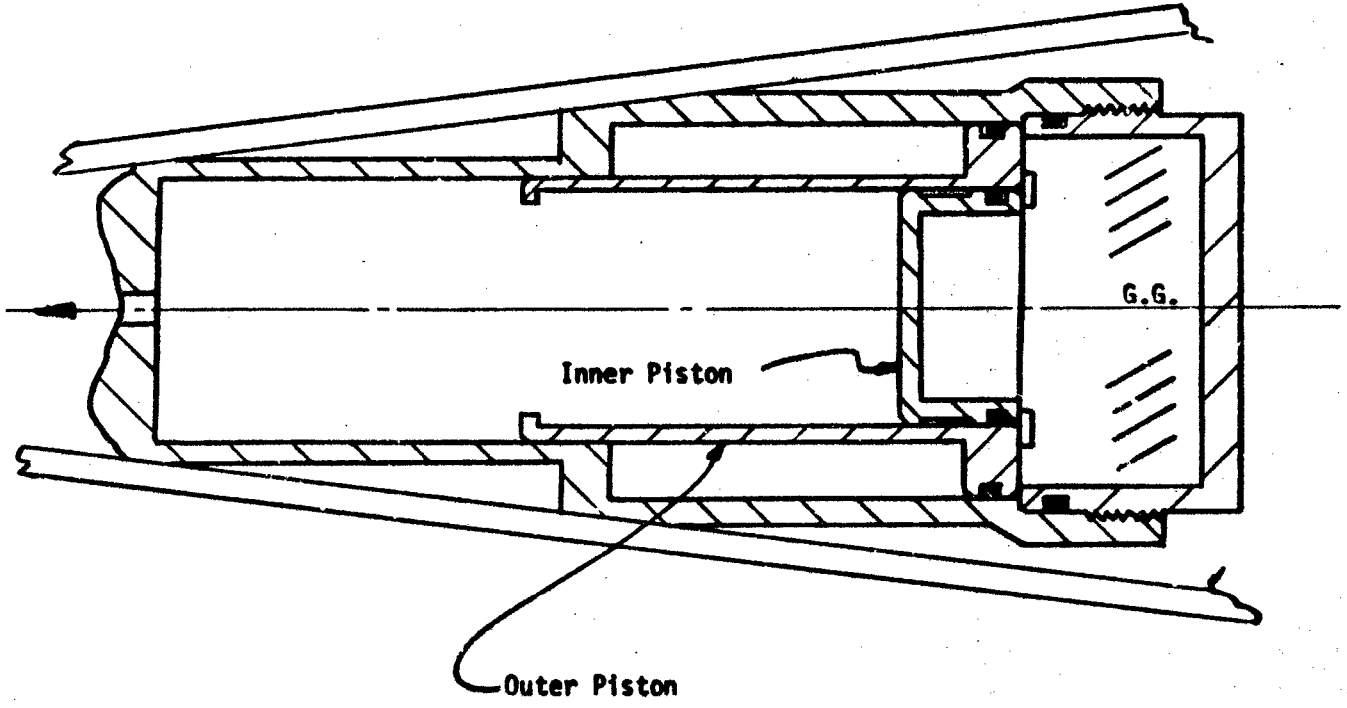


Figure 4-1. Double-Piston Expulsion

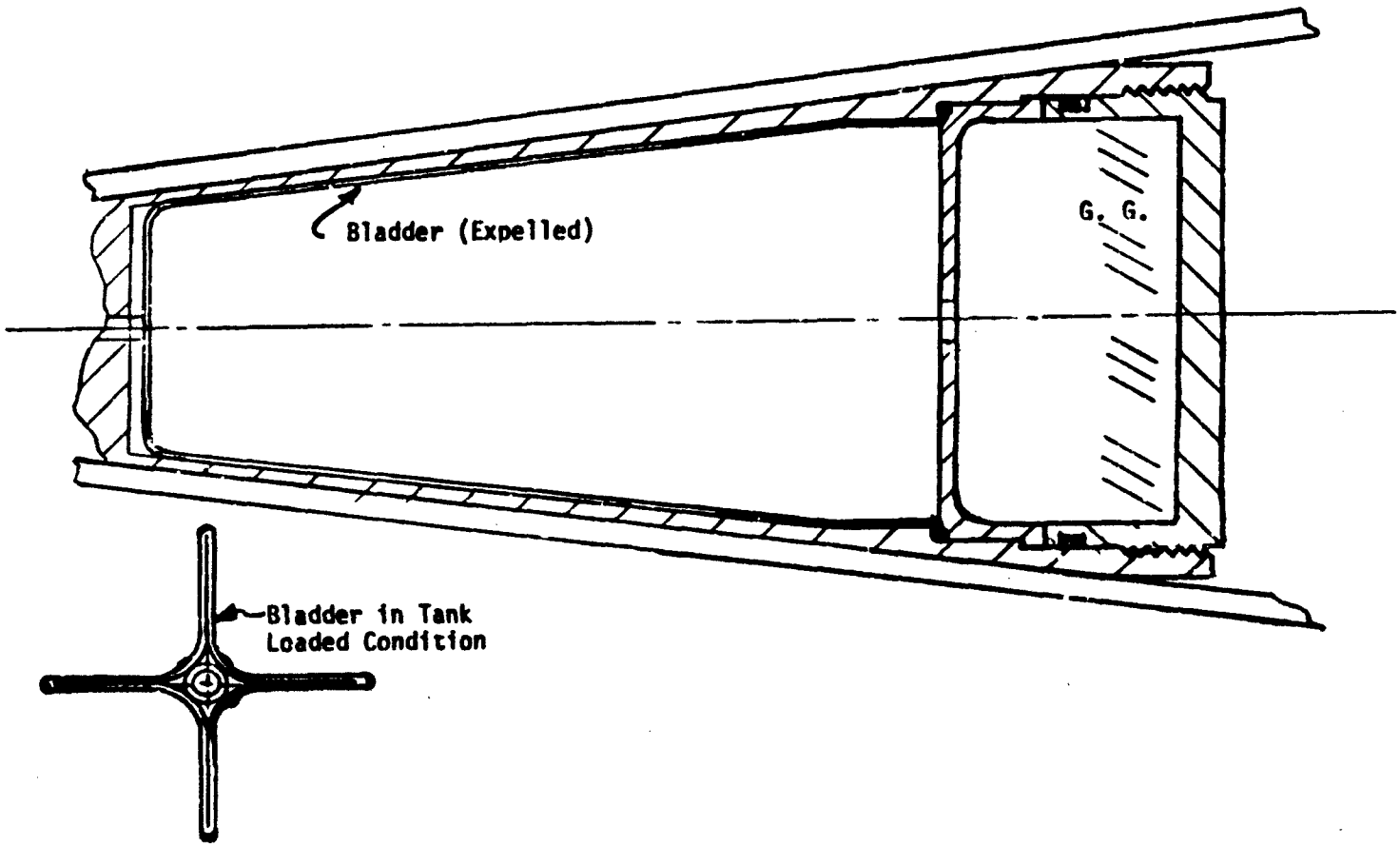


Figure 4-2. Nonmetallic Bladder

bladder, which is located along the centerline of the reservoir, is manufactured in a cruciform shape. Coolant is stored external to the bladder between the bladder and walls of the reservoir. Characteristics of the bladder are unique in that as the bladder is collapsed during fill, its length becomes foreshortened. During the expulsion cycle, the bladder is pressurized internally and expands radially and axially to expel the coolant. This characteristic precludes entrapment of the coolant by the bladder during the expulsion cycle. This is a result of the fact that the bladder can only expand against the forward reservoir wall when it is fully extended from its foreshortened length, and it cannot reach its extended length until it has expanded fully radially, at which time all coolant has been expelled from the reservoir. An additional precaution made to prevent the trapping of coolant is to place several rows of beads along the outside of the bladder. This will hold a small portion of the bladder a very short distance from the wall to provide a path for coolant passage.

4.2.2 Rolling Bladder (Nonmetallic)

The rolling bladder expulsion concept (Figure 4-3) consists of a reservoir made in two halves. One of the halves contains the bladder, which is formed to fit the inside contour of the half reservoir. Each half is internally identical. This enables the bladder to move from one half to the other with the least amount of distortion during the expulsion cycle. To expel the coolant, gas is directed into the half of the reservoir that contains the bladder. The bladder must move forward with a rolling action to expel coolant and enter the second of the reservoir halves. Disadvantages of this concept are as follows: (1) the bladder must turn completely "inside out" to expel the coolant, and the extremely small bend radii associated with the rolling motion may result in shear-induced delamination of the bladder fabric and rubber binder; (2) the utilization factor of the available volume is low; and (3) the bladder may be subjected to undesirable tensile loads during expulsion.

4.2.3 Metallic Bladders

There are two metallic bladder concepts under consideration for coolant expulsion systems. One is a conical container with a stainless steel bladder, currently under development on an AFRPL contract. The other is an adaptation of the ACE control system tank utilizing an aluminum bladder in a

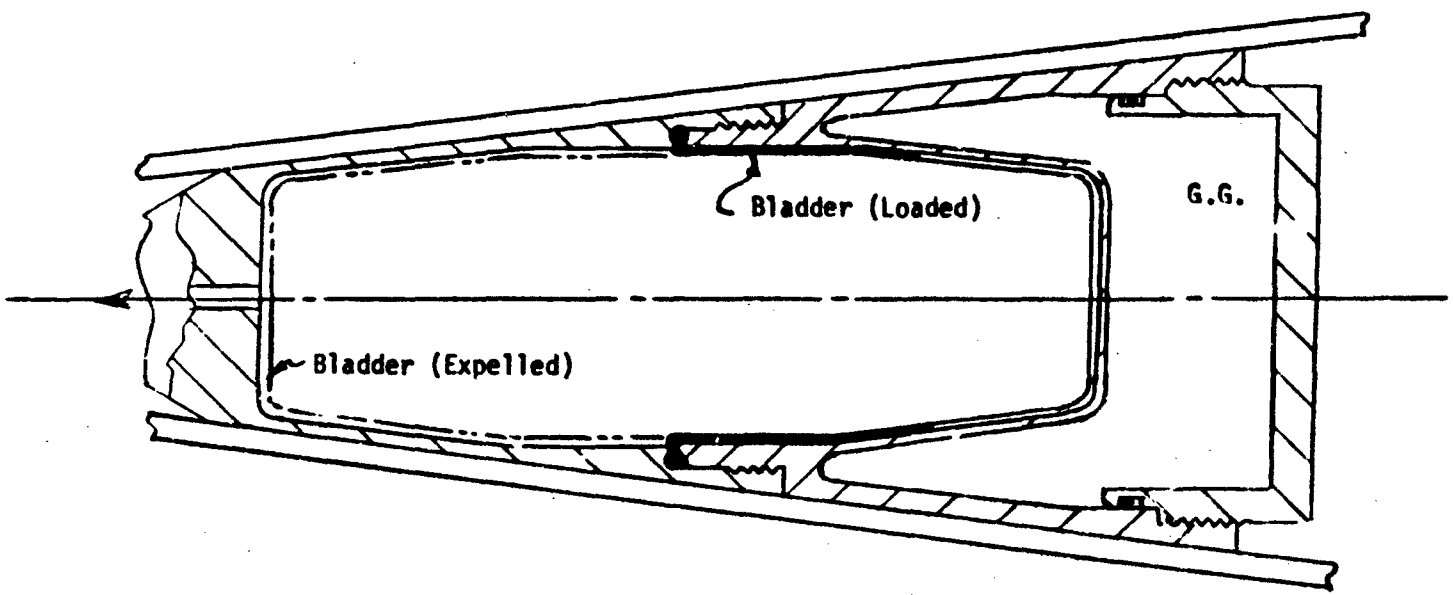


Figure 4-3. Rolling Bladder

cylindrical tank. Recent conversations with the vendor indicate that this can be adapted to the conical shape.

Fortunately, either of these concepts is compatible with the packaging of the elastomeric bladder. Although the elastomeric bladder is considered as a baseline, modification of this decision can be made at a time when development has progressed to the point where sufficient information is available. This can be accomplished without appreciable impact on the system.

As previously mentioned, there is a scarcity of information on the development of the stainless steel bladder unit at this time. However, there are several problem areas inherent in the metallic bladder which do not occur with the nonmetallic, and which must be resolved before it can be used in the expulsion system. These include the following:

A. Center-of-gravity shift during expulsion.
B. Heat transfer to water.
C. Thermal expansion compensation.
D. Ullage transient.

Unlike the piston reservoir, the bladder reservoirs do not completely control the liquid-gas interface in a reservoir. Thus, vehicle accelerations can cause sloshing of the coolant in the reservoir and its attendant dynamic effects.

Additionally, expulsion of liquid by a metallic bladder will normally cause a lateral center-of-gravity shift to occur. For comparison, the elastomeric bladder will produce an axial center-of-gravity shift during expulsion, whereas the piston reservoir can be designed to minimize this shift. The significance of these phenomena is dependent on the vehicle and should be considered in final evaluations.

The effect of water temperature on coolant requirements for the current system was shown in Figure 2-30. This indicates that large temperature increases will require additional coolant and some modification to flow control characteristics. It is therefore desirable to hold the temperature increase to a minimum. Since the major contribution to coolant heatup results from

heat transfer through the bladder, it is necessary to evaluate this effect. Little data has been made available to determine the heating of coolant in the metallic bladder reservoir. Although applications of insulating materials to the bladder could reduce excessive heat transfer, addition of material may negate some of the development testing and require retest and/or redesign.

Another potential problem area with the metallic bladder is the coolant itself. The tank cannot be filled full at ambient temperatures because expansion of the coolant would overpressurize the tank. If an ullage bubble is not left in the tank, or if it is filled at the anticipated high ambient temperature, temperature variations may cause the bladder to flex, which would cause fatigue problems in the metal over long storage times. Additionally, any bubble might become entrained in the coolant going to the nosetip, with undesirable results. A solution may be to provide a small accumulator on the coolant side to accommodate thermal expansion. This would require some development.

Extreme care must be taken in this ullage problem to avoid pressure transients which may occur when the system is initiated. When the ullage bubble collapses, a shock condition may occur which may produce pressure peaks of the order of twice the working pressure. Either steps must be taken to alleviate these pressure peaks, or the tankage strength must be increased to accommodate them. Effects of these transients must also be considered on the other components of the system.

Section 5
PRESSURIZATION

Pressure can be supplied to the coolant in a variety of ways. During this study, cold-gas blowdown, multiple-grain solid-propellant gas generators, and bootstrap and blowdown monopropellant gas generator designs were investigated. These concepts were selected after a preliminary investigation showed that development time and cost of these concepts would be less than for hybrid concepts, and that design would be less complicated than for bipropellant concepts. The critical design constraint on all concepts is to guarantee sufficient pressure, and therefore sufficient coolant, throughout all five trajectories studied.

5.1 COLD-GAS PRESSURIZATION

Cold gas pressurization systems using high-pressure helium were investigated. Although it was anticipated that this system would be large and heavy, such systems are completely developed and more reliable than warm-gas generator designs. The system investigated consisted of a spherical (or nearly spherical) pressure vessel, a squib valve for initiation, and a pressure regulator.

The cold-gas system is identical to the other concepts except that the gas generator is replaced by a high-pressure storage bottle. Operation of this system is as follows. The squib valve, located between the gas bottle and the pressure regulator inlet, is triggered approximately 1 sec before coolant is required at the nosetip. The pressure regulator minimizes initial pressure transients which may harm the reservoir bladder, flow control valve, or filter. This device also maintains a higher gas temperature in the bottle and reservoir due to the damped pressure transients, reduced blowdown rate, and improved heat transfer to the gas from the more torturous flow path. The higher temperature will result in improved gas utilization and reduce the danger of bladder damage due to embrittlement at very low temperature.

Preceding page blank

One of the most important considerations is the storage pressure of the helium gas. Figure 5-1 shows the effect of initial gas pressure on weight and volume, assuming a spherical container. Pressures were assumed and gas volumes were determined by means of a digital computer simulation. At least 100 psi pressure differential was required at all times across the flow control valve. This determined the minimum gas volume. The worst-case pressure requirement occurred at the end of the S-3 trajectory. Total volume and system weight were determined by assuming a burst-pressure factor of safety of 2.6. This value has been used before in similar application on the TOW pressure vessel. The container material was assumed to be 17-4 PH with an ultimate strength of 190,000 psi. The following thick-wall pressure-vessel equation was used to determine system volume:

$$\frac{V_{metal}}{V_{gas}} = \frac{3}{\frac{2\sigma_{ultimate}}{P_{burst}} - 1} \qquad (5\text{-}1)$$

Gas compressibility was calculated using a compressibility factor in the equation of state:

$$PV = Z\ m\ RT \qquad (5\text{-}2)$$

The compressibility factor (Z) was determined from a six-coefficient equation correlated to experimental data up to 15,000 psi (see Reference 5-1). This equation was used in this analysis for pressures considerably above this value. Since no data has been obtained at these high pressures, the Reference 5-1 equation serves only as a best estimate (and probably an optimistic one).

Free convection heat transfer from the container to the gas was considered to be a function of the acceleration history. This method has proven successful during the ACE TCNT development tests (see Reference 5-2). No heat transfer was assumed in the reservoir, which makes the analysis slightly conservative.

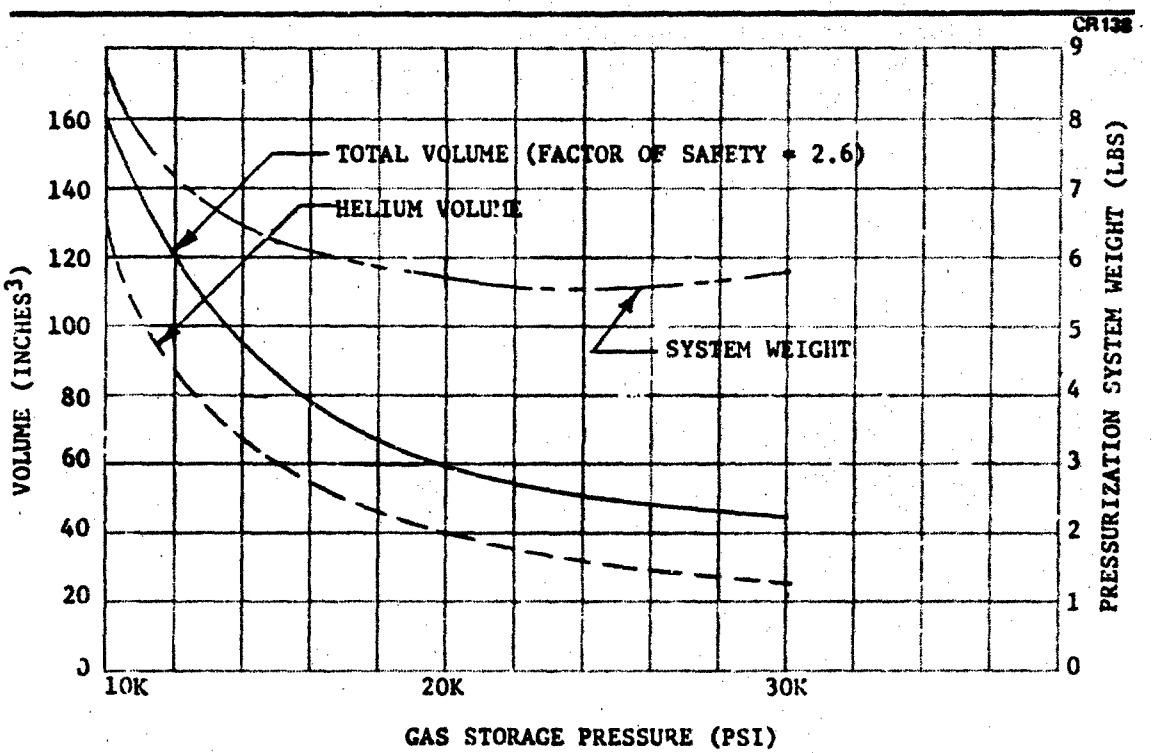


Figure 5-1. Helium Gas Bottle Volume and Weight

A pressure regulator was located between the reservoir and gas bottle. Reservoir pressure was limited to 7,000 psi and dropped below this value only when the gas-bottle pressure became less than 7,000 psi.

The results indicate that increasing the gas-bottle pressure can appreciably reduce the required volume. Unfortunately, this also increases personnel safety problems and enhances the possibility of leaks. Gas temperature is also very low, which may create difficulties for both the bladder and coolant. At the end of the S-3 trajectory, the pressure-vessel gas temperature was calculated to be -62°F, and the reservoir gas temperature was -34°F with this system.

The minimum-weight system, including gas weight, as shown in Figure 5-1, was computed to weigh 5.56 lb. This occurs when the gas storage pressure is 25,000 psi and results in a required gas volume of 30 $in.^3$ and a total system volume of 48.6 $in.^3$.

Figure 5-2 shows the cold-gas pressurization system enclosed within the required envelope. The shape of the pressure vessel and reservoir have been modified in order to fit the envelope. System weight will be higher than that previously discussed due to the modified shape and the addition of the pressure regulator. Total weight of this design would be about twice that of an equivalent warm-gas design.

Because of the weight disadvantage, packaging inflexibility, high-pressure storage, and optimism in the compressibility calculations, cold-gas pressurization is not recommended.

5.2 WARM-GAS PRESSURIZATION

Warm-gas pressurization of an unvented chamber is substantially different from and more difficult to control than pressurization of a system with a pressure relief valve through which excess gases can be vented. Heat transfer is much more important because pressurization directly reflects a decrease in the temperature of the gases, and gas temperatures are much lower with an unvented gas generator compared to a similar vented gas generator design. An accurate description of heat transfer from the gas to surrounding surfaces requires an extensive description of conduction within the walls of the pressure vessel, bladder, and other surfaces in contact with the gas, as well as accurate heat transfer coefficients. The computer program used for this analysis considers all these effects and is capable of accurately describing heat transfer in the entire subsystem. Thermal analysis of the elastomeric bladder and coolant were included as a part of the pressurization analysis.

Another notable difference between the vented and unvented gas generator designs is that condensation of water vapor from the solid-propellant combustion gases can occur in the unvented gas generator and can substantially affect both pressure and heat transfer. Pressures may be 20 percent lower than predicted due to this effect alone, and heat transfer from the gas to surroundings may be several times greater than predicted. This effect has been observed experimentally (Reference 5-3). There are methods that can be used to reduce the amount of condensation that occurs, and these methods

CR138

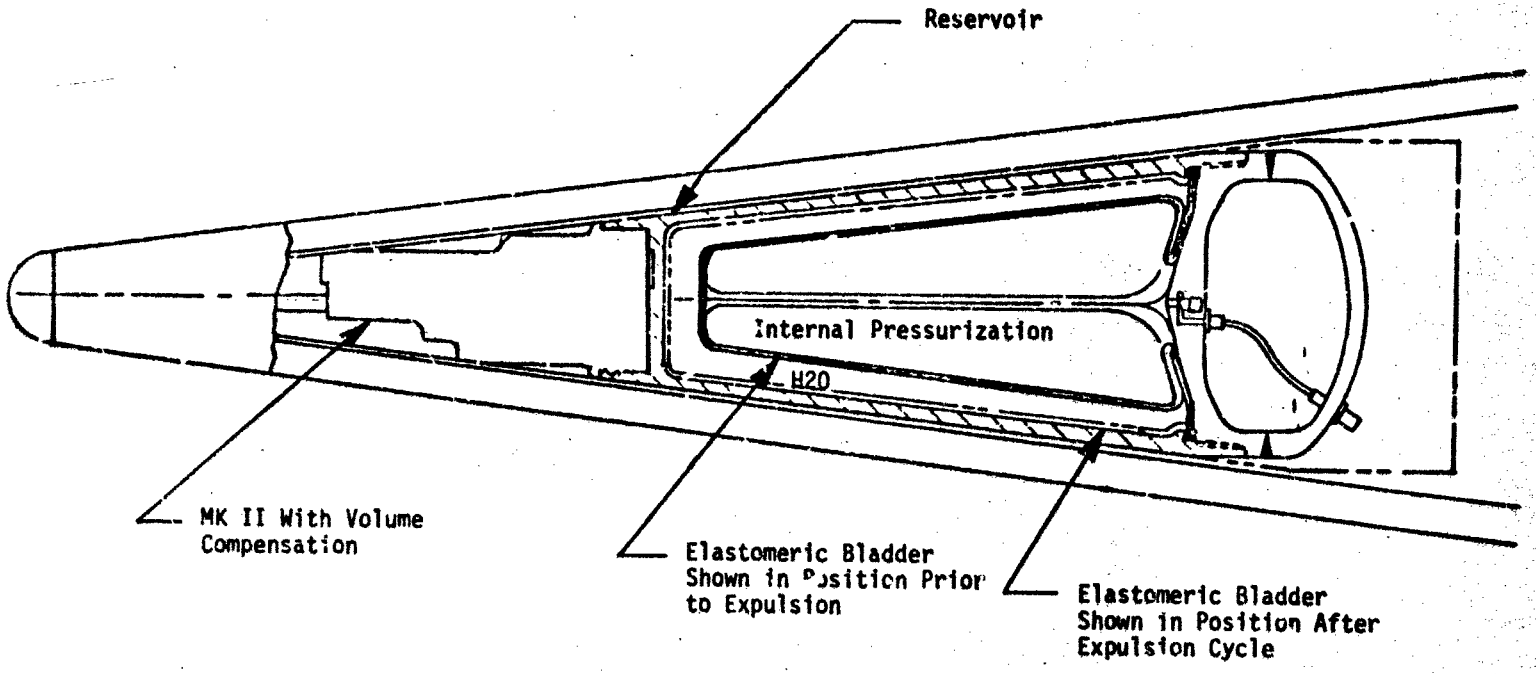


Figure 5-2. Transpiration Coolant Expulsion System

are discussed in the following paragraphs and incorporated into the final recommended design. The computer program used to describe subsystem operation considers condensation in detail.

5.2.1 Solid-Propellant Pressurization Concepts

The advantages of a solid-propellant gas generator include (1) simplicity of design, (2) established high-pressure reliability, (3) relatively small development cost, and (4) a compact unit that is easily adaptable to the subsystem envelope. With a solid-propellant gas generator, there are no moving parts (which increases reliability), and with reasonable quality control, a solid propellant produces reliable and reproducible pressurization. Previous experimental efforts have shown the feasibility of the solid-propellant, unvented gas generator for pressurization of an expulsion system (References 5-3 and 5-4).

The disadvantages of solid propellants are (1) a fixed gas supply rate that is independent of demand and (2) higher gas temperatures than cold-gas or monopropellant gas generators, which may damage an elastomeric bladder or cause excessive heating of the coolant. As will be shown later, these disadvantages can be minimized through careful design.

5.2.1.1 Propellant Requirements

The primary requirement of the propellant is a low flame temperature to minimize heat losses of the gas, degradation of the bladder, and coolant heatup. Numerous propellants are available with flame temperatures of approximately 2,000°F. It is also advisable to select a propellant that has combustion gases with a low water-vapor content within this low-temperature group. Of the warm-gas propellants investigated, the double-base propellants had 6 to 9 percent water vapor, which was substantially lower than AP composite propellants (16 to 30 percent) and AN composite propellants (20 to 28 percent). Since propellant screening was not a primary part of this study, it is very possible that other AN and AP formulations would have less water vapor content. However, double-base propellants were used almost exclusively in this analysis.

Another factor that affects propellant selection is burning rate. Burning rates of approximately 0.2 in./sec at 2,000 psi were selected in order to minimize volume for the envelope and operating conditions under consideration.

The Chemtronics D-198 double-base propellant used in generating the recommended gas generator design is an example of one propellant that could fill the requirements and is currently available. Burning rate is shown in Figure 5-3 for pressures to 6,000 psi, and properties of the combustion gases are described in Table 5-1.

5.2.1.2 Igniters

Adequate igniter size is dependent upon propellant ignition temperature, which is a function of propellant reactivity and burn rate, and heat flux to the propellant surface for a particular ignite. design and igniter material. Ignition temperatures of 500 to 600°K have been determined experimentally for a number of propellants. This temperature is about that which produces thermal decomposition of the binder. Igniter design is seldom based on a rigorous thermal analysis of the propellant surface, and empirical approaches are often used. In addition, it is common practice to use as much igniter material as possible while remaining within the pressure limits of the motor. With an unvented system, the pressure generated by igniter material must be kept fairly low or the pressure generated by the igniter will cause the propellant to burn too fast and overpressurize the subsystem. For this reason, a material that produces a large heat output for a small amount of gas is desirable. Boron potassium nitrate was selected for use in the current study. Experience has shown that small amounts of this material can adequately ignite the Chemtronics D-198 propellant. Igniter weights for the analytical results presented here are based on a 4.0-gram igniter for the first grain, and 1.5-gram igniters for Grains 2 and 3. These will be verified during development testing. Because of the small amount of material being used, powder could be employed. However, small pellets will be used to reduce the safety hazard. The pellets and bridgewire are held between two thin sheets of plastic which can be attached to the surface of the grain.

Table 5-I

D-198 PROPELLANT EXHAUST GAS AND BALLISTIC CHARACTERISTICS

Elemental composition (moles/gram)	C	2.599
	H	3.867
	N	0.758
	O	3.391
Burning rate at 1,000 psia (in./sec)		0.212
Pressure exponent		0.4
Chamber temperature (°F)		2,121
Molecular weight		20.53
Specific heat ratio		1.29
Exit temperature at ϵ = 2 (°F)		1,500
Exit pressure at ϵ = 2 (psia)		100
Exit Mach number at ϵ = 2		1.95
Characteristic velocity (ft/sec)		3,822
Sonic vacuum specific impulse (sec)		148
Propellant density (lb/in.^{3})		0.053
Exhaust gas composition at throat (mole percent)	CO	44.79
	H_2	28.95
	CH_4	0.97
	NH_3	0.02
	CO_2	8.19
	H_2O	9.21
	H_2	7.86

5.2.1.3 Grain Design

The optimum grain design must satisfy two criteria. First, pressures generated by the gas generator must equal or exceed the minimum pressure required to supply an adequate flow of coolant through the nosetip. Second, the grains must form a compact gas generator that can be easily fitted into the specified volume with little wasted space. The gas generator design was changed numerous times during the study as methods were found to decrease size. Final designs shown in Section 7.1 have a 2-in.-long by 4-1/2-in.-diameter gas generator chamber at the large end of the cone. Since it was

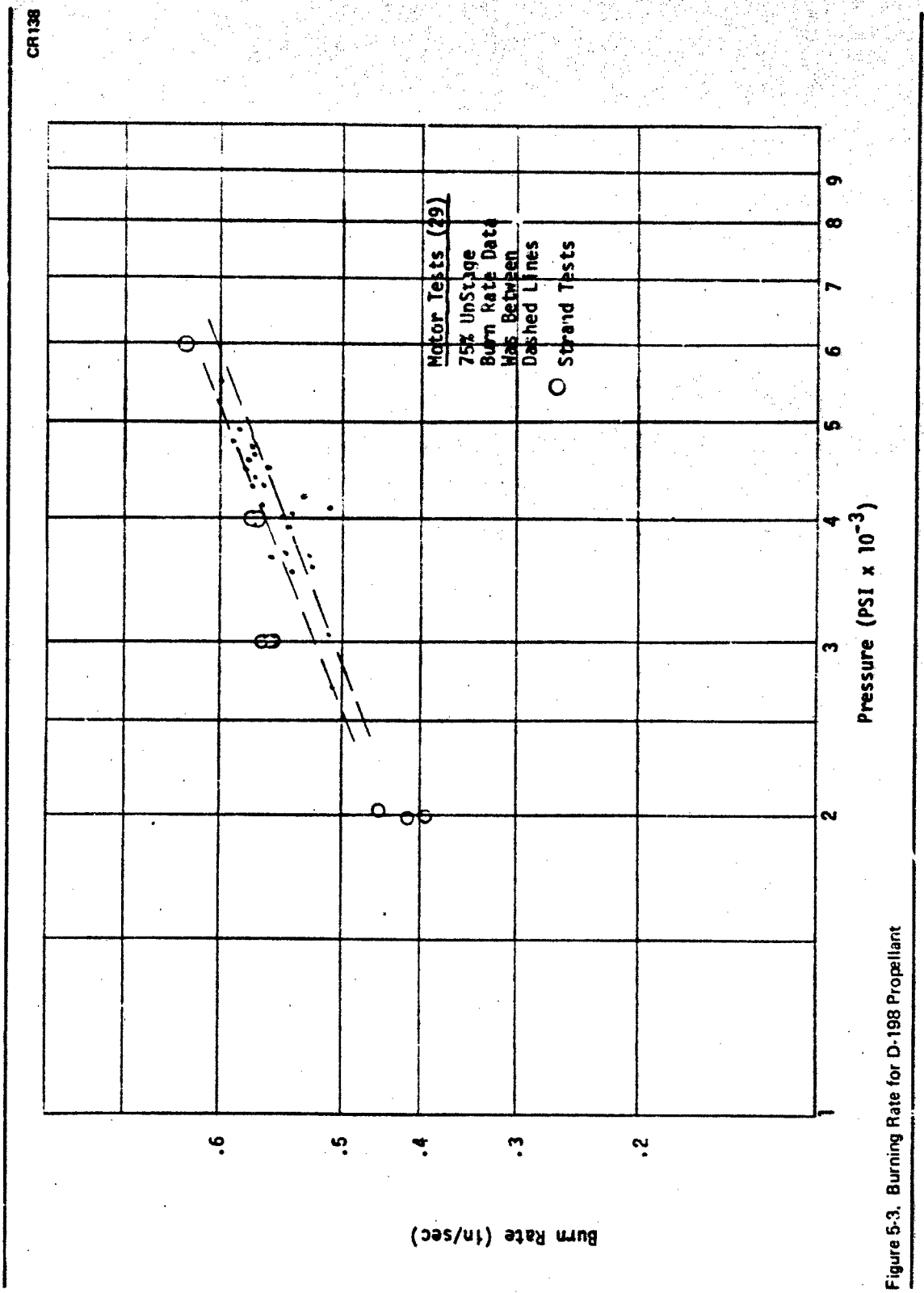


Figure 5-3. Burning Rate for D-198 Propellant

desirable to use two or three grains in this chamber, the grain design selected for the first grain is not commonly used in solid-propellant applications. A circumferential-burning grain design significantly reduced the length of the gas generator. This first grain provides a pressure-sustaining gas flow for several seconds. When the need for an increase in pressure is signaled by the coolant flow valve, an additional grain is ignited. With the two-grain concept, the second grain is ignited when the pressure drop across the valve decreases to 200 psi. With three grains, a more complex ignition circuit is required (Figure 5-4). The sequence of events which results in grain ignition is as follows: (1) receive initiation signal directly at the first grain igniter; (2) lock out the pressure switch signal for approximately 0.5 sec to allow pressure buildup; (3) when the pressure drop across the valve goes below 110 psi, send a signal to the second grain igniter; (4) another 0.5-sec lockout of the pressure switch is required; and (5) if and when the valve ΔP drops to 110 psi, the signal is sent to the third grain igniter.

The pressure requirements for five trajectories were shown in Figure 2-23. The S-3 trajectory is the shortest and requires the highest pressure, and consequently the highest propellant burn rate and the most propellant, of all five trajectories considered. The L-6 trajectory is the longest trajectory and requires a much longer pressurization schedule. To satisfy both trajectories with a single grain and the same size of gas generator requires an extremely heavy pressure vessel capable of withstanding pressures to 70,000 psi. It is completely unreasonable to consider operating at this condition, particularly when the performance of two or three grains is examined.

Figures 5-5 through 5-7 show the pressures generated by a two-grain design, using a circumferential-burning first grain and an end-burning second grain. The S-3 trajectory sizes the total amount of propellant required, with both grains sized to end at impact. The second grain is 15 percent larger than the first. As shown in Figure 5-5, the second grain ignites and burns in the last 2.7 sec, compared with 9.2 sec for the first, because of a proportionately larger burning surface. The reason for this division of the propellant is shown in Figure 5-6, the pressure history for the L-6 trajectory. The end of the first grain occurs substantially before the ignition of the second grain, but at a pressure that is very near the maximum design pressure. If

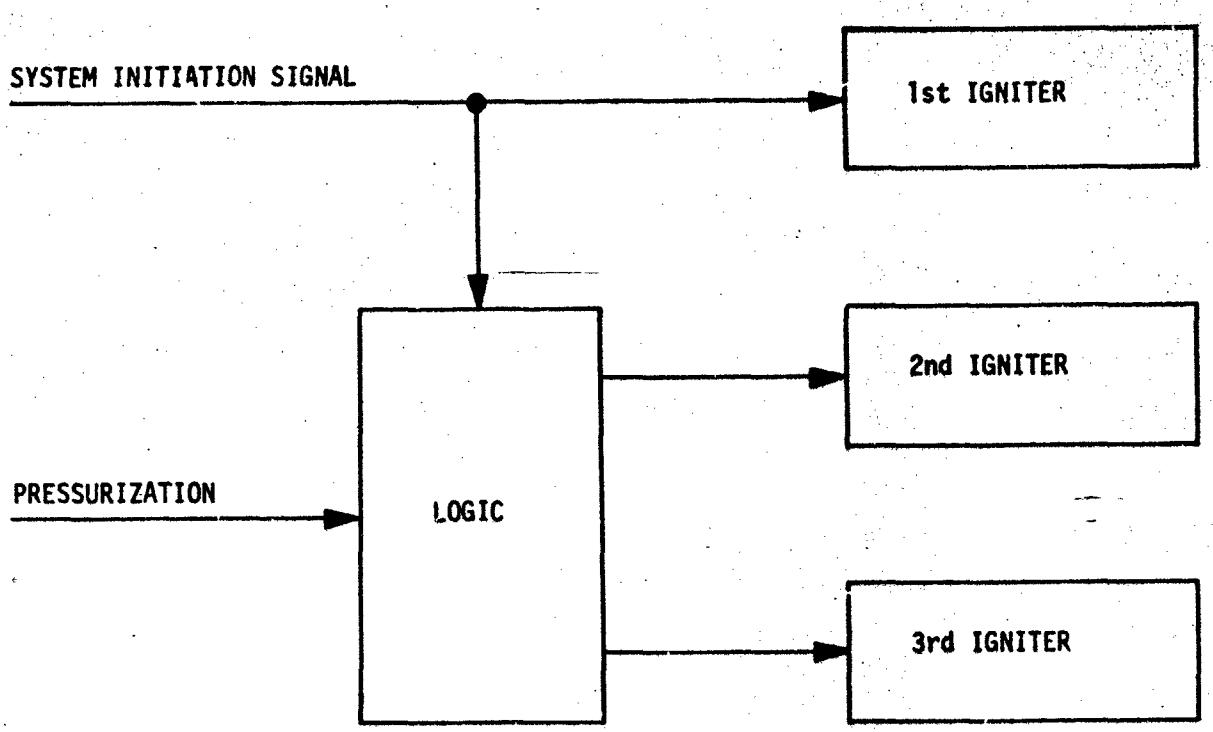


Figure 5-4. Pressurization Igniter Circuit

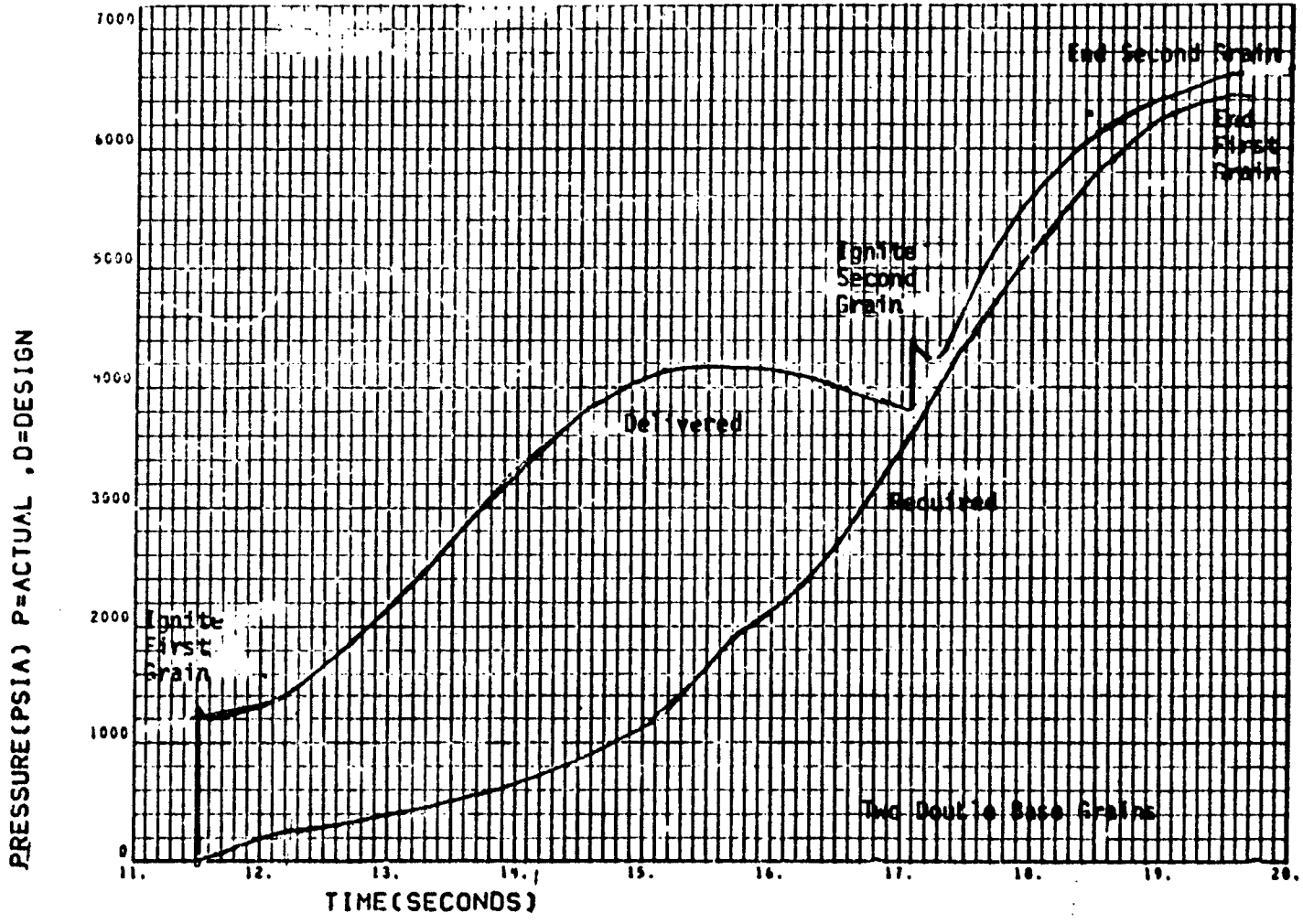


Figure 5-5. Pressure History, S-3 Trajectory

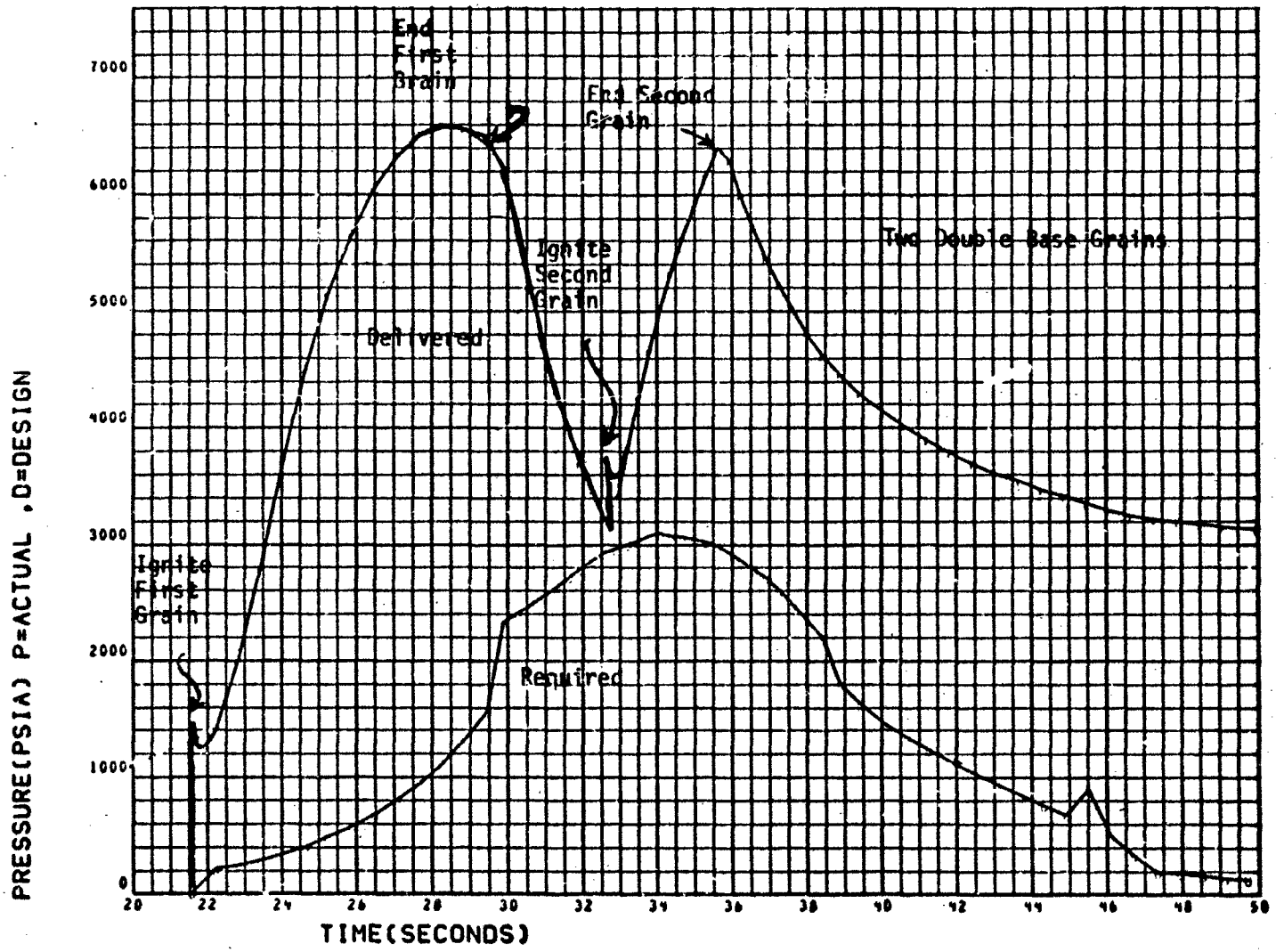


Figure 5-6. Pressure History, L-6 Trajectory

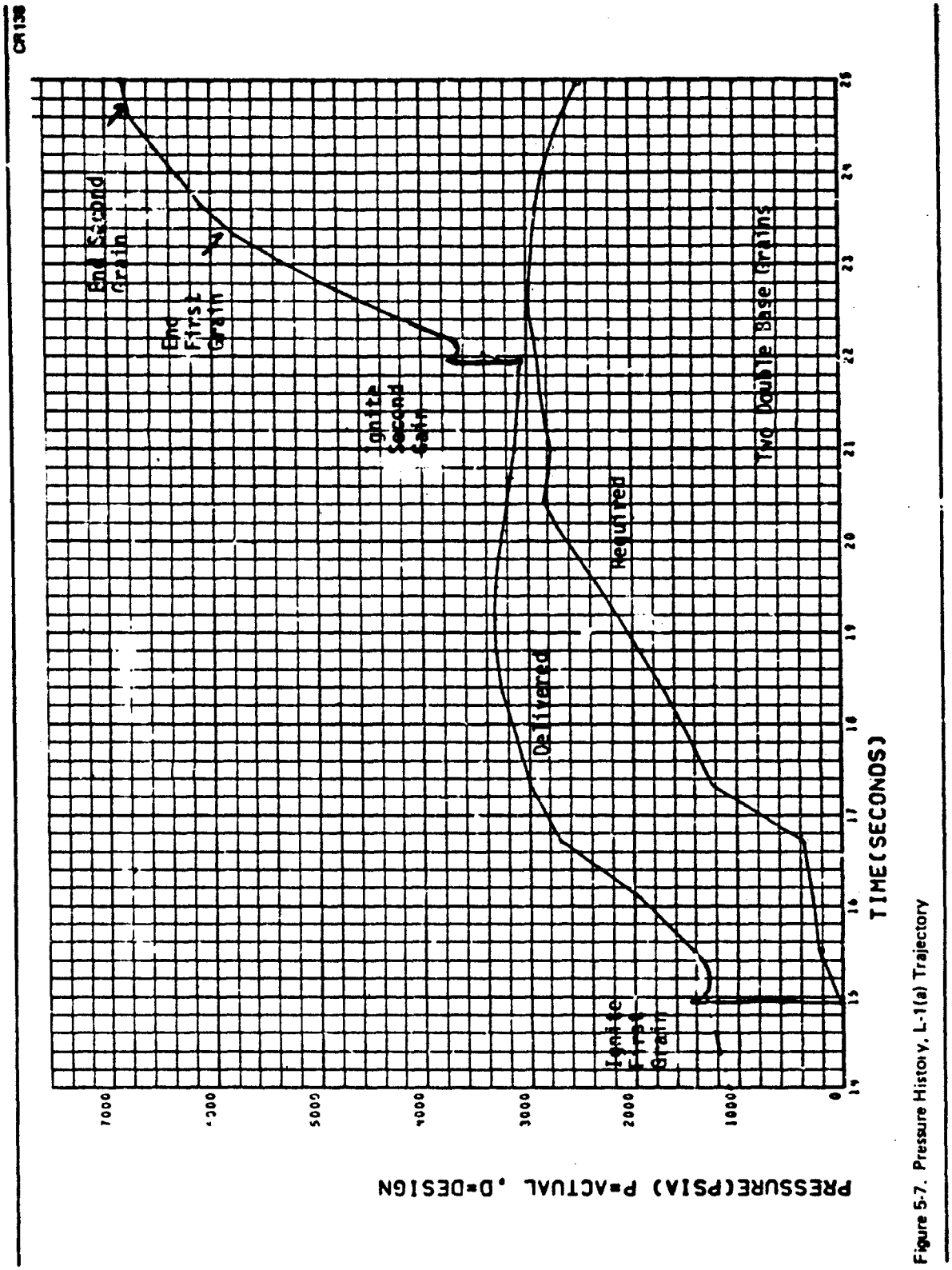


Figure 5-7. Pressure History, L-1(a) Trajectory

the first grain were larger, the maximum design pressure would be exceeded at the end of the first grain, and if the second grain were larger, the maximum design pressure would be exceeded at the end of the second grain. Therefore, the S-3 trajectory, the shortest being considered, fixes the total propellant weight and burning surface of the grains, and the L-6 trajectory, the longest, fixes the division of propellant into individual grains. Pressurization of intermediate trajectories was found to be satisfactory with any grain design that satisfied both the short (S-3) and long (L-6) trajectories. With two grains, the intermediate trajectory that produced a maximum pressure closest to the maximum design value was the L-1(a), shown in Figure 5-7. It is obvious from the figures that two grains will satisfy pressurization requirements adequately for these five trajectories. However, grain design must be precise, or overpressurization will occur on the longer trajectories because the maximum design pressure is approached on three of the five trajectories studied.

To obtain greater versatility and flexibility, a design consisting of a circumferential-burning grain and two end-burning grains was investigated. Three grains have naturally greater versatility, as lesser amounts of gas are brought into the system at any one signal for increased pressure. The result is a pressurization concept that more closely follows the pressure requirements of diversified trajectories. The only disadvantage is increased complexity in the initiation design.

There are an infinite number of grain designs that will satisfy one trajectory. The merit of any particular combination of grains only becomes apparent after the grain design is tested against several trajectories. This was true of the two-grain concept and is even more fundamental for the three-grain concept. The procedure for determining a good grain design began with the investigation of physical grain shapes that could fit within the compact space allotted to the gas generator, and was verified by the determination of pressures for each trajectory. An iteration procedure was accomplished, and after each step of the investigation, a comparison of the results indicated changes which would improve the design. This technique resulted in the design shown in Figure 5-8.

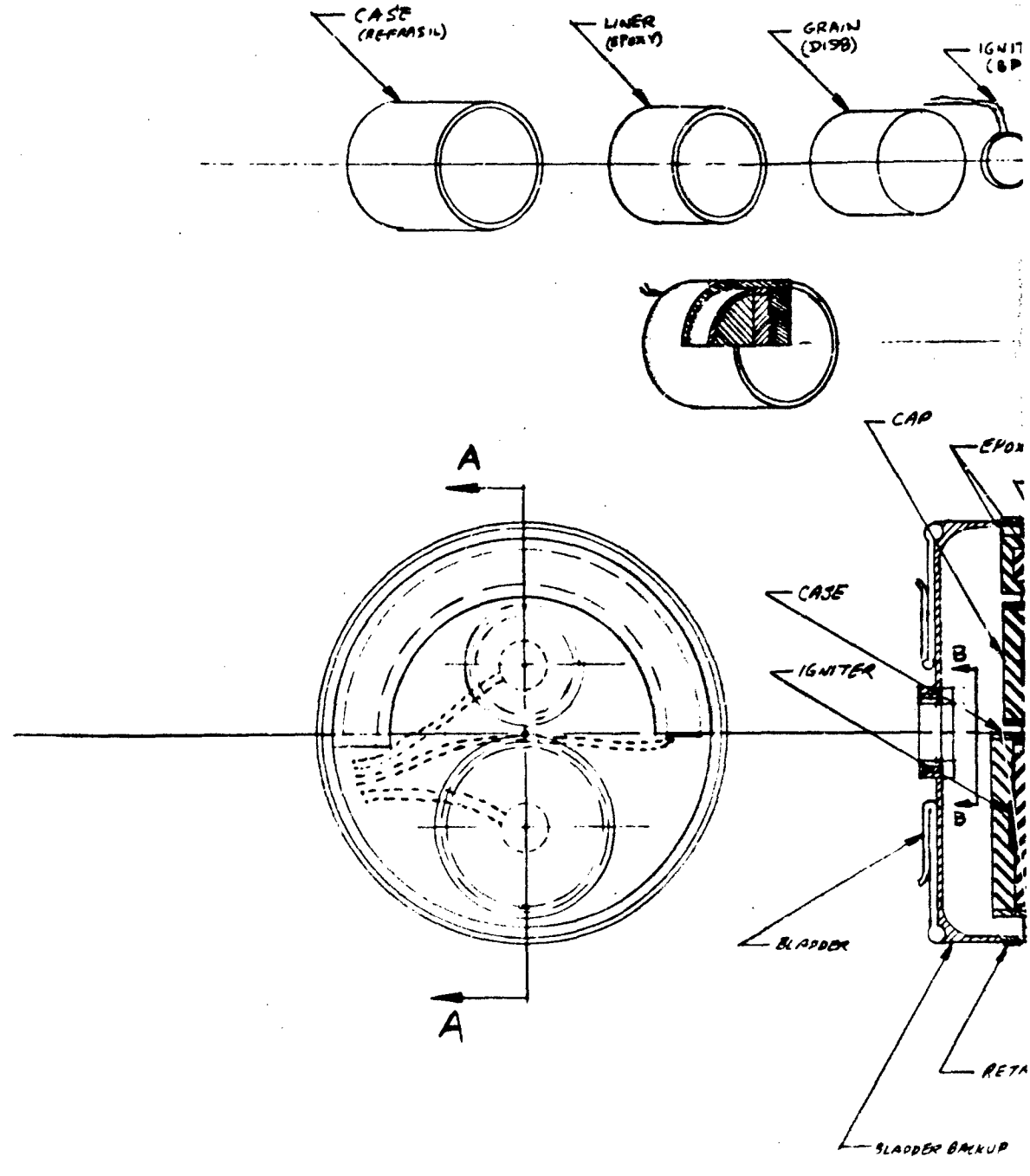
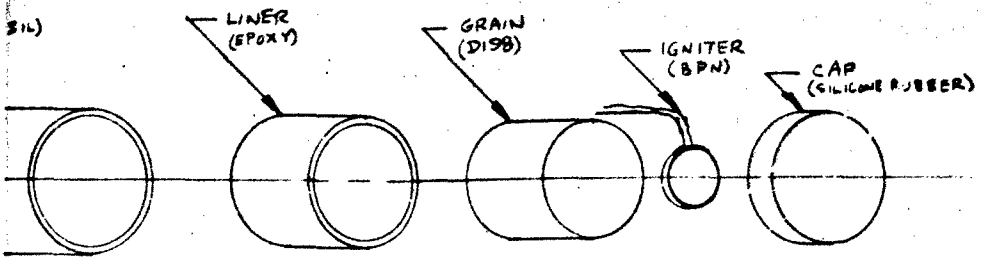
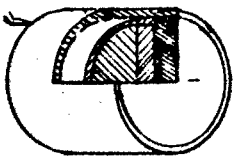
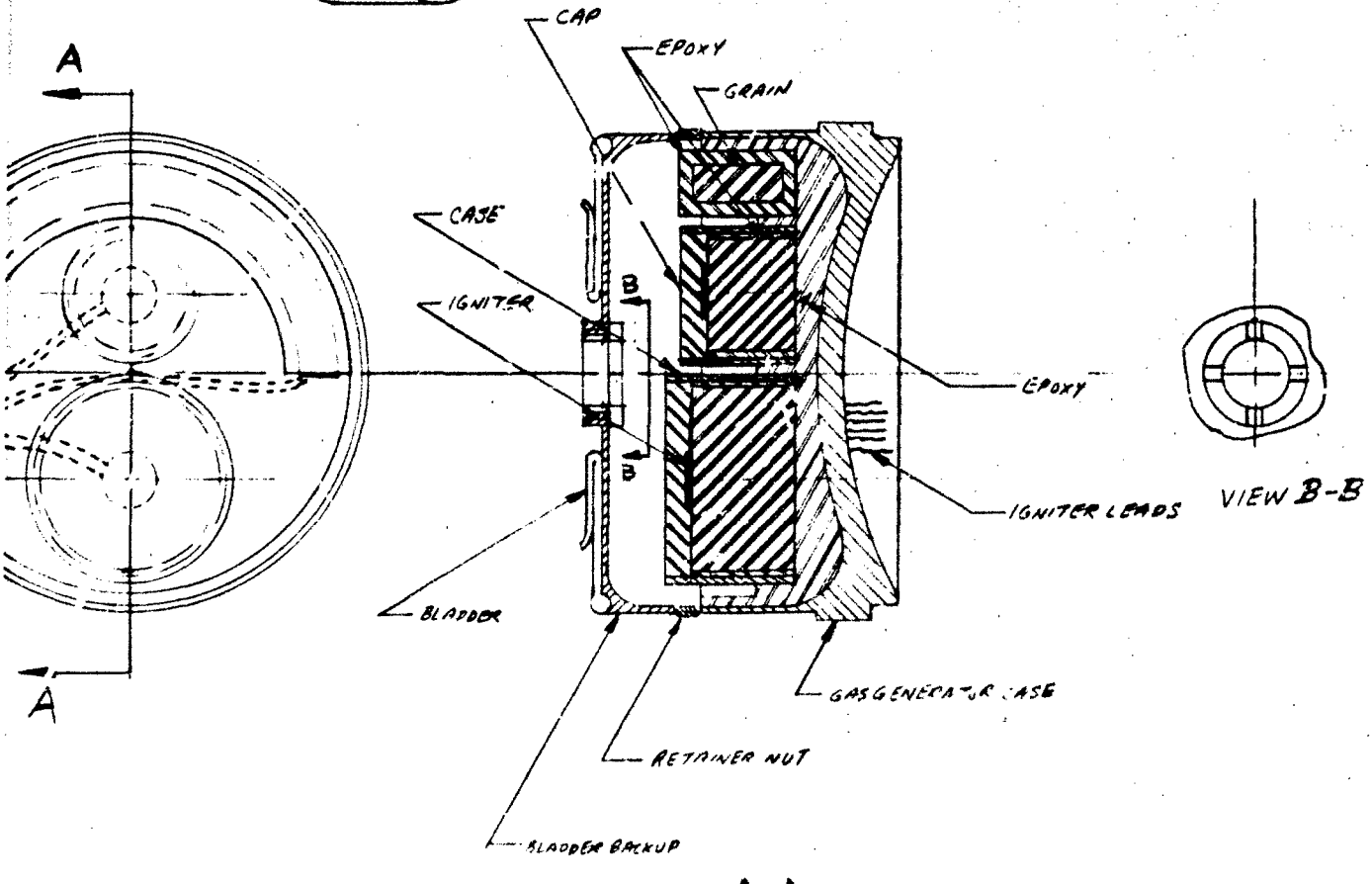


Figure 5-8. Three-Grain Gas Generator







VIEW B-B

VIEW A-A

the first grain were larger, the maximum design pressure would be exceeded at the end of the first grain, and if the second grain were larger, the maximum design pressure would be exceeded at the end of the second grain. Therefore, the S-3 trajectory, the shortest being considered, fixes the total propellant weight and burning surface of the grains, and the L-6 trajectory, the longest, fixes the division of propellant into individual grains. Pressurization of intermediate trajectories was found to be satisfactory with any grain design that satisfied both the short (S-3) and long (L-6) trajectories. With two grains, the intermediate trajectory that produced a maximum pressure closest to the maximum design value was the L-1(a), shown in Figure 5-7. It is obvious from the figures that two grains will satisfy pressurization requirements adequately for these five trajectories. However, grain design must be precise, or overpressurization will occur on the longer trajectories because the maximum design pressure is approached or three of the five trajectories studied.

To obtain greater versatility and flexibility, a design consisting of a circumferential-burning grain and two end-burning grains was investigated. Three grains have naturally greater versatility, as lesser amounts of gas are brought into the system at any one signal for increased pressure. The result is a pressurization concept that more closely follows the pressure requirements of diversified trajectories. The only disadvantage is increased complexity in the initiation design.

There are an infinite number of grain designs that will satisfy one trajectory. The merit of any particular combination of grains only becomes apparent after the grain design is tested against several trajectories. This was true of the two-grain concept and is even more fundamental for the three-grain concept. The procedure for determining a good grain design began with the investigation of physical grain shapes that could fit within the compact space allotted to the gas generator, and was verified by the determination of pressures for each trajectory. An iteration procedure was accomplished, and after each step of the investigation, a comparison of the results indicated changes which would improve the design. This technique resulted in the design shown in Figure 5-8.

The total weight of the three solid propellant grains is 0.255 lb. The weights and burning surfaces of the grains are shown in Table 5-2. Figure 5-9 illustrates the surface-area variation of the first, or circumferential-burning, grain.

Predicted operation of this gas generator design with each of the five trajectories is shown in Figures 5-10 through 5-14. The results obtained for all five trajectories are summarized in Table 5-3 for both the two- and three-grain designs.

On all trajectories, the delivered pressures are closer to the required pressures, and the maximum pressures are further from the maximum design pressure with three grains compared with two grains. The higher three-grain design pressure on the S-3 trajectory reflects an increased operating margin with this design to ensure adequate pressurization with a nominal variation in propellant burn rate. Further work with two grains would also have reflected this increase.

Table 5-2

THREE-GRAIN PROPELLANT DESIGN SUMMARY

Grain No.	Grain Design	Weight (lb)	A_B (in.^{2})	Length (in.)	Diameter (in.)
1	Circumferential burning	0.09	0.33*	5.15	0.88 x 0.375
2	End burning	0.04	0.9	0.838	1.07
3.	End burning	0.125	2.35	1.00	1.73

*Initial.

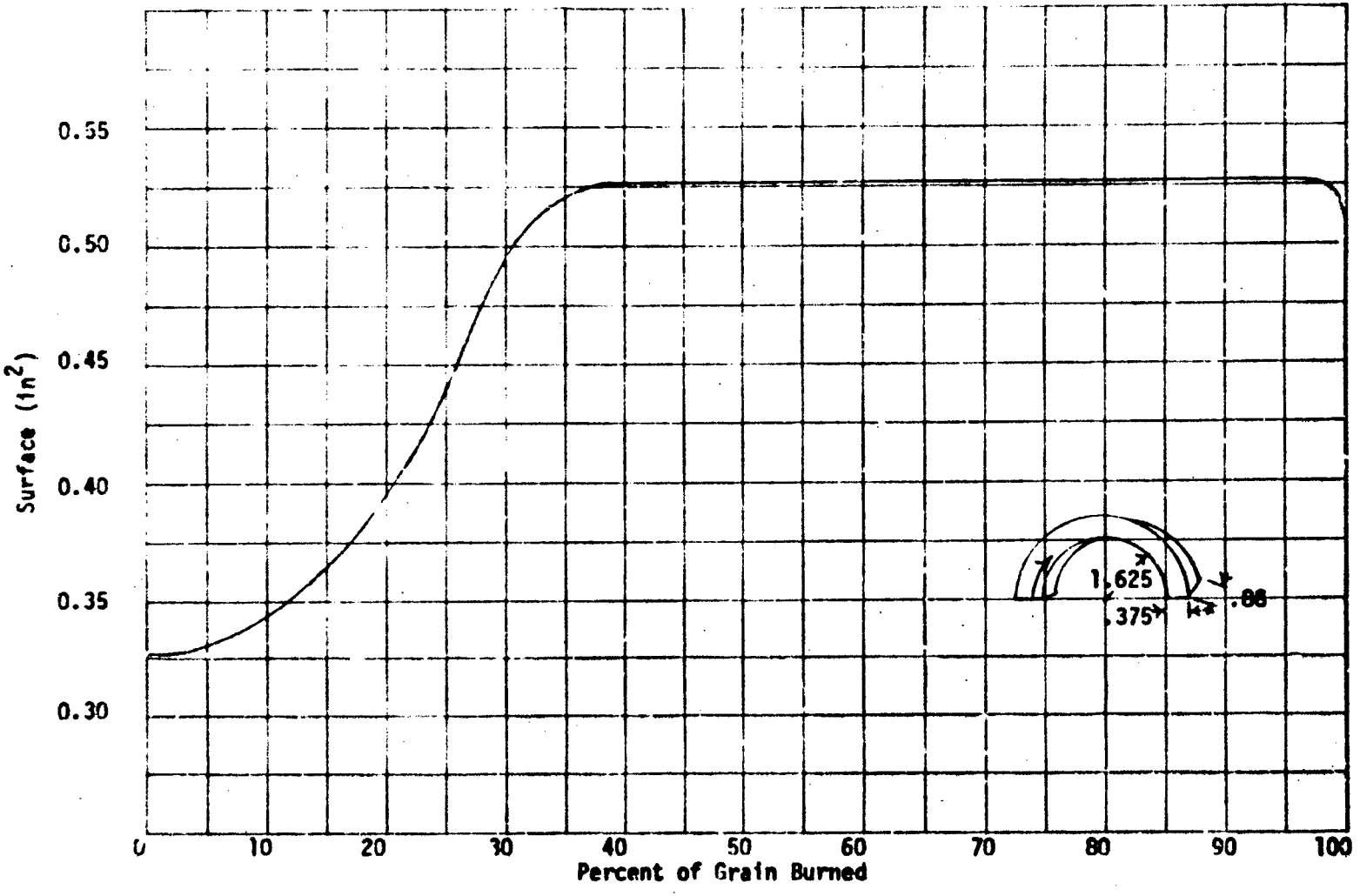


Figure 5-9. Burning Surface for Circum ferential Burning Grain

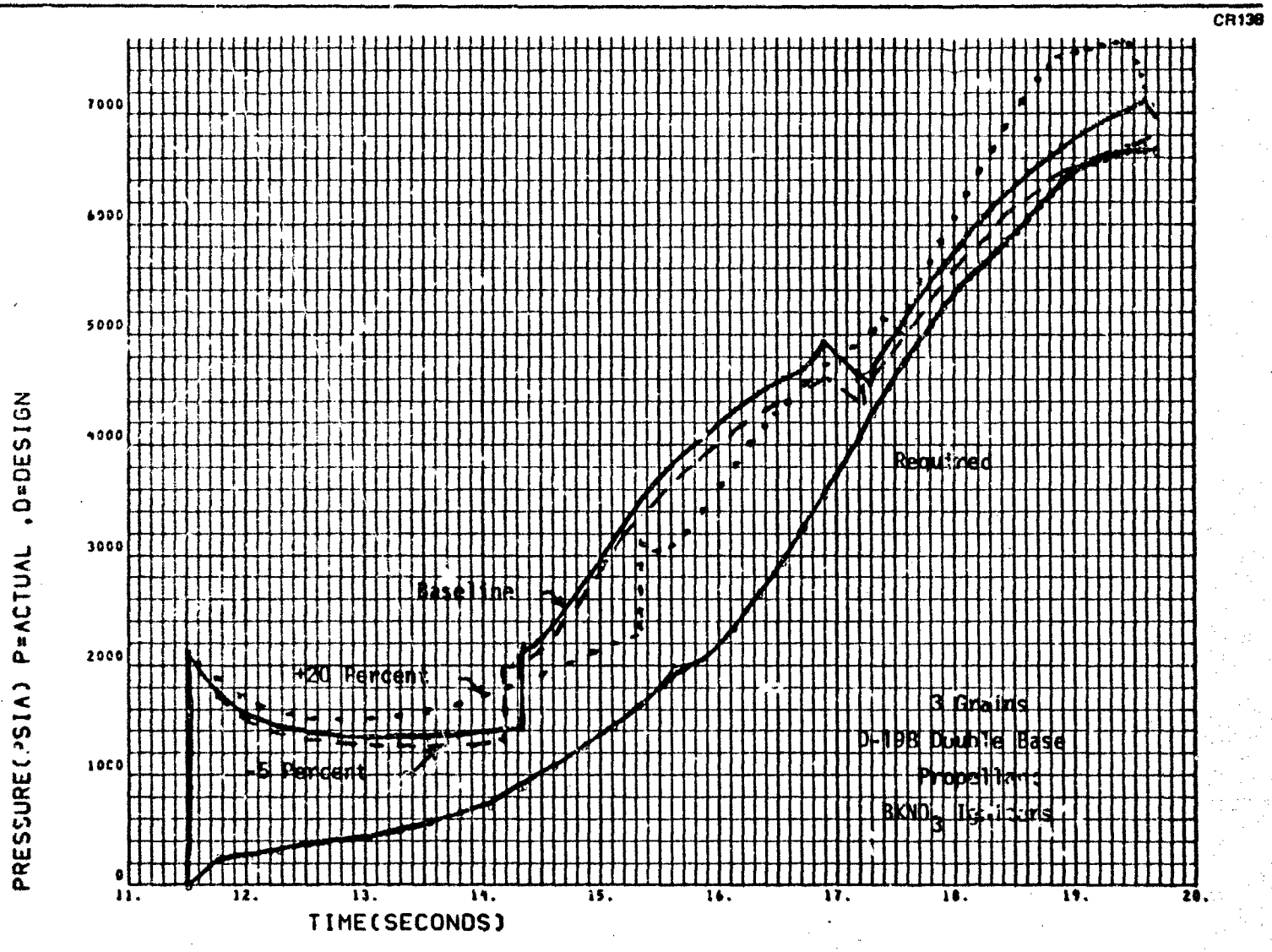


Figure 5-10. Required and Delivered Pressure, S-3 Trajectory

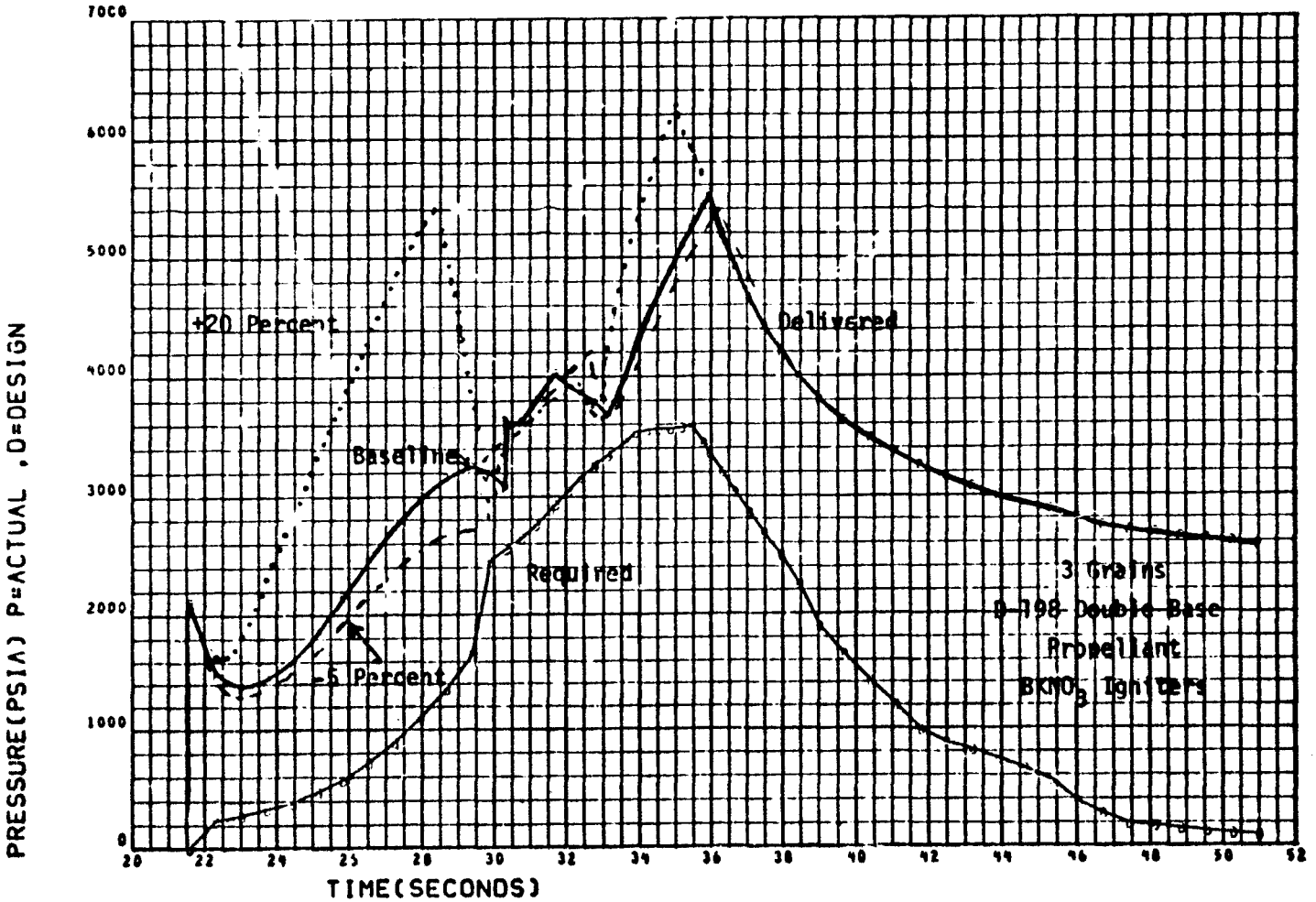


Figure 5-11. Required and Delivered Pressure, L-6 Trajectory

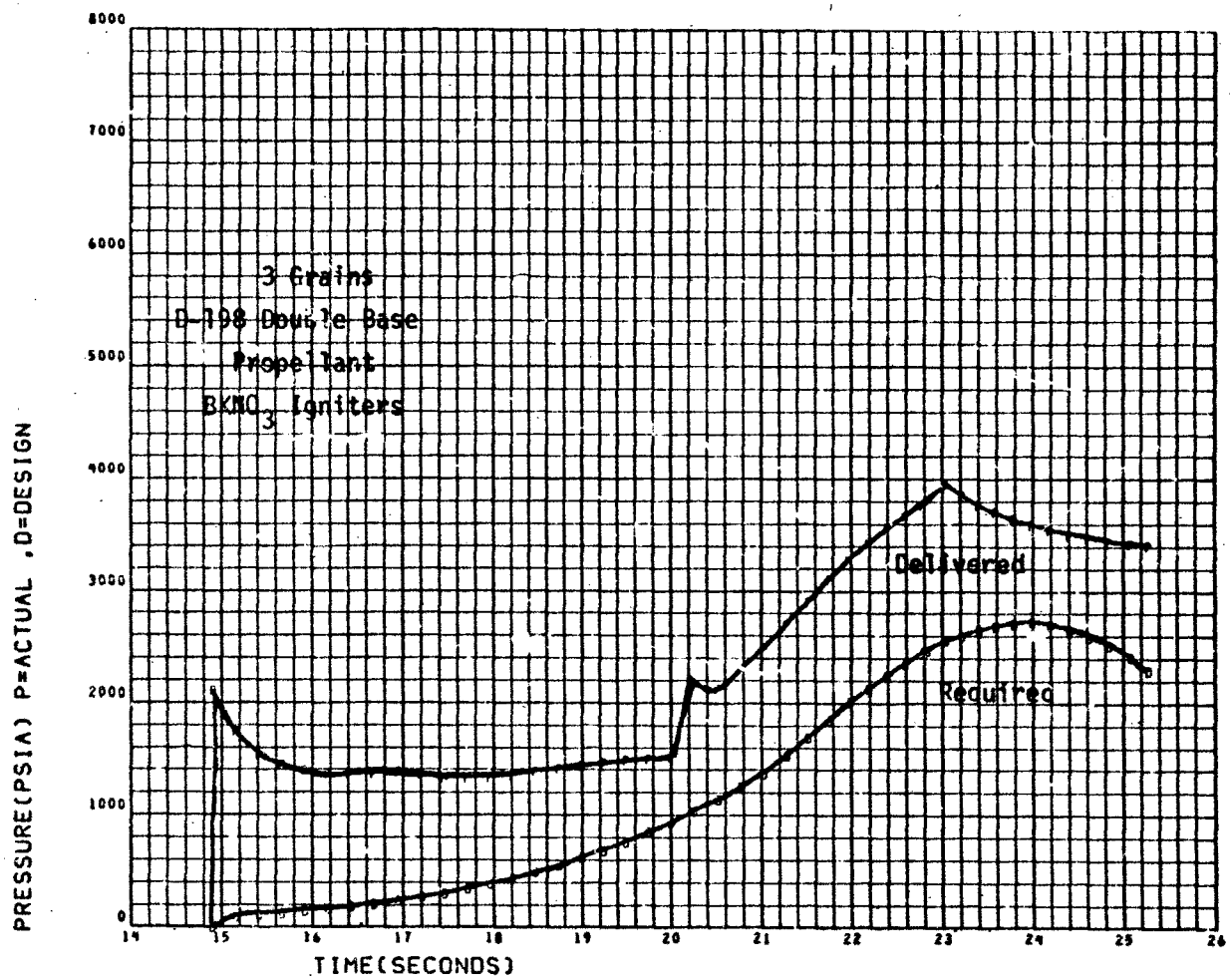


Figure 5-12. Required and Delivered Pressure L-1(a) Trajectory

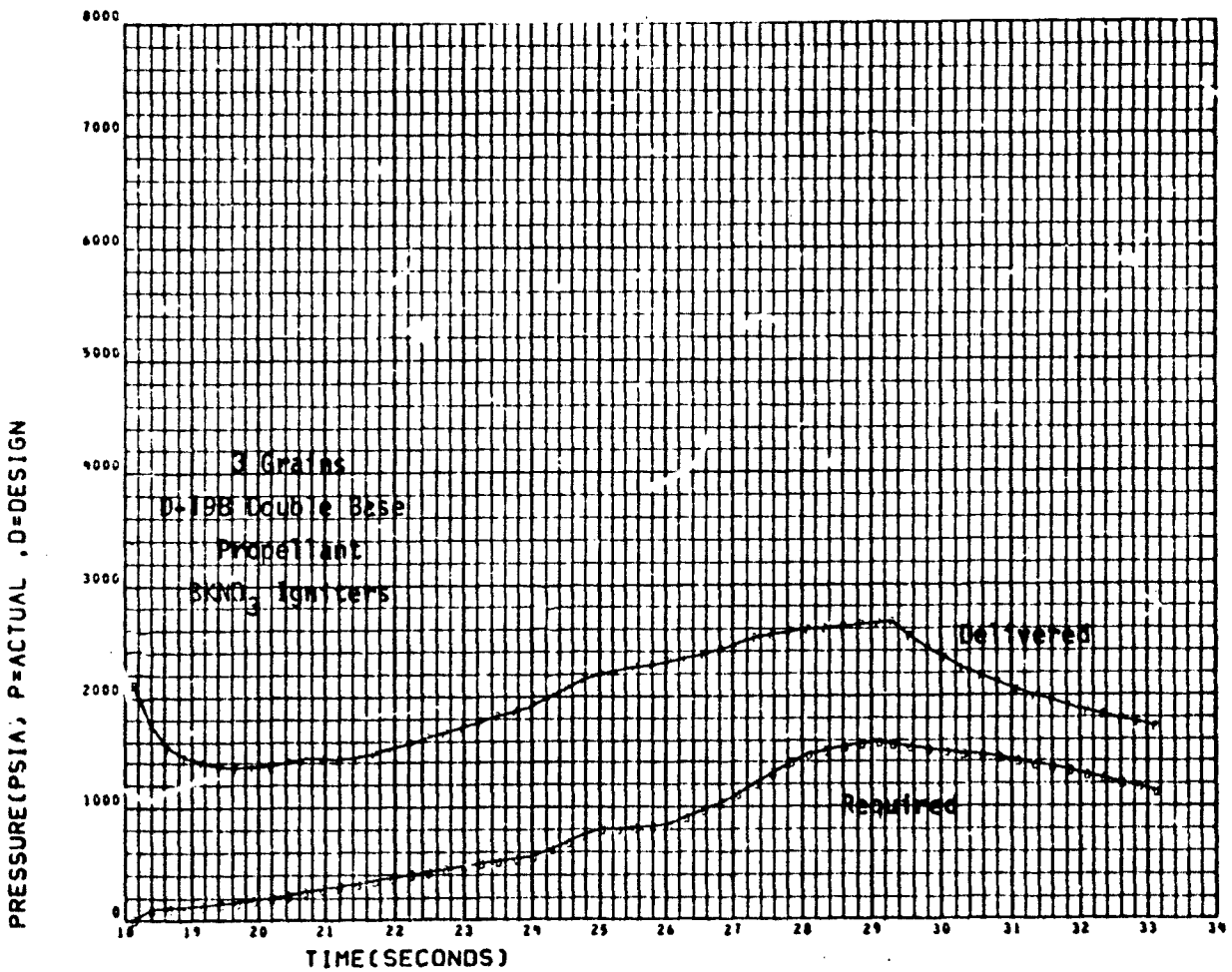


Figure 5-13. Required and Delivered Pressure, L-12 Trajectory

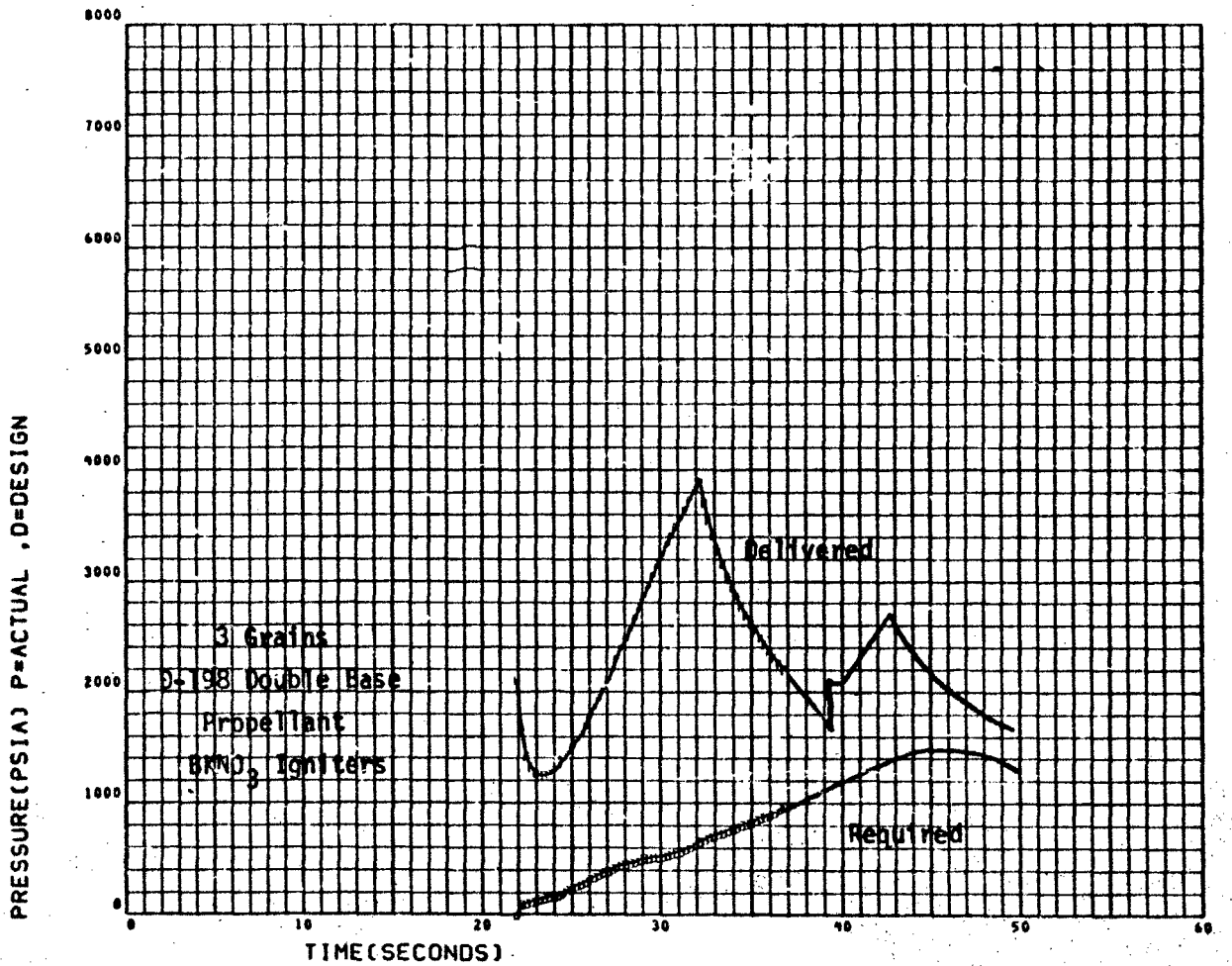


Figure 5-14. Required and Delivered Pressure, 606 Trajectory

Table 5-3

SUMMARY OF PRESSURIZATION WITH SOLID PROPELLANTS

Trajectory	Duration (sec)	Maximum Required Pressure (psi)	Maximum Pressure Generated (psi)	
			Three Grains	Two Grains
S-3	9	6, 600	7, 000	6, 600
L-1(a)	11	2, 500	4, 000	6, 800
L-12	15	1, 600	2, 700	4, 200
606	28	1, 600	3, 900	5, 000
L-6	30	3, 600	5, 600	6, 600

Acceleration effects, thermal effects, pitting or uneven burning of the grain, and small variations in formulation can cause the propellant burning rate to fluctuate from the norm. Most of these effects would serve to increase the burning rate. Testing of the gas generator on a centrifuge would allow acceleration and thermal effects to be included into the factors used to develop a grain design, but this information is not presently available. It is estimated that the burning rate could be as much as 20 percent higher or 5 percent lower than the base burning rate used in the previously discussed grain design. After a series of tests have been made to determine burning rate in the flight environment, the variation in propellant burning rate between similar flights should be approximately ± 5 percent.

Variation in burning rate with the three-grain solid-propellant concept is only important for the S-3 trajectory, where the gas generator develops pressures equal to the maximum design value. Figure 5-10 shows the effect of burning-rate variation. If the gas generator were built without any additional burning-rate information, this design would be expected to deliver pressures somewhere between the dotted lines. In all cases, pressurization is adequate, and in the worst case, overpressurization would be 600 psi, which is far less than the safety factor of the pressure vessel. Figure 5-11 shows the effect of a similar variation for the L-6 trajectory. The maximum design pressure is not exceeded by a 20-percent increase in burning rate.

With three grains, the optimum in grain design is not as clearly indicated as was the case with two grains. It is felt that the three-grain design could be further improved so that generated pressures would match required pressures more closely than is shown in this report. However, these changes would be small, as the design presented is quite good.

5.2.2 Monopropellant Pressurization Systems

Monopropellant systems have found increasing applications in recent years in various missile and space systems because of their "on-off" capability and low-temperature exhaust products. The most commonly used monopropellant fuel has been hydrazine ignited with the now-well-known Shell 405 catalyst. This combination can be used to spontaneously and repeatedly initiate decomposition of hydrazine for a range of exhaust gas conditions such that the temperature of the pressurizing gas can be controlled to reasonably low levels. This is done by controlling the amount of ammonia dissociated in the hydrazine reaction. It is usually desirable to maximize the ammonia dissociation in order to produce a maximum volume of gas with low molecular weight and low temperature, if space permits. An ammonia dissociation of 80 percent is a typical design value, resulting in an adiabatic gas temperature of 1,400°F and an average molecular weight of 11.6. Substantially lower temperatures may also be achieved when dissociation is less. Hydrazine also offers the advantage of efficient, vapor-pressure storage in a liquid form, and simple conventional methods of fluid control. The major disadvantage with the monopropellant concept in the current application is lack of performance data at the high pressures of interest.

Two monopropellant concepts were investigated and compared in this study: a blowdown, pressure-regulated, stored-gas system (Figure 5-15) and a bootstrap system (Figure 5-16). The blowdown system utilizes a single tank with the hydrazine separated from its pressurant by a positive expulsion device. The pressurant is stored at high pressure and expels the hydrazine whenever the control device opens. The regulated pressure is the maximum expected coolant pressure. Disadvantages of the blowdown system are (1) stored high-pressure gas, which is undesirable from the standpoint of safety and reliability during storage; (2) excessive catalyst bed pressure drop, causing rapid catalyst degradation; and (3) volume and weight penalties.

CR138

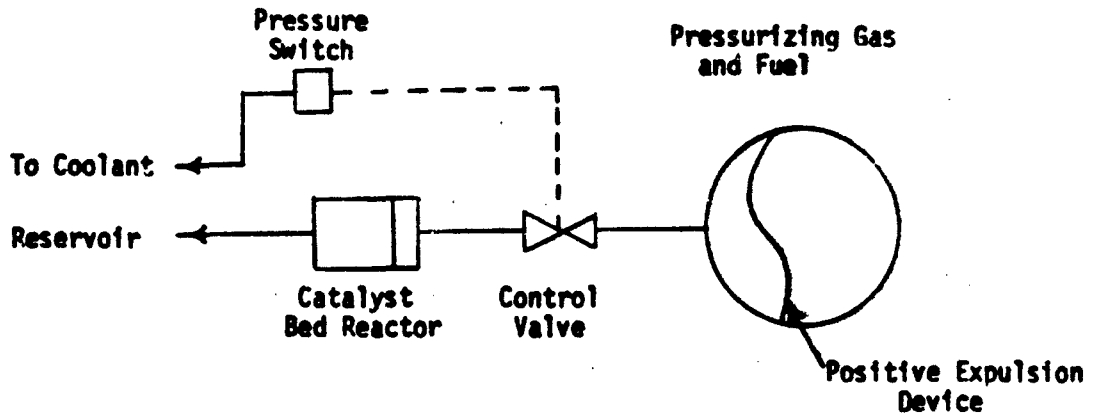


Figure 5-15. Blowdown Monopropellant Concept

CR138

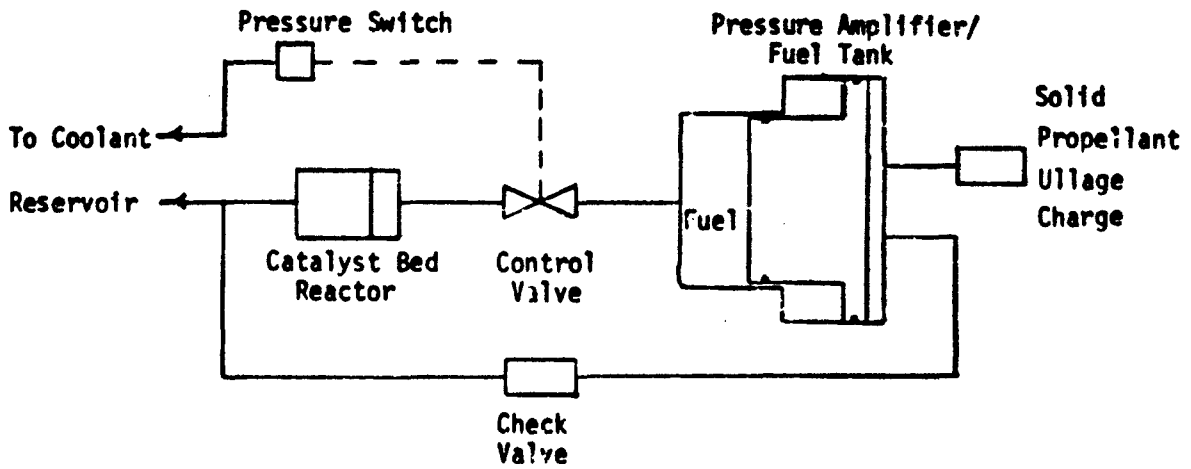


Figure 5-16. Bootstrap Monopropellant Concept

The bootstrap system shown in Figure 5-16 allows the pressurant to be stored at its own vapor pressure. This system may be activated by firing a squib in the forward end of the pressure amplification device (piston) which, in turn, pressurizes the fuel. When the control device opens, hydrazine is forced into the reactor, thus generating gas which is fed back to the top of the pressure amplifier, bootstrapping the system. As with the blowdown system, a simple conventional fuel control device may be used with this concept. Performance of the bootstrap system for the S-3 and L-6 trajectories is shown in Figures 5-17 and 5-18.

The bootstrap concept combines the inherent simplicity of a solid-propellant system (no separate pressurization system or stored high-pressure gas) and the flexibility of a liquid system (greater versatility as a result of the capability of demand operation). Disadvantages of the bootstrap system relative to the solid system are (1) increased complexity because of the number of components required, (2) higher development and unit cost, and (3) a longer development time.

The factors considered in the monopropellant system design studies are summarized in Table 5-4. Comparison of the blowdown and bootstrap concepts was made on the basis of expulsion requirements given in Section 2.4. A computerized model of each system was utilized to generate performance data which could be compared with solid-propellant data. The S-3 and L-6 trajectories were assumed to fix the design. It was also assumed that problems of long-term, high-pressure storage and sealing are solvable, and that operation of a monopropellant gas generator in the 7,000-psi range is not too different from the anticipated performance based on lower pressures.

Fuel volume requirement is the major factor in determining the size of the monopropellant system. Calculations of fuel weight requirements were made for the two extreme trajectory conditions (S-3 and L-6) for a range of values of percent ammonia dissociation. On the basis of these fuel weights, it was found that the fuel weight requirement for the monopropellant system could be slightly less than 0.35 lb (Figure 5-19) and that a short catalyst bed (low ammonia dissociation) would not cause a severe penalty in fuel weight. The

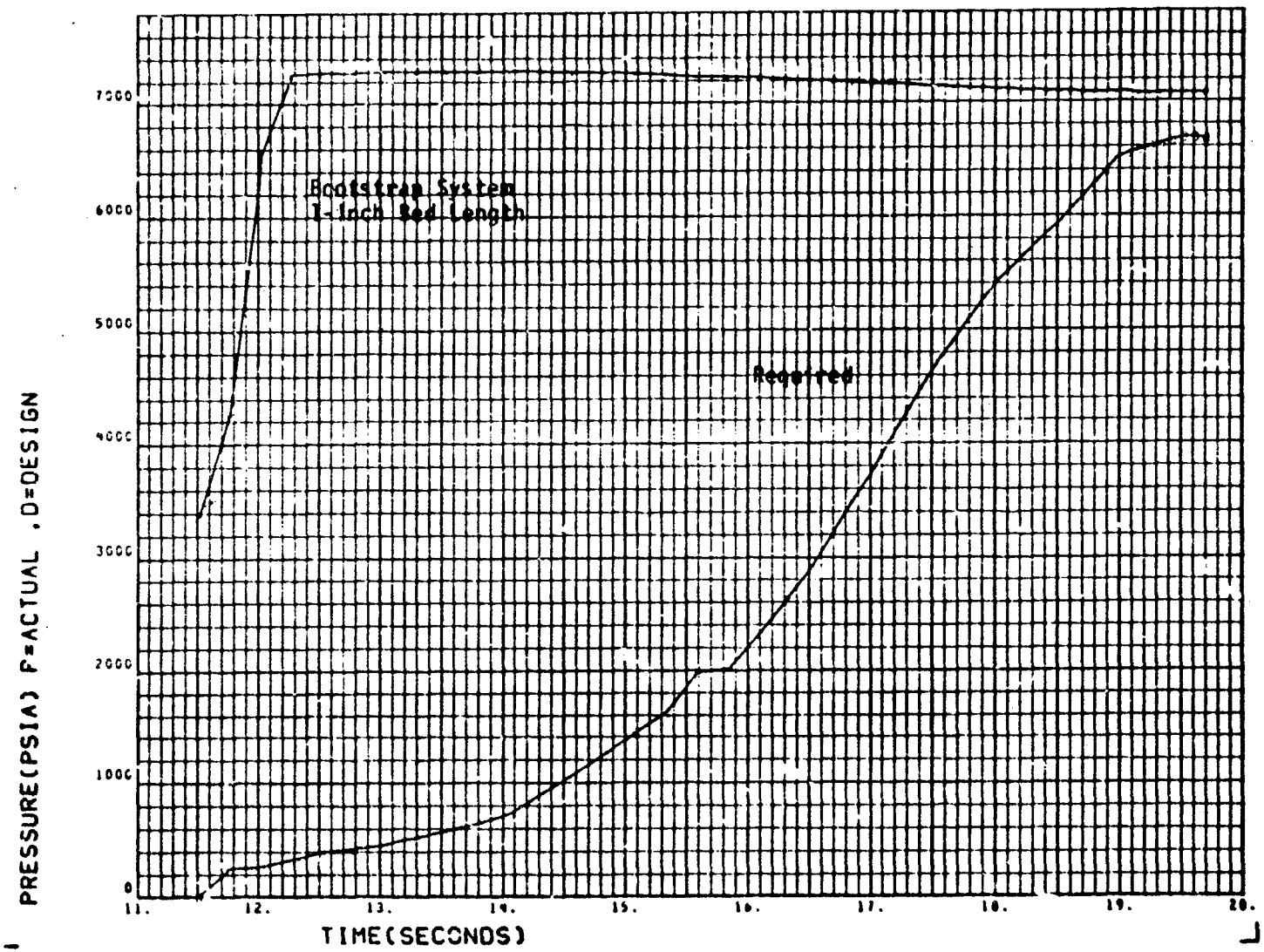


Figure 5-17. Required and Delivered Pressure, S-3 Trajectory

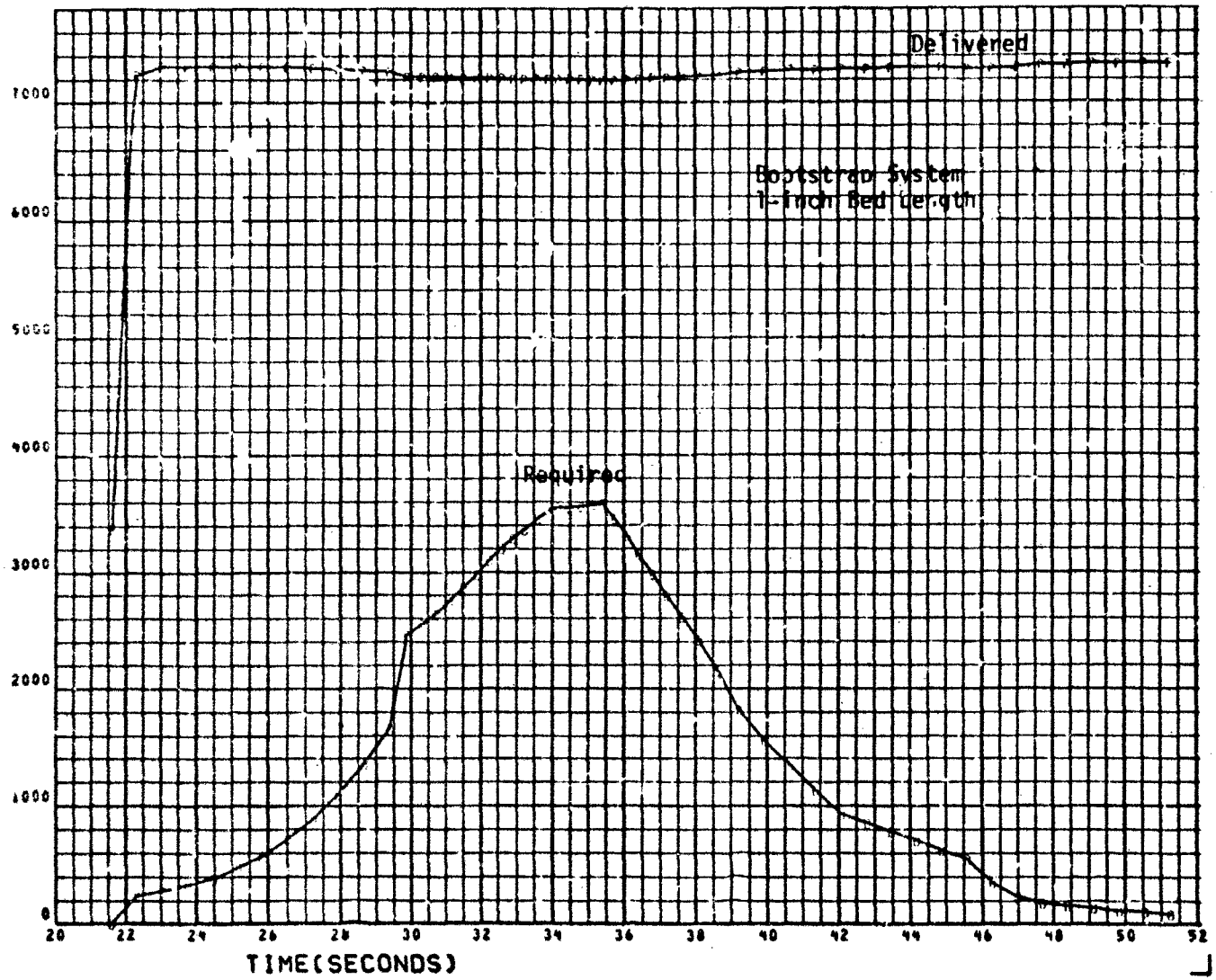


Figure 5-18. Required and Delivered Pressure, L-6 Trajectory

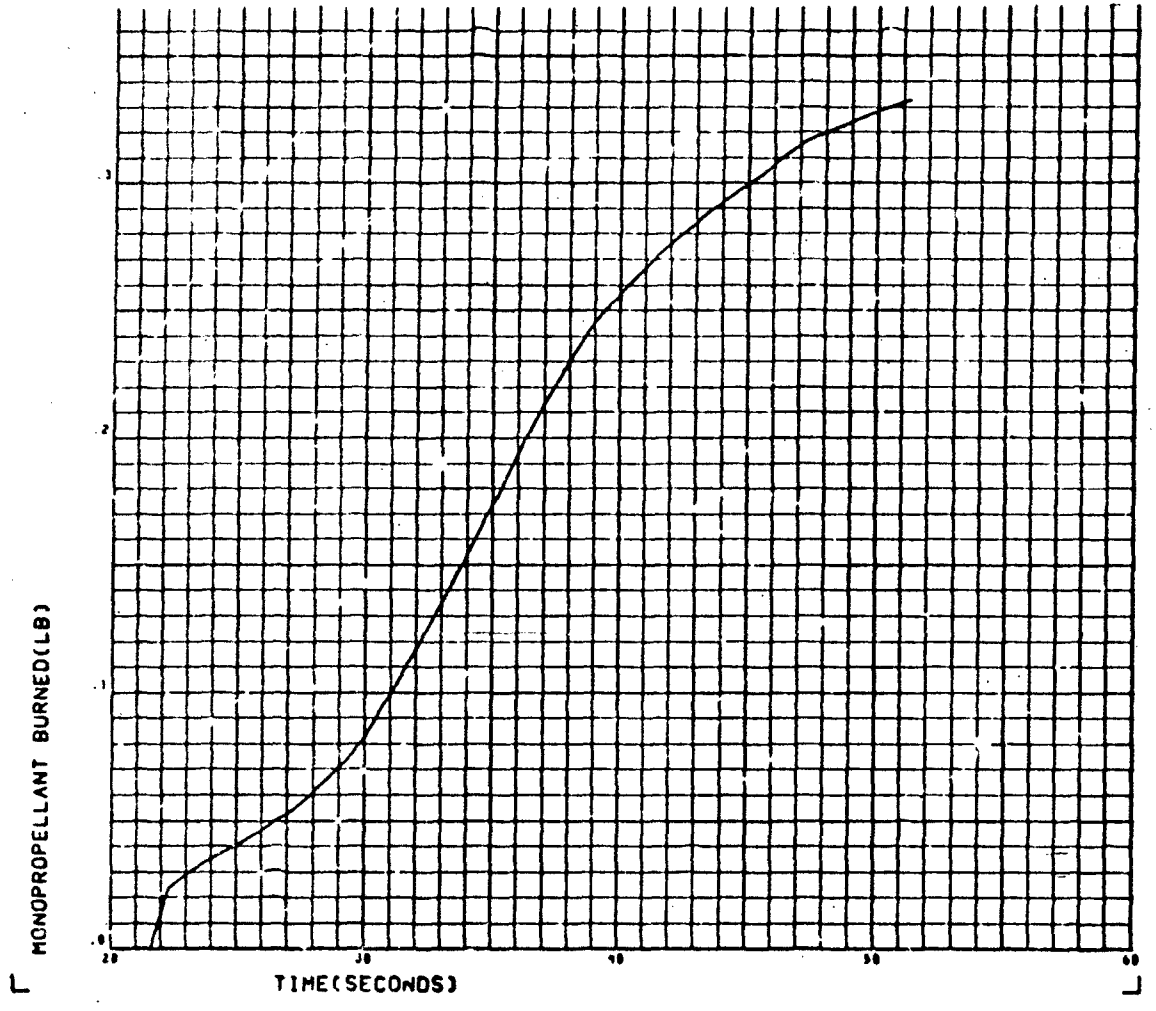


Figure 5-19. Monopropellant Burned, L-6 Trajectory

Table 5-4

CONSIDERATIONS FOR MONOPROPELLANT STUDIES

Design concepts	Blowdown Bootstrap
Sizing	Fuel weight (0.5 lb) Catalyst bed length (1 to 2 in.) Free volume (5.0 $in.^3$) Flow rate (0.05 lb/sec maximum) Igniter (0.005 lb, bootstrap only) Gas volume (12 $in.^3$, blowdown only)
Operating characteristics	Pressure Percent ammonia dissociated Gas temperature Bladder temperature Coolant temperature Fuel usage Tank pressure (blowdown only)

bootstrap system would require slightly more fuel than the blowdown system because of the increase in free volume as fuel is used, but the bootstrap system would have other design advantages, as will be discussed later.

In the interest of minimizing volume requirements, further calculations were made to determine the effect of catalyst bed length for the five trajectories of interest. The gas temperatures resulting from these variations did not appear to have a large effect on the temperature of the bladder and coolant. Therefore, it would be reasonable to make use of a small catalyst bed, on the order of 1 in., thus minimizing hardware volume requirements. The variation in ammonia dissociation for a 1-in. catalyst bed is shown in Figure 5-20 for the L-6 trajectory.

Total volume requirements of a monopropellant pressurization system would be slightly in excess of 40 $in.^3$. While this is somewhat more than that required for a solid-propellant system, there are some packaging advantages for the monopropellant. As shown in Figure 5-21, it would be possible to locate the entire monopropellant system in a small tube down the center core of the bladder, so that full advantage is taken of the space available. Further comparisons of these systems are presented in Section 8.2, and the rationale for selection of a baseline pressurization system design is given.

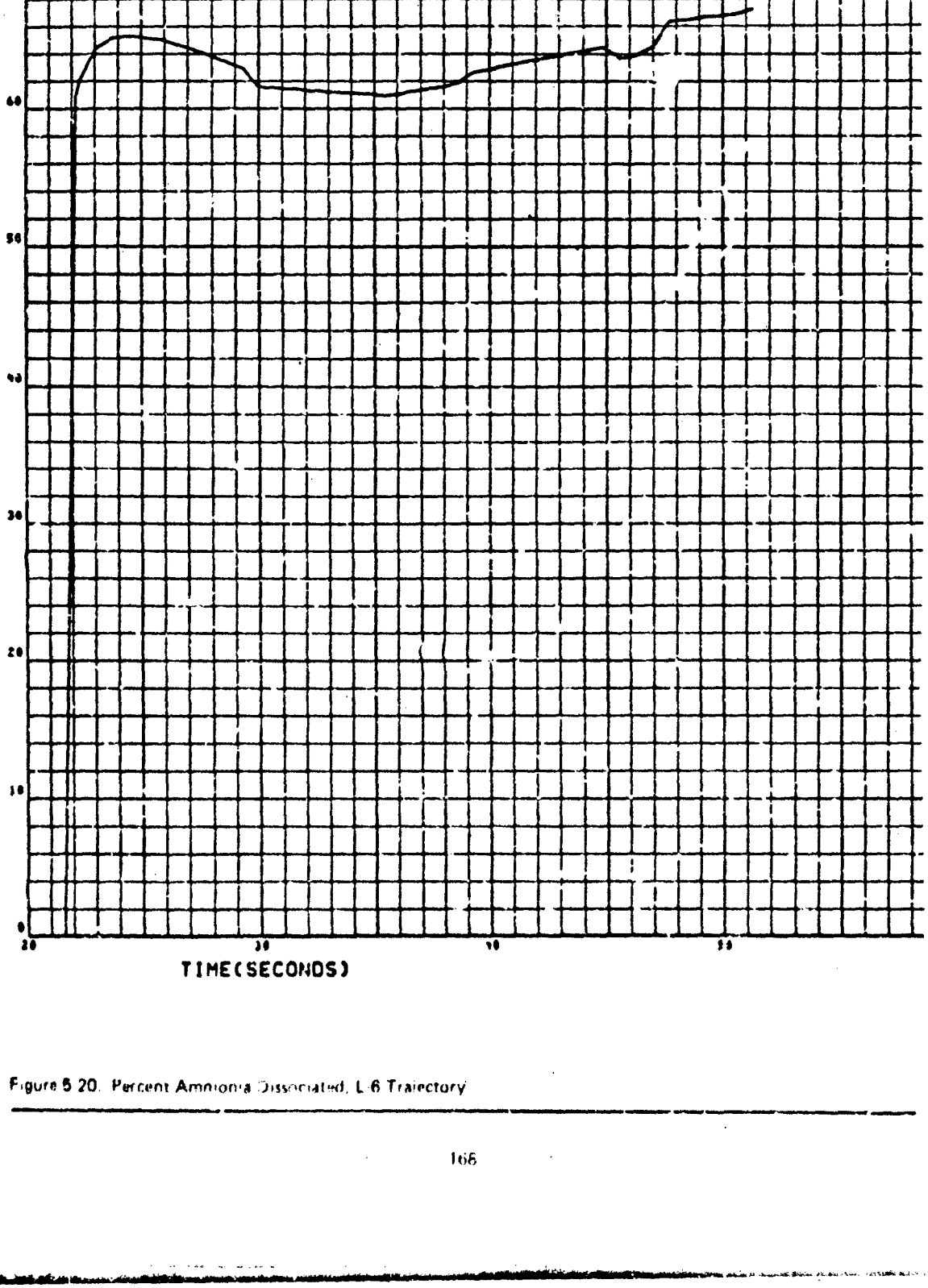
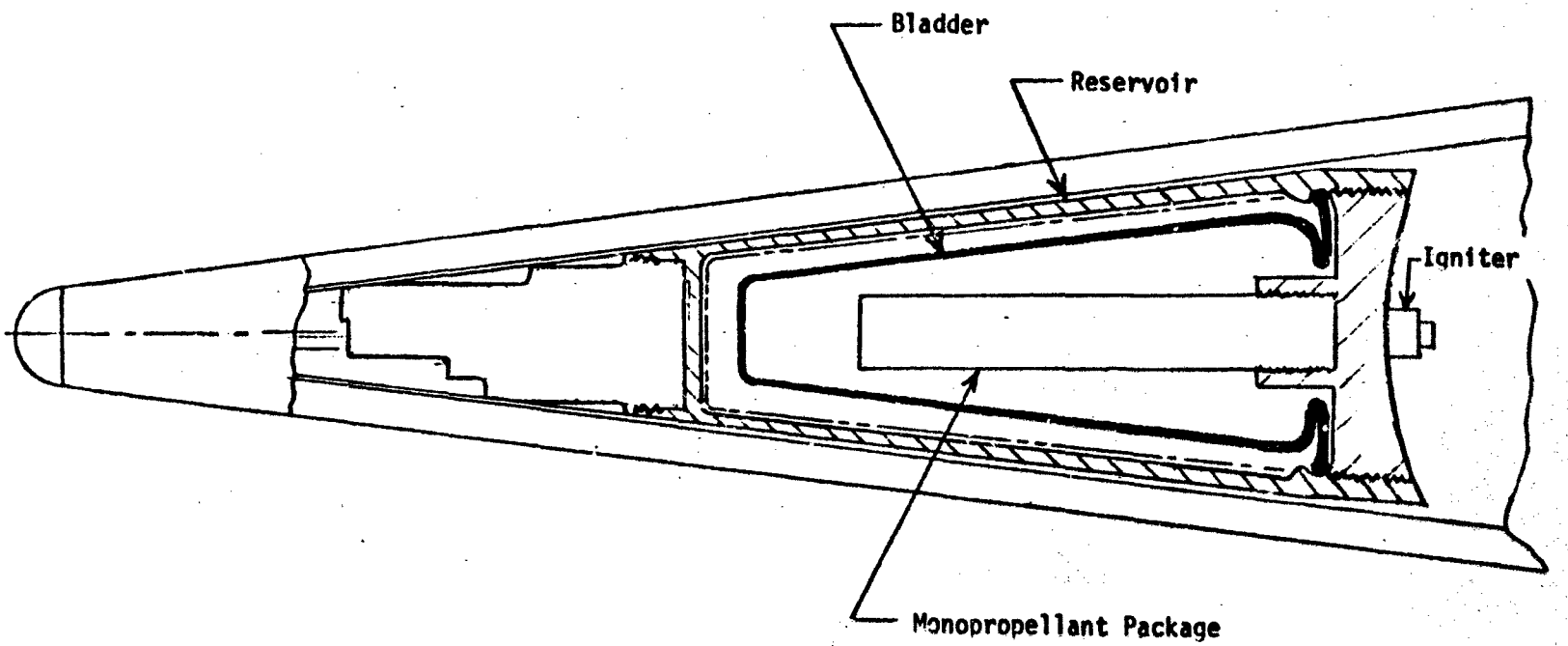


Figure 5 20. Percent Ammonia Dissociated, L-6 Trajectory



169

Figure 5-2: Monopropellant Concept

5.2.3 Compatibility With Expulsion Concepts

Pressurization with combustion gases results in some side effects that are not present with cold-gas pressurization. The bladder material is exposed to relatively high gas temperatures, and the surface of the bladder approaches thermal equilibrium with the gas during the period of operation. Most of the current study was accomplished using elastomeric bladders, which may experience thermal degradation when exposed to a moderate thermal environment. Metallic bladders would have to be insulated, so a similar problem would exist. A maximum operating temperature cannot be estimated with much confidence because final material selection has not been accomplished. The materials being considered may be rubberized composites of some fabrics which can withstand very high temperatures, and other fabrics that melt or char at a few hundred degrees. Only bladder testing with warm-gas pressurization will establish the actual response of the material to this environment.

Thermal analysis of the bladder has been made for all trajectories, different bladder designs, materials, material thicknesses, and pressurization concepts, assuming no thermal degradation. Surface temperatures, presented in Figure 5-22, fluctuate widely, reflecting the dependence of heat transfer coefficients on pressure, axial and lateral g's, and temperatures of the gas and surface. At temperatures below 705°F, heat transfer is complicated by condensation of water vapor from the exhaust gases. Bladder surface temperature directly reflects the temperature of the gases in the bladder, and gas temperature is highest on the S-3 trajectory because all the propellant is burned in the shortest time. Since this was the most critical trajectory, a summary of bladder surface temperatures during this mission for several bladder designs is presented in Figure 5-23. Relatively little difference in bladder surface temperature results from either change in bladder thickness or design as long as the pressurizing gas and bladder material are not changed.

Another potential problem area created by warm-gas pressurization is an increase in the temperature of the coolant. This may cause the amount of required coolant to increase. Since an elastomeric bladder serves as an insulator, this is one of the major reasons why this type of design is attractive for a transpiration-cooled nosetip.

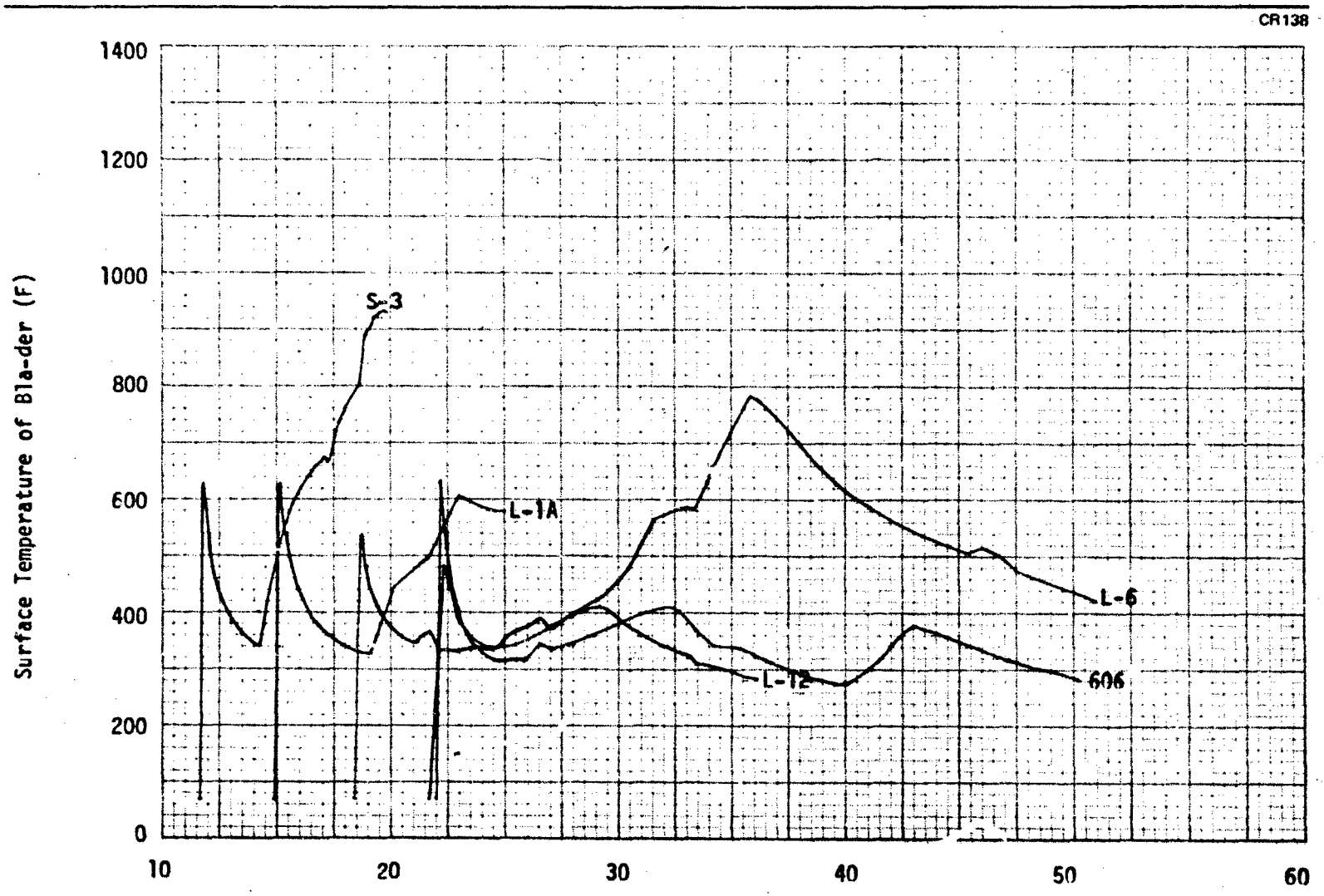


Figure 5-22. Average Surface Temperature of the Bladder

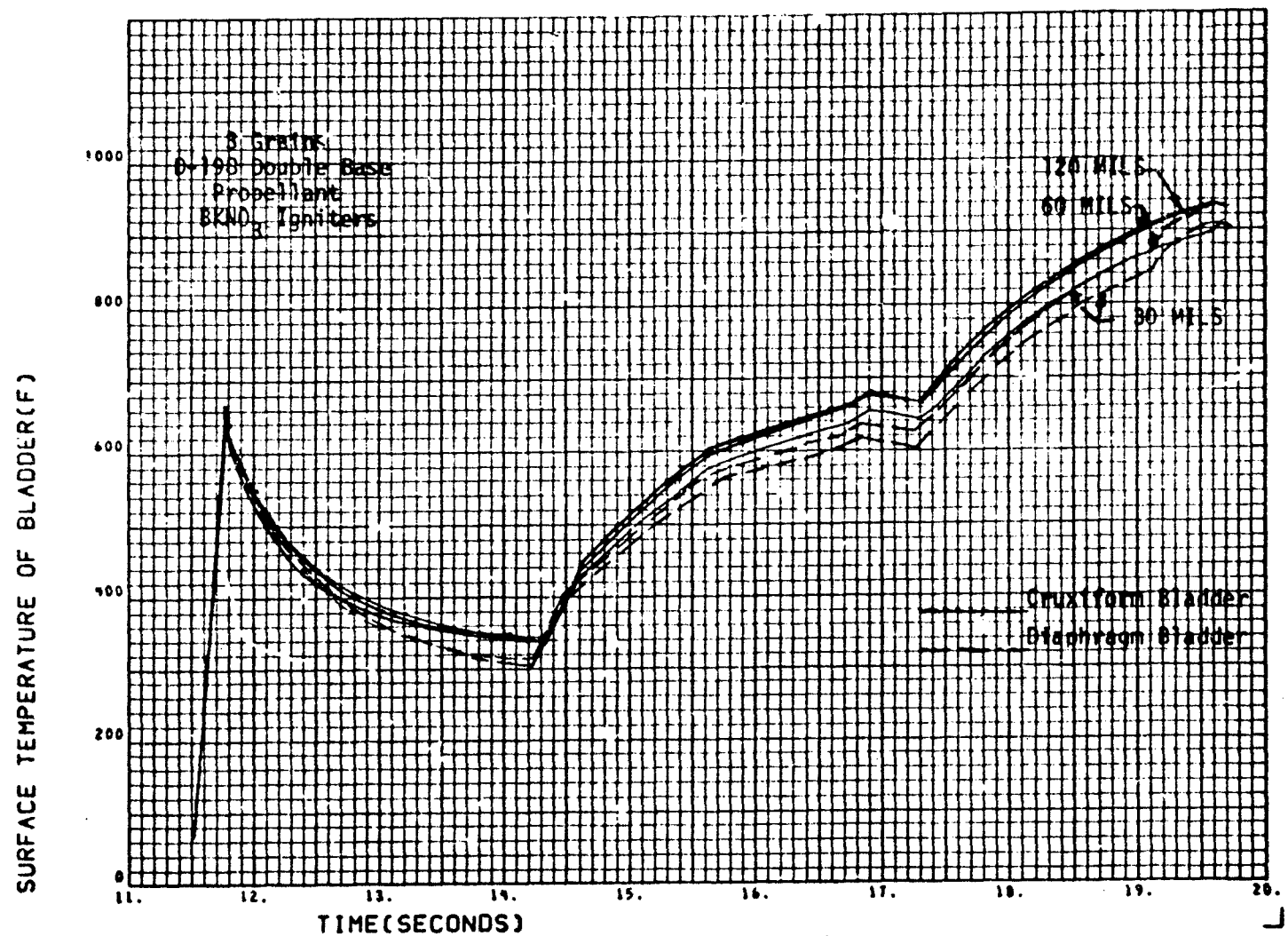


Figure 5-23. Average Surface Temperature of the Bladder, S-3 Trajectory

The elastomeric bladder behaves as a heat sink with a very substantial temperature drop across it. Figure 5-24 shows the temperature distribution through the bladder at numerous times for the L-6 mission. The temperature of the bladder at the gas surface (on the left side of this figure) fluctuates widely according to variations in heat transfer, but the variation is filtered out and the thermal input to the coolant is quite uniform. The influences of material thickness and bladder design and shown in Figure 5-25 for the L-6 trajectory and are summarized in Table 5-5. Figure 5-26 illustrates the coolant temperature histories for all trajectories using the baseline bladder design.

As may be seen from Table 5-5, a major change in design has less effect than a change in thickness. Other factors, such as flexibility and expulsion efficiency, also influence the selection of bladder thickness.

Table 5-5
VARIATION IN COOLANT TEMPERATURE (L-6 TRAJECTORY)

Bladder Type	Surface Area ($in.^2$)	Thickness (in.)	Change in Temperature of Coolant (°F)
Cruciform	130	0.12	6.8
Diaphragm	50	0.06	21.8
Cruciform	130	0.06 (baseline)	25.8
Diaphragm	50	0.03	34.8
Cruciform	130	0.03	34.5

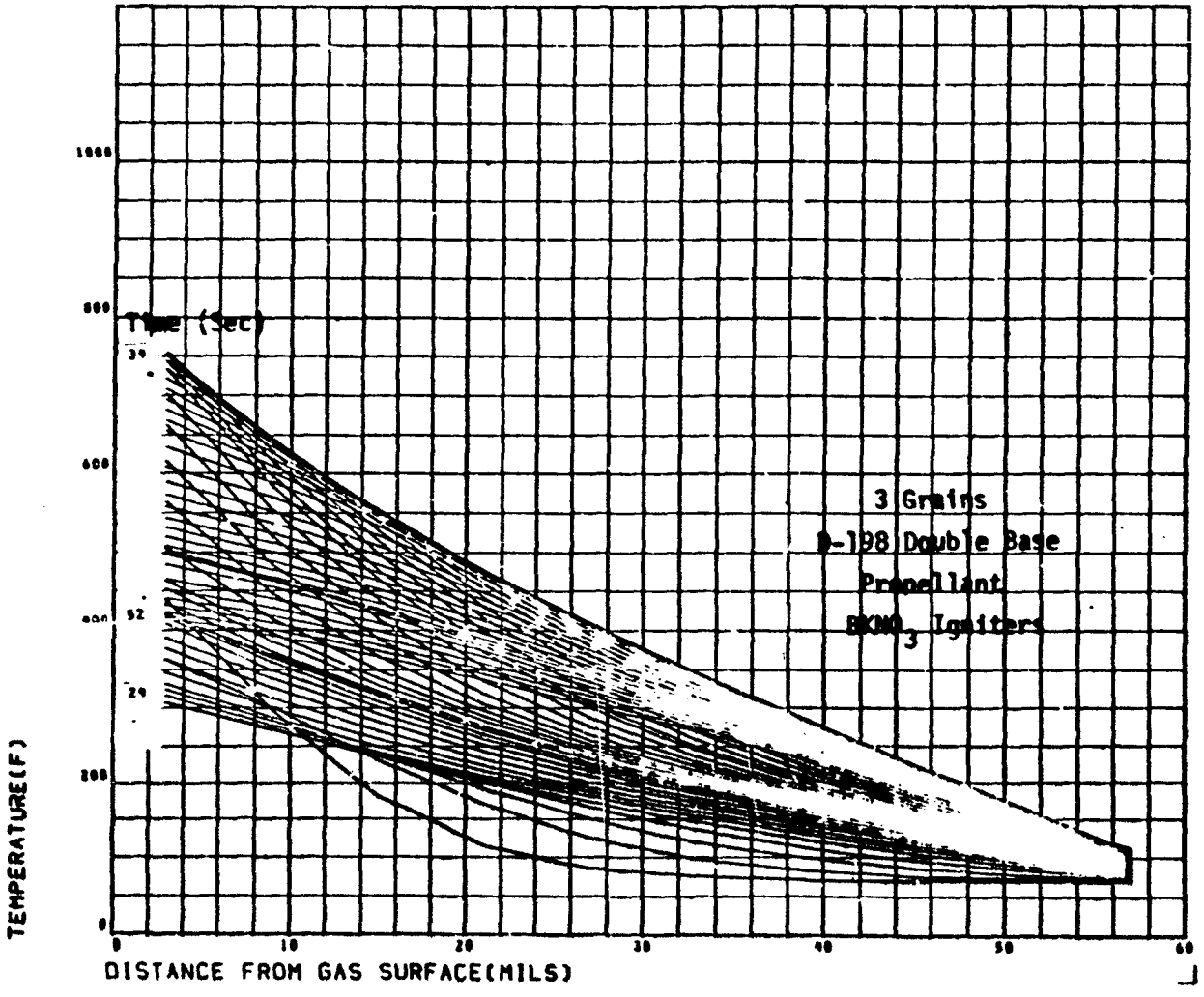


Figure 5-24. Temperature Distribution Through the Bladder, L-6 Trajectory

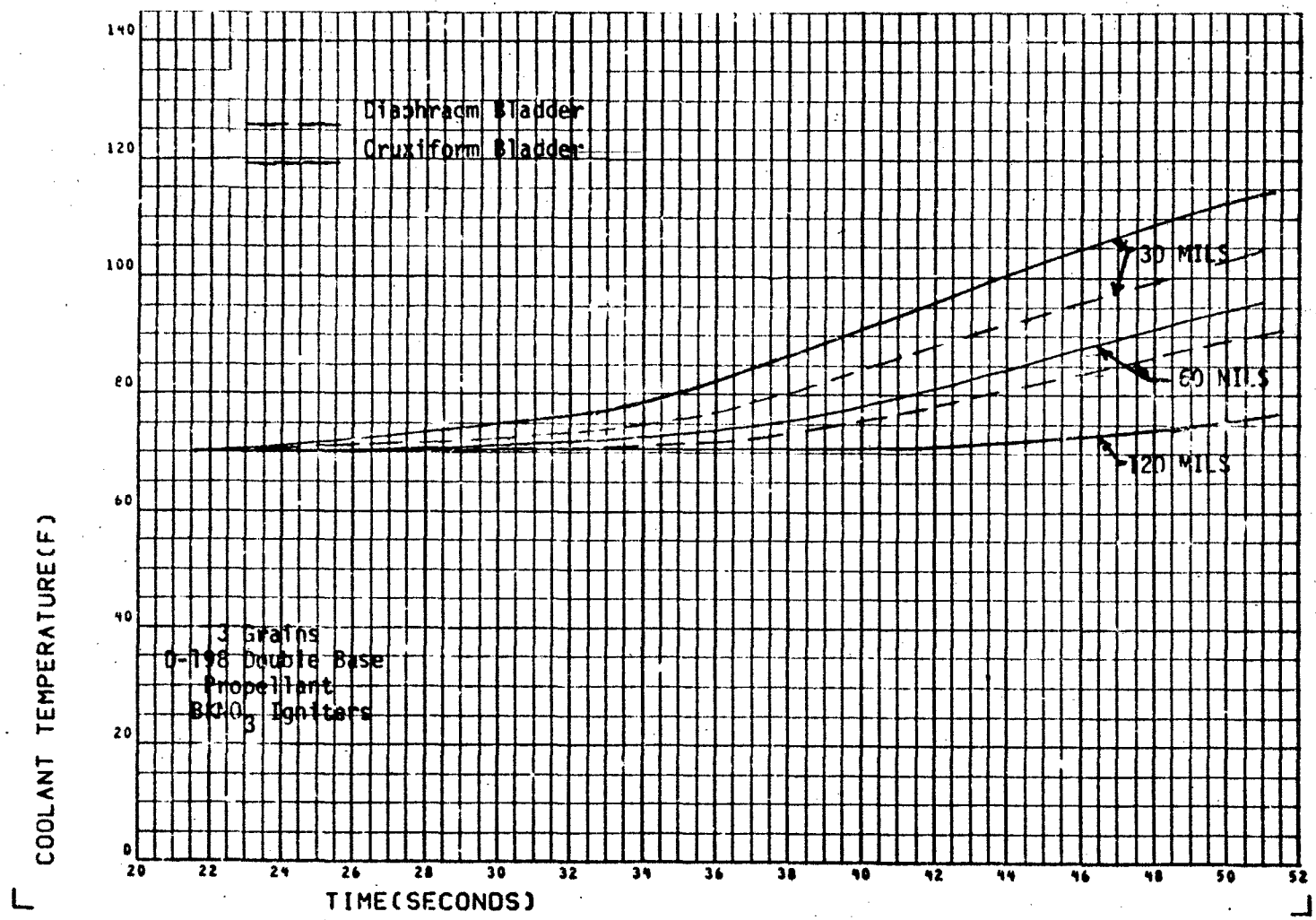


Figure 5-25. Temperature of Well-Mixed Coolant, L-6 Trajectory

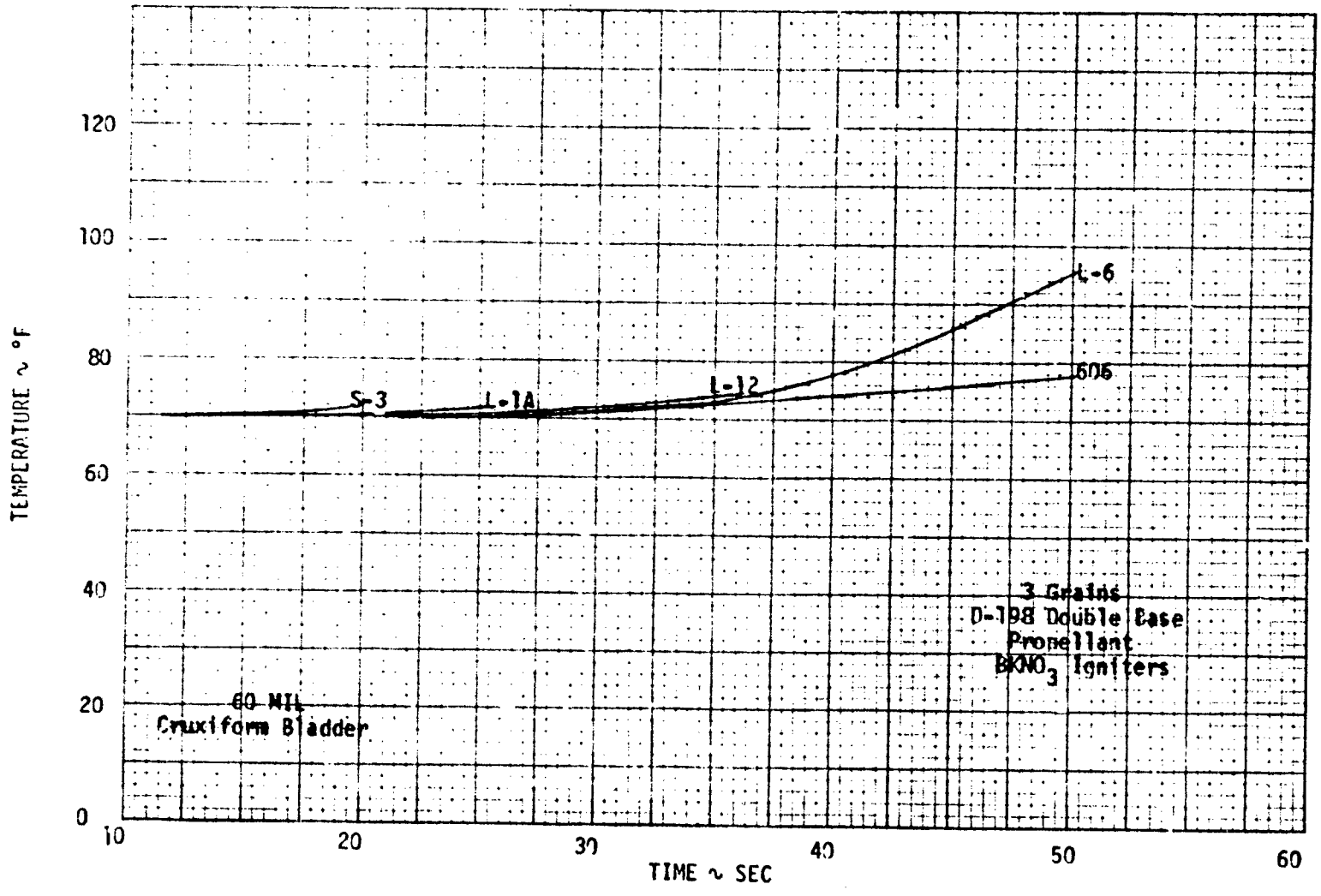


Figure 5-26. Temperature of Well-Mixed Coolant

Section 6
INITIATION CONCEPTS

The choice of the TCNT initiation system depends upon the type of reentry vehicle (RV) autopilot, since a large portion of the initiation system will be an integral part of the vehicle control system. The remaining part of the initiation system is the squib fire mechanism located on the gas generator. Reference 3-1 discusses two types of autopilots. Type A is an open-loop device, and Type B is a full-navigational, closed-loop feedback computer system. This section discusses initiation mechanisms which will be used with each type. The sequence of events required for initiation is shown in Figure 6-1.

An electronic clock with an accuracy of about ± 0.3 percent is started at separation in the Type A system. At approximately 170,000 ft, the clock triggers a circuit which activates a threshold detector. The clock accuracy can predict altitude to within ± 10,000 ft, and the threshold detector activation time will not be updated by the booster.

Accelerometers transmit signals to the threshold detector. When the limit specified by this detector is exceeded, a second timer is started. This timer is used to send the initiation signal to the gas generator and is connected to the same circuits which start despin and activate the control system. The gas generator squibs are fired through relays, which prevents premature initiation caused by extraneous EMF.

Root-mean-square error calculations for the Type A system components indicate a maximum altitude of 157,000 ft at which flow would occur at the nosetip. This error demands that 0.07 lb of excess coolant is required to cover the descent from 157,000 ft to 140,000 ft. The coolant required to fill the nosetip and wand is included in the above number.

•TYPE A RV AUTOPILOT (OPEN LOOP) INITIATION SYSTEM	TYPE B RV AUTOPILOT (FULL NAVIGATION) INITIATION SYSTEM
TOLERANCES o Clock ±.5% o Threshold Detector ± 2MSEC o Accelerometer(s) ± 2MSEC o Timer ± .5% o Fire Circuit ± 2MSEC o Wand and Tip Fill ± .36 SEC	TOLERANCES o Digital Computer Clock < ± .1 SEC o Fire Circuit ± 2MSEC o Wand and Tip Fill ± .36 SEC
EXCESS COOLANT REQUIRED = .07 LBS Separation, Clock Started Threshold Detector Activated Timer initiated on g's 17KFT Squib Fire 140KFT Flow Out Tip ALTITUDE TIME	EXCESS COOLANT REQUIRED = .04 LBS Prelaunch Clock Calibrated for Specific Trajectory Separation, Digital Computer clock started 7KFT Squib Fire 140KFT Flow Out Tip ALTITUDE TIME

Figure 6-1. Initiation System Concepts

More accuracy can be obtained from the Type A system if an additional threshold detector specifically for the initiation system is included in the autopilot. The second timer could then be eliminated. The threshold detector would maintain the same accuracy (± 0.026 g) but would switch at a higher g level. The increase in precision does not appear to justify the added components and circuitry at this time.

If an appreciable angle of attack is expected while the threshold detector is operating, three-axis accelerometer inputs may be required. This would decrease the accuracy of the initiation system and result in a small increase in coolant.

The Type B autopilot will have a very accurate digital clock. The initiation squib will be fired at a specified time interval after separation from the booster. This time interval is input to the RV computer before launch, along with trajectory information. The booster computer will update this information and correct for altitude errors prior to separation.

The clock will have an error of less than 0.1 sec. This translates to a maximum altitude for flow out the nosetip of 147,000 ft. The additional coolant required for initiation errors, nosetip fill, and wand fill is 0.04 lb. For both vehicle control systems, an additional amount of coolant is required to cover the altitude range between 140,000 ft, where initiation is desired, to 125,000 ft, the altitude at which the environmental calculations were initiated. A coolant quantity of 0.1 lb is needed to satisfy this constraint. If, during the development phase, initiation can be allowed to occur at a lower altitude, the excess coolant required by the high-altitude initiation can be reduced.

Section 7

SYSTEM DESIGN CONSIDERATIONS

The baseline design and the constraints imposed on this design due to structural, environmental, manufacturing, and vehicular requirements and reliability considerations are discussed in the following sections.

7.1 PACKAGING

7.1.1 Layout

The layout shown in Figure 7-1 describes the complete baseline system. The system consists of a solid-grain gas generator for pressurization, a conical-shaped reservoir, a nonmetallic bladder, a flow control valve, a porous nose-tip, a wand, and associated attachments. Included also are the heat shield, radiation shielding, and substructure. Forward of the valve and attached to the primary structure are the impact sensors. Wire bundles from the impact sensors and valve pressure switch are routed aft between the reservoir and radiation shield. The gas generator is located aft of the coolant reservoir. The nosetip and wand assembly are welded together and slipped into the supporting structure. An alternate method of incorporating an all-beryllium nosetip and wand assembly is shown in View A of Figure 7-1. In this design, the wand-nosetip assembly is spring-loaded so that the nosetip fits snugly against the heat shield, locking it in place. The nosetip and wand assembly are allowed to float if required due to thermal expansion of the heat shield.

7.1.2 Materials

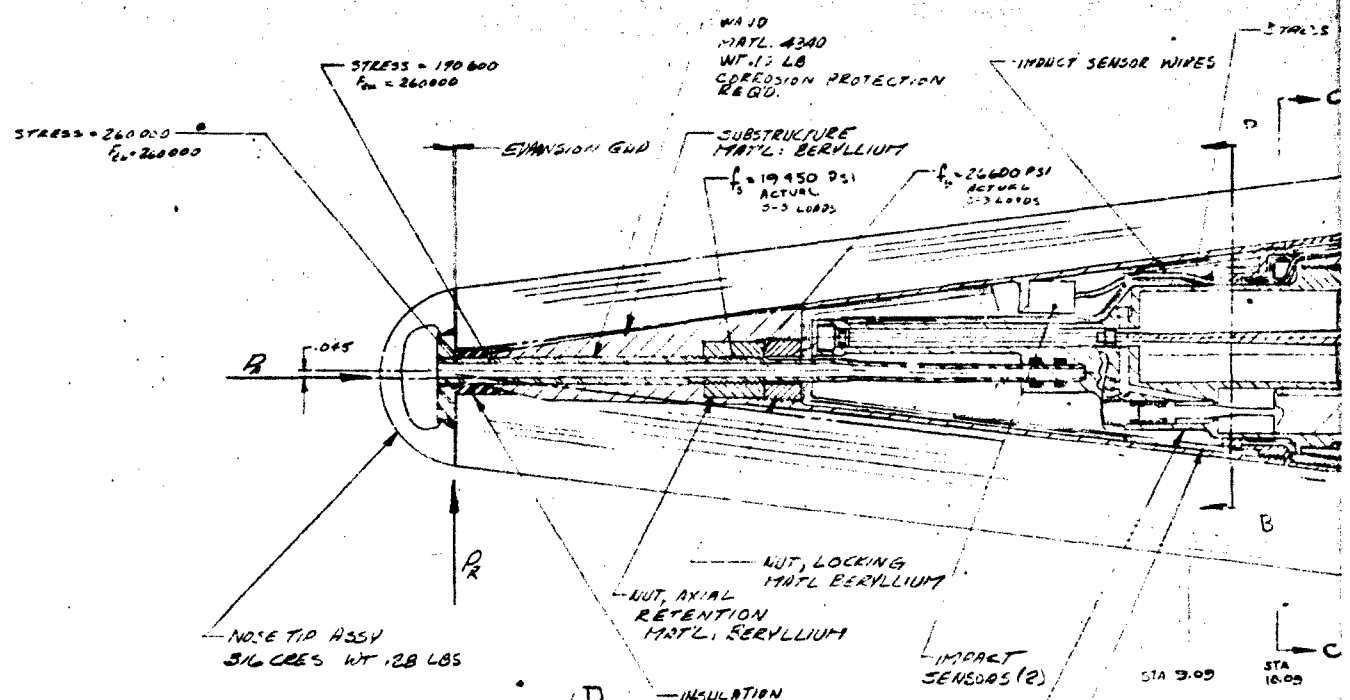
The materials of construction for the system were selected on the basis of strength (to minimize system weight) and compatibility with the coolant to provide for long-term storage. Material for the bladder was selected after a series of tests were performed on various materials using warm gas as the pressurant and water as the expelled liquid. Table 7-1 summarizes the components and materials selected.

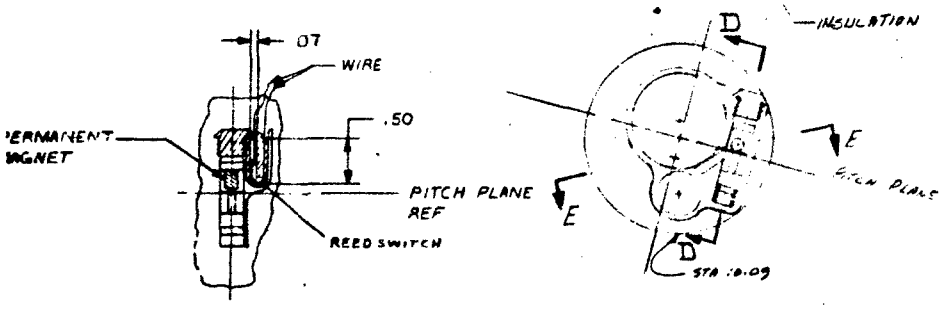
CRITICAL LOAD SUMMARY

TRAJECTORY	TIME	VELOCITY	ALTITUDE	ANGLE OF ATTACK	P_A	P_R	M_A	M_R
L-1(a) (BLAST)	24.5	10255	7384	9.17	2079	418	19.5	15.3
L-6	43.4	5803	11347	15.95	609	139	6.15	4.79
S-3	19.7	15144	0	3	5646	256	12.1	9.5

NOTES:

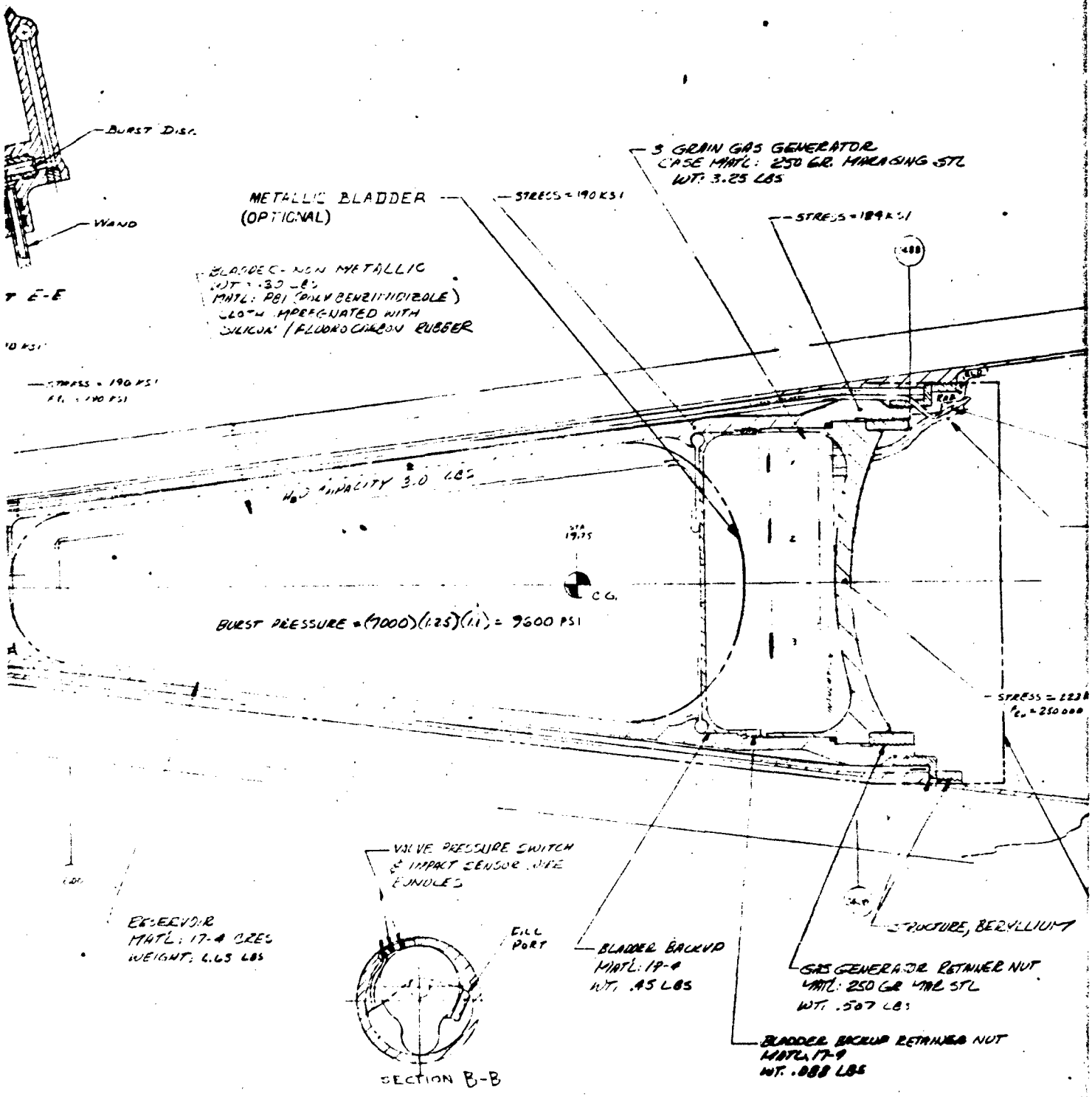
1. FOR STRUCTURAL COMPONENTS - DESIGN LOAD = 1.25 × FLIGHT LOADS
2. FOR PRESSURE COMPONENTS - DESIGN LOAD = 1.25 × OPERATING PRESS. + 1.25 × ACCELERATION LOADS
3. STRESSES INDICATED CALCULATED USING ABOVE DESIGN LOADS
4. SEE SHT 2 VIEW A FOR ALTERATE NOSE TIP ATTACHMENT





VIEW D-D

SECT C-C


BURST DISC.
WAND
T E-E
3 GRAIN GAS GENERATOR
CASE MATL: 250 GR. MARAGING STL
WT: 3.25 LBS
METALLIC BLADDER
(OPTIONAL)
STRESS = 190 KSI
STRESS = 184 KSI
BLADDER - NON METALLIC
WT = .30 LBS
MATL: PBI (POLY BENZIMIDIZOLE)
CLOTH IMPREGNATED WITH
SILICON / FLUOROCARBON RUBBER
STRESS = 190 KSI
H2O CAPACITY 3.0 LBS
STA 19.75
C.G.
BURST PRESSURE = (7000)(1.25)(1.1) = 9600 PSI
STRESS = 223
250 000
VALVE PRESSURE SWITCH
& IMPACT SENSOR WIRE
FUNDLES
RESERVOIR
MATL: 17-4 CRES
WEIGHT: 6.65 LBS
FILL
PORT
BLADDER BACKUP
MATL: 17-4
WT. .45 LBS
STRUCTURE, BERYLLIUM
GAS GENERATOR RETAINER NUT
MATL: 250 GR MAR STL
WT. .507 LBS
BLADDER BACKUP RETAINER NUT
MATL 17-4
WT. .088 LBS
SECTION B-B

CR138

WT SUMMARY

PART	MATL	ρ_{LB/IN^3}	LBS WT	REMARKS
GAS GENERATOR	250 GR MAR	.29	3.25	.85 GRAIN WT
RESERVOIR	17-4 PH	.29	6.65	INCLUDES SEALS
BLADDER BACKUP	17-4 PH	.29	.45	
BLADDER			.30	
GG RETAINER NUT	250 GR MAR	.29	.507	
BLADDER B.U. RET NUT	17-4	.29	.088	
VALVE ASSY	17-4 PH	.29	1.500	TANTALUM WT. INCLUDED
WA'D	4340	.29	.100	
NOSE TIP ASSY	316 CRES	.29	.280	
RADIATION SHIELD			.65	
SUBSTRUCTURE NUTS	Be	.066	.10	

TOTAL WT.

DRY	13.88
H_2O	3.00
WET	16.88

IN GAS GENERATOR
MATL: 250 GR. MARAGING STL
3.25 LBS

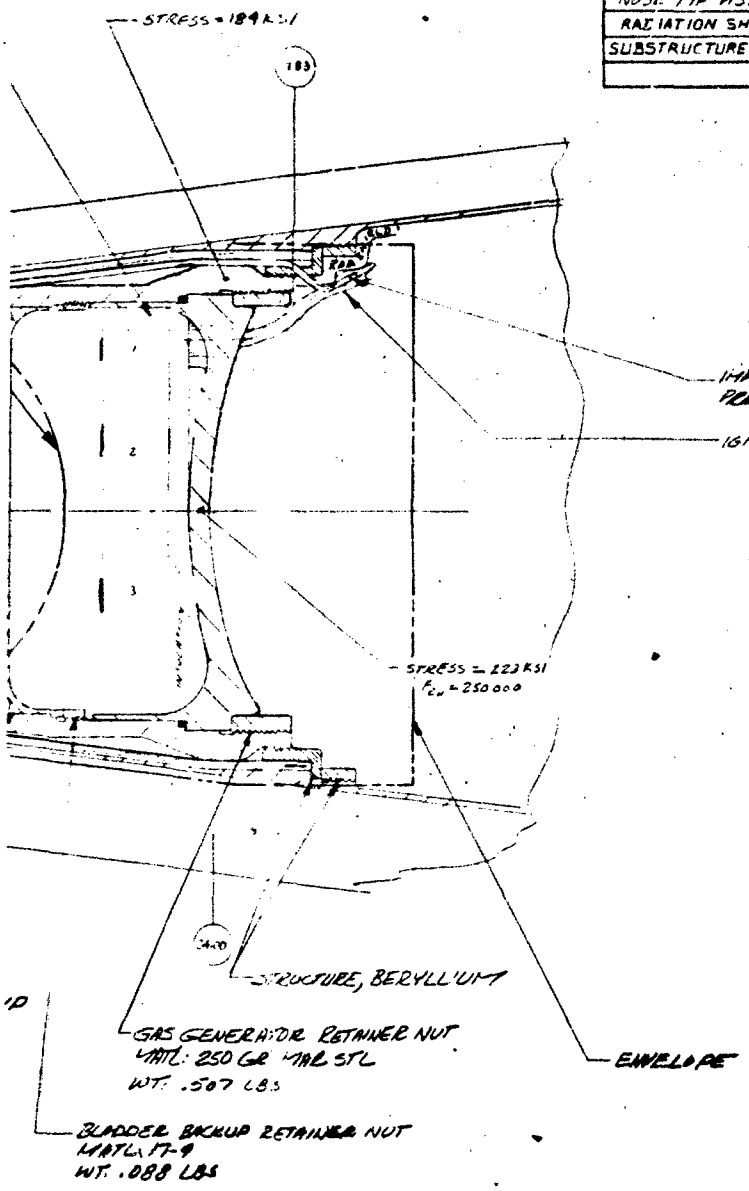


Figure 7-1. Baseline System Layout (Page 1 of 2)

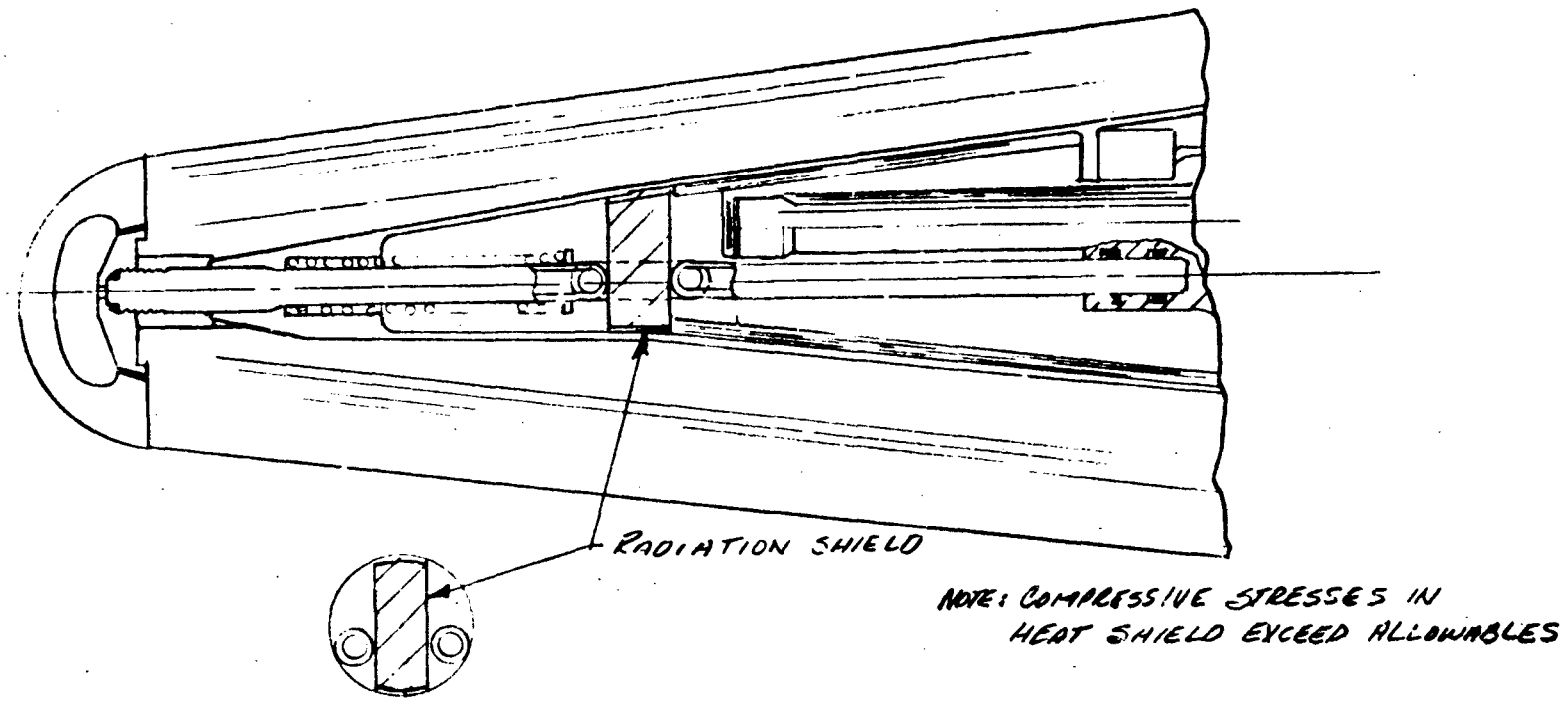


Figure 7-1. (Page 2 of 2)

Table 7-1

MATERIAL SELECTION

Component	Material
Reservoir	17-4 PH
Gas generator case	Maraging 250 GR STL
Gas generator retainer nut	Maraging 250 GR STL
Bladder backup retainer nut	17-4 PH
Bladder backup	17-4 PH
Bladder	PBI cloth, silicon rubber
Valve parts	17-4 PH
Wand	17-4 PH (Be)
Nosetip	316 (Be)
Wand adjustment nut	17-4 PH
Wand locking nut	17-4 PH
O-ring	Silicon

7.1.3 Assembly

Referring to Figure 7-1, assembly of the system is accomplished as follows:

A. The control valve is assembled as a separate component. The burst disc is not included at this time.

B. The control valve is assembled onto the reservoir by means of the threaded attachment, with the O-ring and backup ring in place. Orientation of the valve with respect to the reservoir is not required, since an annulus is provided in the reservoir forward wall to direct coolant flow to the valve inlet passages.

C. A plate is installed in place of the gas generator to facilitate proof pressure testing. The entire system is pressurized to 7,700 psi.

D. The burst disc is intalled in the valve and proofed to 500 psi to leak-check the burst disc.

E. The bladder is installed into the reservoir with the bladder backup and bladder backup retainer nut securing it in place. The water side of the bladder is pressurized to 15 psig with helium and leak-checked with a mass spectrometer.

F. All air is evacuated from the system, and coolant is introduced. The evacuation is required to remove air from the coolant. After the reservoir and valve are filled, the fill port is closed and the vacuum on the gas side is relieved.

G. A sterilization cycle is then accomplished by heating the entire assembly to 250 ± 10 °F for 2 hr. After cooling, a final leak check is performed.

H. At this point it is assumed that assembly of the substructure, heat shield, and impact sensor is complete. The nosetip-wand assembly is pushed through the hole in the insulation and substructure. The wand axial adjustment nut is threaded onto the wand and against the substructure shoulder. Adjustment is made by positioning the adjustment nut to provide the required gap between the nosetip and heat shield. The wand locking nut is then installed to secure the wand and nosetip assembly into its adjusted position.

I. The gas generator can be installed at this time or at any time after the reservoir and valve assembly is installed into the vehicle. Mating of the gas generator to the reservoir is accomplished by inserting the gas generator with the metal seal in place into the aft end of the reservoir. The gas generator is retained in position by the gas generator retaining nut. Prior to torquing the nut, the gas generator can be positioned to provide the proper orientation of the igniter lead wire bundles.

J. The axial retention nut is screwed onto the threaded outside diameter of the reservoir. The valve, reservoir, and gas generator subassembly are inserted into the substructure cavity. The subassembly is supported radially by the substructure at the valve. The coolant exit cavity is slightly bell-mouthed to compensate for misalignment of the wand. The subassembly is pushed forward until the axial retention nut bottoms against the substructure shoulder. The axial locknut is then installed to retain the subassembly in position.

7.1.4 Comparison With Contract Envelope

The completed assembly fits well within the contract envelope. Part of the conical section of the envelope is used for heat shielding on the windward side. Lengthwise, the assembly is shorter than the contract envelope by 1.35 in., when measured from the aft end of the envelope to the threaded aft end of the reservoir. The envelope is shown relative to the assembly in Figure 7-1.

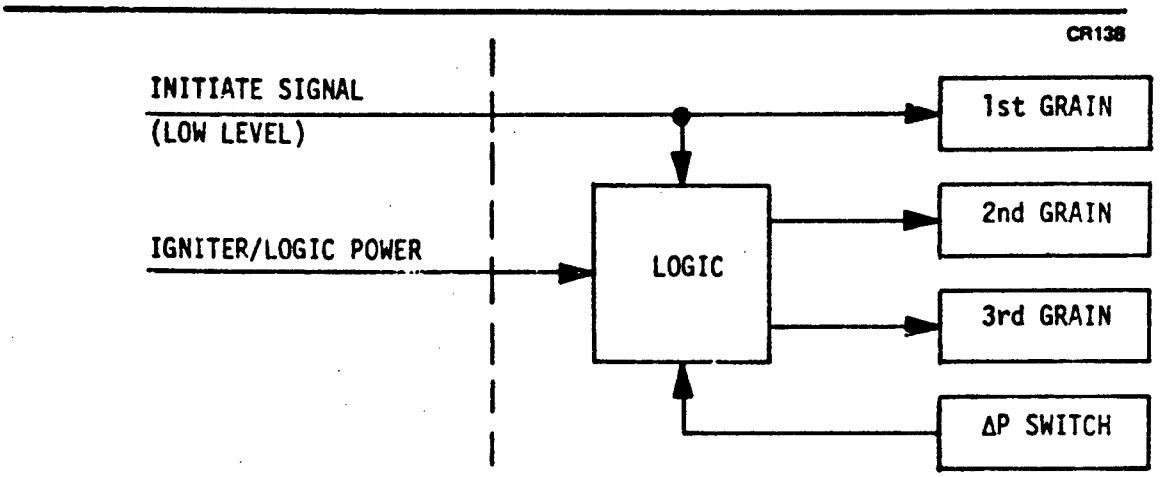
7.1.5 Interface Requirements

Interface requirements with the rest of the vehicle have been defined for the baseline (Mark II) flow control concept and the additional demands created by two optional concepts. These requirements are shown schematically in Figure 7-2. For the Mark II valve, only the initiation signal (see Section 6) and the power for the gas generator ignition circuit are required (Figure 7-2(a)). Figure 7-2(b) illustrates the additional power requirements for a nosetip response sensor flow control technique. This power is required to operate the computer and the electromechanical valve. Requirements for the free-stream parameter concept over and above those needed for the baseline system are shown in Figure 7-2(c). The type of vehicle control system will dictate whether the autopilot or a computer is required to generate the free-stream parameters.

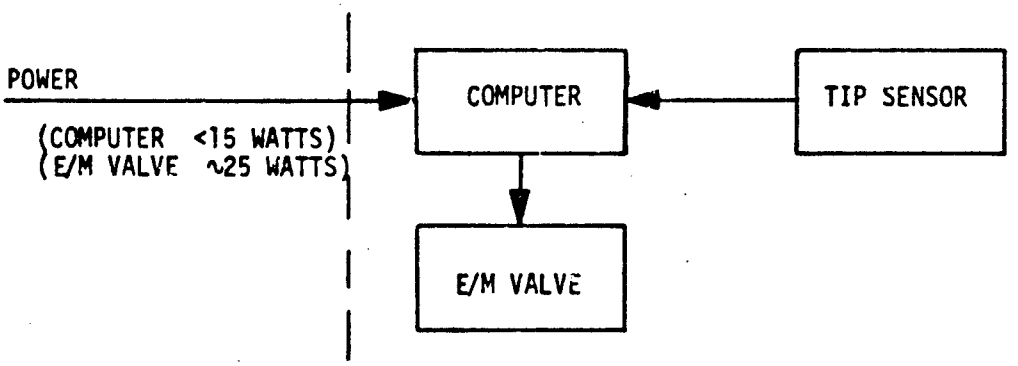
7.2 STRUCTURAL EVALUATION

7.2.1 Critical Load Definition

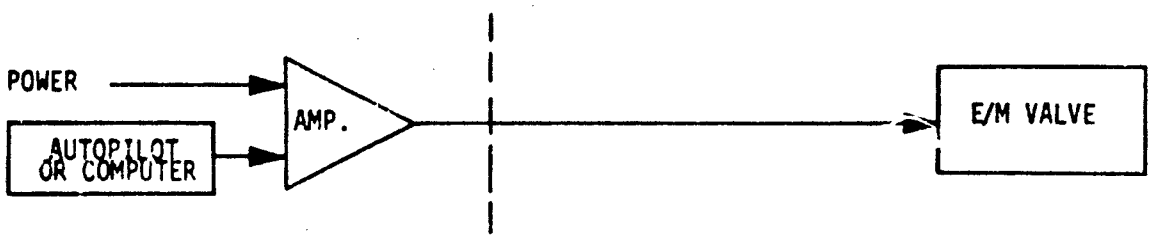
Pressure loads on the nosetip, consisting of both axial and radial forces and moments, were computed by integrating the supplied local pressure distributions over the nosetip. Figures 7-3 to 7-8 give the axial force and moment histories for each of the trajectories, including the L-1(a) modified to include passage through a nuclear fireball. Blast loads were computed by increasing the pressure loads by the same ratio as the stagnation pressure was increased. This results in a conservative loading condition. Figure 7-9 contains a summary of the critical loads for the three worst cases. Figures 7-10 through 7-12 show the nosetip pressure distributions for the points tabulated in Figure 7-9. Figures 7-13 through 7-15 give the heat shield temperature



(a) BASELINE SYSTEM



(b) ADDITIONAL FOR SENSOR



(c) ADDITIONAL FOR FREE STREAM SYSTEM

Figure 7-2. System Interface

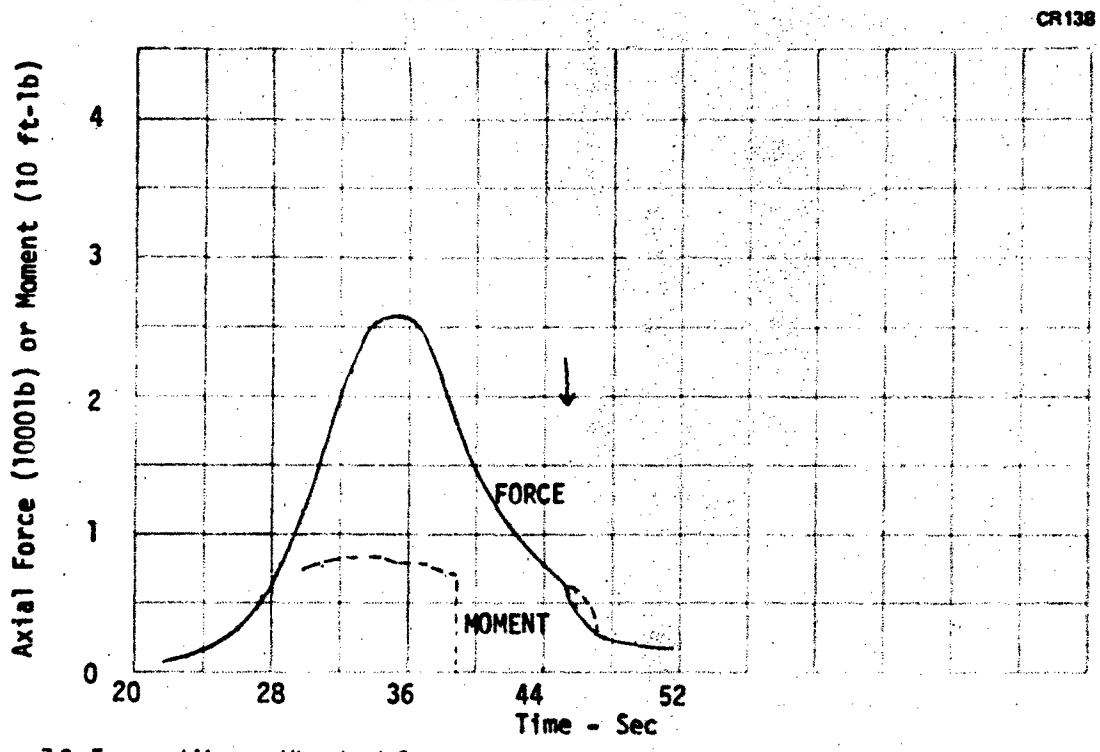


Figure 7-3. Force and Moment Histories, L-6

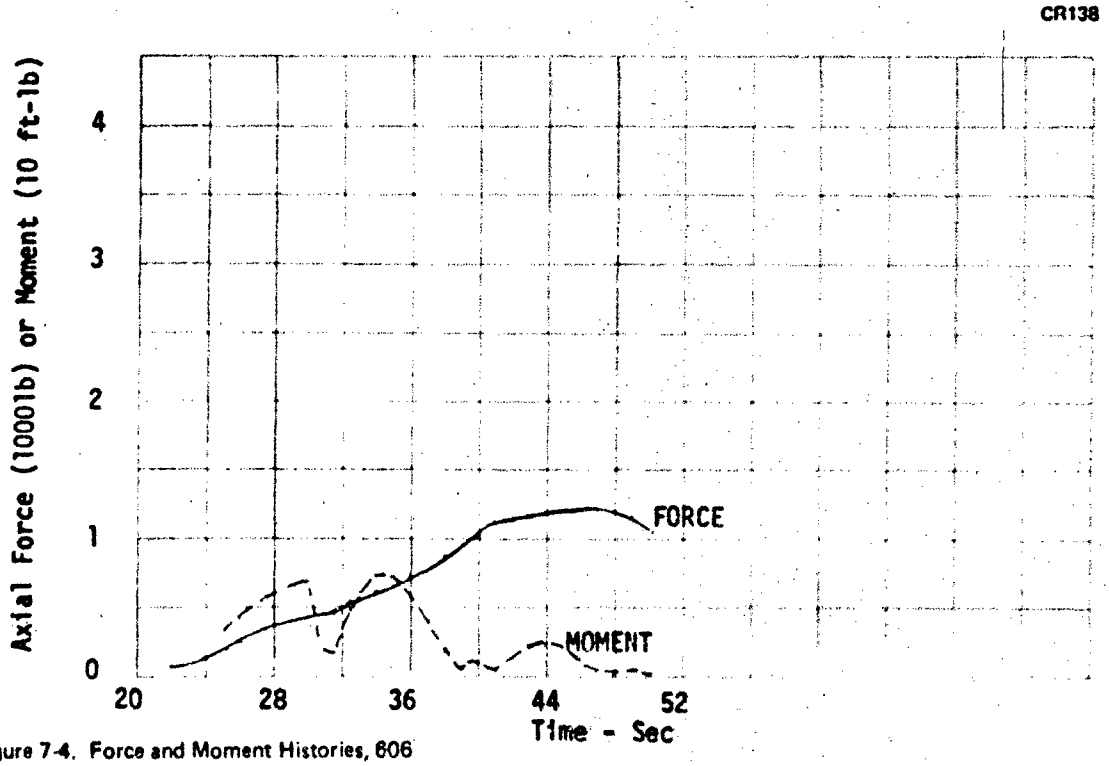


Figure 7-4. Force and Moment Histories, 606

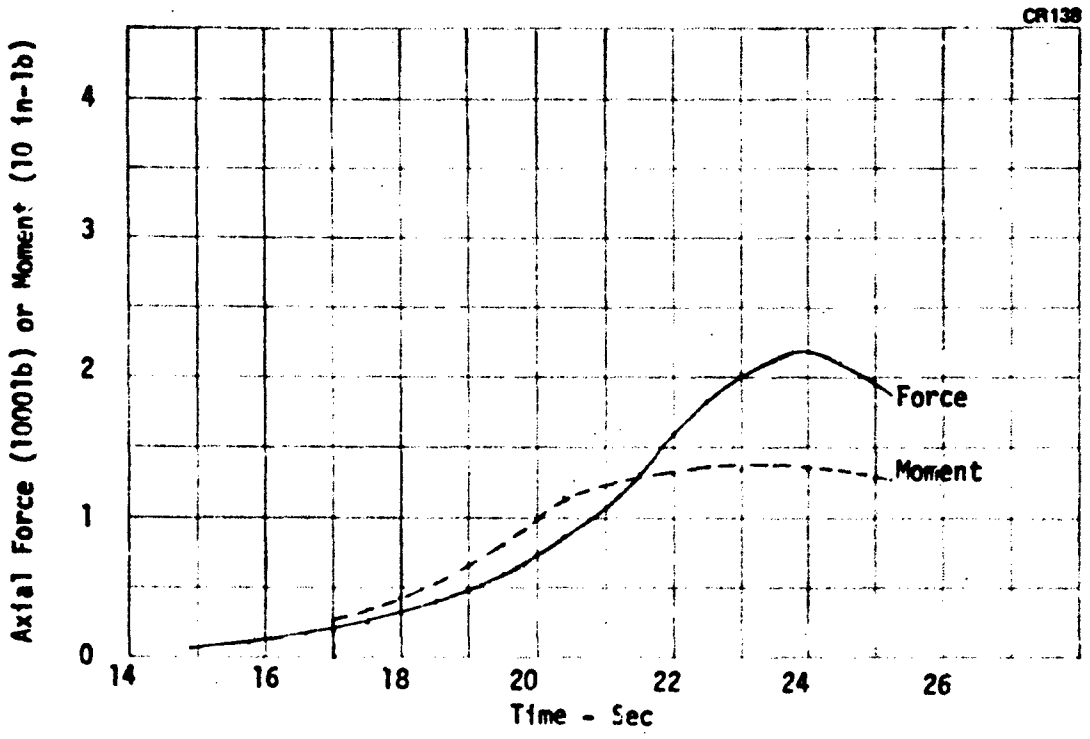


Figure 7-5. For .e and Moment Histories, L-1(+)

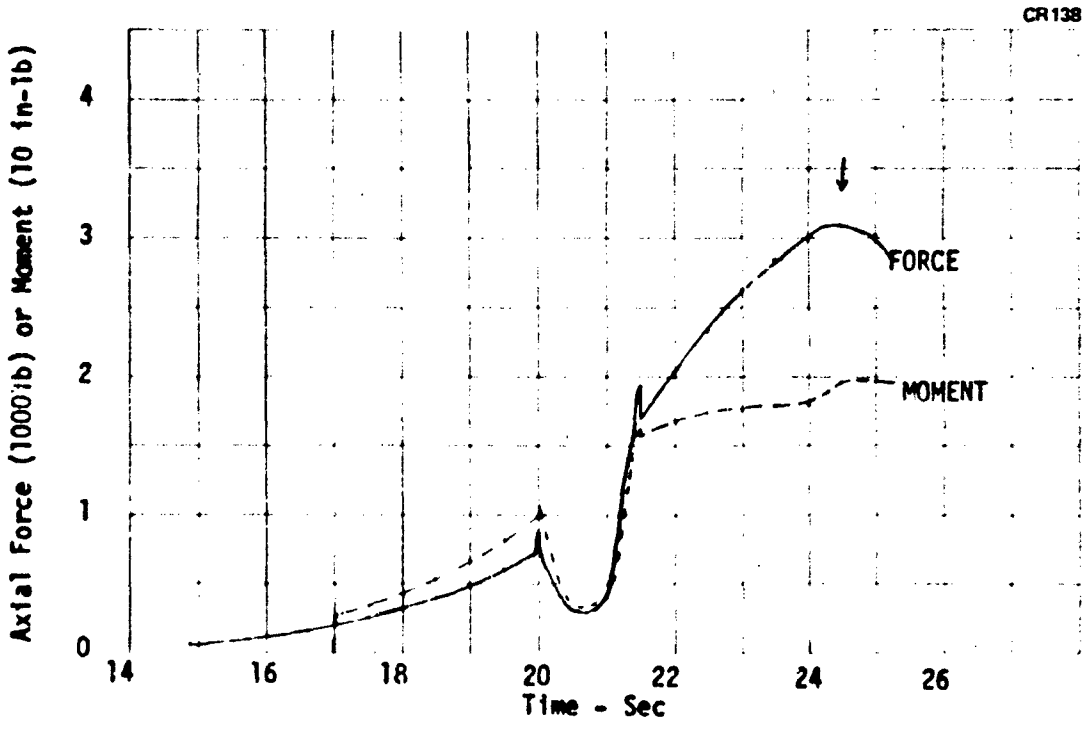


Figure 7-6. Force and Moment Histories, L-1(a), 60,000-Ft Blast Encounter

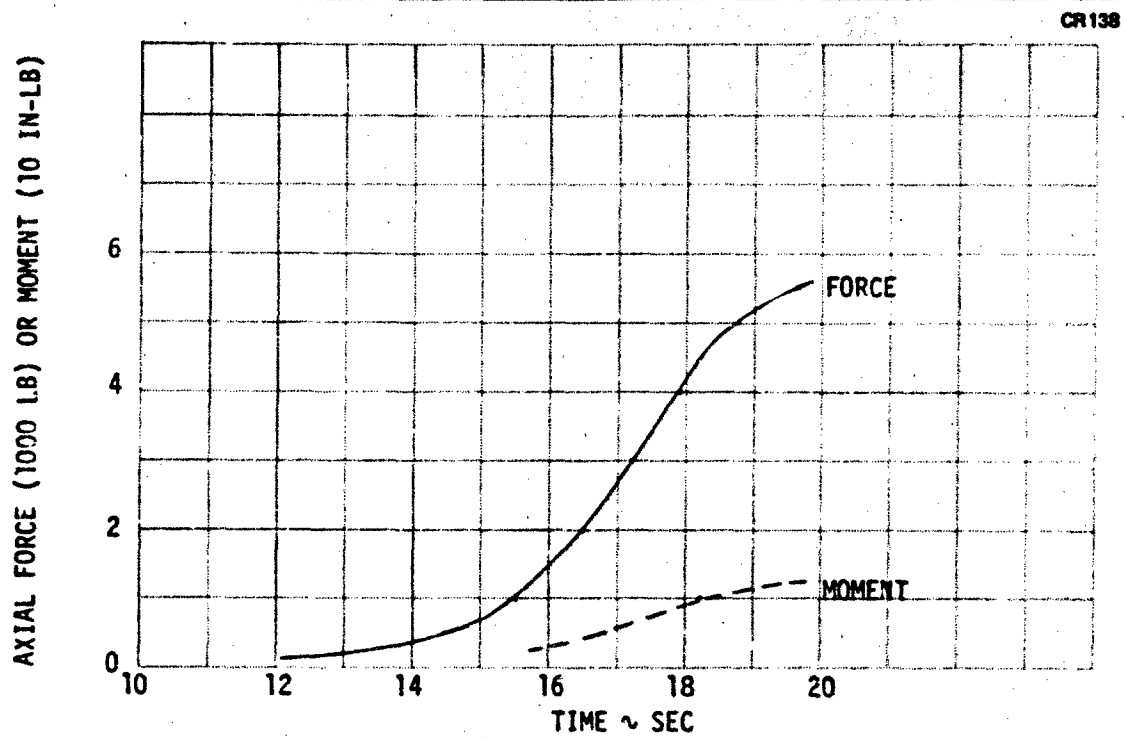


Figure 7-7. Force and Moment Histories, S-3

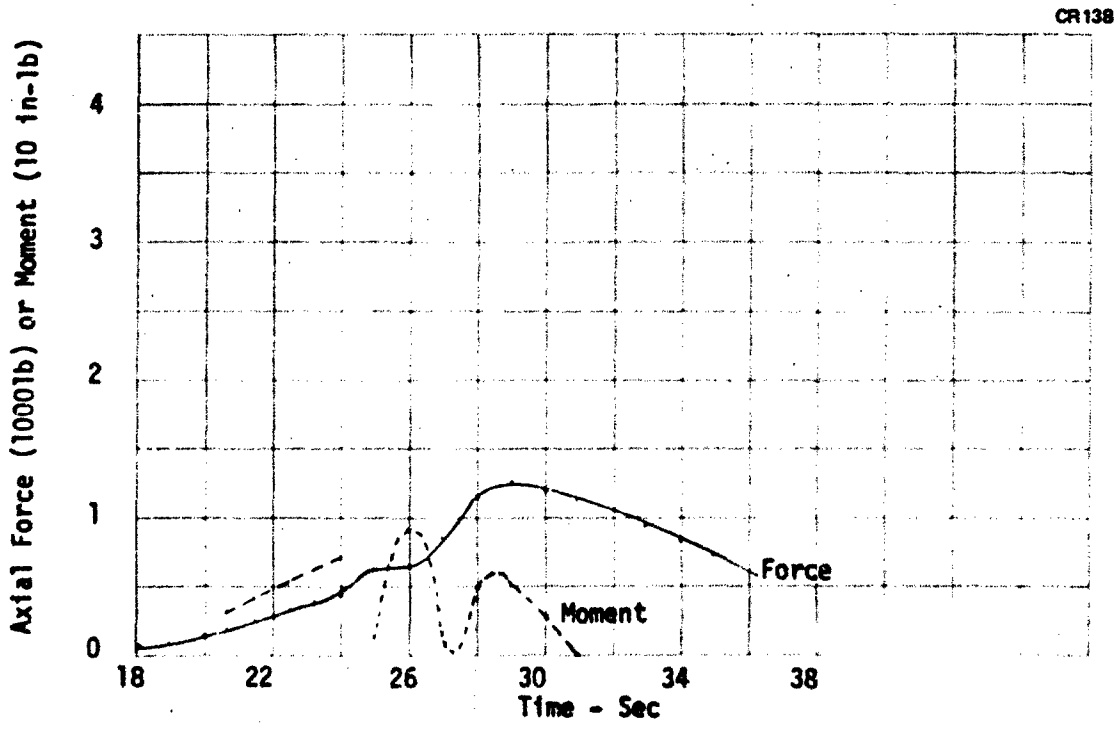
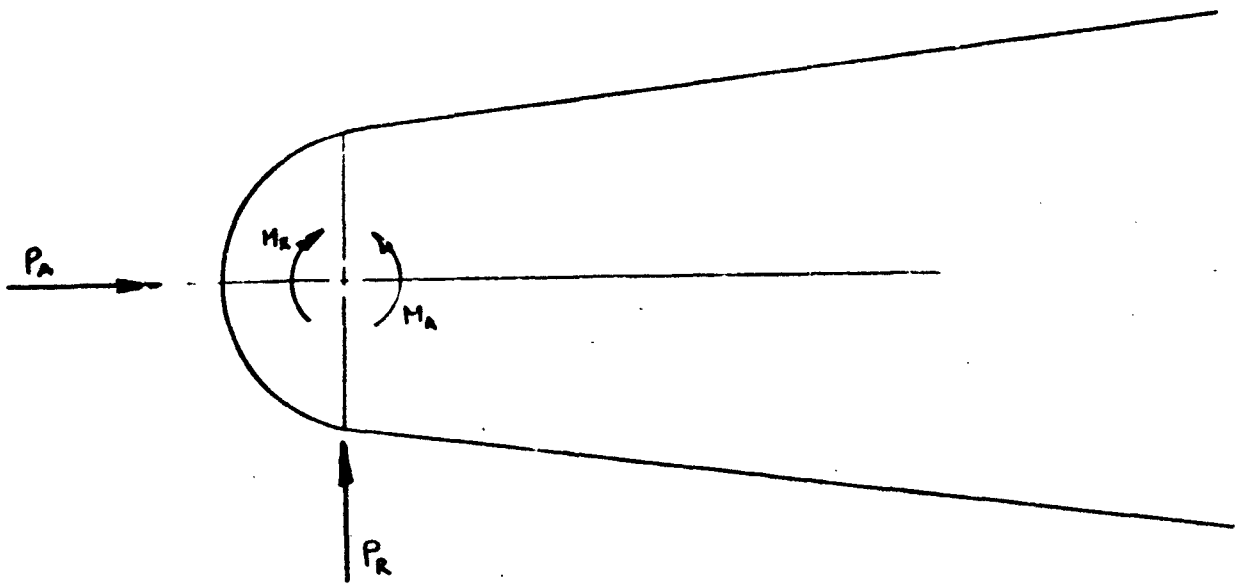


Figure 7-8. Force and Moment Histories, L-12



TRAJECTORY	TIME SEC.	VELOCITY FT/SEC	ALTITUDE FT	ANGLE OF ATTACK DEGREES	P_A LBS	P_R LBS	M_A FT-LB	M_R FT-LB
L-1(a) Blast	24.5	10255	7384	9.17	3079	418	19.5	15.3
L - 6	45.4	5803	11347	15.95	609	134	6.15	4.79
S - 3	19.7	15144	0	3	5646	256	12.1	9.5

Figure 7-9. Critical Load Summary

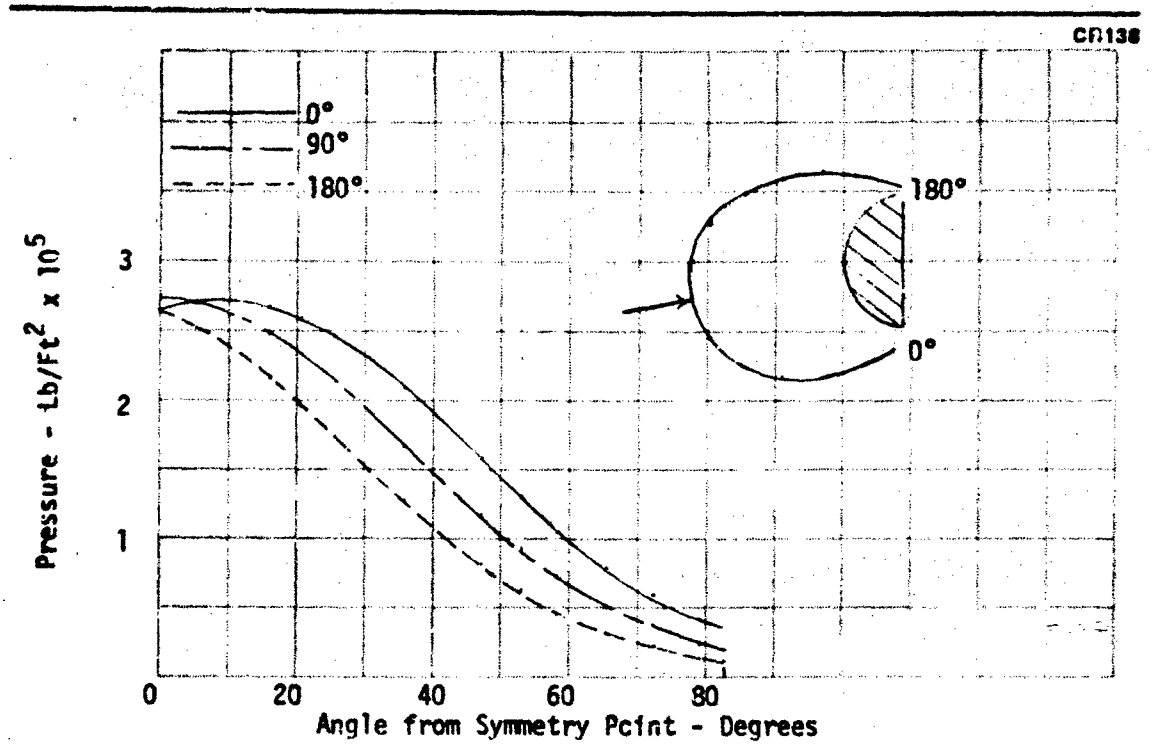


Figure 7-10. Nosetip Pressure Distributions, L-1(a) with Blast, Flight Time = 24.5 Sec

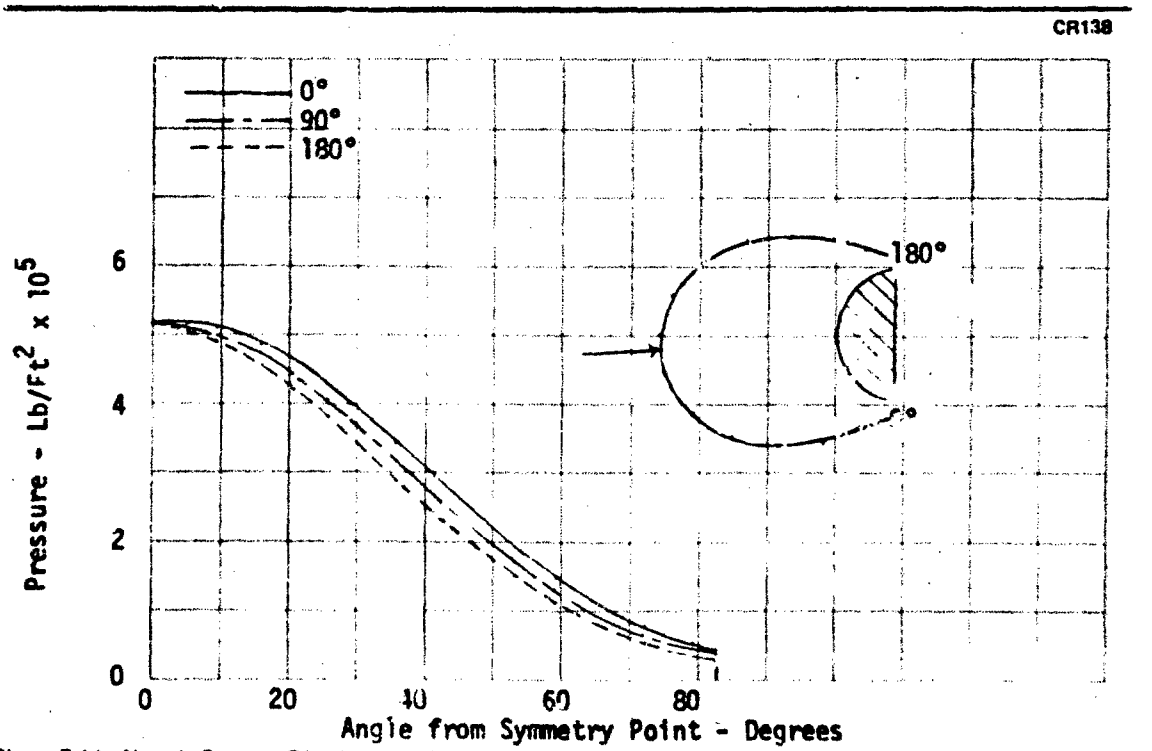


Figure 7-11. Nosetip Pressure Distributions, S-3, 19.7 Sec

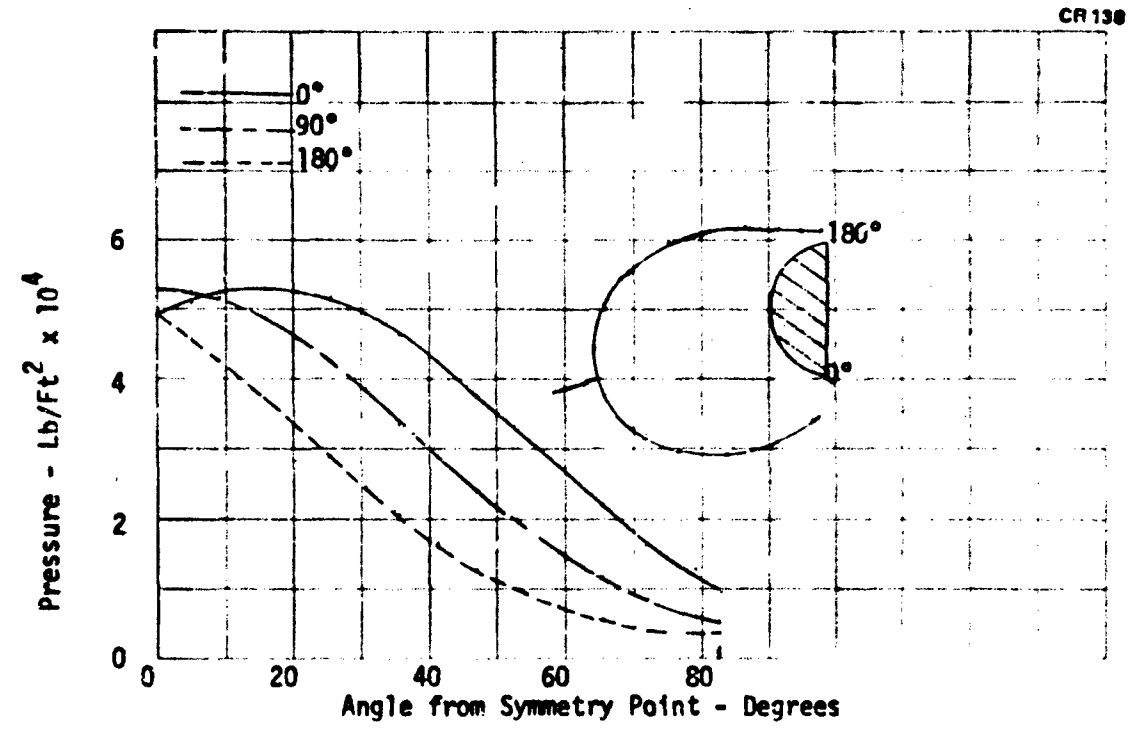


Figure 7-12. Nosetip Pressure Distributions, L-6, 45.4 Sec

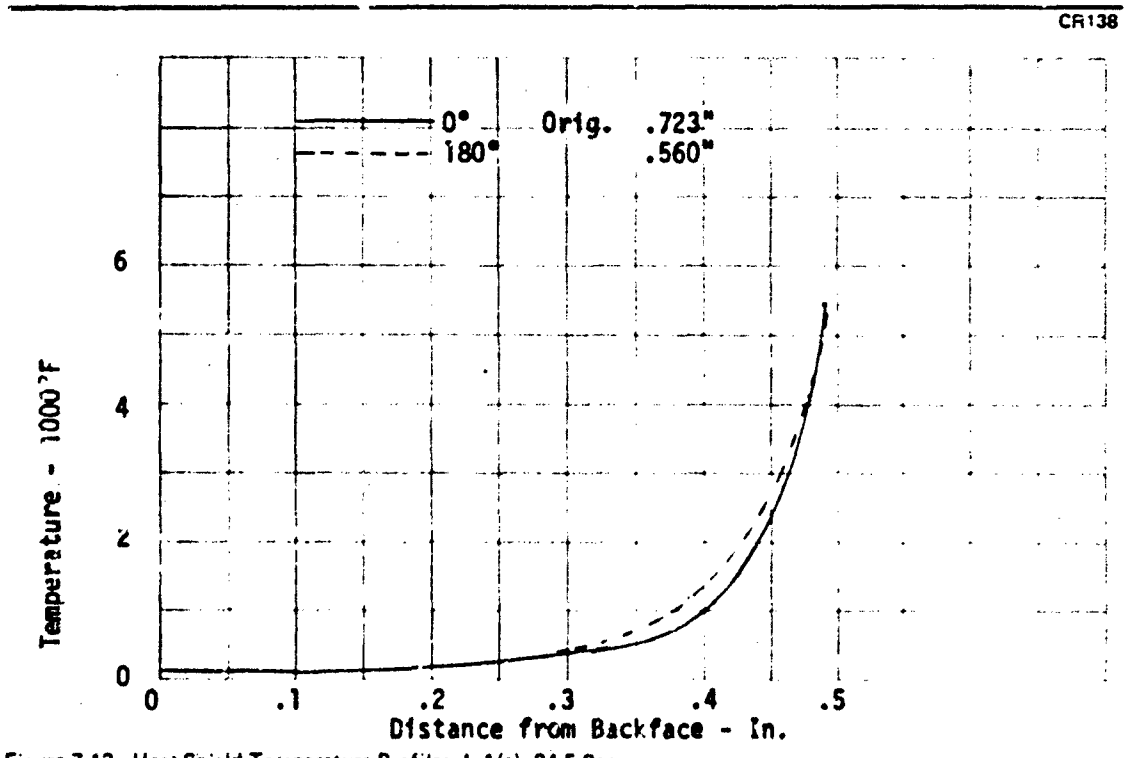


Figure 7-13. Heat Shield Temperature Profiles, L-1(a), 24.5 Sec

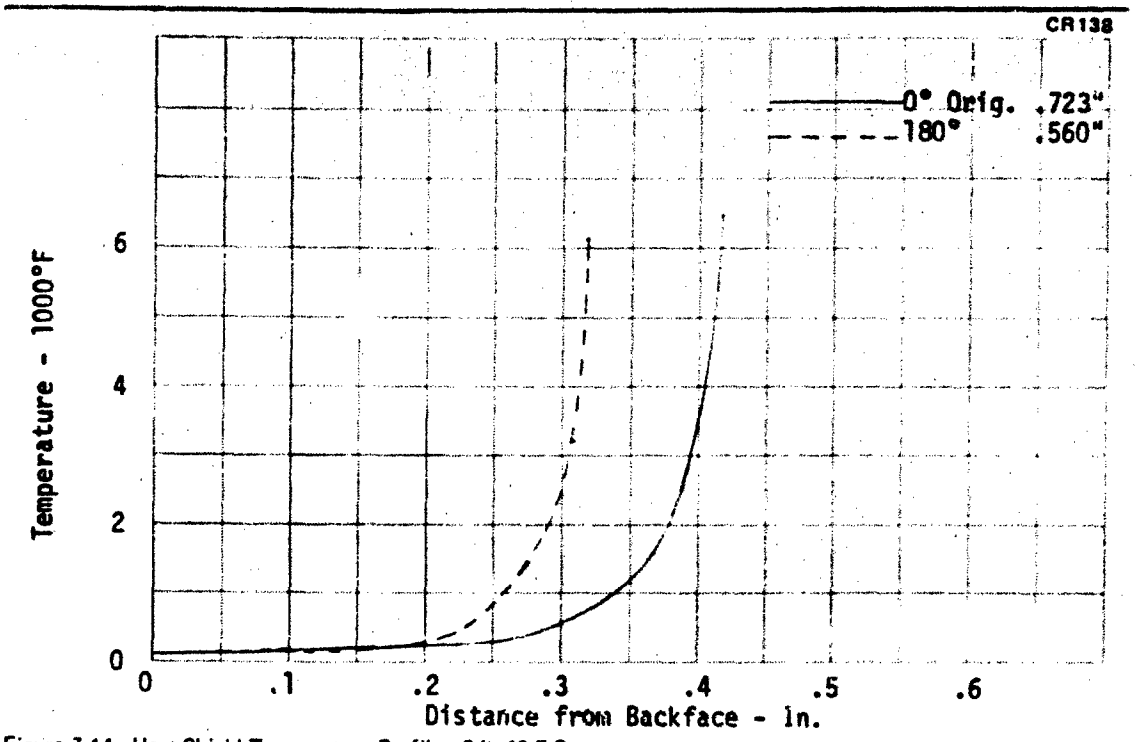


Figure 7-14. Heat Shield Temperature Profiles, S-3, 19.7 Sec

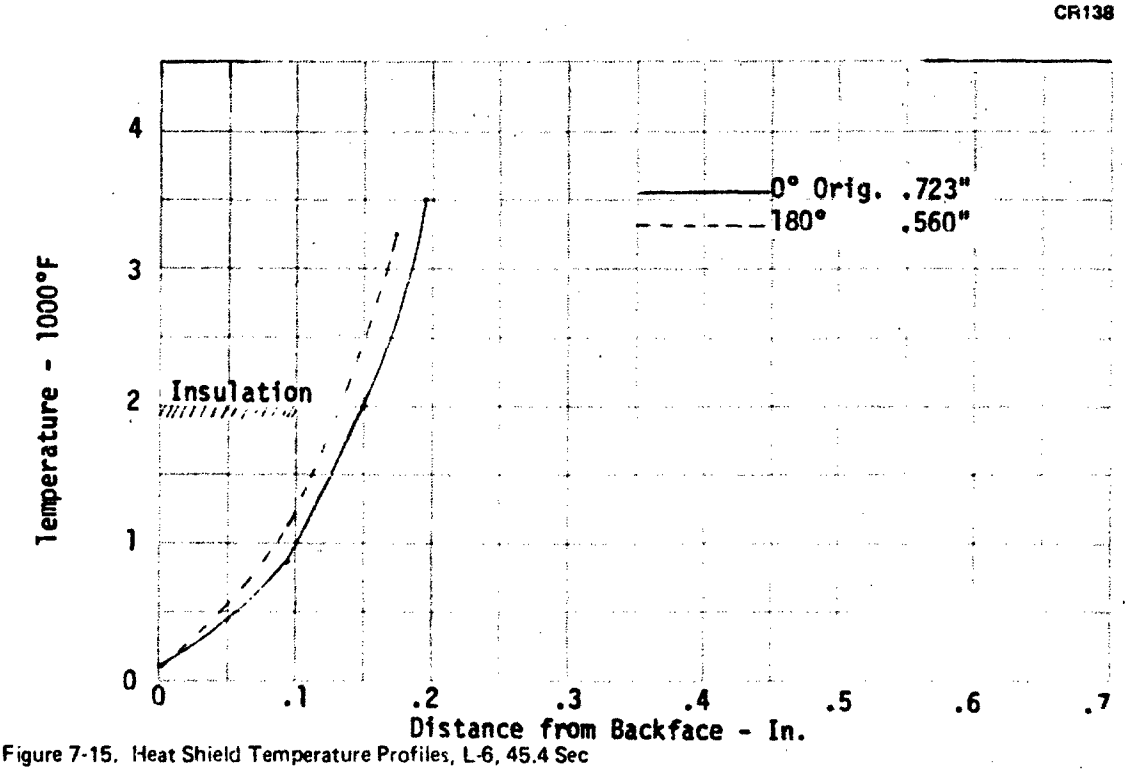


Figure 7-15. Heat Shield Temperature Profiles, L-6, 45.4 Sec

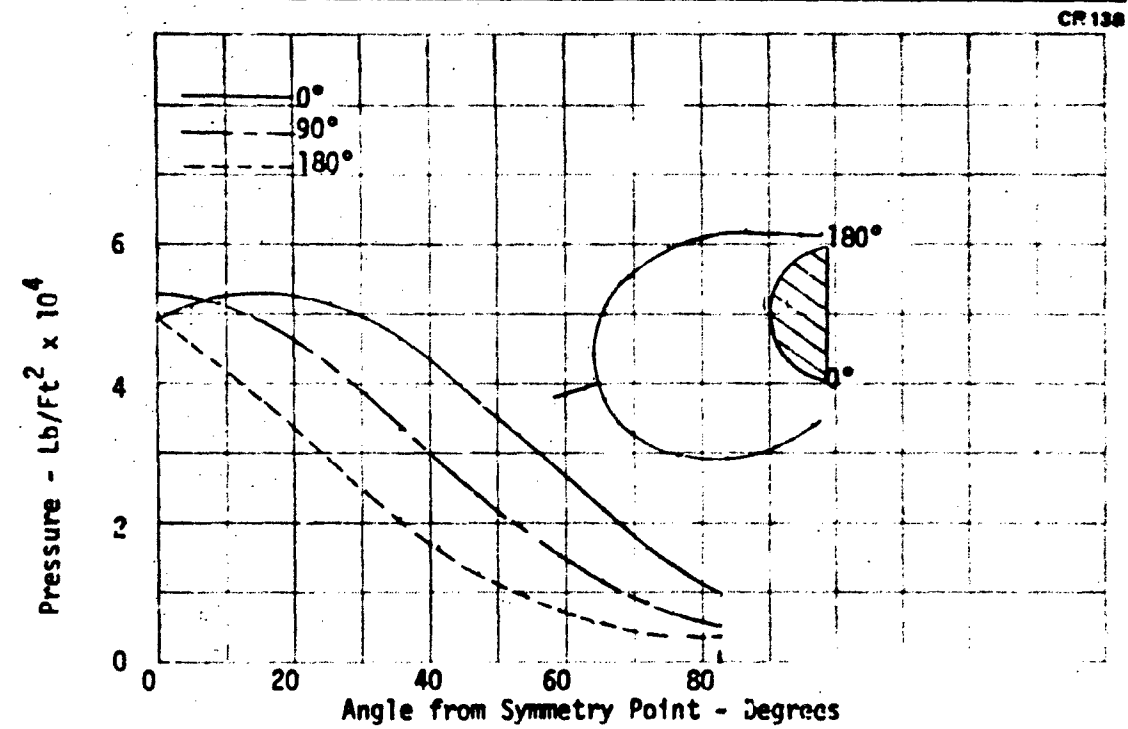


Figure 7-12. Nosetip Pressure Distributions, L-6, 45.4 Sec

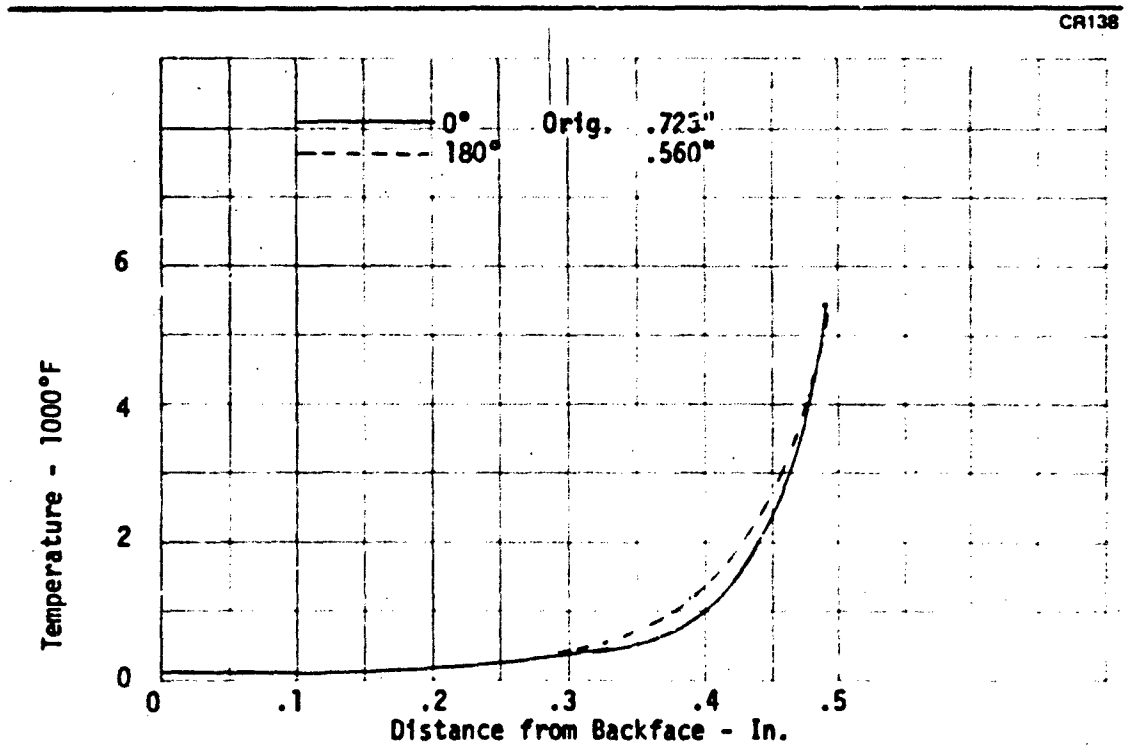


Figure 7-13. Heat Shield Temperature Profiles, L-1(a), 24.5 Sec

profiles for these same trajectories and time points. The critical case is at 19.7 sec into the S-3 trajectory. Accelerations were obtained from the supplied environments.

7.2.2 Component Analysis

A structural analysis was completed for all system components. For structural members, a factor of 1.25 times flight loads was used. For pressurized components, a factor of 1.25 times operating pressure plus 1.25 times flight loads determined the design. Maximum operating temperature of the component was considered in determining the allowable material stress. In consideration of the heat shield as a structural member, only the thickness of heat shield below a temperature limit of 600°F, as determined from Figures 7-13 to 7-15, was used. Details of the calculations are shown in Appendix E.

Figure 7-16 indicates the component critical stress areas. Table 7-2 summarizes the critical stress areas with a tabulation of the loads, considering actual stress, material, allowable stress, and margin of safety.

7.3 MASS PROPERTIES

7.3.1 Detailed Breakdown

Table 7-3 lists each component of the assembly with its material density and individual weight. The total weight shown includes coolant but does not include any parts which are classified as substructure. The change in total system weight for a change in coolant requirements has been computed. For each pound of water, the system weight (including water) will change by 2 lb. This change will also alter system length by 0.5 in.

The center of gravity of the system of weights shown in the table is located as indicated in Figure 7-1.

7.3.2 Possible Improvements

Possible improvements in the design to reduce the weight of the system include use of higher-strength steel (not yet investigated), use of more precise flow control to reduce the amount of coolant, and use of composite

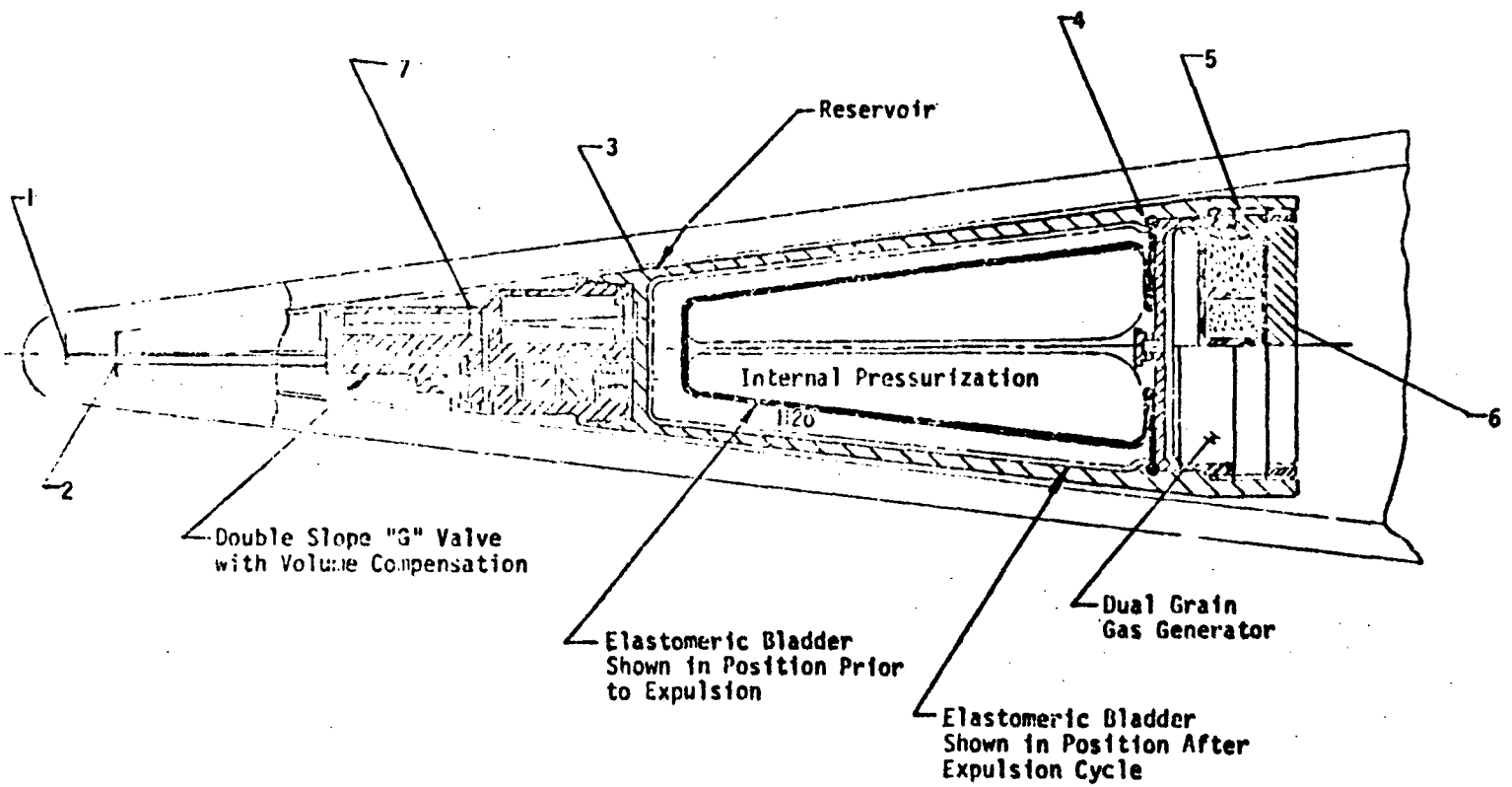


Figure 7-16. Critical Stress Areas

Table 7-2

CRITICAL STRESS RESULTS

Stress Area (Figure 7-15)	Component	Material	Ultimate Load Stress (psi)	Ultimate Allowable Stress (psi)	Stress Concentration Factor	Margin of Safety (percent)
1	Wand	4340	260,000	260,000	-	0
2	Wand	4340	190,600	260,000	-	36.5
3	Reservoir	17-4	190,000	190,000	2	0
4	Reservoir	17-4	190,000	190,000	2	0
5	Reservoir	17-4	184,000	190,000	2	3.4
6	Gas generator case	Maraging 250 GR	223,000	250,000	2.5	12
7	Valve body	17-4	190,000	190,000	2	0

*See Note 3 on Figure 7-1 for design loads.

Table 7-3
MASS PROPERTIES

Component	Density (lb/in.^{3})	Weight (lb)
Reservoir	0.29	6.65
Gas generator case	0.29	2.40
Gas generator grain and insulation	---	0.85
Gas generator retainer nut	0.29	0.507
Bladder backup retainer nut	0.29	0.088
Bladder backup	0.29	0.45
Valve assembly	0.29	1.50
Wand	0.29	0.10
Nosetip	0.29	0.28
Bladder	---	0.30
Water	0.036	3.00
Total weight		16.125

structures such as glass or boron wrap on the conical and cylindrical sections of the reservoir. Use of the composite structures is the most promising at present, since the major portion of the weight is contained in the reservoir. Both of these procedures are similar, as use is made of thin fibers which have extremely high tensile strength. The fibers are wrapped around the reservoir in the hoop direction and carry a substantial portion of the hoop stress when the reservoir is pressurized. A steel reservoir would still be used with boron fibers, while the glass fibers would be impregnated with a resin to form a completely nonmetallic structure. As a result, the reservoir walls can be reduced in thickness to a point which is determined by the longitudinal stress in the walls. The net reduction in weight using a boron wrap amounts to 35 percent of the steel weight, or 1.45 lb.

7.4 NUCLEAR HARDENING

In order to ensure survivability of the subsystem during a nuclear encounter,

protective shielding is required. An external boot is required to protect the nosetip and forward part of the wand. An internal shield, approximately 0.07 in. thick, is needed to protect the rest of the system. This shield was sized to prevent the water temperature from increasing more than 7.5°F.

7.5 ENVIRONMENTAL PERFORMANCE

Table 7-4 lists the environments which must be considered for an operational vehicle. The first four of these should pose no problem if the nosetip is protected. This should not be difficult, since a boot over the tip is required to protect the tip during the initial stages of reentry.

Table 7-4
ENVIRONMENTAL PERFORMANCE CONSIDERATIONS

Humidity
Dust
Salt fog
Rain
Fungus
Long-term storage
Temperature and pressure during storage, launch, and reentry
Vibration and shock during storage, launch, and reentry
Acceleration
Acoustic
Electrointerference
Electro-explosive devices

The principal area of concern during long-term storage is preventing deterioration of the water contained in the reservoir. Unless suitable precautions are taken, algae will grow in the water. The algae can cause plugging of both the valve and the nosetip pores. Two approaches are available to prevent algae growth: introduction of a biocide and sterilization.

The addition of a biocide to the water prevents the growth of any algae present. Two problems are associated with this approach. The first is

longevity of the biocide. There is some questions as to whether biocides, particularly iodides, will retain full effectiveness over a five-year storage period. The second problem is that of corrosion. The introduction of biocide ions into the water increases the problems of galvanic corrosion, especially between parts of the system made of different alloys. To ensure against this possibility, only 17-4 stainless steel has been used for metallic components in contact with water.

The alternative approach to the algae problem is to use sterilization. The manufacturing processing is more complex, but it avoids the problems of biocide longevity and corrosion. The sterilization procedure is to place the water and all contacting components (as an assembly) into an autoclave. This is the approach currently favored for this sytem.

Another potential problem encountered during long-term storage is that of corrosion (galvanic, pitting, or stress) in metal components. Corrosion possibilities have been minimized by careful selection of materials and heat treatments. Use of the information obtained during a current AFRPL contract will be made for final material selections.

The most critical thermal problem is to prevent freezing of the coolant when exposed to the environments specified in the contract. If the time periods during which freezing is expected are cyclic, then transient analyses should be performed to determine whether or not freezing will occur. If there is a possibility, then heaters will be required.

The structural integrity of the system under vibration, acoustic, and shock environments must be determined through test. The worst expected environments are the ground storage shock and the boost-phase vibration and acoustic loads. It is not anticipated that these environments will dictate the need for any design changes.

The most critical component of the system will be the elastomeric bladder under acceleration loads. Adequate testing of the component will be performed to assure that the bladder will expand properly and deliver the full volume of coolant under all acceleration histories.

The flow control valve will be designed to withstand and operate under the environmental criteria. It may be necessary to utilize a low-friction bushing to support the acceleration-sensitive mass of the valve to preclude sensitivity to lateral accelerations. Similar measures were taken with the ACE flow control valve.

7.6 RELIABILITY AND SAFETY

Table 7-5 lists several possible failure modes of expulsion system components. Their effect on system performance has been estimated. Ways of minimizing their occurrence will be obtained during the development phase.

The proposed flow control system is mechanically similar to those successfully used in the RVTO-1A and -2A reentry vehicles developed by MDAC. Because of this similarity, no problem areas are anticipated.

Since bladders and gas generators of the designs required for the current application have not been previously developed, a considerable amount of testing will be required to ensure the reliability of these components.

The only safety problems expected are connected with the gas generator propellants. The most serious of these concerns the igniters, since the propellants themselves are not considered a hazard. The real problem is to prevent premature firing of the igniters through a spurious electrical signal. This will be prevented by proper design of the igniter, use of shielded leads, and requiring a shaped ignition signal (see Section 6).

7.7 MANUFACTURING

Most of the system components (gas generator, coolant reservoir, valve, and wand) present no particular manufacturing problems and will be fabricated using conventional aerospace manufacturing techniques. The porous nosetip and its connection to the wand require unique technology and will be described in more detail.

The nosetip is fabricated from a billet of porous stainless steel. The billets are produced by MDAC to the specific permeability requirement of the end item using a powder metallurgy process. Permeability is controlled by

Table 7-5

FAILURE MODES AND EFFECTS

Component	Failure Mode	Effect	Solution
Flow control valve	Acceleration-sensitive spool jams	Constant flow rate	Design and test
	Acceleration-sensitive spring breaks	Full flow, early depletion	Design and test
	Pressure regulator spool jams	Flow varies with pressures	Design and test
	Pressure regulator spring breaks	Low flow rate	Design and test
	Volume compensator jams	Excessive flow, early depletion	Design and test
	External leaks develop	Loss of coolant	Analysis, proof test
	Orifice plugged	Flow wrong for conditions	Design, use of filter
Bladder reservoir	Bladder ruptures	May mix gas with liquid	Test, analysis
	External leakage	Loss of coolant	Analysis, proof test
	Improper bladder collapse	Fluid may be trapped	Test
Gas generator	Improper ignition	Insufficient pressure	Test
	Improper ΔP switch operation	Rapid pressure decay	Design and test
	Wrong burn rate	Wrong pressure	Test
	External leakage	Loss of pressure	Analysis, proof test

appropriate selection of stainless steel powder size and size distribution, pressing pressure, and sintering time and temperature. To make a billet, accurately characterized stainless steel powder of the selected size is placed in a flexible mold and compacted in an isostatic press. The "green" billet formed by thus compacting the powder has sufficient strength to be removed from the mold and placed in a furnace retort. It is then sintered in a vacuum atmosphere to achieve the desired properties. The sintered billet is then nondestructively inspected for flaws and is tested to characterize its strength and permeability.

The characterized porous billet is then machined to the nosetip configuration using tools and techniques specifically designed to minimize "cold working" or smearing of the surface metal, which would cause blockage of surface pores. The configuration for the system under study in this report will be machined with an "open back side" to permit tool access for achieving the complex shape required.

The machining operation is followed by an electrochemical surface etch to remove the last traces of surface smearing. The etched tip is then tested for gross flow through the tip and for consistency of flow through sections of equal thickness and permeability.

A back closure is next assembled to the nosetip to close the open back side and to provide an attachment point for the wand (coolant pipe). The back closure is attached by electron beam welding. The electron beam process was selected because the small weld bead size attainable with this process causes a minimum of perturbation of the adjacent porous, permeable nosetip material. A second advantage of the process is that the vacuum atmosphere required minimizes nosetip contamination by dust or welding fumes such as would be likely with other welding processes.

A butt weld joint was selected for the electron beam weld. The butt joint contains a step at the bottom, as may be seen in Figure 7-1. This design was chosen for two reasons. First, the step at the root of the joint prevents any weld dropthrough spatter from impinging on the porous interior of the nosetip and plugging the pores. The step also provides a positive method of locating the part during assembly, making it self-jigging and thus avoiding the use of additional weld-locating tooling.

The nosetip assembly is shot-peened on the back surface to prevent coolant loss through this area. The assembly is given a final flow check to verify both the absolute permeability and the uniformity of the flow distribution. The nosetip is then ready for final assembly on the completed system. If required, porous beryllium nosetips can be manufactured using similar procedures (Reference 7-1).

Section 8
CONCEPT DEFINITION

To assist in the selection of concepts for this final recommended design, a ranking system was developed. This system was applied to each component, and ratings for the different concepts were obtained. The designs having the highest ratings were then selected.

8.1 RANKING SYSTEM

The ranking system is comprised of two parts. The first is made up of the weighting factors for the various parameters being considered. These are shown in Table 8-1. Length and weight must be judged on overall system effects, since it is possible for one concept to weigh less or be shorter than another but have the reverse effect on the total system. Adaptability is a very arbitrary quantity which corresponds to the ability of a given concept to perform other missions than the ones studied during this contract. Effectiveness is simply a measure of the amount of excess coolant required by an individual concept. Hardenability is the difficulty encountered in protecting against a nuclear encounter. Reliability is an estimate of the confidence in the design and performance of a given component. Development and operation are measures of the difficulty expected during the development and operational phases. Operational considerations include safety, long-term storage, and manufacturing procedures. Rating on development included estimates of development risk and cost, and of problems expected in testing the various concepts.

The second part of the ranking system is the rating value assigned to each parameter for each concept. An attempt was made to generate analytic functions to obtain these values. However, due to the nature of these parameters, this was not possible for all cases. In fact, it was believed that a purely subjective approach based on the relative merits of each concept would result in a more accurate ranking. Therefore, rating values from 0.0 to 1.0 were given to each concept for each of the parameters being considered.

Preceding page blank

Table 8-1
RANKING SYSTEM

Parameter	Weighting Factor
Length	10
Adaptability	8
Effectiveness	7
Weight	6
Harcenability	5
Reliability	4
Operation	3
Development	3

After the rating values were assigned for each parameter and concept, they were multiplied by the weighting factor for the corresponding parameter. The results obtained for each concept were then summed to obtain the final rating. The concept with the highest rating was selected for the final design. This procedure has been applied to each of the three primary components (valve, reservoir, and pressurization) to obtain the final design.

8.2 CONCEPT RANKING

Separate rankings were performed for each of the three major components: flow control, expulsion, and pressurization.

8.2.1 Flow Control

Table 8-2 shows the rating values and the ranking totals for several concepts. Discussion of how these values were developed is included below.

Rating for the weight, length, and effectiveness parameters is almost completely dependent upon the amount of coolant used. Table 8-3 summarizes the results obtained for each of the concepts studied. The closed-loop design using a nosetip sensor has not been included in this table, since insufficient analysis and no experimental data have been generated to define coolant requirements accurately. However, good estimates of the performance of this system based on the data presented in Section 3.3 can be made.

Table 8-2

FLOW CONTROL RANKING

Parameter	Weight	$\sqrt{a}$	Dual Slope	Mark II	v,ρ,α	Pressure	Preprogrammed	Sensor
Length	10	0.3	0.8	1.0	0.8	0.2	0.7	1.0
Adaptability	8	0.6	0.9	0.9	1.0	0.6	0.4	1.0
Effectiveness	7	0.4	0.9	1.0	0.8	0.4	0.6	1.0
Weight	6	0.4	0.9	1.0	0.8	0.4	00.6	1.0
Hardenability	5	0.8	0.7	0.7	0.6	0.8	0.8	0.6
Reliability	4	1.0	0.8	0.8	0.4	0.6	0.8	0.4
Operational	3	0.8	0.6	0.6	0.5	0.7	0.7	0.4
Development	3	1.0	0.7	0.7	0.5	0.6	0.8	0.4
Weighted totals		26.4	37.5	40.8	34.0	22.3	29.7	38.0

Table 8-3

COOLANT REQUIREMENTS

System	Nominal Weight (lb)	Excess (percent)	Margin (percent)	Actual Weight (lb)
Design (L-6)	2.31	0	--	--
$\sqrt{g}$	4.99	115	3	5.14
Dual slope, volume compensator	2.76	20	10	3.04
Mark II, volume compensator	2.43	5	10	2.67
u,ρ,α	2.56	11	10(?)	2.82
Preprogramming	2.84	22	10	3.02

Adaptability of the candidate systems to different trajectories was difficult to evaluate. While the system operating from trajectory data will compensate automatically for new conditions, it is felt that it is possible to define envelopes for all feasible trajectories for a given vehicle with the Mark II system without exceeding the requirements of the most severe.

There is very little difference in the hardenability requirements for most of the concepts, since they can be contained completely within the protective shield. Both electromechanical concepts require extra equipment which must be outside the main shield. For this reason they were rated lower.

The systems using the electromechanical valves were penalized in considering reliability, operation, and development by the anticipated development time and difficulty for these valves. Starting with the RESEP program in 1967, a number of efforts have been made to find an electromechanical valve which would meet the requirements of a transpiration system. The most concentrated effort was made in 1970 for the ACE proposal, when a request for information was submitted to a number of valve vendors. There were two replies, neither of which were adequate for a subsystem.

Early in the present study, the feasibility of an electromagnetic valve which would meet flow control system requirements was established. Discussion of this valve will be found in Section 3.2.3. However, it appears that development time for this valve might not fall within the development schedule for the proposed system (9 to 12 months).

8.2.2 Expulsion

Table 8-4 presents rating values and ranking totals for the expulsion concepts. Adaptability and effectiveness were not included in this ranking, since it was felt these will be identical for all expulsion systems.

The poor performance of the piston system in the length and weight categories is a result of its poor volumetric efficiency. There is no difference between the two bladder concepts for these two considerations.

The advantage of a piston system becomes evident by considering the last three parameters. It is a highly reliable, well-developed design. There is insufficient data available on the bladder concepts to differentiate between them at this time. The metallic bladder was graded slightly lower in reliability because of the problems with the coolant discussed in Section 4.2.3.

Table 8-4
EXPULSION SYSTEM RANKING

Parameter	Weight	Piston	Metallic Bladder	Elastomeric Bladder
Length	10	0.7	1.0	1.0
Adaptability	8	---	---	---
Effectiveness	7	---	---	---
Weight	6	0.8	1.0	1.0
Hardenability	5	0.6	0.6	0.6
Reliability	4	1.0	0.8	0.9
Operation	3	1.0	0.8	0.8
Development	3	1.0	0.7	0.7
Weighted totals		24.8	26.7	27.1

8.2.3 Pressurization System

Five different pressurization system designs were considered in the comparisons shown in Table 8-5. These were the two- and three-grain solid systems, the blowdown and bootstrap monopropellant liquid systems, and a cold-gas system. The cold-gas system was included as a basis for comparison.

Table 8-5
PRESSURIZATION RANKING

Parameter	Maximum Weighting Factor	Solid		Monopropellant		Cold Gas
		3-Grain	2-Grain	Bootstrap	Blowdown	
Length	10	9	9	8	7	2
Adaptability	8	6	4	7	7	7
Effectiveness	7	7	7	7	7	7
Weight	6	5	5	4	4	2
Hardenability	5	2	2	2	2	2
Reliability	4	3	4	3	3	4
Operation	3	3	3	1	1	2
Development	3	2	2	1	1	2
Weighted totals	46	37	36	33	32	28

The length of the pressurization and expulsion system is directly related to the size and design flexibility of the gas generator device. The solid gas generator requires less volume for packaging than the monopropellant and has no particular length requirements, except to provide sufficient web length for the necessary burn time. The maximum web length is sufficiently small so that the solid system can be packaged circumferentially. Thus, no penalty is imposed on the length of the total system. The design of the monopropellant systems, on the other hand, requires more total length than the solid system because of the difficulty in packaging the system in a small-length-to-diameter volume. The bootstrap system is more compact than the blowdown system because it is self-pressurizing.

The monopropellant system is somewhat more adaptable to a variety of situations than the solid-fuel system because of its "on-off," or "demand" capability. Increasing the number of solid grains to more closely approximate a demand system would not be feasible because of the corresponding decrease in reliability.

The solid-fuel system weight advantage reflected in Table 8-5 results mainly from the differences in hardware complexity. The requirements for a catalyst bed and a means for pressurizing the fuel in the monopropellant system result in additional weight not required by the solid system.

None of the pressurization systems considered in this study are, in themselves, nuclear-hardenable. This would be accomplished by enclosing the system in an appropriate case.

The major factors affecting the relative reliabilities of the solid and monopropellant systems are hardware complexity and state of the art. The solid system is considered more reliable at the present time because it is inherently more simple, and more solid propellant data have been generated at high pressures. Also, high g effects are now sufficiently well-characterized that burning-rate problems appear to be solvable. However, it is believed that the monopropellant system can be designed with a high reliability through adequate ground tests.

The primary factors considered in comparing operation of the pressurization systems are safety, long-term storage, and manufacturing. Solid systems have a decided advantage in each of these categories. Monopropellant hydrazine, for example, is toxic and, because it is a liquid, is not as storable as solid fuels. Manufacturing problems related to solid-fuel systems would also be less complicated because of the differences in hardware complexity.

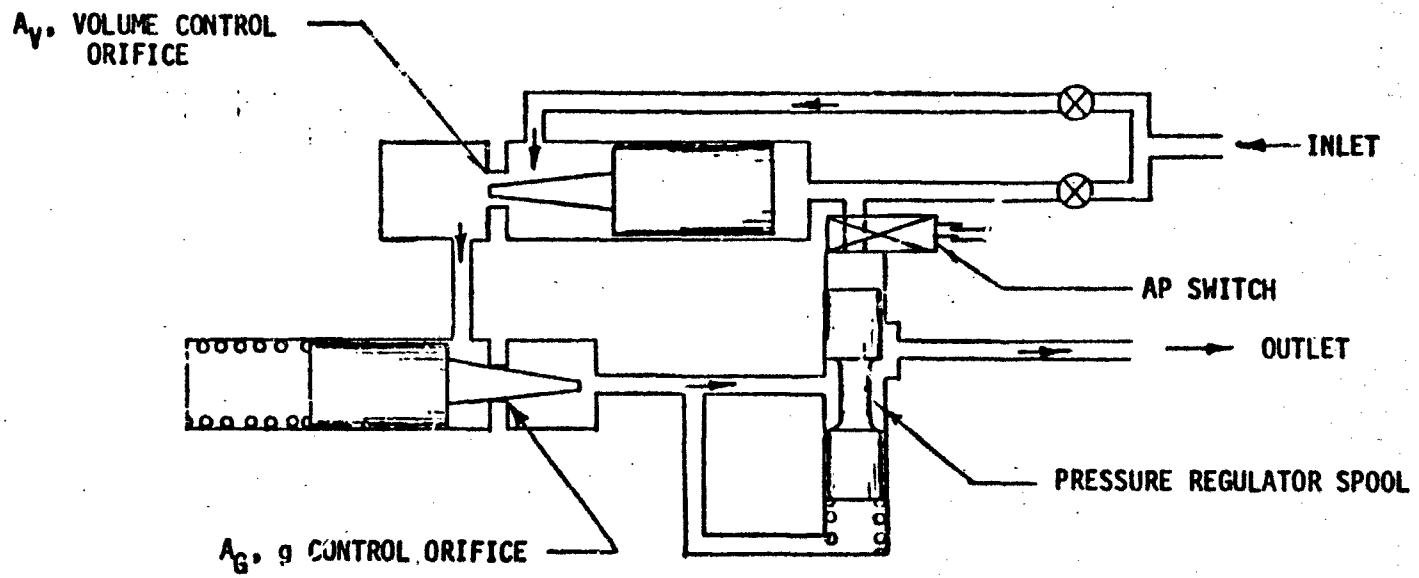
Considerable development would be required to fully characterize monopropellant system performance, since little high-pressure data is presently available. While it is not expected that high-g effects would be important in such a system, obtaining basic high-pressure performance data would require a considerable amount of testing with relatively sophisticated and costly equipment. Both systems would require considerable centrifuge testing, but the solid fuels are known to be more sensitive to g effects.

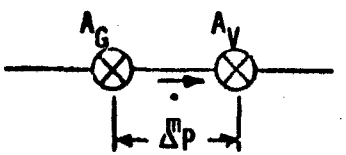
8.3 SELECTED DESIGNS

The recommended flow control design is a Mark II flow control valve with volume compensation. A schematic of this valve is shown in Figure 8-1. Actual and design pressures and flows are shown in Figures 8-2 through 8-4.

This selection was made because this system minimizes the actual coolant requirements and because it is felt that it fits the development time schedule better than the runner-up. If adaptability becomes an increasingly important parameter, and if further studies show that the selected concept will not satisfy the new missions, then the free-stream parameter method with an electromechanical valve would have to be used. However, the possibility of this occurring without a large change in vehicle requirements is felt to be small. The nosetip sensor concept is not recommended due to the large and lengthy development program which would be required.

The nonmetallic cruciform bladder shown in Figure 4-2 has been selected as the current baseline. As was shown in Table 8-4, this choice was made on the basis of an extremely small margin. It is felt that a final choice should be delayed several months until more data on both this concept and the metallic bladder design is available. Substitution of the metallic bladder in the current design could be accomplished with practically no basic design changes.





$$\dot{m} = \frac{3.28\ \Delta P}{\sqrt{\frac{1}{A_V^2} + \frac{1}{A_G^2}}} \quad \text{(LBS/SECOND)}$$

Figure 8-1. Mark II Flow Control Valve Schematic

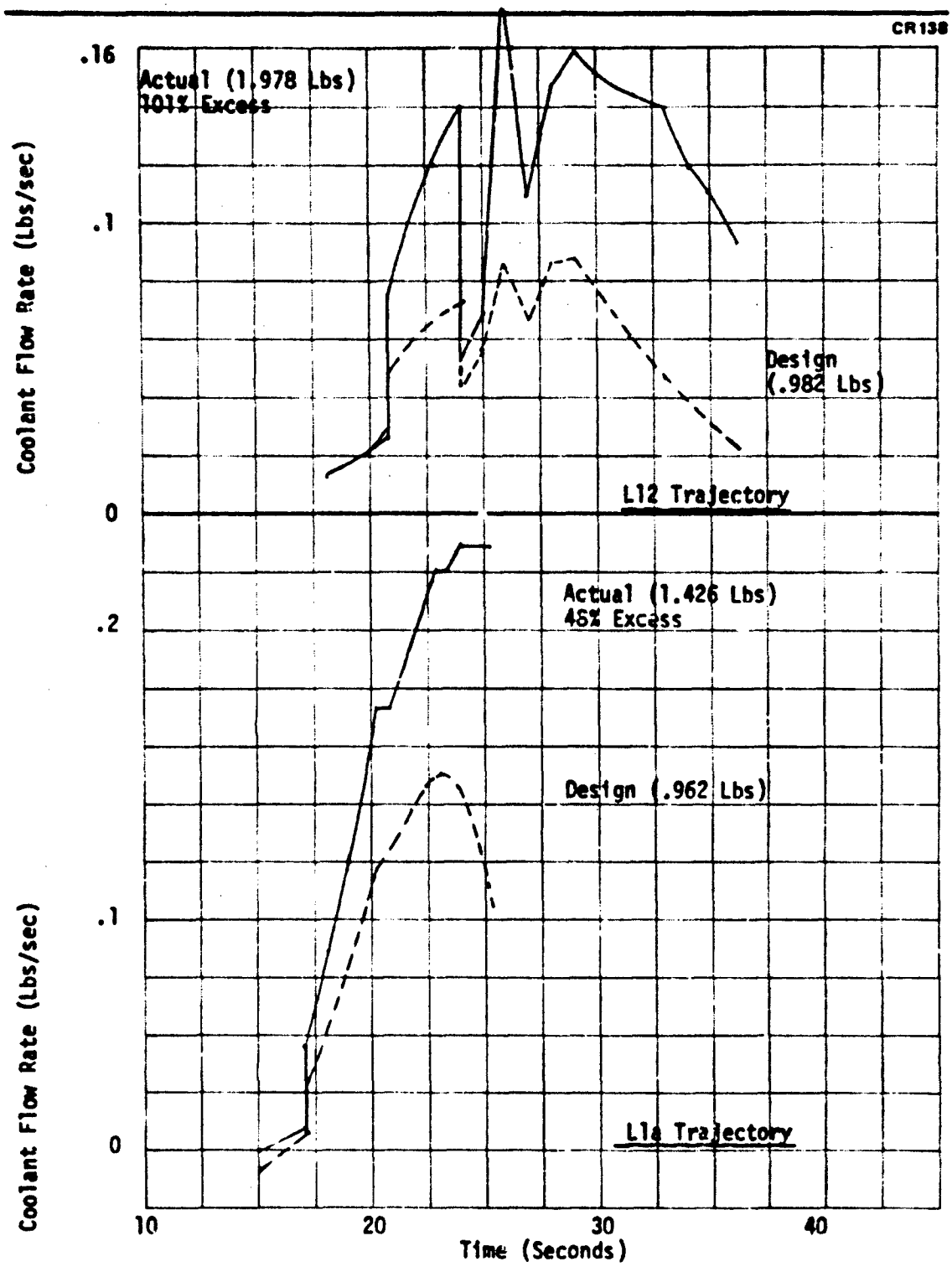


Figure 8-2. Mark II Valve Flow History – L-12 and L-1(a) Trajectories

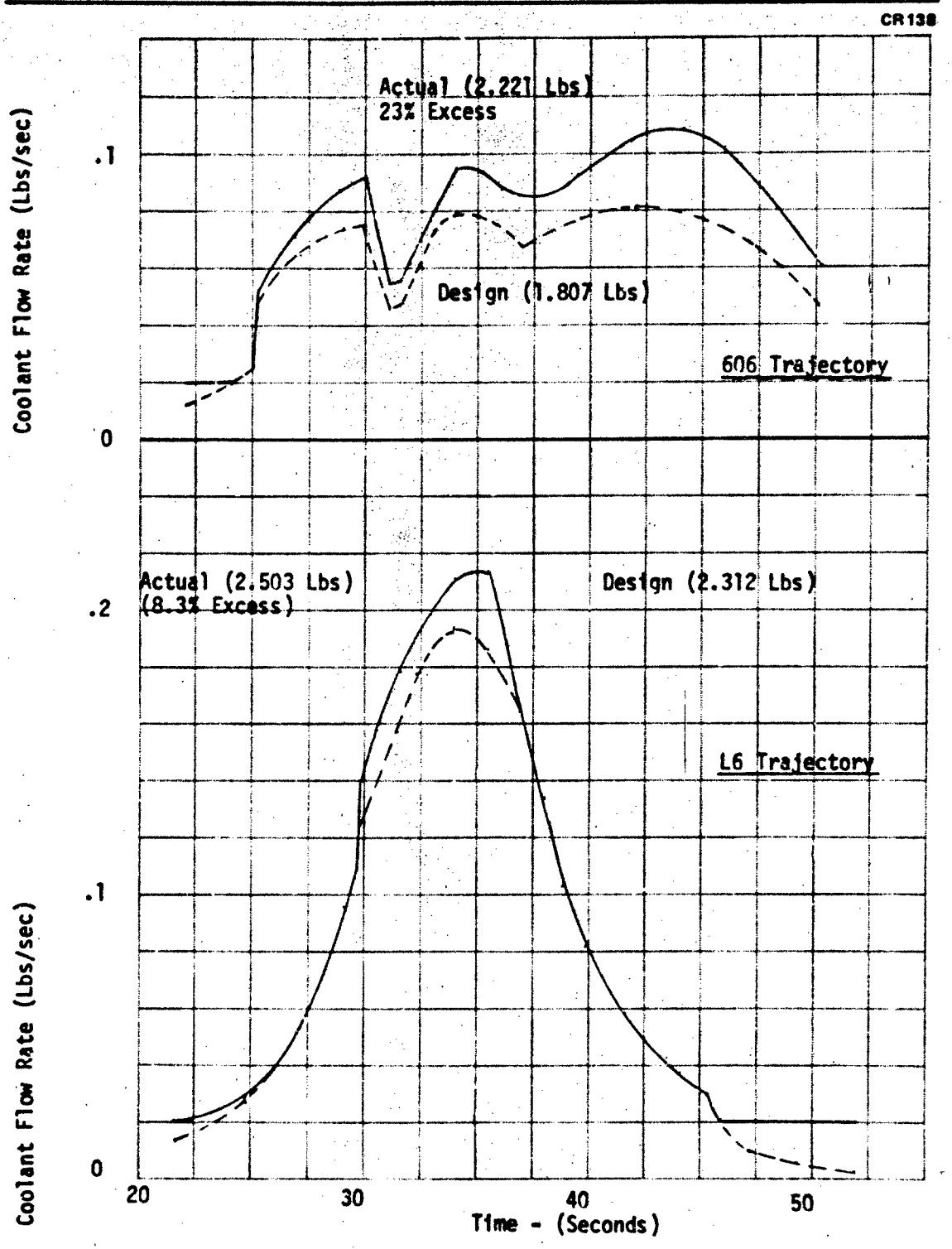


Figure 8-3. Mark II Valve Flow History – 606 and L-6 Trajectories

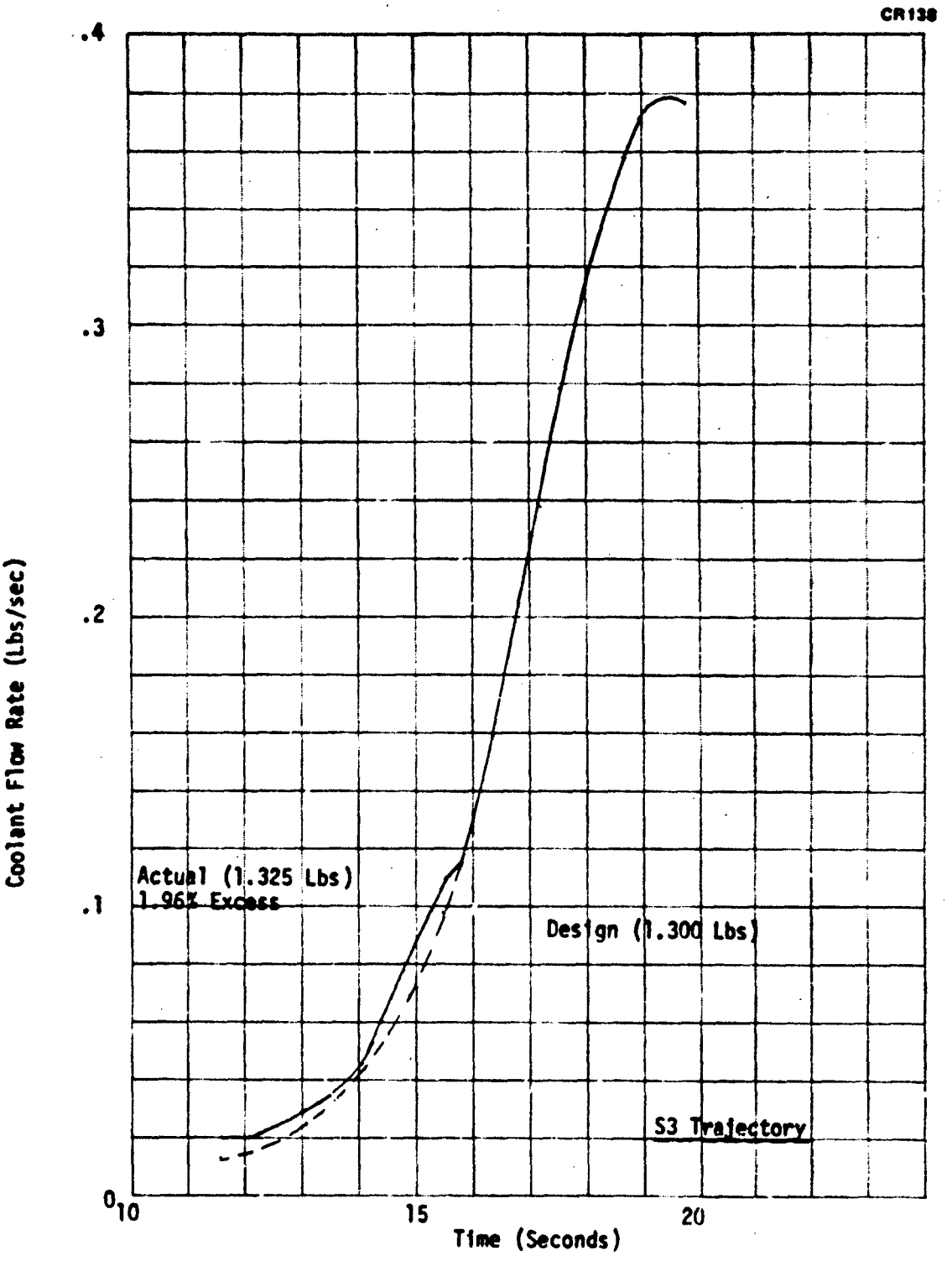


Figure 8-4. Mark II Valve Flow History – S-3 Trajectory

The three-grain solid-propellant concept (Figure 5-8) has been selected for use with the current design. It has been shown that a significant reduction in subsystem size and weight can be obtained through the use of this design, as well as other warm-gas pressurization concepts, as compared to cold-gas pressurization. The three-grain system is selected over the two-grain system to reduce the sensitivity of the design to small changes in mission requirements.

Section 9
ROCKET SLED TEST

The performance of a reentry vehicle nosetip may be severely degraded if the vehicle must pass through any environment containing particles, i.e., ice, rain, or dust. Current analytical predictions of the damage inflicted by this environment are very limited due to the lack of test data. This is particularly true for a transpiration-cooled nosetip. The test on the Holloman rocket sled track conducted in this program is the first step in the generation of the required data.

The problem associated with transpiration tips is more difficult to evaluate than for passive tips. For passive tips, increased recession is the most important item, but it is only one of the considerations for an active tip. Based on available data, recession for a metal tip will be much less. However, the permeability of the transpiration tip may be altered, resulting in a change in the flow characteristics of the tip. Unfortunately, the effect of this change on system performance is difficult to determine. It is quite likely that all material change will occur near the surface. This will block the flow and, in a real flight, cause the surface to heat up and perhaps melt. This may remove the densified material, and the tip will once again operate close to its design condition. Determination of this phenomenon must be made by testing.

The purpose of this program was to determine if a transpiration tip will experience any material degradation as a result of passing through a heavy rainfall at approximately 5,000 ft/sec. The total damage was not quite as severe as that expected during flight, but the water content was much higher.

Two tests were planned, but only one was performed. The second test was cancelled as a result of damage to the expulsion system during a test with another contractor's nosetip.

9.1 FACILITY DESCRIPTION

The Holloman rocket sled track (Figure 9-1) is described in Reference 9-1, and only a brief summary will be presented here. The track is 35,000 ft long and is equipped with spray nozzles for rain simulation. The rain field can be as long as 6,000 ft; however, only 2,400 ft were used for this test. While monorail or two-rail sleds can be used for rain erosion tests, a monorail vehicle was used here. Vehicle slowdown was accomplished by water braking.

9.1.1 Rocket Sled Configuration

The rocket sled hardware and motors were provided by the Holloman sled test track. The specific configuration used for the test was to achieve a peak velocity of 5,800 ft/sec through the rain field and consisted of six HVAR's, a Little John, and a Gila IV. A sketch of the rocket sled configuration is shown in Figure 9-2. A peak velocity of 5,580 ft/sec was eventually achieved prior to entry into the rain field.

9.1.2 Environment

The velocity of the sled as a function of time is given in Table 9-1. The time at which each of the three rockets fired is indicated.

The length of the rain field selected for this test was 2,400 ft. The mean drop size was 1.89 mm, and the liquid water content was 6.87 g/m^3 with a rain rate of 6.6 in./hr.

9.1.3 Data Acquisition and Instrumentation

Data was generated from both onboard and external detectors. Onboard data, consisting of flow rate, temperature, and pressure, was obtained through a frequency-multiplexed IRIG proportional-bandwidth FM/FM telemetry system. The FM data that was to be obtained from the telemetry system was (1) bottle pressure, (2) tip pressure, (3) tip water temperature, and (4) water flow rate. The external data consisted of sled velocity and photographic observations. Data was only obtained for the first 3.5 sec of the test because of a short in the telemetry system.

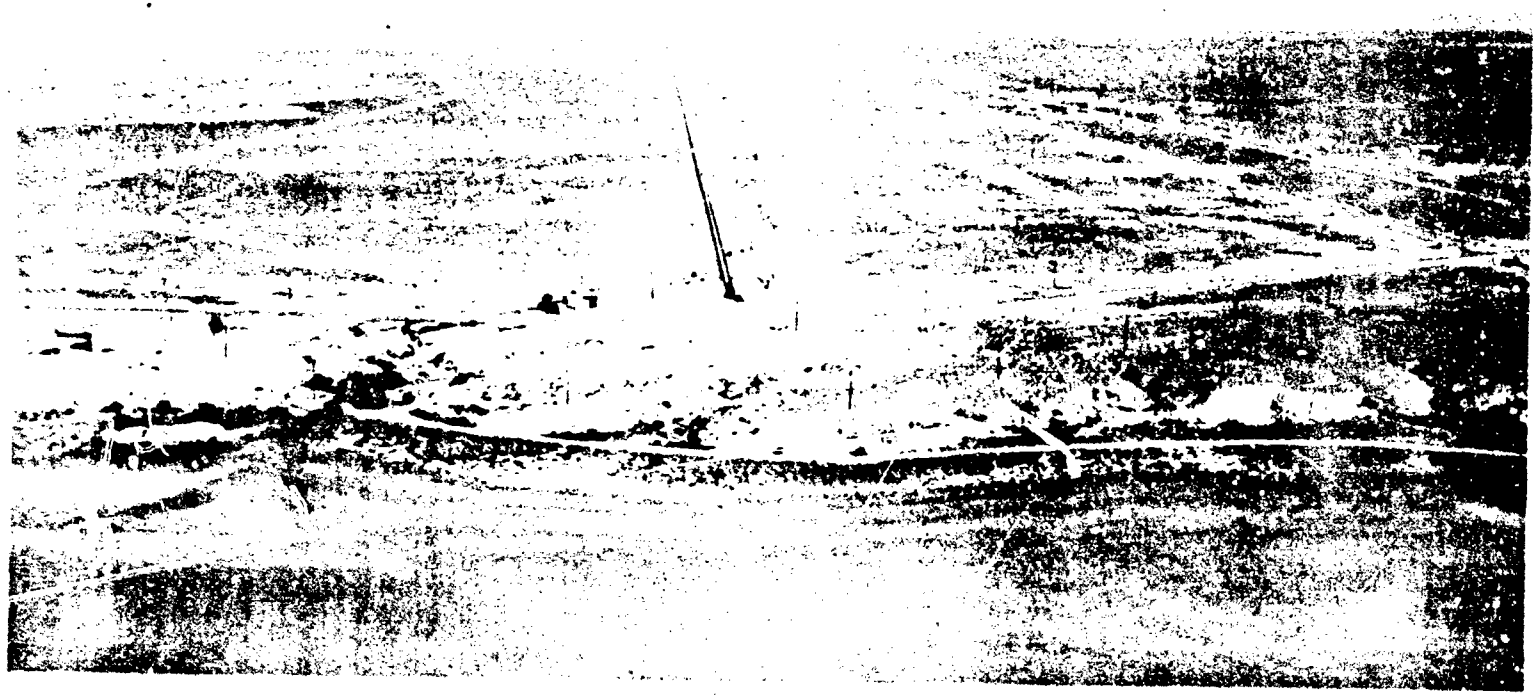
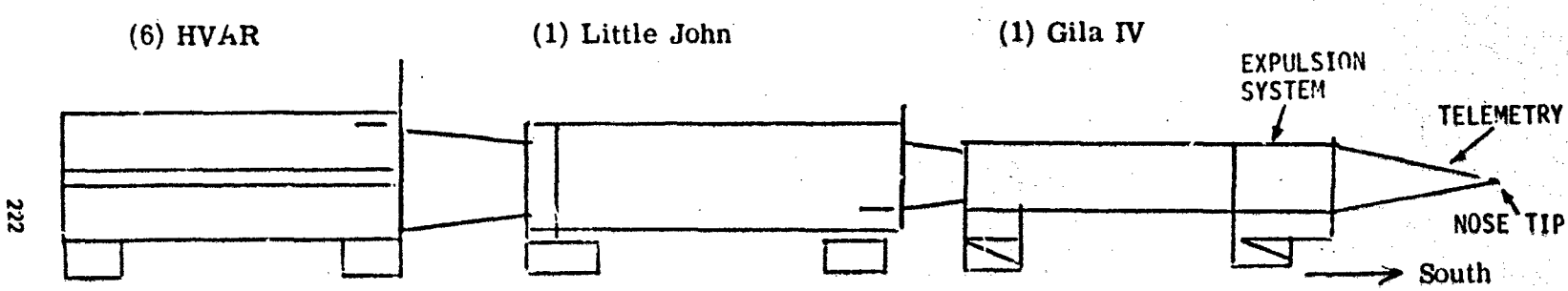


Figure 9-1. Photograph of Holloman Sled Track



222

Figure 9-2. Rocket Sled Test Configuration

Table 9-1

SLED TEST ENVIRONMENT

Field = 3.51 to 3.97 sec

Time (sec)	Velocity (ft/sec)	Rocket
0	0	6 HVAR's (0 to 1 sec)
1.0	690	1 Little John (1.0 to 2.67 sec)
2.0	1,675	
2.5	2,875	
3.0	4,512	1 Gila IV 2.67 to 17.69 sec)
3.2	5,296	
3.4	5,574	
3.8	5,067	
4.0	4,840	
4.5	4,440	
5.0	4,010	
6.0	3,490	
7.0	3,010	
8.0	2,630	
9.0	2,300	
10.0	2,030	
10.5	1,250	

Photographic coverage for these runs included seven stations of image motion cameras (IMC's), 10 stations of 16-mm fixed motion pictures cameras (FX's), and still documentary (before and after) photography. The image motion technique provided a full-length view of the test sample at intervals through the rain field.

Documentary coverage with color and black-and-white still photos was obtained to show the condition of the test cones, the vehicle, and the propulsion system before and after firing.

9.2 TEST MODEL

A schematic of the entire model is shown in Figure 9-3, and the detailed design is shown in Figure 9-4. As seen in these figures, the model consists of a transpiration nosetip, an explosive valve, a thermocouple assembly, a coiled stainless steel tube, a cavitating venturi, two pressure transducers, a turbine flow meter, a flow control mechanism, an expulsion system consisting of a water and gas reservoir, two hand valves, two stainless steel shells, and two expulsion system supports.

The nosetip is a porous 316L stainless steel tip having a 3/4-in. radius nose, a 0.265-in. skirt with a 7-deg cone half-angle, and a 0.152-in. wall thickness at the stagnation region. The tip is supported by a stainless steel 9-deg shell. The flow rate and pressure characteristics of the nosetip that was tested are shown in Figure 9-5. Point probe measurements were also made, as discussed in Reference 9-2. Details of the expulsion system and instrumentation are available in Reference 9-2.

9.3 POST-TEST ANALYSIS AND DATA REDUCTION

Post-test analyses have been performed to estimate the environmental effects on the nosetip. These include considerations of rough-wall and particle-induced heat transfer.

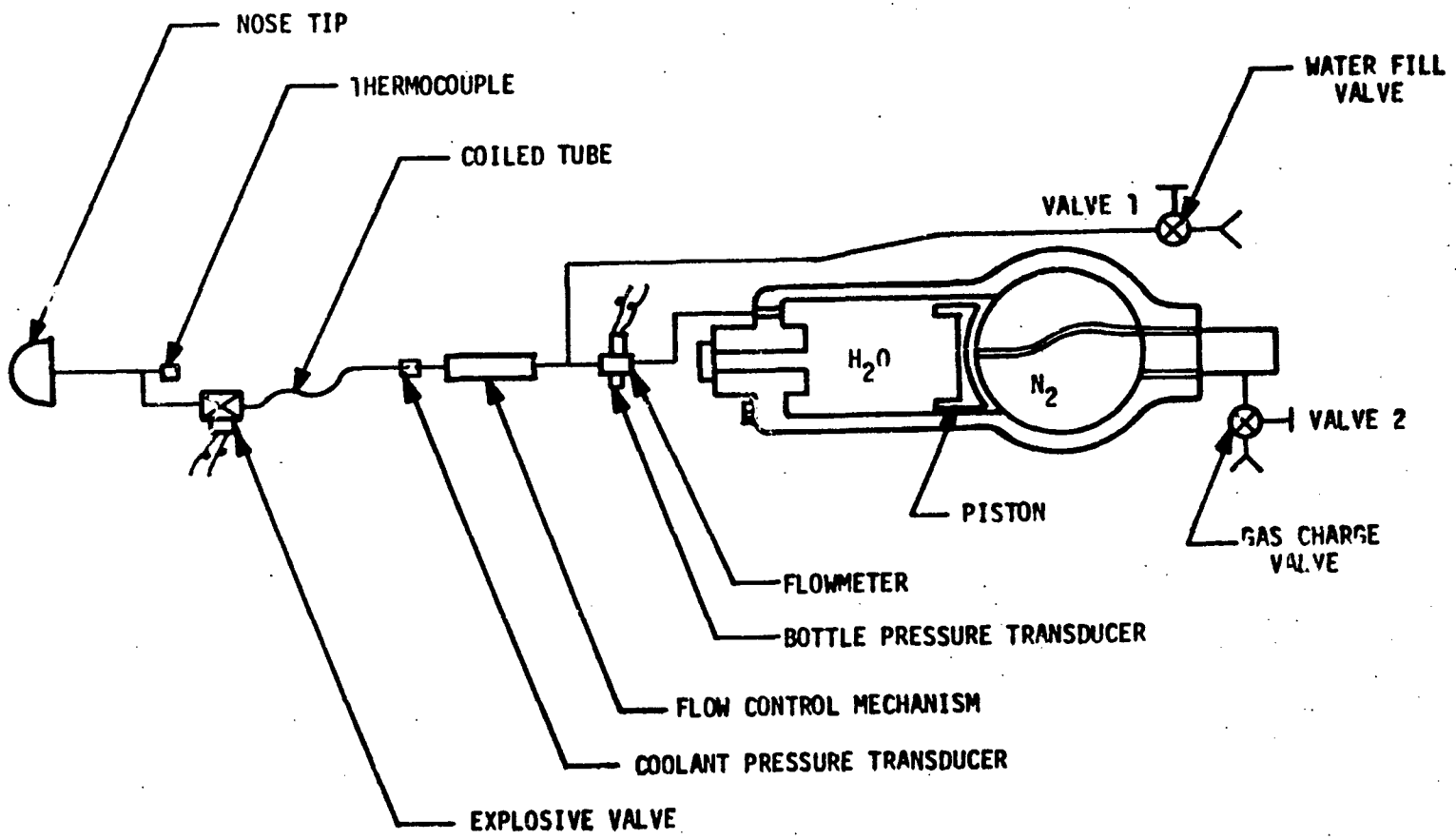
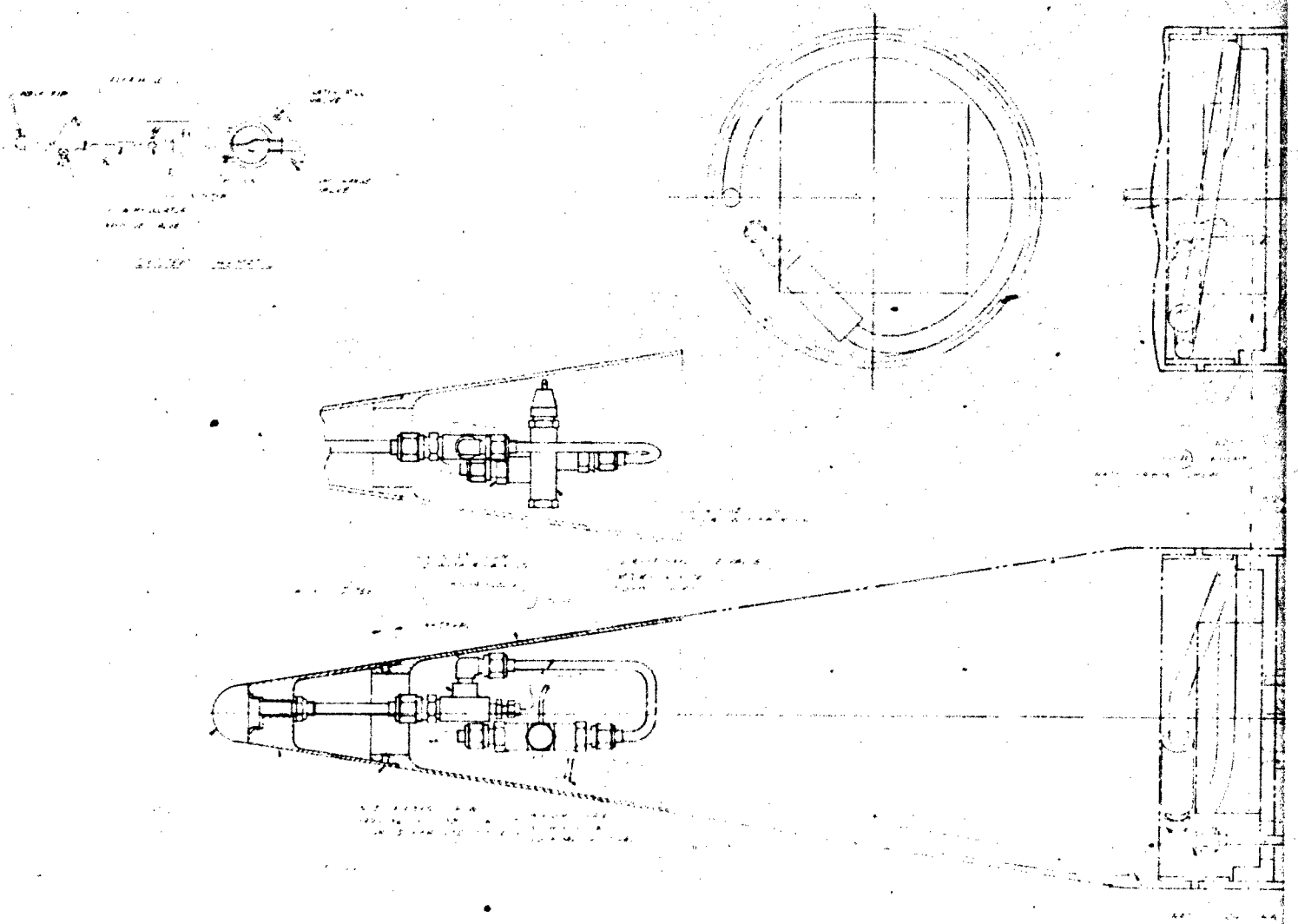
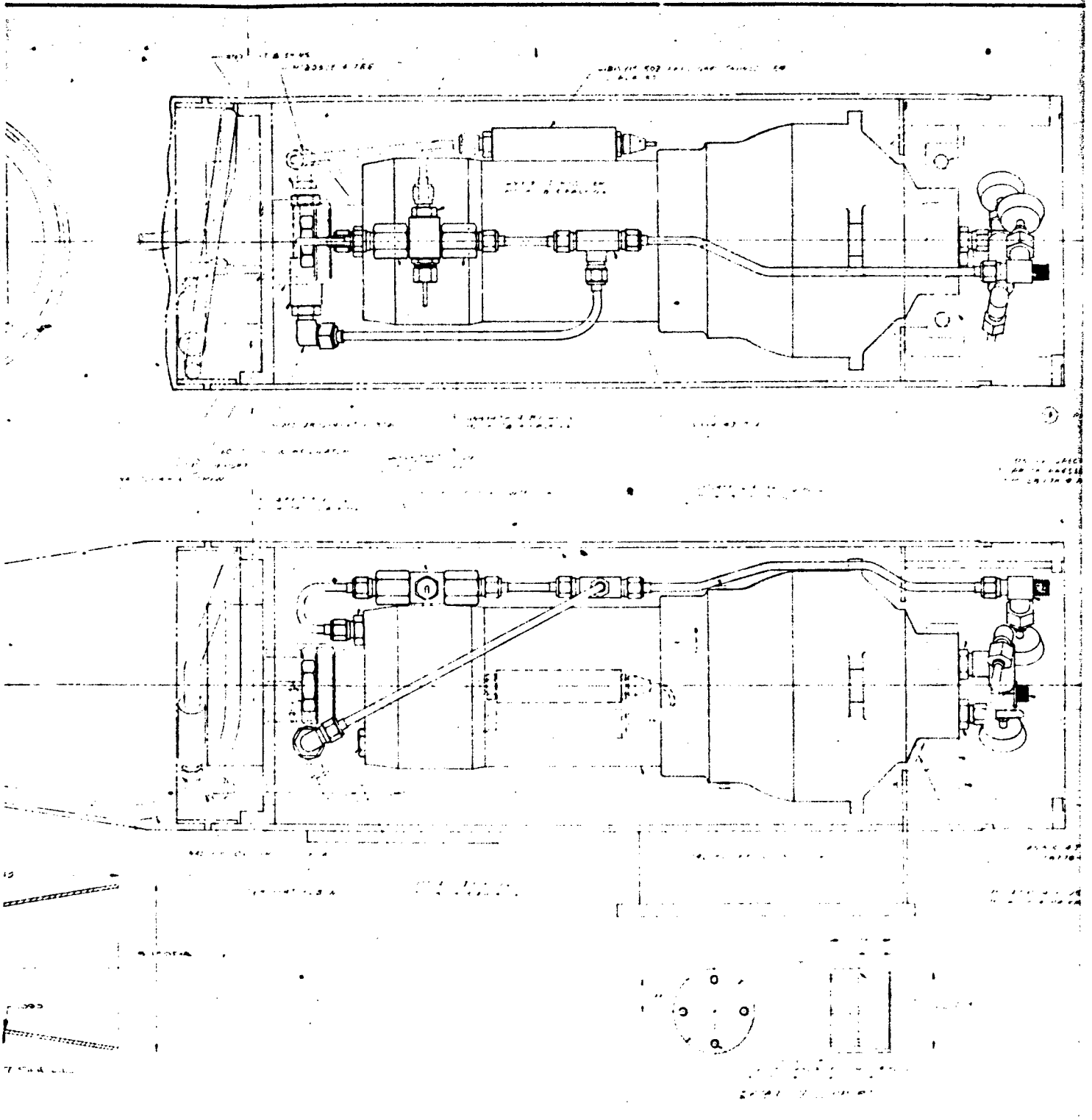


Figure 9-3. Sled Test Transpiration System Schematic





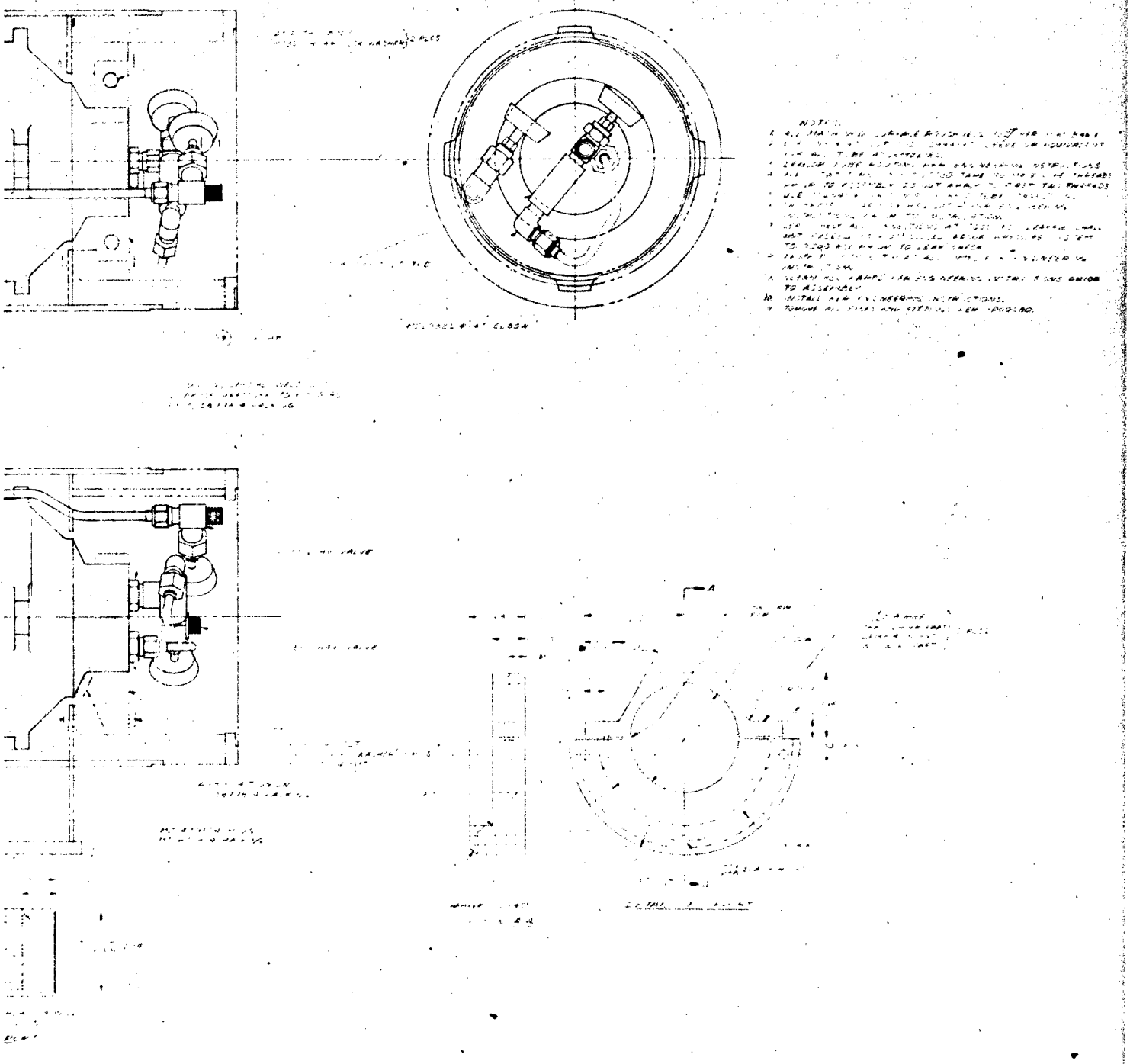


Figure 9-4. Rocket Sled Test Model

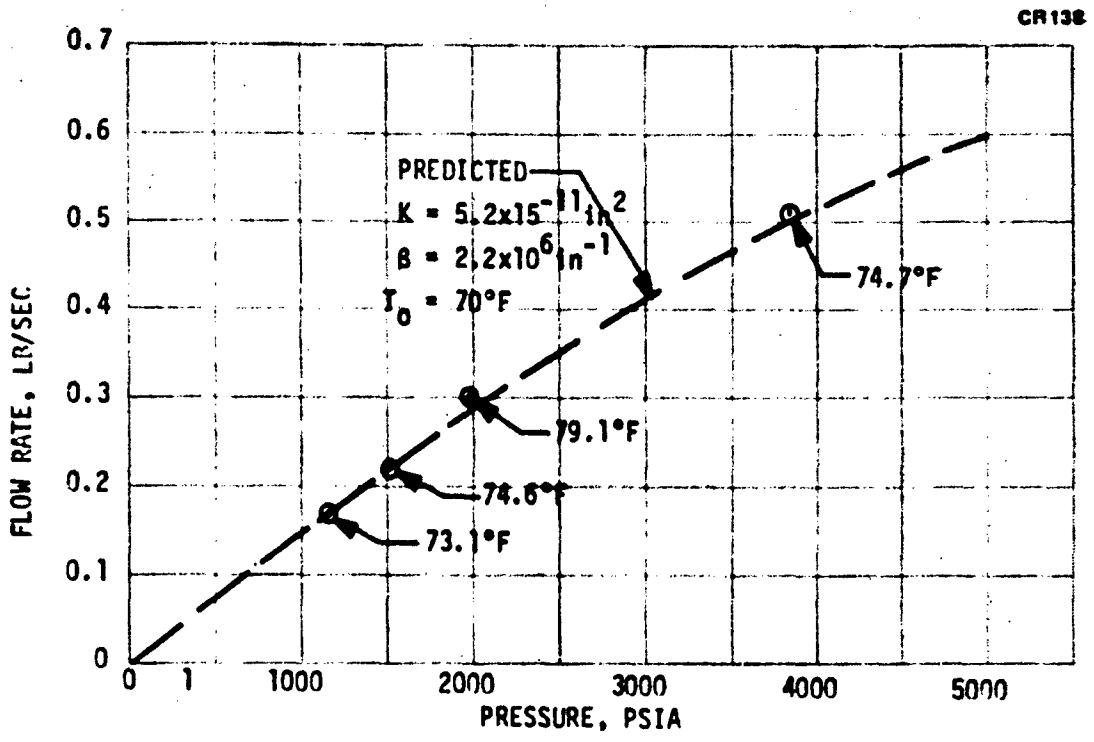


Figure 9-5. Nosetip Flow Rate vs Pressure for Tip No. 538-6

9.3.1 Environment

The velocity history actually experienced by the sled is shown in Figure 9-6. Peak velocity was not experienced within the rain field due to staging differences between the test and predicted sled performance. Stagnation pressure and smooth-wall heat transfer histories are given in Figure 9-7. In addition to the smooth-wall heating, the effect of particle impact on the stagnation heat transfer has been evaluated.

The technique used to estimate the particle-induced heating is that described in Reference 9-3. This method is empirical, based on tests with small dust particles impacting spherical models. Based on the results presented, the heat transfer increase is caused by the occurrence of a separation region in front of the tip due to interference between particles. Figure 9-8 shows the flow phenomena observed. The application of this method to a rain environment is questionable, since much of the particle interference is caused by rebounding from the nosetip surface, and this phenomenon should be less

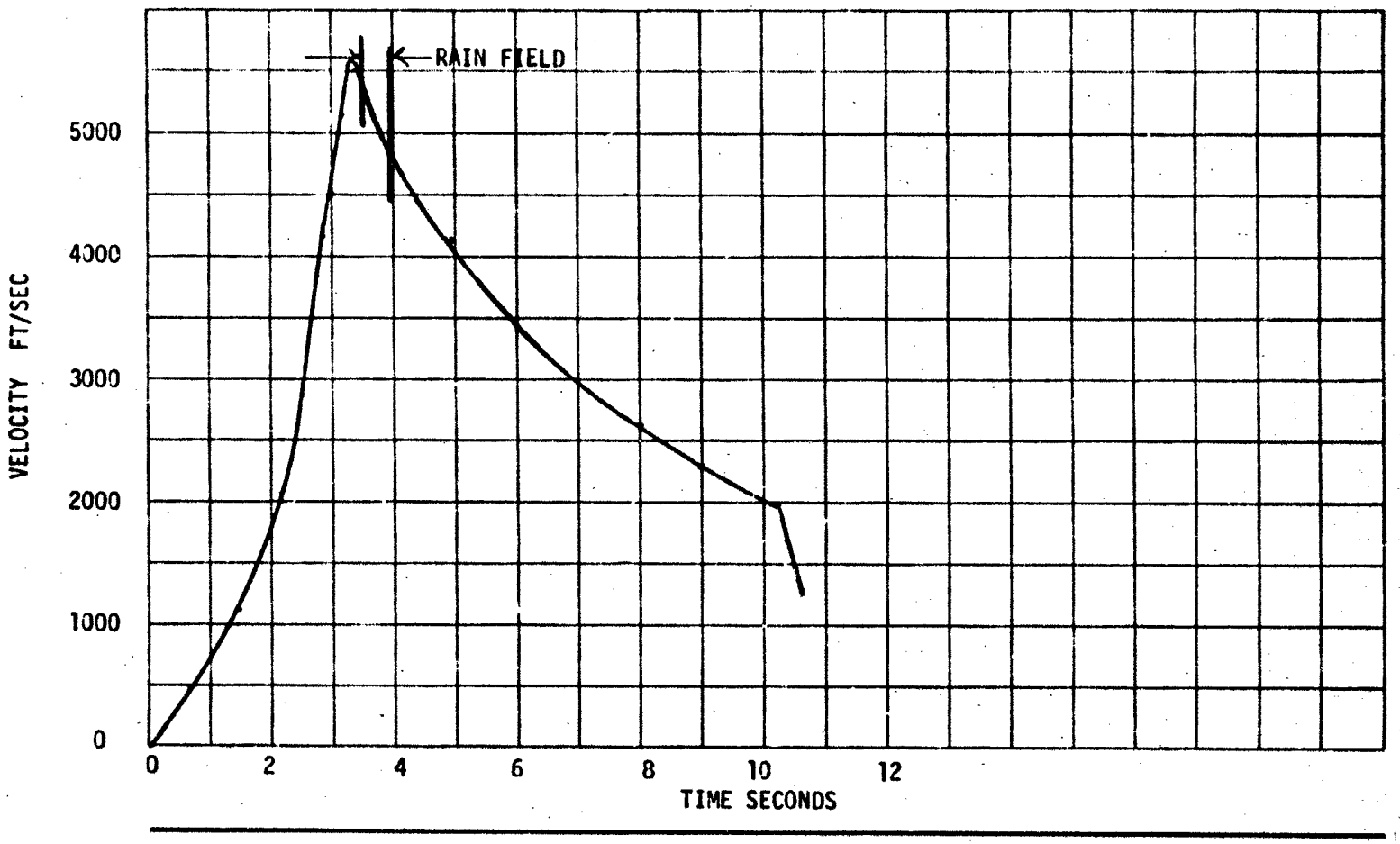


Figure 9-6. Sled Velocity History

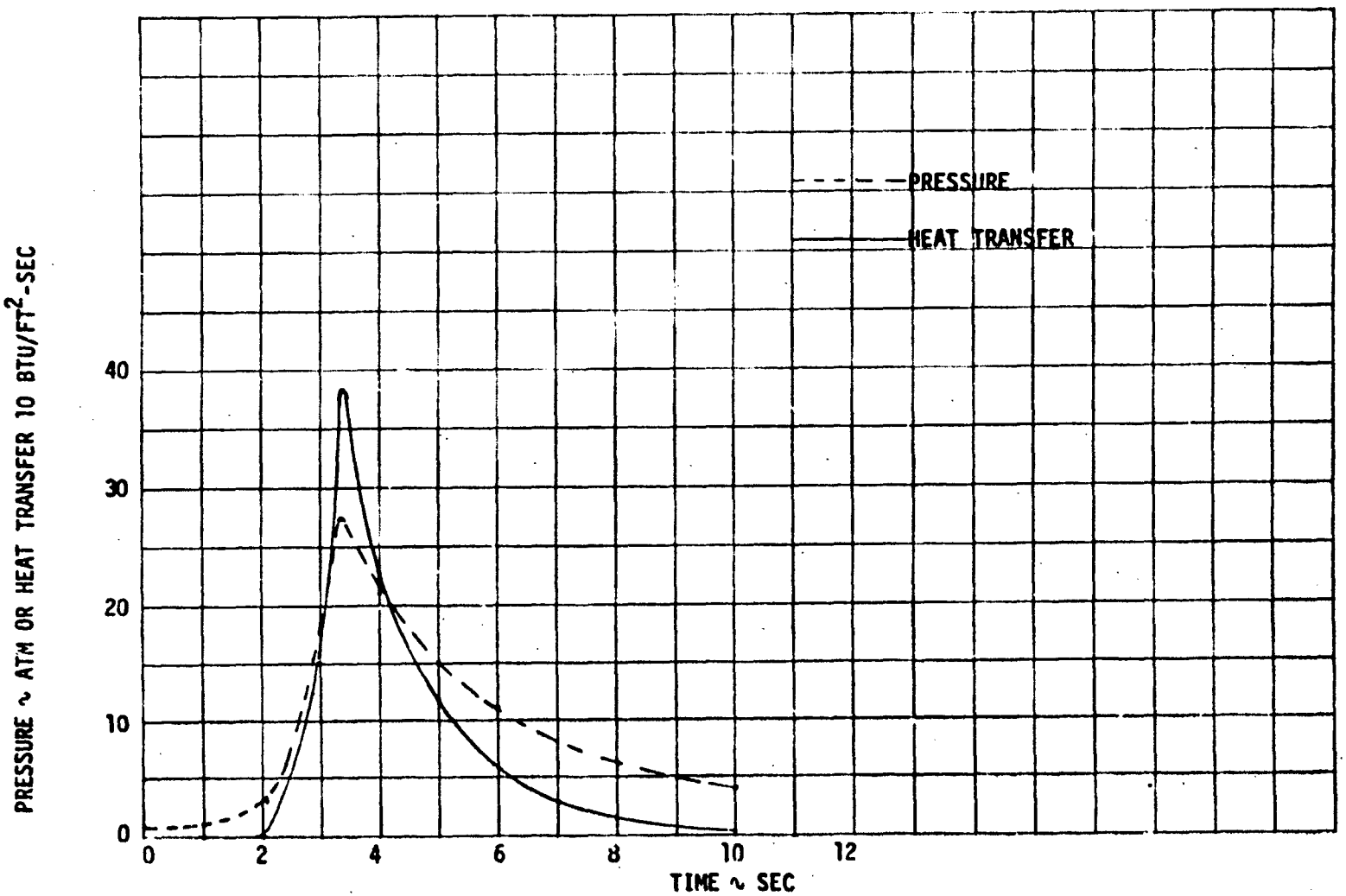


Figure 9-7. Stagnation Point Heat Transfer and Pressure Histories

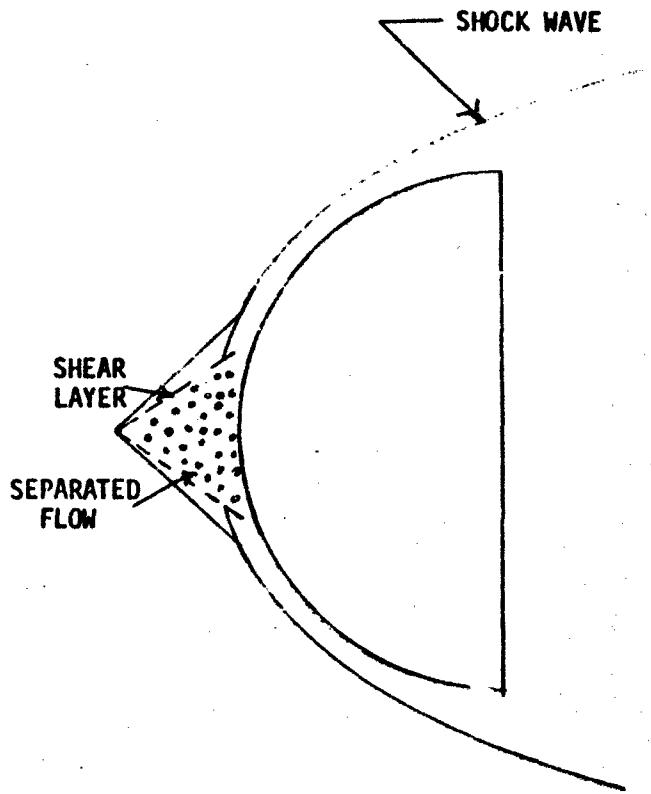


Figure 9-8. P[illegible] .Juced Flow Separation

with rain. However, the particle densities are greater for the Holloman field than for the tests of Reference 9-3. It may be that the phenomenon would still occur, but to a lesser extent. Schlieren movies through the rain field would be required to accurately evaluate the real occurrence of this phenomenon. Since none have been obtained, calculations of the particle-induced heating were accomplished as described in Reference 9-3 (Equation 9-1). This relationship

$$\frac{N_{c_{rain}}}{N_{c_o}} = 1.0 + \left[\left(\frac{M_\infty^2 \, Re_\infty}{2.24 \times 10^5} \right)^{0.3} - 1.0 \right] \left[1.0 - \frac{1.0}{\frac{955 \, m_{H_2O}}{2 m_{air}} + 1.0} \right] \quad (9\text{-}1)$$

showed an increase in stagnation-point heat transfer by a factor of 9. This is an extremely large increase, and although it is likely to be conservative, it indicates that the heating environment could be much higher than anticipated. The data available indicates that the heating around the nosetip decreases from the stagnation point values similar to a laminar flow distribution. No indication is given for the combined effects of particle-induced separation and rough-wall turbulent flow. Since there is no data available for the coupled phenomena, particle heating has only been analyzed for the stagnation point.

Both smooth-wall and rough-wall heat transfer were computed for the turbulent flow regions away from the stagnation point. Rough-wall heat transfer was computed using the correlation recommended in Reference 9-4. The roughness height used was the average crater depth measured after the test. These values are shown in Figure 9-9 for a point 17 deg away from the stagnation point, or the point of minimum coolant margin. These values are approximately 30 percent lower than the peak heating values. As can be seen, the rough-wall heating is about 2.5 times as high as the smooth-wall heating.

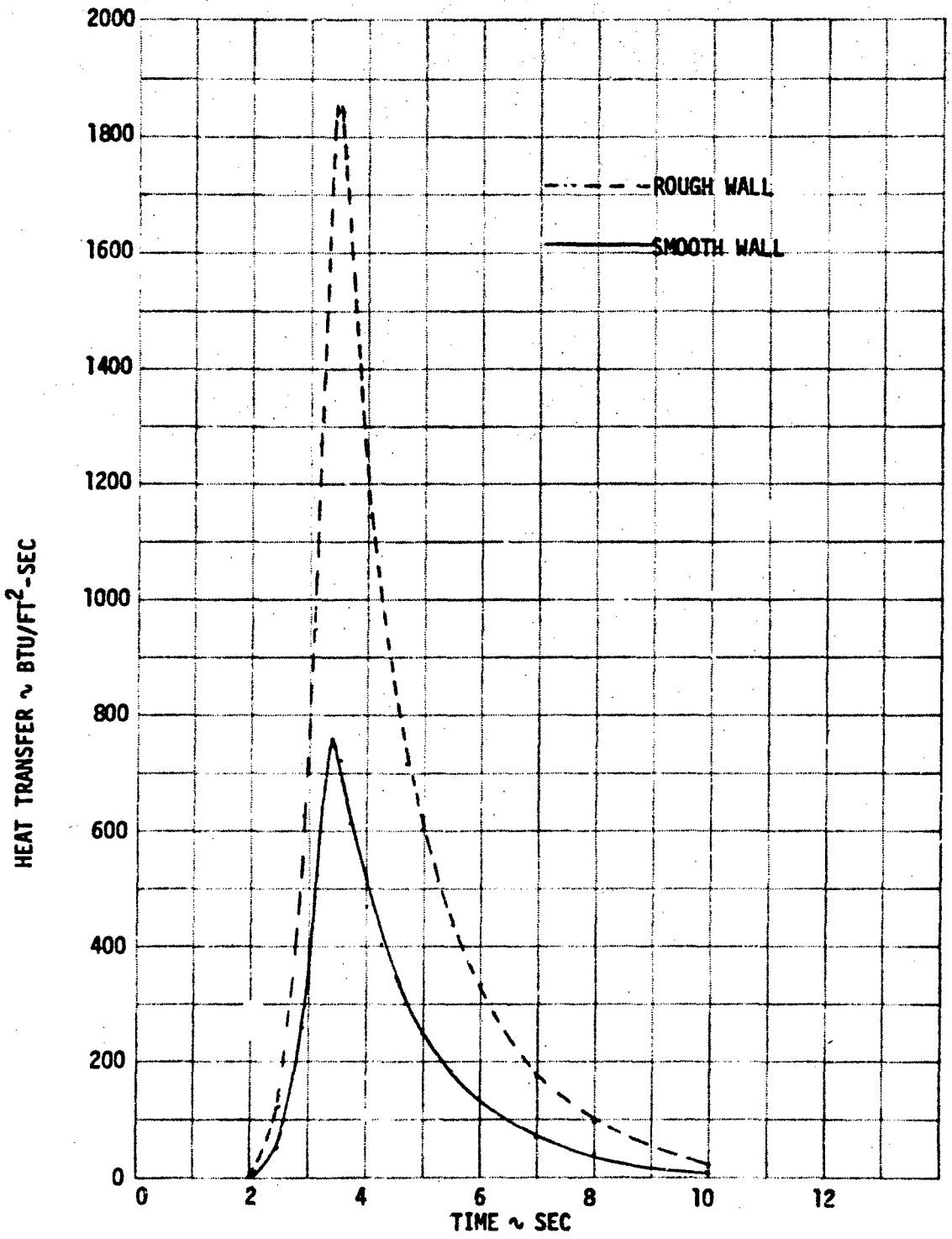


Figure 9-9. Heat Transfer Histories at Location of Minimum Coolant Margin

9.3.2 Coolant Flow Margins

Coolant margins were computed for each of the environments discussed above. This was accomplished by first determining the coolant flow rates achieved during the test. Since telemetry was lost after 3.5 sec, the flows could not be measured directly for most of the test. The flow history given in Figure 9-10 has been extrapolated from the early time measurements using the pretest analytic model. Flow distributions through the tip were then computed using a three-dimensional porous matrix flow computer program. It was assumed that the permeability of the tip was not changed during the test.

Coolant margins were then computed by applying Equation 9-2 at each point around the nosetip.

$$\text{Margin} = \frac{\dot{m}_{actual}}{\dot{m}_{ideal}} \qquad (9\text{-}2)$$

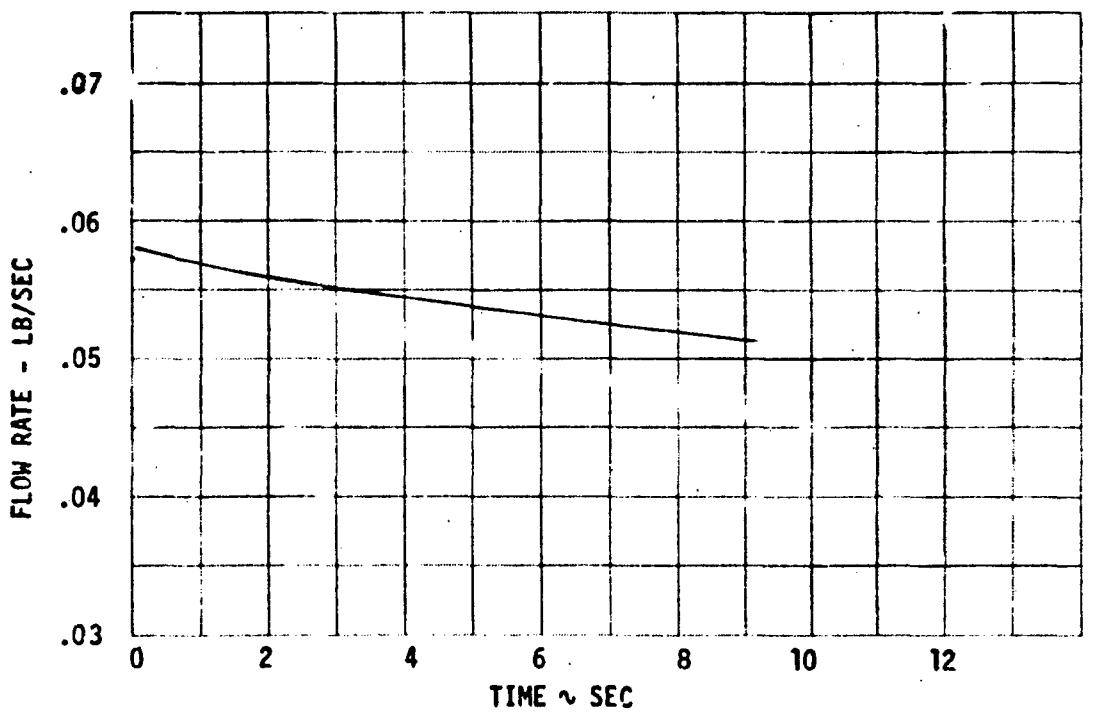


Figure 9-10. Flow Rate History

The minimum margin for both the rough-wall and smooth-wall cases occurred at a point 17 deg from the stagnation point. These margins during the critical time period are shown in Figure 9-11. As can be seen, if rough-wall heating existed through the entire rain field, margins less than 1 were possible. This means that insufficient coolant was reaching the surface to keep the surface at or below the boiling point of water.

For the environment created by particle interference, coolant margins considerably below 1 exist through the entire rain field. These margins have been used to correlate the damage experienced by the tip.

9.3.3 Nosetip Temperatures

Surface temperatures have been computed for a variety of conditions to determine the maximum temperatures possible. Calculations were performed for all environments for both the stagnation point and the point of maximum heating. All analyses were conservative in that they neglected the effect of water flow through the trip.

Stagnation-point temperatures were predicted for the following cases: (1) nominal heat transfer through the entire test; (2) no heat transfer until the rain field was encountered, and then nominal heat transfer for the remainder of the test; and (3) no heat transfer until entry into the rain field, particle heating through the field, and nominal heating thereafter. Heating was neglected prior to the rain field in an attempt to simulate a condition where coolant was flowing prior to the rain field and was prevented from flowing after the encounter with the rain. The results for the three cases mentioned above are given in Figure 9-12. As expected, the worst case is for the particle-heating environment.

Figure 9-13 gives the surface temperatures predicted at the peak heating point for the following three cases: (1) all smooth-wall heating; (2) all rough-wall heating; and (3) no heating until the rain field was encountered, then rough-wall heating for the remainder of the test.

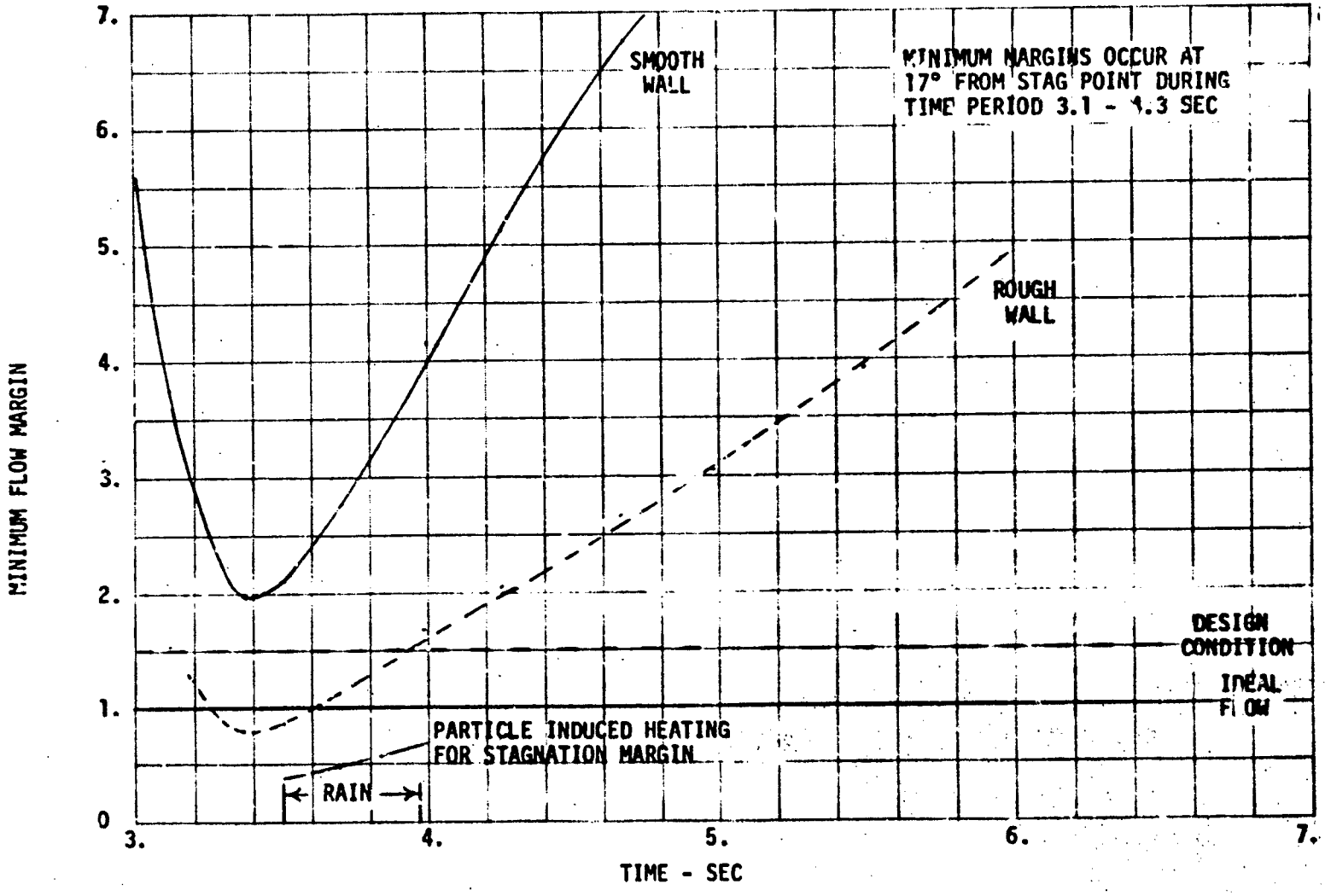


Figure 9-11. Coolant Flow Margins for Sled Test

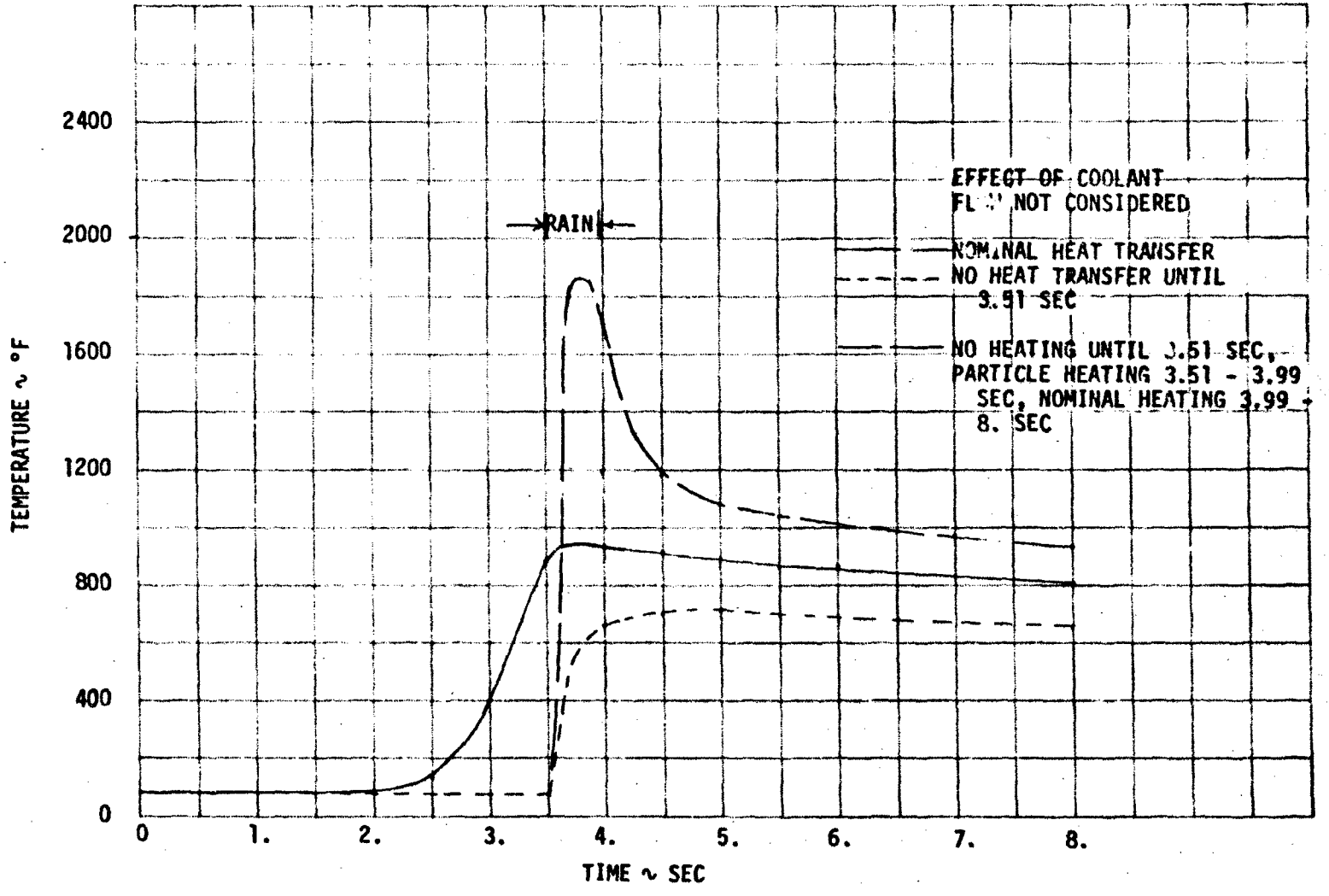


Figure 9-12. Predicted Sled Test Stagnation Point Temperature Histories

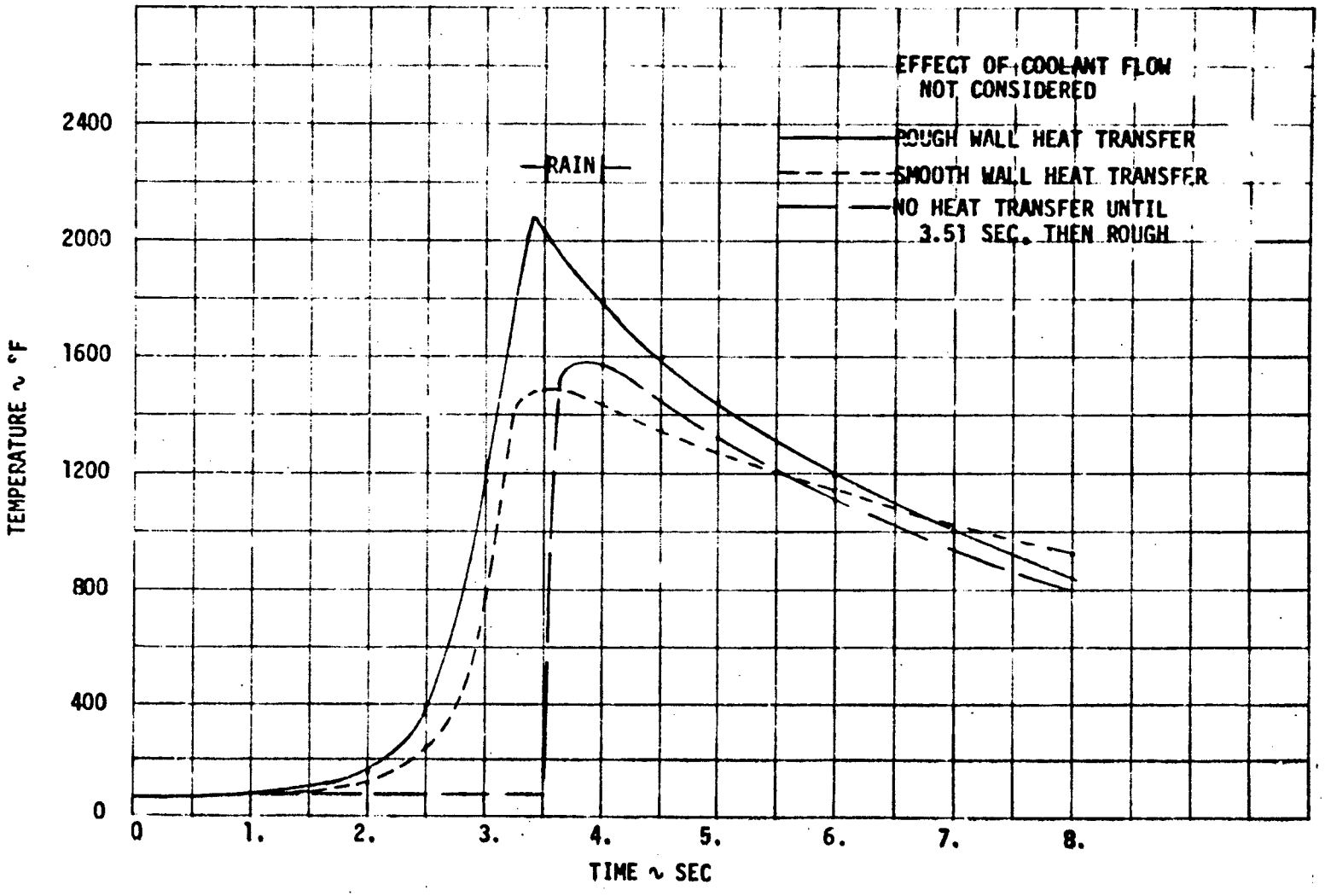


Figure 9-13. Predicted Sled Test Temperature Histories at Peak Heating Location (33 Deg)

From these results, it can be concluded that there was almost no chance of the nosetip melting, regardless of the phenomena which occurred. However, it is quite possible that the material got hot enough to become quite soft, particularly for the particle-induced heating environment.

9.3.4 Physical Damage

The nosetip did experience some damage in the forward region. Penetration by the rain into the material averaged slightly less than 30 mils. The permeability reduction in the damaged region was measured at about 50 percent.

9.4 RESULTS OF RELATED TESTS

9.4.1 Holloman Sled Tests of Dry, Porous, 316L Stainless Steel

Thirteen 316L porous stainless steel flat-plate specimens were tested at the Holloman facility under the direction of George F. Schmitt, Jr. The samples were furnished by MDAC and were subjected to the rain field in a strictly dry condition (i. e., no water in the porous matrix).

9.4.2 Test Environment, Matrix, and Models

Table 9-2 presents the environment (rain conditions, velocity, exposure time, etc.), the configuration, data tested, and the exposure angle at which the models were exposed.

The models shown in Figure 9-14 were 1.25 in. square with a 1.0-in. square exposure area. Plate thickness was 0.5 in.

9.4.3 Test Configuration and Propulsion Systems

The plates were mounted on three types of test configurations (Figures 9-15, 9-16, and 9-17) which were designated the 13.5-deg cone, the 30-deg cone, and the small wedge. Additional details of these configurations and mountings may be found in References 9-5 and 9-6. Table 9-3 indicates the Mach number, test fixture, and propulsion systems used for each test.

Table 9-2

MATRIX OF HOLLOMAN SLED TESTS OF DRY, POROUS SAMPLES

Test No.	Test Date	Mach No. (Approximate)	Rain Field Length (ft)	Rain Rate (in./hr)	Particle Size (mm)	Average Velocity (ft/sec)	Exposure Angle (deg)	Exposure Time (sec)
3OR-D2	8 Dec 70	5.0	2,080	4.6	1.9	5,455.35	30.0	0.3815
3OR-E3	6 Dec 70	5.0	2,090	4.6	1.9	5,447.8	13.5	0.3831
3OR-F1	9 Mar 71	4.0	2,010	4.6	1.9	4,196.4	45	0.479
3OR-G1	16 July 71	5.5	6,020	4.6	1.9	3,168.35	45 and 60	1.9005
3OR-K5A	6 June 72	5.5	2,120	4.6	1.9	6,559.38	13.5	0.3229

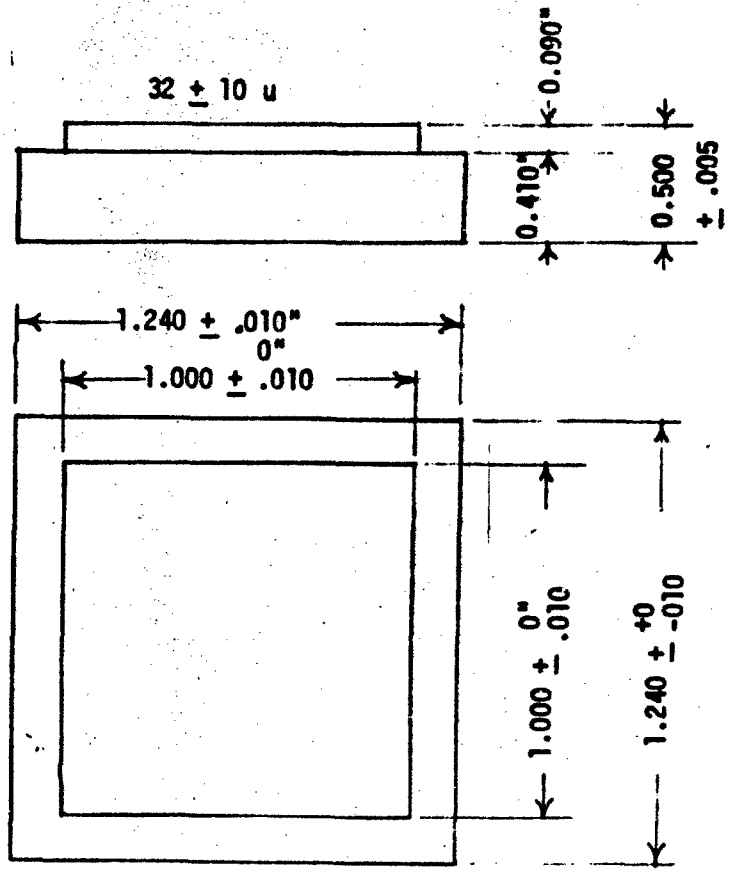


Figure 9-14. Sample

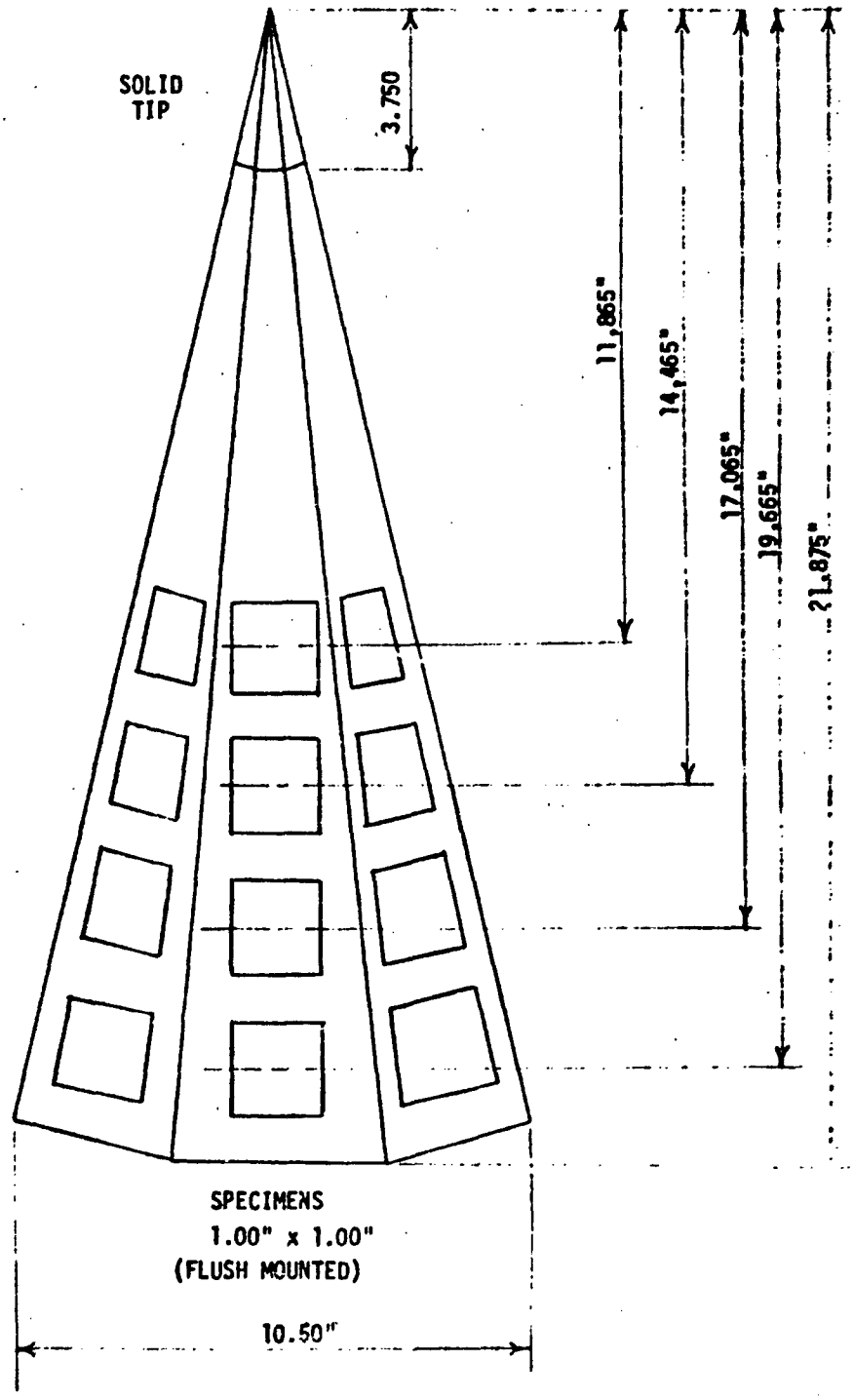


Figure 9-15. AFML 13.5-Deg Half-Angle Cone Schematic

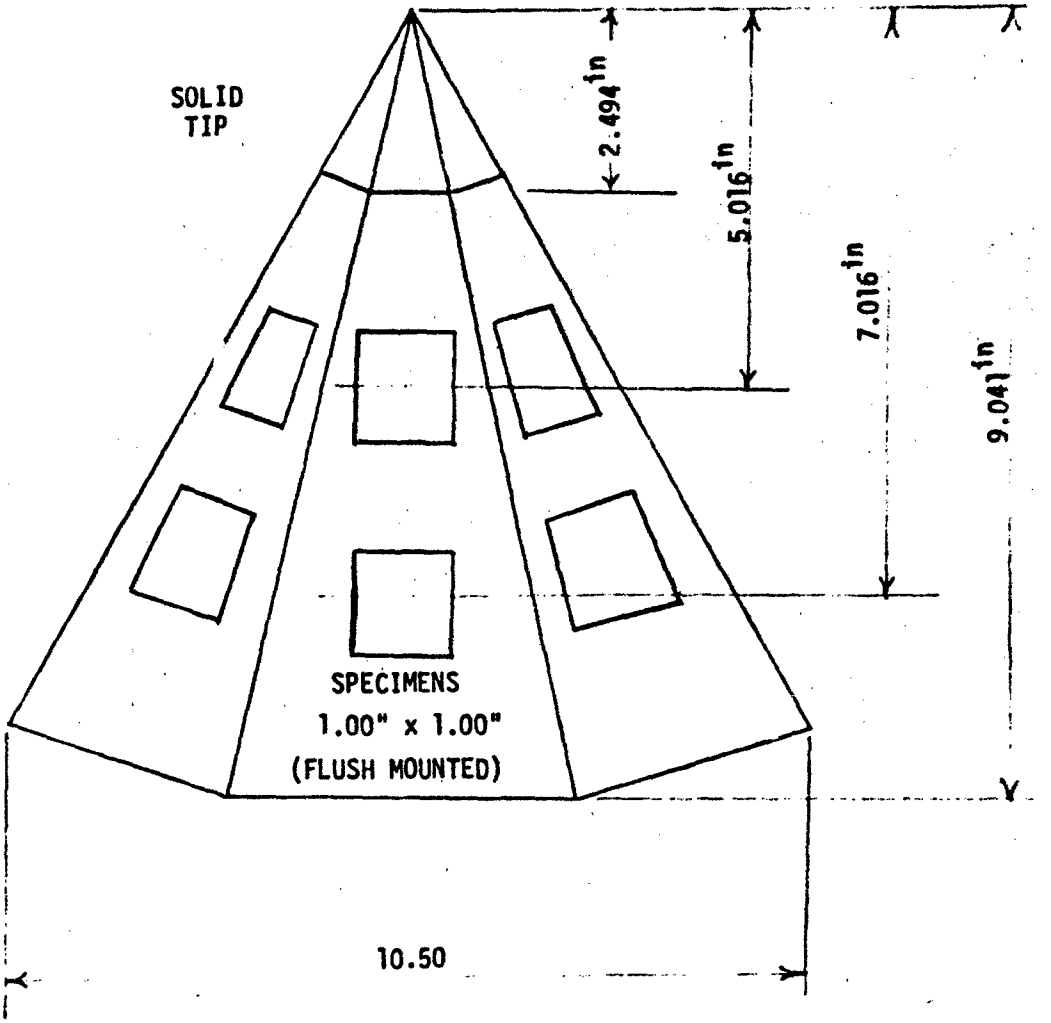
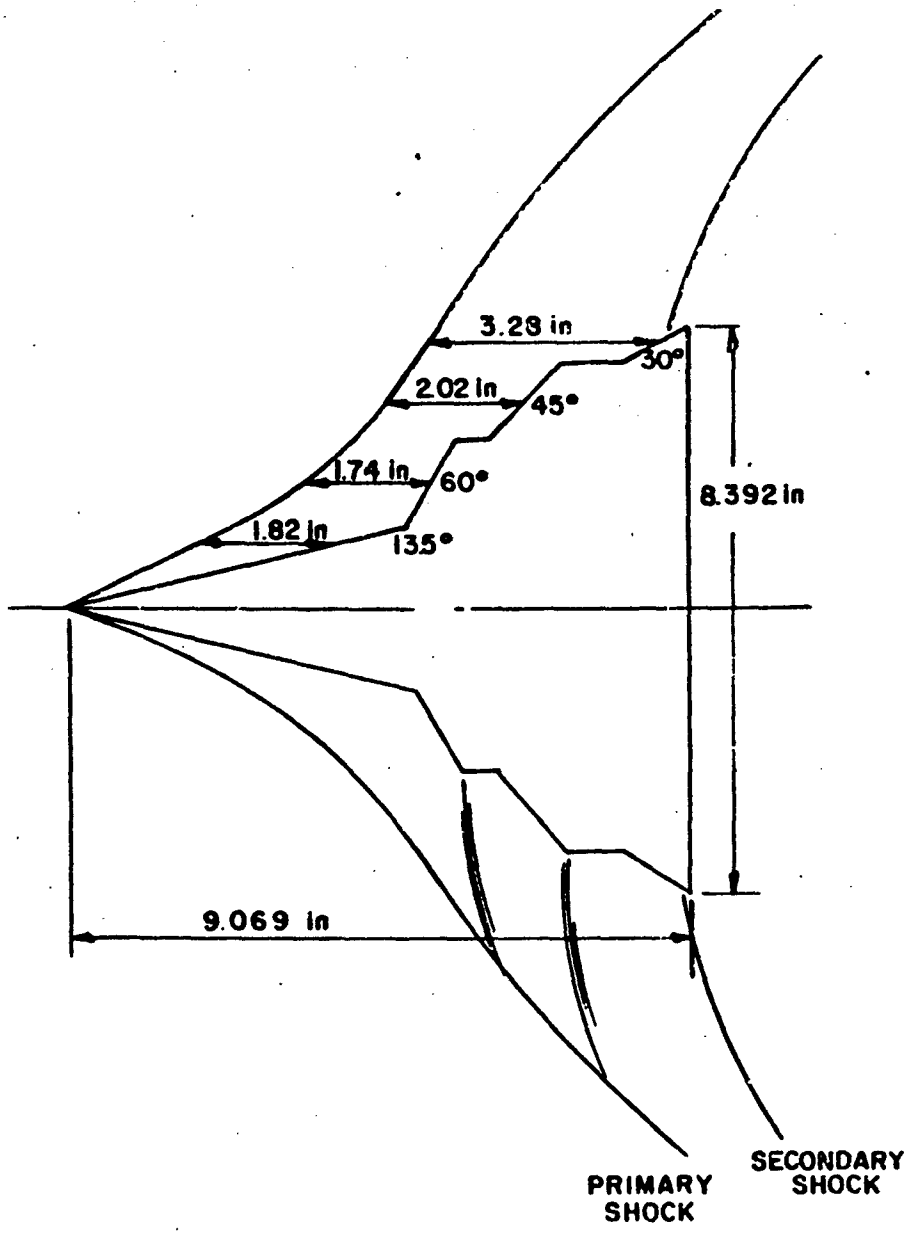


Figure 9-16. AFML 30-Deg Half-Angle Cone Schematic



SCHLIEREN PHOTOGRAPH OF RUN 12R-F6
29 AUGUST, 1968

$V_{PHOTOGRAPH}$ = 4644 FPS

Figure 9-17. Mach 4.0 Schematic and Shock Wave Pattern for Small Wedge

Table 9-3
VEHICLE TEST CONFIGURATION

Run No.	Mach No.	Test Fixture	First-Stage Booster	Second-Stage Booster	Third-Stage Booster
3OR-D2	5.0	30-deg cone	1 LaCrosse	1 Gila IV	------
3OR-E3	5.0	13.5-deg cone	4 HVAR's	1 Little John	1 Gila IV
3OR-F1	4.0	Small wedge	1 Nike	1 Nike	4 M-58's
3OR-G1	3.0	Small wedge	1 Nike	1 Nike	4 M-58's
3OR-K5A	5.5	13.5-deg cone	4 HVAR's	1 Little John	1 Gila IV

9.4.4 Procedures

Photographs were taken at low and high magnifications to record surface damage. A weight measurement was made of each sample tested and was compared to weight values obtained prior to test in order to determine weight loss from erosion. Nitrogen gas flow measurements were made and compared to pretest values. The gas-flow evaluation was conducted by measuring the time required to collect 100 cc of nitrogen gas at a pressure of 100 psi passed through the specimen from a 1/4-inch orifice. Percent increase in time to collect 100 cc of gas was calculated.

Surface roughness measurements were made to determine the maximum difference in surface contour high and low values. A dial gage with an approximate 1/32-in.-diameter rounded tip was used. The machined surface at the edge of the exposed area was used for the reference plane. Further surface damage evaluation was made using the scanning electron microscope. A metallographic cross section was made of the sample exhibiting the most severe surface damage to determine extent of subsurface deformation.

9.4.5 Results and Discussion

9.4.5.1 Reduction in Gas Flow

Tabulated results for the weight change, surface roughness, and reduction in gas flow (as measured by percent increase in time required to fill 100 cc

when forcing nitrogen gas through the erosion specimen) are presented in Table 9-4. The surface appearance of all test specimens is shown in Figure 9-18. The most severe surface damage occurred for the Mach 5.0, 30-deg exposure condition (MDAC Specimen No. 259-4, Figure 9-19), which also had the highest percent time increase for gas flow. The effect of exposure angle on surface damage was more significant than the effect of velocity for the Mach 5.0 and Mach 5.5 specimens (Figure 9-19). Specimen 259-8, exposed to Mach 5.5 at 13.5 deg, had only a 15-percent gas flow time increase, as compared to Specimen 259-4, exposed to Mach 5.0 at 30 deg, which had a 3,720-percent gas flow time increase. The percent gas flow time increase, as a function of exposure angle and velocity, is presented in Figure 9-20. The percent gas flow time increase (gas flow reduction) was greater for the Mach 3.0 specimens than for the Mach 4.0 specimens for equal exposure impingement angles. This is to be expected when noting that the Mach 3.0 specimens were exposed in the rain field approximately four times longer than the Mach 4.0 specimens, i.e., 1.9 sec compared to 0.48 sec (Table 9-4). This condition would allow much more time for the water drops to close the surface pores in relation to only a slight increase in velocity. The rain field length for the Mach 3.0 specimens was 6,020 ft, compared to only approximately 2,050 ft for all other specimens.

9.4.5.2 Surface Roughness

Evaluation by surface roughness, although not as revealing or precise, did show the same trends (as a function of exposure angle and velocity, Figure 9-21) as shown for reduction in gas flow, Figure 9-20. A distinction between Mach 3.0 and Mach 4.0 sample surface roughness was not observed. In fact, distinction in surface roughness would not necessarily be expected, since the lower velocity and longer time experienced by the Mach 3.0 samples could result in more surface pore closing, and possible 1- to 2-mil damage depth, without creating deeper pits. Therefore, the reduction in gas flow would be greater, but the depth of surface irregularities could be equal for the Mach 3.0 and Mach 4.0 samples.

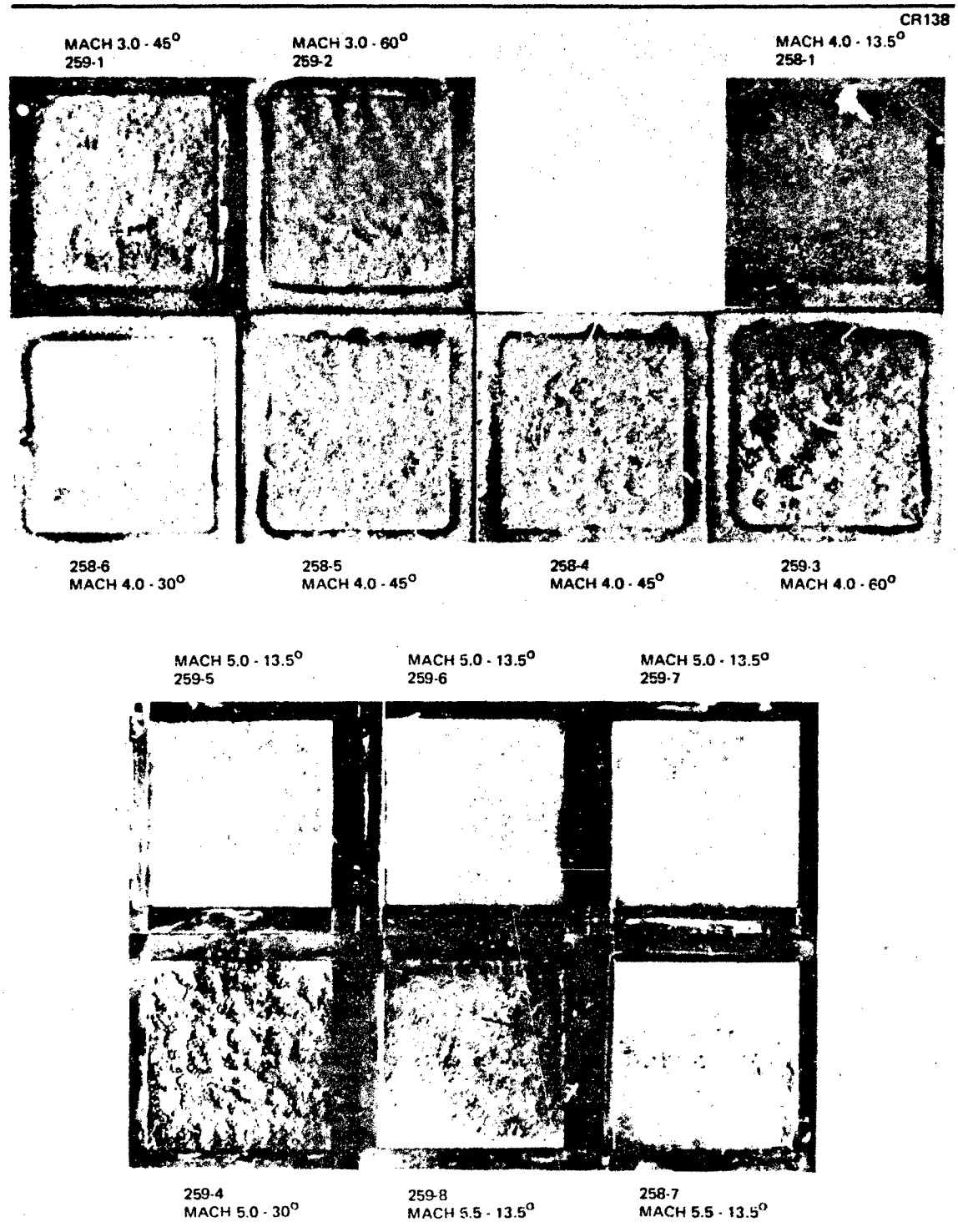
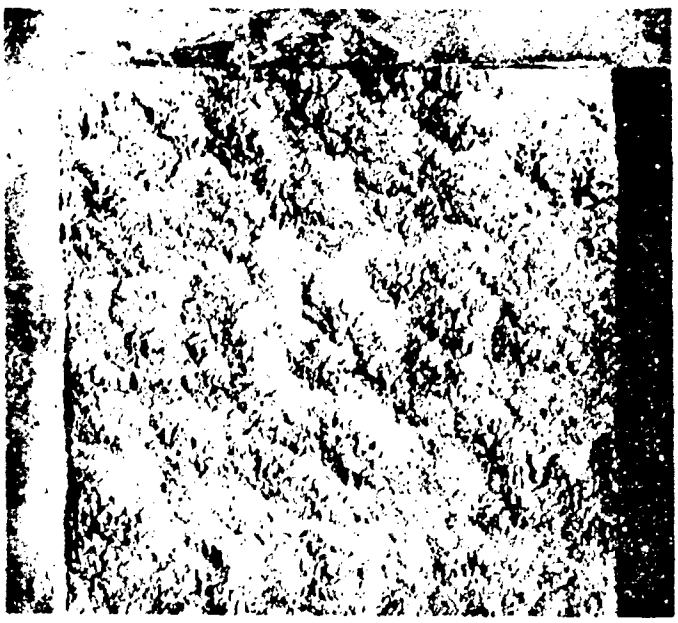


Figure 9-18. Rain Erosion Specimens



3.5X

259-8 MACH 5.5 - 13.5° 15% GAS FLOW TIME INCREASE



3.5X

259-4 MACH 5.0 - 30° 3,720% GAS FLOW TIME INCREASE

Figure 9-19. Effect of Exposure Angle on Surface Appearance and Percent Gas Flow Time Increase

Table 9-4

RAIN EROSION SPECIMEN DAMAGE EVALUATION DATA

MDAC Specimen No.	Hellion an Code	No.	Mach Number	Exposure Angle (deg)	Average Velocity (ft/sec)	Exposure Time (sec)	Rain Field Length (ft)	Weight (grams)			N_2 Gas Flow ** (1/4 in. Orifice, 100 psi/100 cc)			Surface Roughness * (in.)		
								Pre-test	Post-test	Change (percent)	Pre-test	Post-test	Change (percent)	High	Low	Difference
259-1	15-4.0-R-6	18	3.0	45	3,168.4	1.90	6,020	83.9453	83.9478	+0.0025	61.0	81.3	+33.3	0.0020	0.0025	0.0045
259-2	15-4.0-R-7	19		60				83.4023	83.3945	-0.0078	79.9	1,444.5	+1,710	0.0025	0.0070	0.0095
258-1	15-4.0-R-1	33	4.0	13.5	4,196.4	0.479	2,010	83.4169	83.4196	+0.0027	61.6	66.0	-7.1	0.0015	0.0	0.0015
258-6	15-4.0-R-5	40		30				84.3498	84.3519	+0.0027	73.9	78.3	+6.0	0.0010	0.0010	0.0020
258-5	15-4.0-R-3	35		45				83.6714	83.6755	+0.0041	71.0	65.7	-7.4	0.0020	0.0020	0.0040
258-4	15-4.0-R-4	39		45				84.4650	84.4673	+0.0023	69.5	77.4	+11.4	0.0020	0.0030	0.0050
258-3	15-4.0-R-2	34		60				84.4462	84.4468	+0.0006	63.2	367.0	+480	0.0030	0.0070	0.0100
259-5	15-5.0-R-3	17	5.0	13.5	5,447.8	0.383	2,090	77.9695	77.9715	+0.0020	84.2	88.2	+4.6	0.0010	0.0005	0.0015
259-6	15-5.0-R-4	18		13.5				77.3158	77.3180	+0.0022	69.2	83.7	+21.0	0.0015	0.0010	0.0025
259-7	15-5.0-R-5	19		13.5				78.4964	78.4982	+0.0018	80.0	83.4	+4.3	0.0020	0.0005	0.0025
259-4	15-5.0-R-2	15		30.0	5,455.4	0.382	2,080	77.7657	77.7263	-0.0394	76.2	2,909.0	+3,720	0.0030	0.0090	0.0120
259-8	15-5.0-R-6	17	5.5	13.5	6,559.4	0.323	2,120	78.2456	78.2516	+0.0060	73.0	84.3	+15.5	0.0040	0.0010	0.0050
258-7	15-5.0-R-1	19	5.5	13.5				77.9077	77.9145	+0.0068	68.0	111.6	+64.2	0.0030	0.0010	0.0040

*Dial gage was used with a smooth edge of the specimen as the reference plane.

**Time in seconds required to collect 100 cc of N_2 gas at a pressure of 100 psi through a 1/4 in. orifice.

Notes

1. Rain rate: 4.6 in./hr
2. Mean drop size: 1.9 mm dia
3. Test dates: Mach 3.0 - July 1971, Mach 4.0 - Mar 1971, Mach 5.0 - Dec 1970, Mach 5.5 - June 1972.

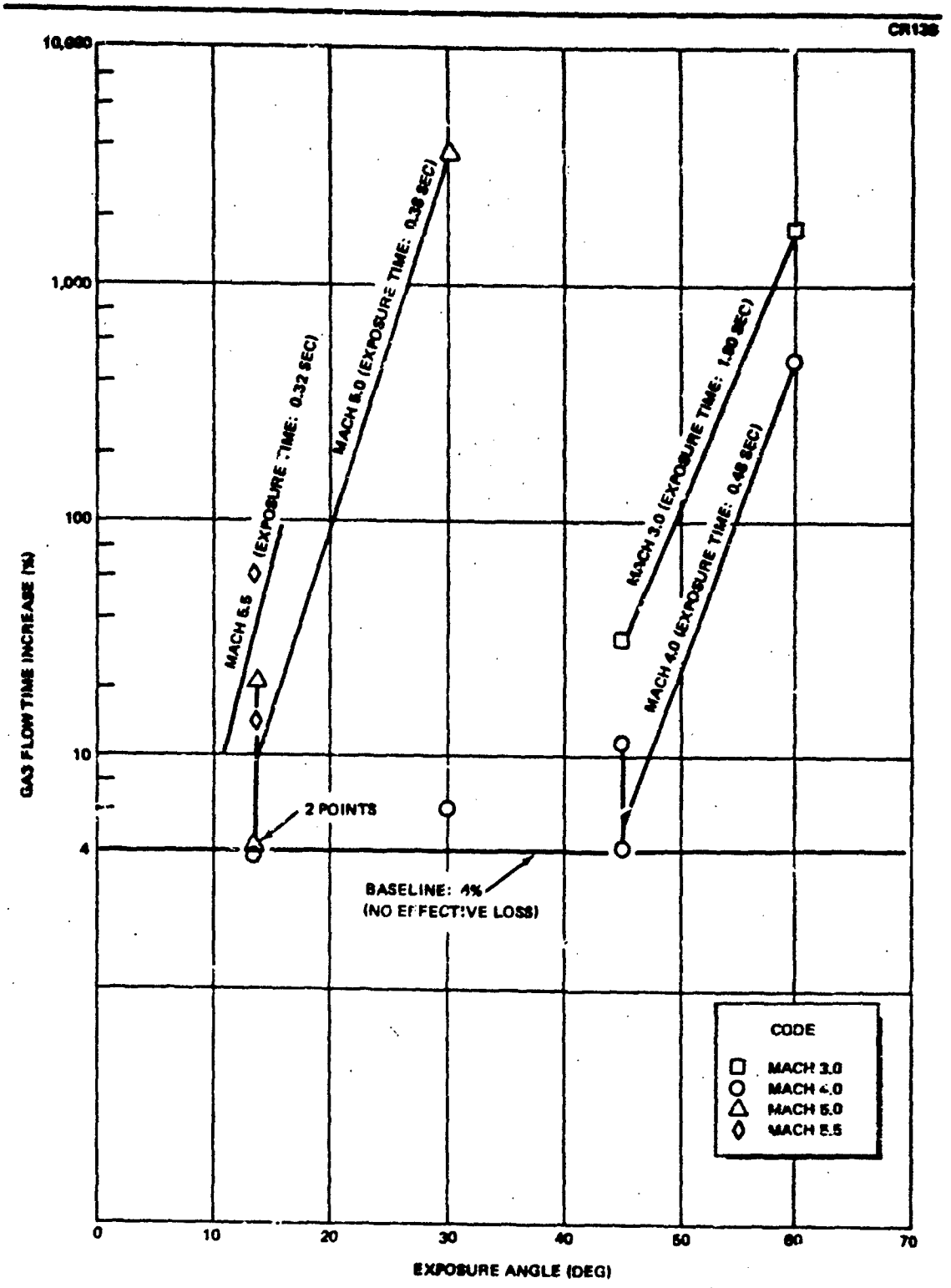


Figure 9-20. Time Increase for Nitrogen Gas Flow as a Function of Exposure Angle and Velocity

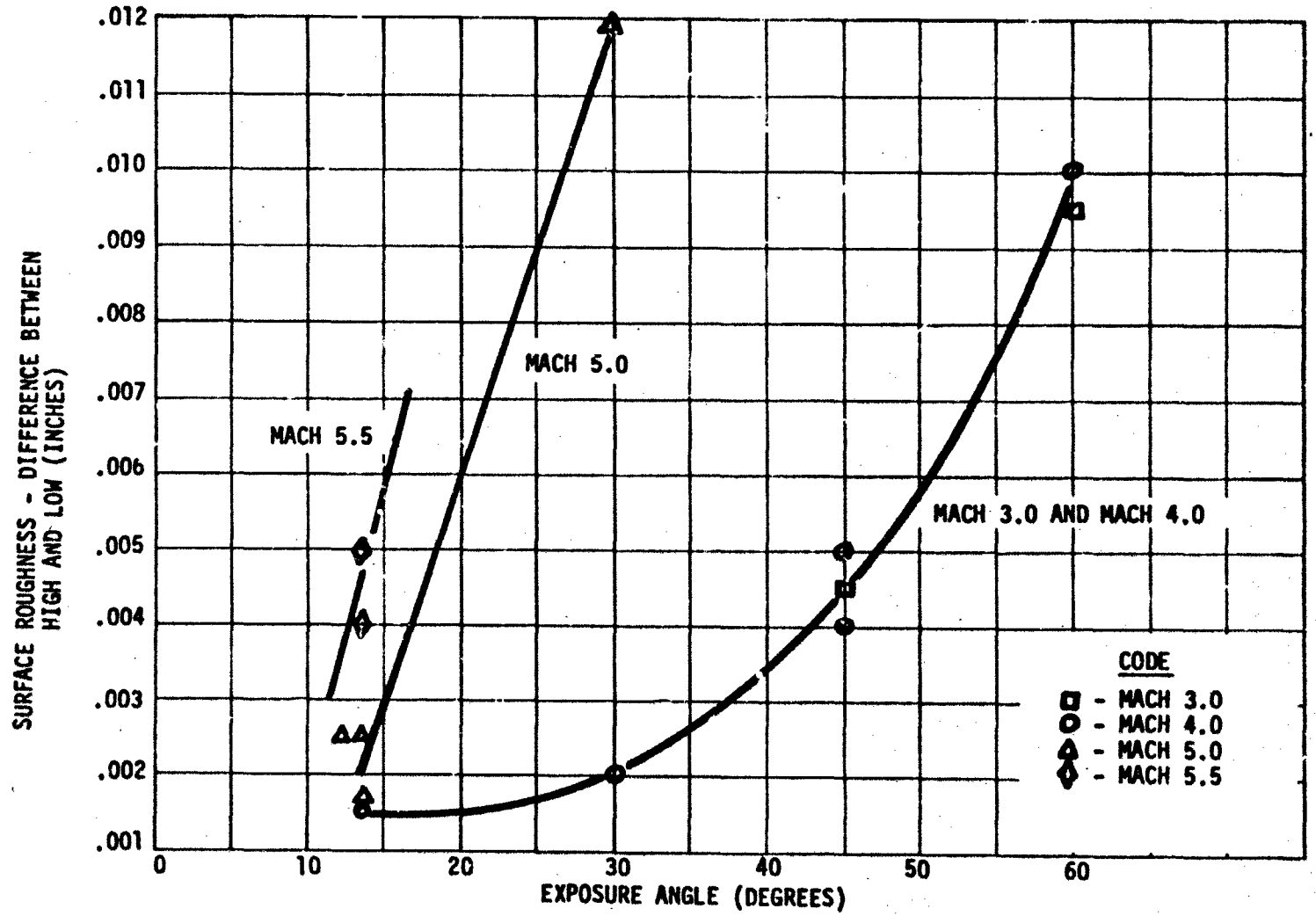


Figure 9-21. Surface Roughness as a Function of Exposure Angle and Velocity

9.4.5.3 Weight Change

The weight change data is shown in Table 9-4 and in Figure 9-22. Again, the same trend is shown when plotted as a function of exposure angle and velocity. For most of the samples, a very slight (2- to 6-milligram) weight gain was observed. This weight gain may have been due to microscopic dirt particles embedded or lodged in the samples as they passed through the rain field. Also, some contamination may have accumulated on the specimens as a result of three years of handling since 1970, when the pretest weight measurements were taken.

Scanning electron micrographs were taken on specimens showing the most severe surface damage, medium surface damage, and slight or essentially no significant surface damage (Figure 9-23). The surface of MDAC Specimen No. 259-4 at 260X shows that water impact has closed nearly 100 percent of the surface pores for an exposure of Mach 5.0 to 30 deg. This resulted in a 3,720-percent time increase for gas flow compared to the pretest gas flow time required to fill 100 cc. MDAC Specimen No. 258-3 (Mach 4.0 at 60 deg) showed less closing of the surface pores and only a 480-percent gas flow time increase. The surface appearance of MDAC Specimen No. 258-6 (Mach 4.0 at 30 deg) was found to be typical of porous stainless steel as etched, and resulted in only a 6-percent gas flow time increase.

9.4.5.4 Cross Section

A metallographic cross section of MDAC Specimen No. 259-4 (Mach 5.0 at 30 deg) is shown in Figure 9-24. The photomicrograph at 40X shows an approximate 0.016-in. damage depth from the surface in which the pores were effectively closed by the impinging water drops. This subsurface damage was sufficient to increase the gas flow time (to fill 100 cc) from about 1.2 min to almost 30 min, a severe degradation in permeability. Other than collapsing of the pores near the surface, no other internal damage was observed.

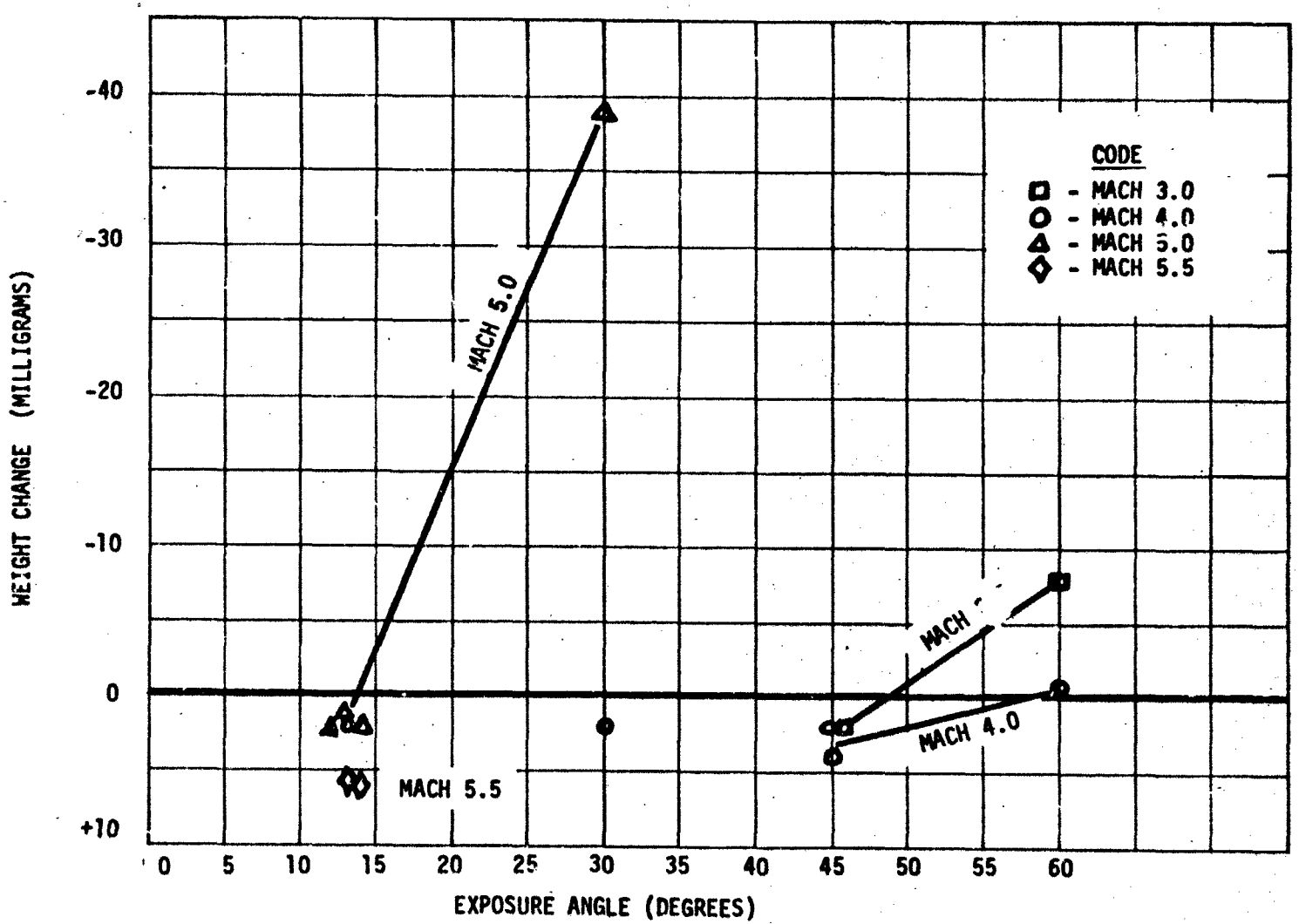
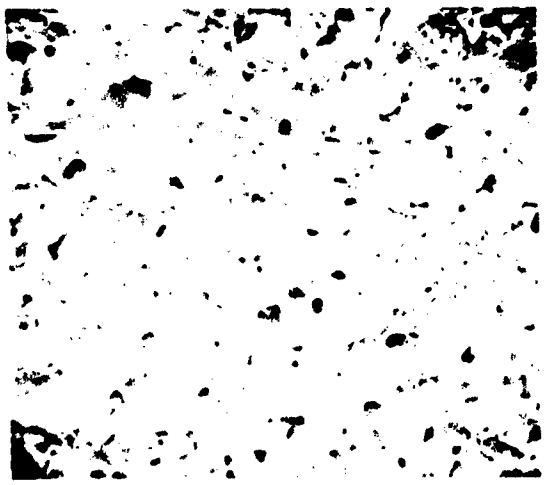


Figure 9-22. Weight Change as a Function of Exposure Angle and Velocity

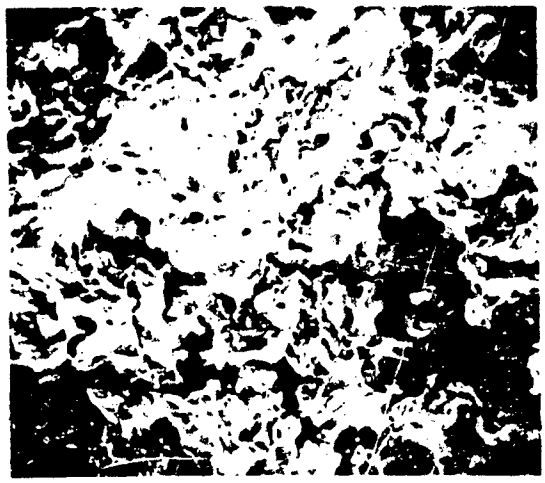


NO. 8693

MDAC SPECIMEN NO. 259-4
3,720% GAS FLOW TIME INCREASE

(NEARLY 100% CLOSING OF PORES
FOR EXPOSURE OF MACH 5.0 AT
30-DEG EXPOSURE ANGLE)

214X

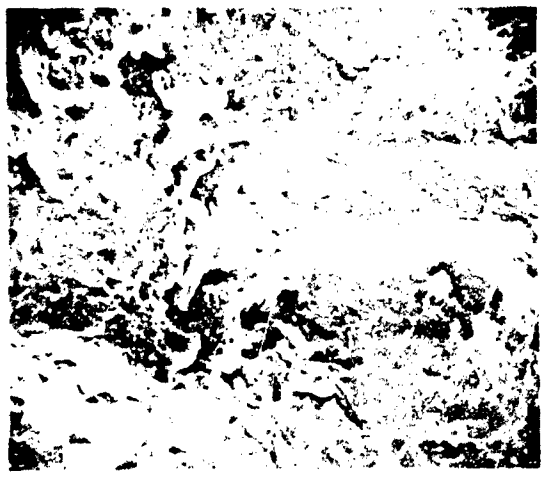


NO. 8688

MDAC SPECIMEN NO. 258-3
480% GAS FLOW TIME INCREASE

(CONSIDERABLE CLOSING OF PORES
FOR EXPOSURE OF MACH 4.0 AT
60-DEG EXPOSURE ANGLE)

214X



NO. 8673

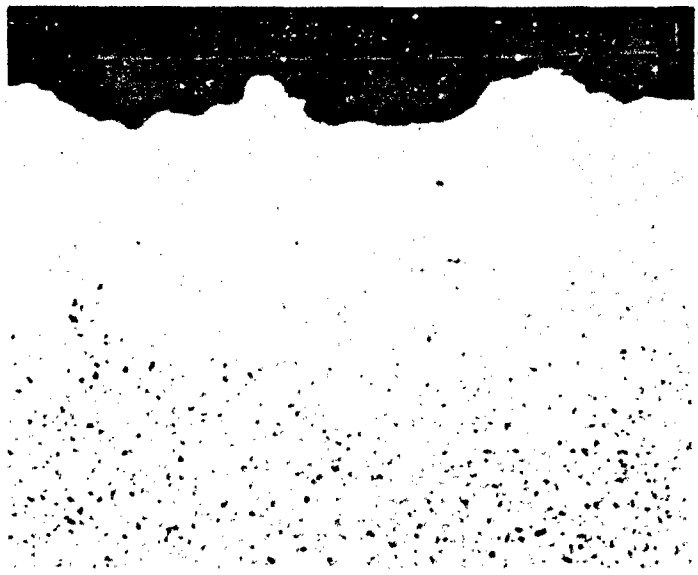
MDAC SPECIMEN NO. 258-6
6% GAS FLOW TIME INCREASE

(NEAR-NORMAL SURFACE APPEARANCE
FOR POROUS STAINLESS STEEL.
EXPOSURE OF MACH 4.0 AT 30-DEG
EXPOSURE ANGLE)

214X

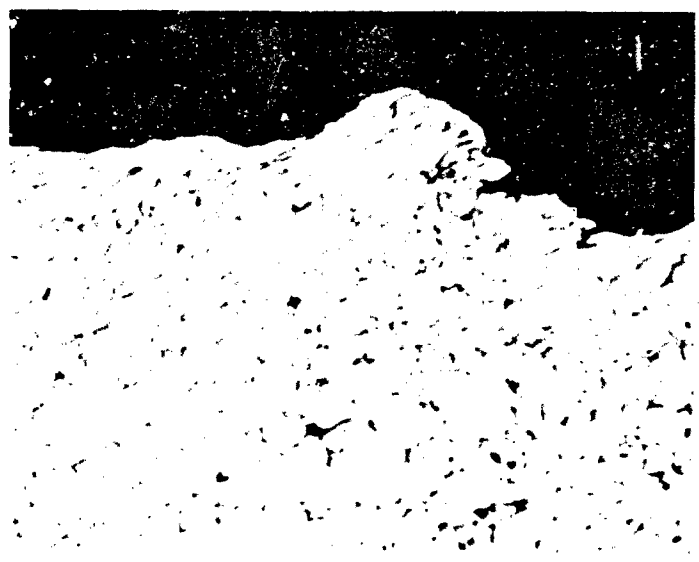
Figure 9-23. Scanning Electron Micrographs of Surface Damage

CR138



NO. 2625 UNETCHED 40X

(SHOWS 8-MIL-DEPTH SURFACE ROUGHNESS AND 16-MIL SUBSURFACE CLOSED-PORE DEPTH)



NO. 2626 ETCHED 200X

(SEVERELY DEFORMED GRAINS NEAR SURFACE)

Figure 9-24. Typical Cross-Section View of Sample 259-A (shows subsurface deformation and closing of pores resulting in a 3,720-percent gas flow time increase)

9.4.6 Significance of Results

The test results are considered significant in the following respects:

A. An increase in exposure time (increased rain-field length) is more damaging than an increase in velocity from Mach 3.0 to Mach 4.0.

B. Increased exposure (impingement) angles greater than 45 deg result in severe gas flow loss for Mach 3.0 and Mach 4.0 exposures.

C. Increased exposure angles greater than 13.5 deg result in severe gas flow loss for Mach 5.0 exposures.

D. An exposure angle of 13.5 deg resulted in very little surface damage and only a slight gas flow loss for the Mach 5.5 exposure.

E. No internal material damage was observed, other than closing of pores near the surface.

Section 10

REFERENCES

2-1. D. Quan and N. C. Campbell. R&D Test Reports, Transpiration Nose Tip Development Tests. CDRL A020, McDonnell Douglas Astronautics Company, MDC G2845, 3 March 1972.

2-2. D. E. Florance. Results of a Digital REKAP Analysis of Phenolic Graphite and Phenolic Carbon. AVCO and Cornell Test Data, GE-RESD-PIR-TPSD-8151-142, April 1964.

2-3. Thermal Properties of Heat Shield, Bond, and Structural Material. GE-RESD-9151-TPSD-327, June 1971.

2-4. W. A. Clayton. Thermal Conductivity of Phenolic-Carbon Chars. AFML-TR-69-313, December 1969.

2-5. Reentry Materials Handbook. Aerospace Corporation, Technology Division, San Bernardino Operations, San Bernardino, California, December 1967.

2-6. C. J. Katsikas, G. K. Castle, and J. S. Higgins. Ablation Handbook, Entry Materials Data and Design. AFML-TR-66-262, November 1966.

2-7. D. R. Hender. Aft-Facing Ablating Step Analysis and Computer Program P0336 (AFASP). McDonnell Douglas Astronautics Company, MDC G1195, October 1969.

2-8. Baker, D. L., et al. PANT Series C Wind Tunnel Test Data Report. Aerotherm Project 7043, January 1972.

3-1. J. C. Bailey. ANES Program Technical Requirements. Aerospace Corporation Letter 072-3870-JCB-104, 23 May 1972.

3-2. I. D. Liu and M. Steinberg. Time-Resolved Spectra for Some Simple Laboratory Simulated Reentry Models. J. Quant. Spectrosc. Radiation Transfer, Vol 8, pp 161-169, 1968.

5-1. T. C. Briggs. Compressibility Data for Helium Over the Temperature Range -5°C to 80°C at Pressures to 800 Atmospheres. Bureau of Mines Report of Investigations, R17352, March 1970.

5-2. R. A. Glickman. TCNT Expulsion System Development Test. McDonnell Douglas Astronautics Company, MDC G2890, 31 March 1972.

Preceding page blank

5-3. T. E. Ward. The Testing and Analysis of Solid Propellant Pressurization/Expulsion Systems. McDonnell Douglas Astronautics Company, MDC G2638, November 1971.

5-4. R. A. Glickman and T. E. Ward. Hot Gas Expulsion System Test Program. McDonnell Douglas Astronautics Company, MDC G2601, February 1972.

7-1. S. N. Rosenwasser, D. M. Goddard, and M. J. Hovan. Development of Porous Beryllium. AFML-TR-71-241, January 1972.

9-1. Track Test Directorate. The Holloman Track Facilities and Capabilities. Air Force Missile Development Center Technical Report MDC-TR-65-2. June 1965.

9-2. G. P. Johnson and T. G. Lee. Active Nosetip Evaluation Study, Rocket Sled Pre-Test Report. McDonnell Douglas Astronautics Company, MDC G4562, April 1973.

9-3. W. A. Fleener and R. H. Watson. Convective Heating in Dust-Laden Hypersonic Flows. AIAA Paper 73-761, to be presented at the AIAA 8th Thermophysics Conference, Palm Springs, California, 16-18 July 1973.

9-4. Third Quarterly Progress Report for Thermomechanical-Thermochemical Evaluation of Advanced RV Nosetip Concepts Utilizing the Ballistic Range. Aerotherm Corporation, Contract F33615-70-C-1704, March 1971.

9-5. George F. Schmitt, Jr., and Allan H. Krabill, Lt., USAF. Velocity-Erosion Rate Relationships of Materials in Rain at Supersonic Speeds. Technical Report AFML-TR-70-44, October 1970.

9-6. George F. Schmitt, Jr. Rain Erosion Behavior of Materials at 5500 Feet Per Second. Technical Report AFML-TR-72-64, September 1972.

Appendix A
CALCULATION OF THERMALLY IDEAL COOLANT FLUX

By performing an energy balance on the surface of the liquid film, the following equation can be written:

$$\frac{N_c}{N_{c_o}}\left[N_{c_o}\left(h_r - h_w\right)\right] = \epsilon\sigma\left(T_w^4 - T_{sink}^4\right) + \dot{m}\,\Delta h \qquad \text{(A-1)}$$

where Δh is the net enthalpy rise of the coolant, including subcooling, heat of vaporization, and surface superheat; and N_c/N_{c_o} represents the apparent reduction in heat transfer coefficient due to the mass transfer "blocking" occurring in the boundary layer. In order to solve the above equation, the blocking reduction must be computed.

Bartle and Leadon (Reference A-1), Rubesin (Reference A-2), and Arne (Reference A-3) have presented design correlations, based on similarity, for the ratio N_c/N_{c_o}. The correlations of Arne are presented here. For a laminar boundary layer,

$$\frac{N_c}{N_{c_o}} = 1.0 - \left(\frac{C_{p_v}}{C_{p_e}}\right)^{0.4}\left[0.68\,\frac{\dot{m}}{N_{c_o}} - 0.08\left(\frac{\dot{m}}{N_{c_o}}\right)^2\right] \qquad \text{(A-2)}$$

For a turbulent boundary layer,

$$\frac{N_c}{N_{c_o}} = \frac{\left(\frac{C_{p_v}}{C_{p_e}}\right)^{0.8}\frac{\dot{m}}{N_{c_o}}}{\left[1.0 + 0.2\left(\frac{C_{p_v}}{C_{p_e}}\right)^{0.8}\frac{\dot{m}}{N_{c_o}}\right]^4 - 1.0} \qquad \text{(A-3)}$$

where C_{p_v}/C_{p_e} is the ratio between the coolant vapor specific heat and free-stream species specific heat, evaluated at the local surface pressure and specified local surface temperature.

For the laminar case, Equations A-1 and A-2 are solved explicitly for the thermally ideal coolant flux.

$$\dot{m} = 6.25\, N_{c_o} \left(\frac{C_{p_v}}{C_{p_e}}\right)^{-0.4} (h_r - h_w)^{-1.0} \left\{ 0.68 \left(\frac{C_{p_v}}{C_{p_e}}\right)^{-0.4} (h_r - h_w) + \Delta h - \left(\left[0.68 \left(\frac{C_{p_v}}{C_{p_e}}\right)^{0.4} (h_r - h_w) + \Delta h \right]^2 - 0.32 \left(\frac{C_{p_v}}{C_{p_e}}\right)^{0.4} (h_r - h_w) \left[h_r - h_w - \frac{\epsilon\sigma}{N_{c_o}} \left(T_w^4 - T_{sink}^4 \right) \right] \right)^{0.5} \right\} \tag{A-4}$$

For the turbulent case, a technique such as Newton-Raphson linear iteration must be used on the coolant flux, utilizing Equations A-3 and A-1 until convergence is obtained.

Based on the previous equations, Figure A-1 presents thermally ideal coolant fluxes for water as a function of boundary layer enthalpy potential, surface temperature, and no-blowing surface heat transfer coefficient. It can be seen by examining Equations A-1 through A-4 that for high heat transfer coefficients, a solution is approached in the form of the dimensionless ratio $\dot{m}/N_{c_o}$. As can be seen from Figure A-1, for the range of surface temperature presented, this ratio becomes essentially independent of N_{c_o} at a value of 1.0.

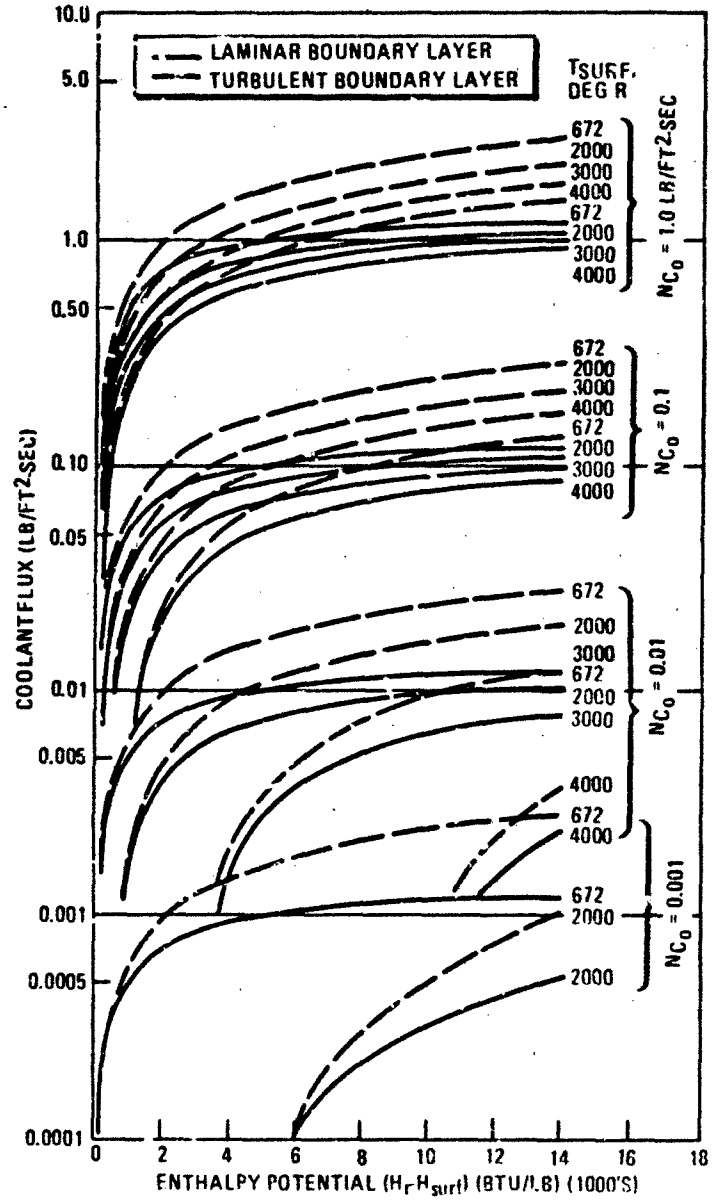


Figure A-1. Ideal Coolant Flux for Water

REFERENCES

A-1. E. R. Bartle and B. M. Leadon. The Effectiveness as a Universal Measure of Mass Transfer Cooling for a Turbulent Boundary Layer. Proceedings of the 1962 Heat Transfer and Fluid Mechanics Institute, University of Washington, Seattle, Washington, June 1962.

A-2. M. W. Rubesin. An Analytical Estimation of the Effect of Transpiration Cooling on the Heat-Transfer and Skin-Friction Characteristics of a Compressible Turbulent Boundary Layer. NACA TN 3341, December 1954.

A-3. C. L. Arne. Ablative Materials Subject to Combustion and Thermal Radiation Phenomena. McDonnell Douglas Astronautics Company, Paper 1851, January 1964.

Appendix B
HEAT SHIELD ANALYSIS METHODOLOGY

This appendix presents a short description of the analytical techniques used in the MDAC F678 computer program. More detailed descriptions may be obtained from References B-1 and B-2. Inherent in the analysis used in this design is (1) equilibrium thermochemistry at the ablating surface, (2) exclusion of mechanical removal mechanisms, (3) neglect of internal radiation, and (4) obtaining internal decomposition through a single Arrhenius rate equation. The ablating surface energy balance (Equation B-1) is solved to obtain the net heat transfer at the surface (q_w).

$$q_w = N_c (h_r - h_{we}) - \dot{m}_w \Delta Q - \sigma \epsilon \left(T_w^4 - T_{sink}^4 \right) \qquad \text{(B-1)}$$

The heat transfer coefficient to the wall (N_c) is obtained from the aerodynamic heating (predicted without ablation) reduced to account for mass transfer. These mass transfer corrections are the same as that discussed in the ideal coolant flux calculation section (Appendix A). The second term on the right side represents the combustion occurring within the boundary layer and is defined by Equation B-2.

$$\Delta Q = -\frac{\dot{m}_g}{\dot{m}_w} H_q - \frac{\dot{m}_c}{\dot{m}_w} H_c - \left(\frac{1}{\sum_j K_{jw}} - 1 \right) h_{we} + \frac{1}{\sum_j K_{jw}} h_w \qquad \text{(B-2)}$$

The first and second terms on the right-hand side of Equation B-2 are the energy carried to the surface by the pyrolysis gas and the char, respectively. The specie mass fraction, K_{jw}, is defined for each j element as follows:

$$K_{jw} = \frac{\dot{m}_{jw}/N_c}{\left(\frac{\dot{m}_w}{N_c} + 1 \right)} \qquad \text{(B-3)}$$

The enthalpy at the wall conditions is designated h_{we} for the free-stream gas and h_w for the reaction products. This latter value is obtained by assuming that thermochemical equilibrium exists between the free-stream gas, pyrolysis gas, and char.

This analysis is capable of accurate predictions in all ablation regimes.

The in-depth material response is obtained by the solution to a transient one-dimensional relationship (Equation B-4).

$$\rho c_p \frac{\partial T}{\partial t} = \frac{\partial}{\partial x}\left(k \frac{\partial T}{\partial x}\right) + \dot{m}_g \frac{\partial h_g}{\partial x} + \Delta H_{dp} \frac{\partial \rho_{dp}}{\partial t} + \dot{s}\rho c_p \frac{\partial T}{\partial t} \qquad \text{(B-4)}$$

Sensible energy exchange	Conduction	Energy exchange due to gaseous transfer	Energy exchange due to decomposition	Energy exchange due to the moving coordinate system

To obtain a solution, the material is divided into layers, and an energy balance is performed on each lamina. The coordinate system maintains the surface at a fixed location, and material is removed from the back. Standard finite difference techniques are used. The conduction into the surface is equal to the net heat transfer at the surface (Equation B-1).

The gaseous flow rate for the jth lamina is determined from the layer beneath it (Equation B-5).

$$\dot{m}_{g_j} = \dot{m}_{g_{j+1}} + \left(\frac{\partial \rho_{dp}}{\partial t}\right)_{j+1} \Delta b_{j+1} \qquad \text{(B-5)}$$

The pyrolysis heat of decomposition for each lamina is derived from an energy and mass balance and is presented in terms of energy per unit mass of pyrolysis gas formed.

$$\Delta H_{dp_j} = \frac{1}{f_B (1 - \gamma')} \int_{T_o}^{T_j} c_{p_{vi}} dT - \left[\frac{1 - f_B (1 - \gamma')}{f_B (1 - \gamma')} \right] \int_{T_o}^{T_j} c_{p_c} dT$$

$$- \frac{\Delta b_j}{\Delta b_j + \Delta b_{j-1}} \left(h_{g_{j-1}} - h_{g_j} \right) - h_{g_j} \qquad \text{(B-6)}$$

The decomposition gas formation rate is computed using Equation B-7.

$$\frac{\partial \rho_{dp}}{\partial t} = f_B \rho_i \left[\frac{\rho - \rho_i (f_B + \gamma' f_B)}{f_B \rho_i (1 - \gamma')} \right]^n A e^{-E^*/T} \qquad \text{(B-7)}$$

Other terms in Equation B-4 are self-explanatory. Temperature-dependent material properties, specific heat and conductivity, are input for both the virgin and char materials. The properties for each lamina are computed both as a function of the temperature and the density of the lamina.

$$MP_j = \frac{\rho_j - \left[\rho_i - \rho_i f_B (1 - \gamma') \right]}{\rho_i f_B (1 - \gamma')} MP_{vij} + \frac{\rho_i - \rho_j}{\rho_i f_B (1 - \gamma')} MP_{cj} \qquad \text{(B-8)}$$

where MP represents either the specific heat or the conductivity.

REFERENCES

B-1. C. L. Arne. Ablative Materials Subject to Combustion and Thermal Radiation Phenomena. McDonnell Douglas Astronautics Company, Paper No. 1851, January 1964.

B-2. H. G. Timmer, C. L. Arne, T. R. Stokes, Jr., and H. H. Tang. Ablation Aerodynamics for Slender Reentry Bodies—Volume I. AFFDL-TR-70-27, Volume I, March 1970.

Appendix C

APPROXIMATION OF COOLANT FLOW REQUIREMENTS WITH FREE-STREAM PARAMETERS

C.1 AERODYNAMIC HEATING

Reference C-1 presents the results of a study that was conducted to simplify the relationships for predicting turbulent heating on a hemisphere in hypersonic flow fields. A series of reentry heating conditions were analyzed utilizing MDAC computer program H586 (Reference C-2), which is the real-gas analysis program usually employed to estimate aerodynamic heating on hemisphere/cones. The results of the detailed analysis were then correlated using basic flow field parameters and utilized in conjunction with van Driest's equation for turbulent heating, which is

$$\dot{q}_A = \frac{0.042}{Pr^{2/3}} R_{e_s}^{-0.2} \rho_e u_e (h_r - h_w) \qquad \text{(C-1)}$$

Using the H586 results, u_e/u_∞ is correlated by the following equation

$$u_e/u_\infty = 0.41\theta \text{ above } 70,000 \text{ ft}$$

$$u_e/u_\infty = 0.48\theta \text{ below } 70,000 \text{ ft} \qquad \text{(C-2)}$$

where θ is the local angle to the stagnation point. Above a local angle of 60 deg, this relation deviates from the H586 results. The local boundary layer edge viscosity is correlated on the basis of stagnation point viscosity by Equation C-3,

$$\frac{\mu_e}{\mu_s} = (1 - 0.1677\theta^2)^{0.5} \qquad \text{(C-3)}$$

while the stagnation viscosity is correlated by Equation C-4.

$$\mu_s = 1.55 \times 10^{-9} \; u_\infty^{0.767} \tag{C-4}$$

In attempting to correlate local pressure, the popular cosine-squared distribution left much to be desired, while the power law expression in Equation C-5 matches the H586 results well.

$$\frac{P_e}{P_s} = 0.275^{\theta^2} \tag{C-5}$$

Utilizing the relation

$$\frac{H_e}{H_s} = 1 - \left(\frac{u_e}{u_\infty}\right)^2 \tag{C-6}$$

and making the assumption that

$$\frac{\rho_e}{\rho_s} = \frac{P_e/P_s}{f\,(h_e/h_s)} \tag{C-7}$$

the boundary layer edge density is found to be correlated by Equation C-8.

$$\frac{\rho_e}{\rho_s} = \frac{0.275^{\theta^2}}{(1 - 0.1667\,\theta^2)} \tag{C-8}$$

The curve fit of the ratios of free-stream to stagnation-point density is approximated well by Equation C-9 in the range of free-stream velocity from 7,000 ft/sec to 20,000 ft/sec.

$$\frac{\rho_\infty}{\rho_s} = 6.05\; u_\infty^{-0.424} \tag{C-9}$$

Making the necessary substitutions, a local enthalpy heat transfer coefficient may be defined based on Equation C-1, and is found to be

$$N_c = \frac{0.00322\ \rho_\infty^{0.8}\ u_\infty^{1.29}}{Pr^{2/3}\ R_N^{0.2}} \quad \frac{\theta^{0.6}\ (0.275)^{0.8\theta^2}}{(1 - 0.1667\ \theta^2)^{0.7}} \qquad \text{(C-10)}$$

Figure C-1 presents the angular distribution of $N_c/N_{c_{max}}$ for Equation C-10.

The distribution is conservative, in the sense that it lies above the H586 results for high local angles. This result is primarily due to the use of the boundary layer edge velocity distribution in Equation C-2. The turbulent heating distribution peaks at an angle of 34 deg away from the stagnation point. Figure C-2 presents the peak turbulent heat transfer coefficient for several time points from the reentry trajectory that was analyzed. It can be seen that fair agreement exists.

For low surface temperature, such as would exist on a transpiration-cooled nosetip, the enthalpy potential for heat transfer is

$$h_r - h_w \approx h_r \qquad \text{(C-11)}$$

while the recovery enthalpy is

$$h_r = r\,h_s + (1-r)\,h_e \qquad \text{(C-12)}$$

Utilizing Equations C-6 and C-2 in conjunction with Equation C-12, the recovery enthalpy becomes

$$h_r = h_s \left| r + (1-r)\left[1 - 0.1667\ \theta^2\right] \right| \qquad \text{(C-13)}$$

For a recovery factor of 0.89, the recovery enthalpy at the tangency point of a 7-deg hemisphere/cone is over 95 percent of the total enthalpy. Therefore, the recovery enthalpy can be well approximated by

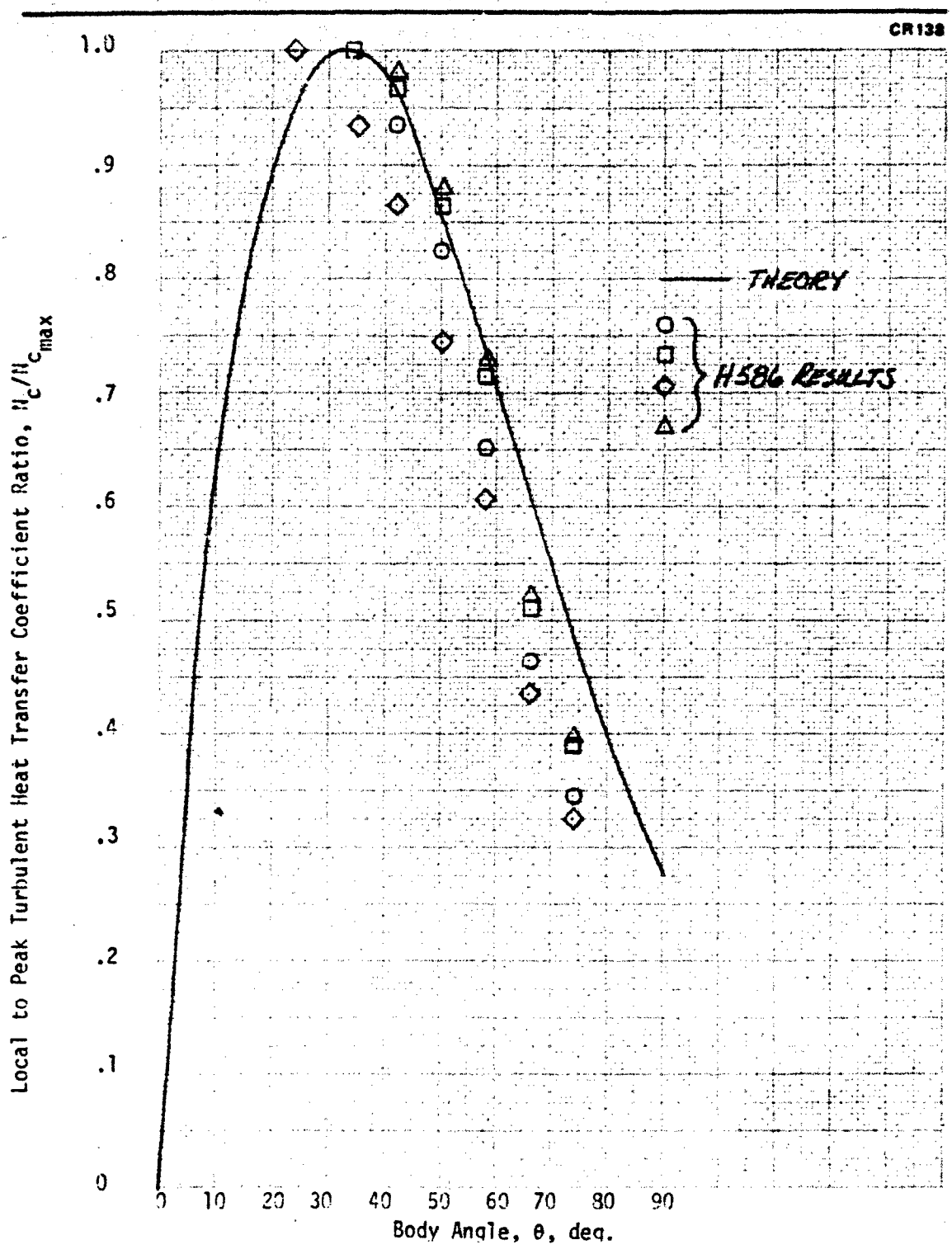


Figure C-1. Comparison of Turbulent Heat Transfer Coefficient Distribution

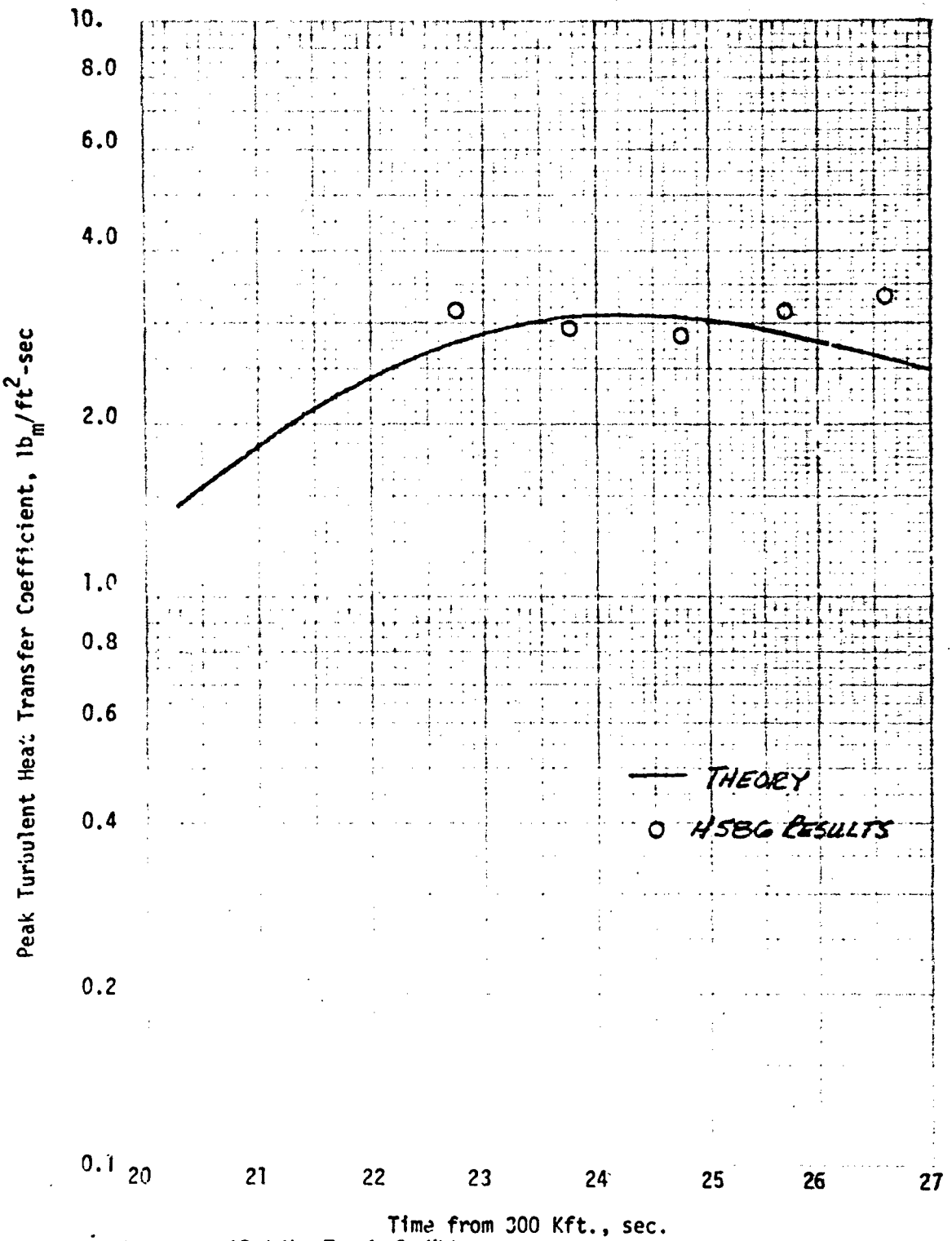


Figure C-2. Comparison of Peak Heat Transfer Coefficients

$$h_r \approx h_s \approx \frac{u_\infty^2}{2GJ} \qquad \text{(C-14)}$$

Combining Equations C-10 and C-14, and assuming a Prandtl number of 0.7, the heat flux from Equation C-1 becomes

$$\frac{\dot{q}}{A} \approx 8.18 \times 10^{-8} \frac{\rho_\infty^{0.8} u_\infty^{3.29}}{R_N^{.2}} \frac{\theta^{0.6} (0.275)^{0.8\theta^2}}{(1 - 0.1667\,\theta^2)^{0.7}} \qquad \text{(C-15)}$$

C.2 BOUNDARY LAYER MASS TRANSFER EFFECTS

For relatively low surface temperature, such as would occur with liquid transpiration cooling, the radiation terms in Equation A-1 can be neglected, and the equation becomes

$$\left.\frac{\dot{q}}{A}\right|_o = \frac{\dot{m}\Delta h}{N_c/N_{c_o}} \qquad \text{(C-16)}$$

Expressing the heat flux in terms of the boundary layer enthalpy differential and the aerodynamic heat transfer coefficient, and making use of Equation C-11, Equation C-16 can be rearranged to

$$\frac{\dot{m}}{N_{c_o}} = \frac{h_r}{\Delta h} \frac{N_c}{N_{c_o}} \qquad \text{(C-17)}$$

Substituting the turbulent mass transfer blocking relationship of Equation A-3, and rearranging, the mass flux can be expressed as

$$\dot{m} = \frac{4\,N_{c_o}}{(C_{p_v}/C_{p_s})^{0.8}} \left\{ \left[1.0 + \frac{h_r}{\Delta h} \left(\frac{C_{p_v}}{C_{p_s}} \right)^{0.8} \right]^{1/4} - 1.0 \right\} \qquad \text{(C-18)}$$

Utilizing Equations C-10 and C-14, and assuming a specific heat ratio of 2.0 and a coolant net enthalpy rise of 1,150 Btu/lb_m, the local ideal coolant flux at an effective angle, θ, from the stagnation point becomes

$$\dot{m} = \frac{7.4 \times 10^{-3} \rho_\infty^{0.8} u_\infty^{1.29}}{Pr^{2/3} R_N^{0.2}} \left\{ \left[1.0 + 3.03 \times 10^{-8} u_\infty^2 \right]^{1/4} - 1.0 \right\}$$

$$\frac{\theta^{0.6} (0.275)^{0.8\theta^2}}{(1-0.1667\theta^2)^{0.7}} \qquad \text{(C-19)}$$

Equation C-19 can be combined with the expression for differential surface area on a hemisphere to obtain the local ideal coolant flow over an angular increment, $d\theta$:

$$\dot{m}dA = 4.65 \times 10^{-2} \frac{R_N^{1.8}}{Pr^{2/3}} \rho_\infty^{0.8} u_\infty^{1.29}$$

$$\left\{ \left[1.0 + 3.03 \times 10^{-8} u_\infty^2 \right]^{1/4} - 1.0 \right\} \frac{\theta^{0.6} (0.275)^{0.8\theta^2} \sin\theta}{(1.0 - 0.1667\theta^2)^{0.7}} \, d\theta$$

(C-20)

The angular dependent parameter appearing in Equation C-20 has been numerically integrated and is presented in Figure C-3. For a half-cone angle of 7 deg and a zero-deg angle of attack, the thermally ideal coolant flow rate is

$$\dot{m} = 1.584 \times 10^{-2} \frac{R_N^{1.8} \rho_\infty^{0.8} u_\infty^{1.29}}{Pr^{2/3}} \left\{ \left[1.0 + 3.03 \times 10^{-8} u_\infty^2 \right]^{1/4} - 1.0 \right\} \qquad \text{(C-21)}$$

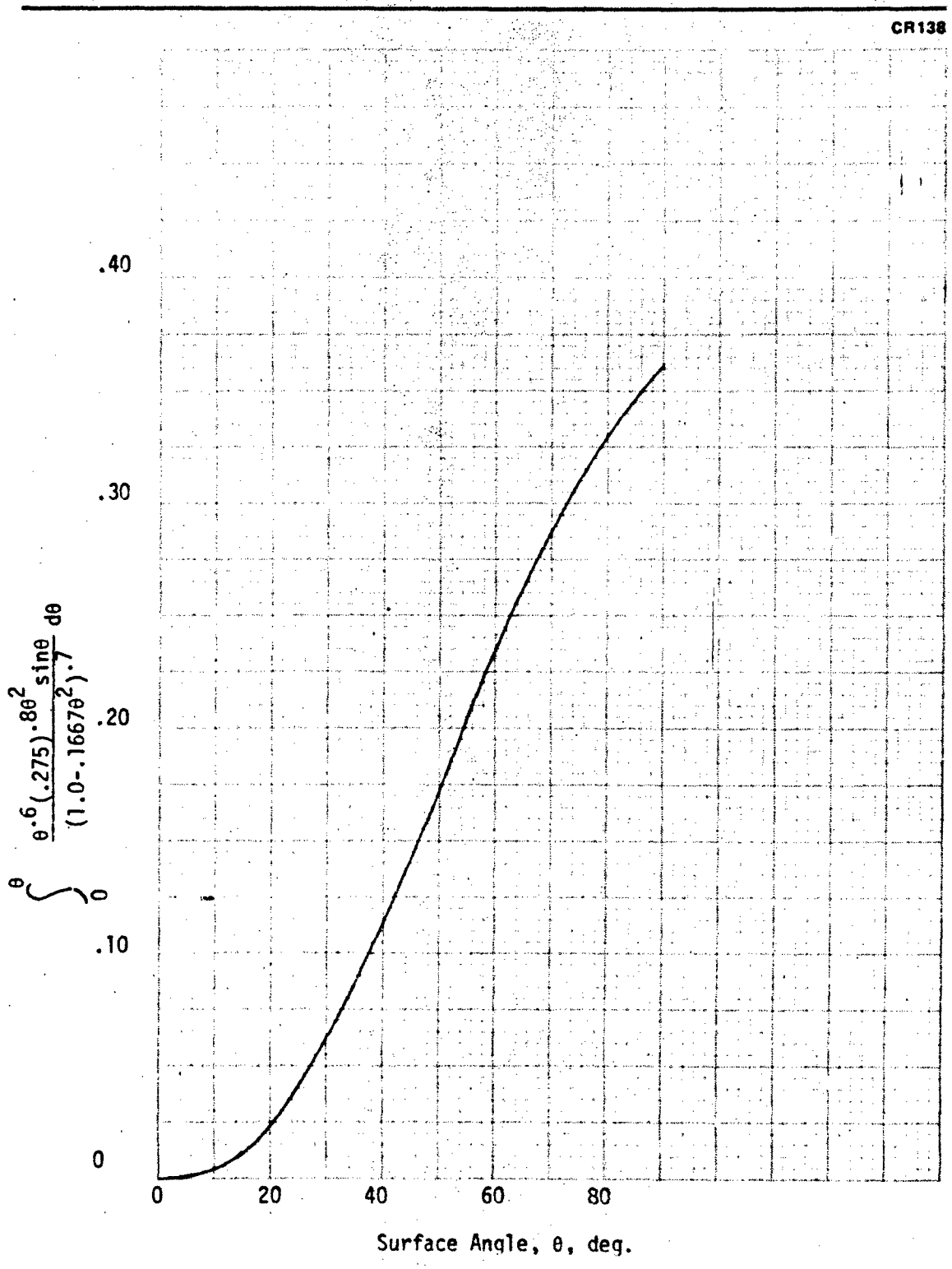


Figure C-3. Ideal Coolant Flux Surface Integral

C. 3 COOLANT POROUS FLOW

A fair approximation can be made to the coolant flow distribution through the porous nosetip by performing a local one-dimensional solution in spherical coordinates. This approximation becomes less accurate for increasing stagnation pressure.

The modified Darcy equation is utilized to estimate porous flow pressure gradient,

$$-G\frac{dP}{dR} = \left(\frac{a\mu}{\rho} + \frac{\beta\dot{m}}{\rho}\right)\dot{m} \qquad \text{(C-22)}$$

where a is the porous material viscous pressure-drop constant, and β is the inertial pressure-drop constant.

The local coolant flux within the porous material is related to the flux at the surface by the radius ratio.

$$-G\frac{dP}{dR} = \left(\frac{a\mu}{\rho} + \frac{\beta\dot{m}_{out}}{\rho}\frac{R_{out}^2}{R^2}\right)\dot{m}_{out}\frac{R_{out}^2}{R^2} \qquad \text{(C-23)}$$

Rearranging and integrating between the inner and outer surfaces,

$$P_{in} - P_{out} = \frac{a\mu R_{out}}{\rho G}\left\{\frac{R_{out} - R_{in}}{R_{in}}\right\}\dot{m}_{out} + \frac{\beta R_{out}}{3\rho G}\left\{\frac{R_{out}^3 - R_{in}^3}{R_{in}^3}\right\}\dot{m}_{out}^2 \qquad \text{(C-24)}$$

Section 2. 3 of this report utilizes Equation C-24 to approximate the optimum inner contour of the nosetip, which is later refined by a detailed three-dimensional analysis.

C.4 ANGLE OF ATTACK

Equation C-21 requires free-stream density and velocity in order to define thermally ideal coolant flow rate. These parameters can be readily evaluated from acceleration measurements on the three vehicle axes. In general terms, the normal and axial accelerations due to aerodynamic forces on a reentry vehicle are

$$\eta_N = \frac{\rho_\infty u_\infty^2 A_B C_N}{M} \tag{C-25}$$

and

$$\eta_Z = \frac{\rho_\infty u_\infty^2 A_B C_Z}{M} \tag{C-26}$$

while the normal acceleration is the resultant of that on two axes.

$$\eta_N = (\eta_x^2 + \eta_y^2)^{1/2} \tag{C-27}$$

The normal drag coefficient is a first-order function of angle of attack, and the axial drag coefficient can be represented as a second-order function of angle of attack.

$$C_N = K_o \alpha \tag{C-28}$$

$$C_Z = K_1 + K_2 \alpha + K_3 \alpha^2 \tag{C-29}$$

By taking the ratio of the normal and axial accelerations, Equations C-25 through C-29 can be solved for the vehicle angle of attack.

$$|\alpha| = 0.5 \left(\frac{C_2}{\xi_N} - C_1\right) \pm \left[0.25 \left(C_1 - \frac{C_2}{\xi_N}\right)^2 - C_3\right]^{1/2} \tag{C-30}$$

where ξ_N is the ratio of normal to axial acceleration.

$$\xi_N = \frac{\eta_N}{\eta_Z} \tag{C-31}$$

and

$$C_1 = \frac{K_2}{K_3}$$

$$C_2 = \frac{K_0}{K_3}$$

$$C_3 = \frac{K_1}{K_3} \tag{C-32}$$

C. 5 FREE-STREAM VELOCITY

The vehicle accelerations on body axes can be resolved into a coordinate system based on the vehicle flight path or free-stream velocity vector. Two components result: a drag component parallel to the free-stream vector, and a lift component perpendicular to the free-stream vector.

$$\eta_D = \eta_Z \cos \alpha + \eta_N \sin \alpha \tag{C-33}$$

$$\eta_L = \eta_Z \sin \alpha + \eta_N \cos \alpha \tag{C-34}$$

Vehicle velocity can be well approximated by integrating the drag acceleration.

$$u_\infty = u_o + \int_{t_o}^{t} (\eta_Z \cos \alpha + \eta_N \sin \alpha)\, dt \tag{C-35}$$

C.6 FREE-STREAM DENSITY

Free-stream density can be approximated in several ways. It can be derived from the dynamic pressure and free-stream velocity.

$$\rho_\infty = \frac{q}{\frac{1}{2} u_\infty^2} \tag{C-36}$$

It can be derived from the free-stream velocity and axial deceleration.

$$\rho_\infty = \frac{M}{A_B} \frac{\eta_Z}{\frac{1}{2} u_\infty^2 C_Z} \tag{C-37}$$

where the axial drag coefficient, C_Z, can be defined as a function of angle of attack as in Equation C-29. Finally, free-stream density can be evaluated if vehicle altitude is known and a suitable atmospheric density model is available. Vehicle altitude could be determined from a radar altimeter or by integration of vehicle accelerations and use of a suitable coordinate transformation.

A first-order approximation to atmospheric density is usually made utilizing an exponential relationship, as in Equation C-38.

$$\rho_\infty = \rho_{ref} e^{-\beta H} \tag{C-38}$$

where Loh (Reference C-3) recommends the following values:

$$\beta = \frac{1}{23,500 \text{ ft}}$$

$$\rho_{ref} = 0.002377 \text{ slug/ft}^3$$

Figure C-4 presents a plot of the ARDC model atmosphere (1959) along with Equation C-38. The mismatch is due primarily to variations in atmospheric temperature. Figure C-5 presents the corresponding atmospheric temperature variation. It appears as though it can be approximated by a third-degree

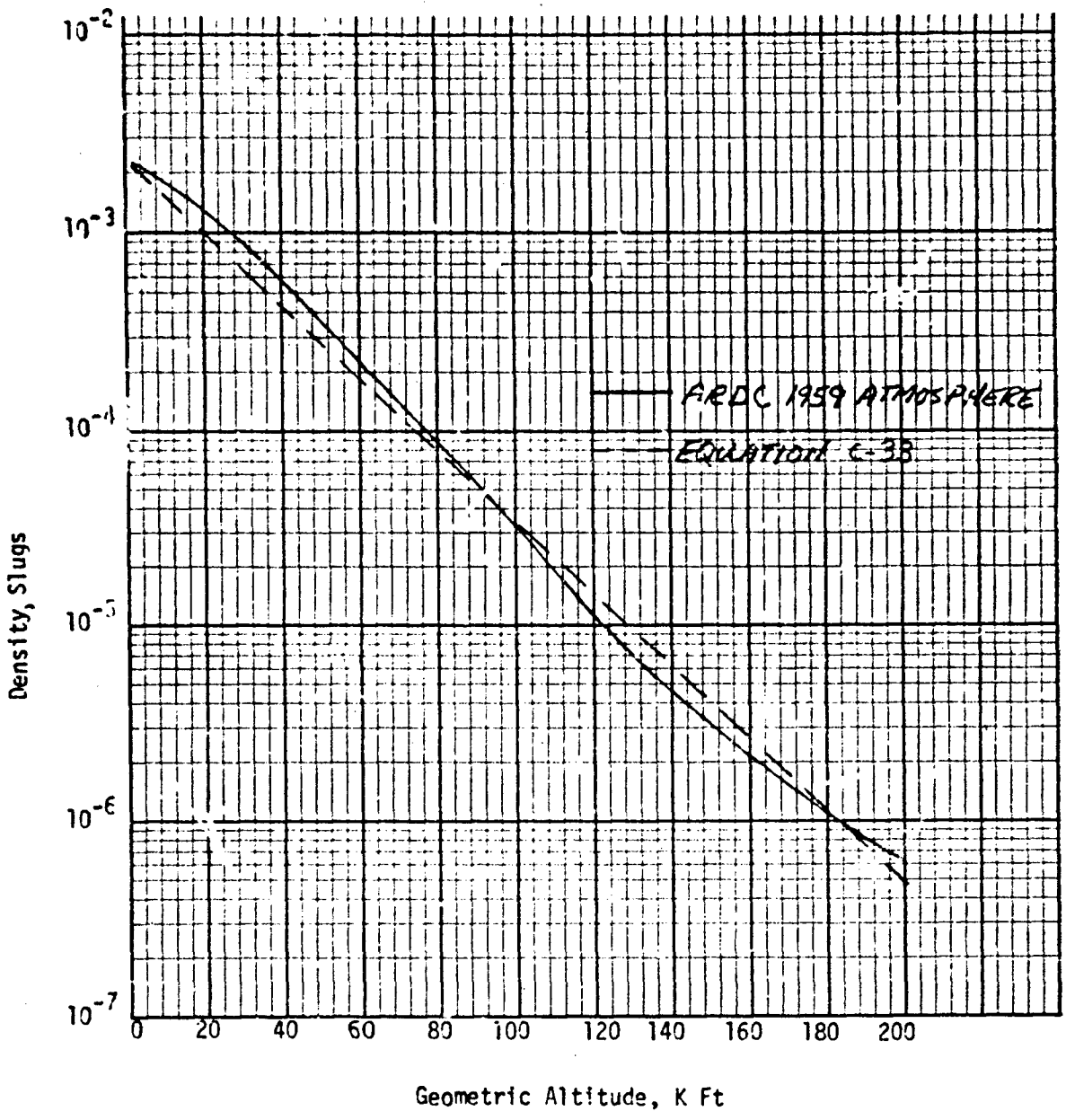


Figure C-4. Atmospheric Density

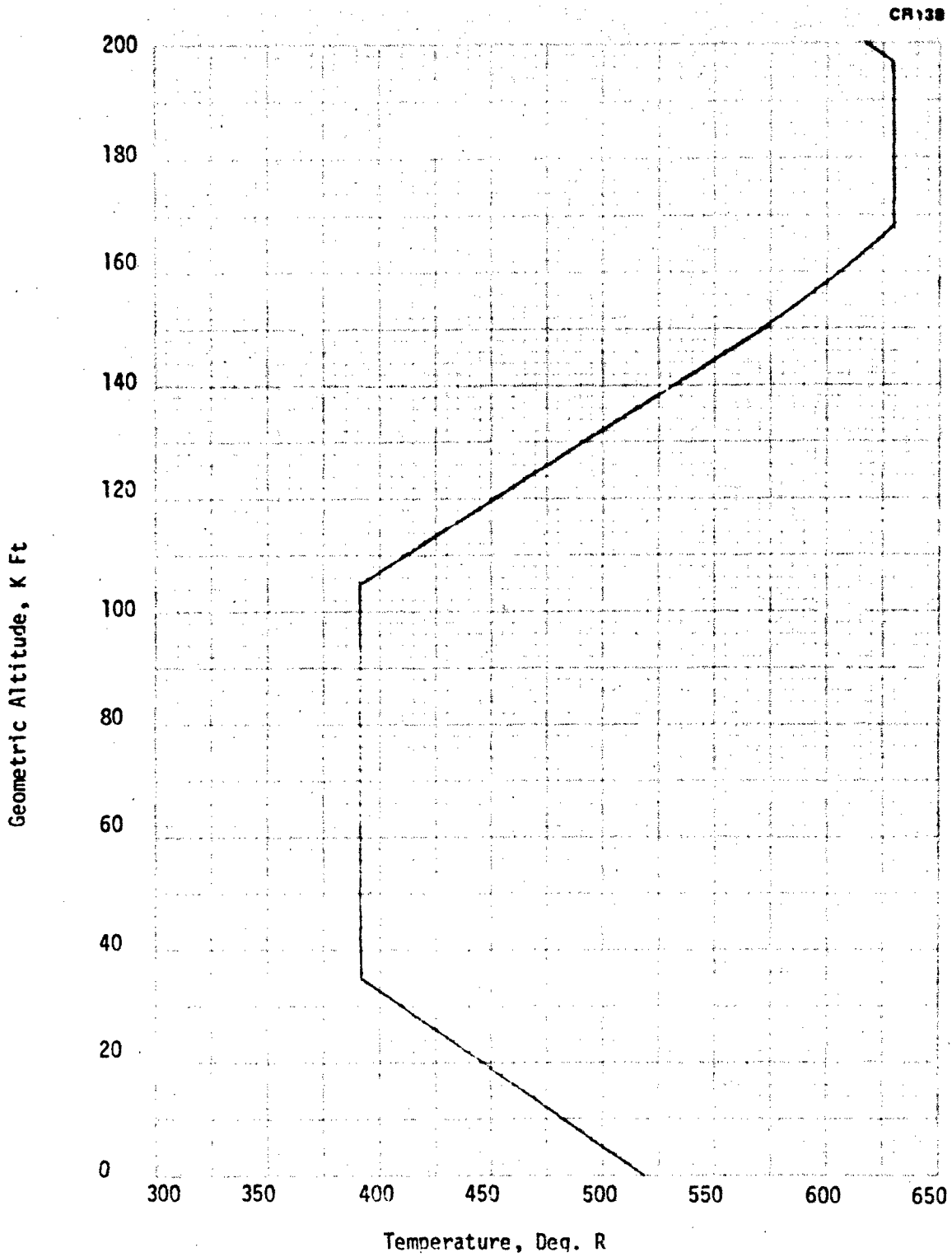


Figure C-5. Atmospheric Temperature

polynomial up to 150,000 ft. Therefore, an improvement can be made on Equation C-38 in the form of

$$\rho_\infty = \rho_{ref} e^{(\beta_o + \beta_1 H + \beta_2 H^2 + \beta_3 H^3)} \quad \text{(C-39)}$$

where the reference density and temperature coefficients would be based on conditions within the expected reentry area.

Using the form of Equation C-39 in conjunction with the ARDC 1959 atmosphere model, a least-square fit of the natural logarithm of density with altitude has led to Equation C-40 for a density fit between sea level and 200,000 ft geometric altitude.

$$\rho_\infty = 0.002337\, e^{(0.0419 - 3.05\times10^{-5} H - 1.96\times10^{-10} H^2 + 7.15\times10^{-16} H^3)} \quad \text{(C-40)}$$

The density error is relatively small and is presented in Figure C-6.

C.7 REFERENCES

C-1. D. R. Hender. Turbulent Heating on Hypersonic Hemispheres. McDonnell Douglas Astronautics Company, Paper 10182, May 1969.

C-2. T. G. Lee and C. B. Mason. Sphere/Cone Flowfield and Heat Transfer Analysis Computer Program H586. McDonnell Douglas Astronautics Company, DAC-63147, February 1969.

C-3. W. H. T. Loh. Dynamics and Thermodynamics of Planetary Entry. Prentice-Hall, Inc., 1963.

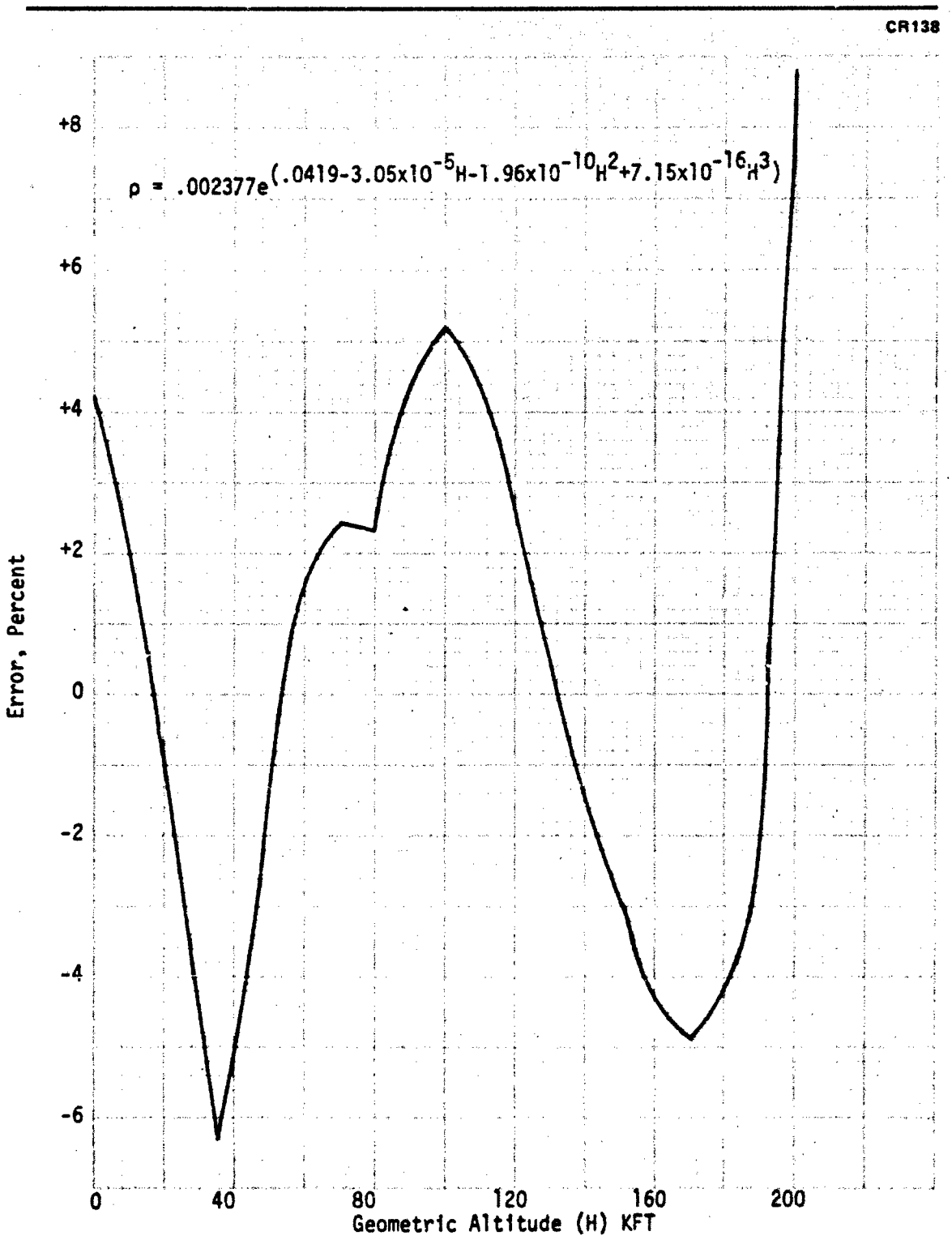


Figure C-6. Correlation of Atmospheric Density (ρ) with ARDC 1959 Atmosphere Model

Appendix D
TRANSPIRATION NOSETIP TRANSIENT THERMAL ANALYSIS

In order to aid in the definition of a flow control system, it is desirable to know the thermal response of the nosetip to changes in heating environment. To provide this information, a computer program has been developed that performs a transient, one-dimensional analysis of a transpiration matrix under conditions of increased surface heating. The program uses fourth-order Runge Kutta integration, can treat a matrix consisting of two materials, and permits coolant phase change and matrix surface melt.

D.1 POROUS MATRIX EQUATIONS

The basic equations for the porous matrix include conservation of coolant mass, the modified Darcy equation for pressure drop,

$$-G\,\nabla P = \left(\alpha\frac{\mu}{\rho} + \beta\frac{\dot{m}}{\rho}\right)\overline{\dot{m}} \qquad \text{(D-1)}$$

and the porous flow energy equation,

$$-k_e\,\nabla^2 T - (\nabla k_e)\;(\nabla T) + \nabla\cdot(H_c\,\overline{\dot{m}}_c) = -\frac{\partial}{\partial t}(\rho h)_e \qquad \text{(D-2)}$$

The viscous pressure drop constant, α, is the inverse of the porous matrix permeability, and the constant β is to account for additional pressure drop due to inertial effects. The quasi-steady approximation is made that the coolant flux is uniform between the inner and outer surfaces over a time interval, and the flux is evaluated at the end of each interval. The local effective thermal conductivity is that of the infiltrated matrix and is determined by

$$k_e = \gamma k_{co} + (1-\Gamma)(1-\gamma)\,k_s \qquad \text{(D-3)}$$

where

k_{co} = the local coolant conductivity.

k_s = local conductivity of porous matrix parent material.

γ = void fraction of porous matrix.

Γ = porous matrix tortuosity.

The local effective energy density is that of the infiltrated matrix and is

$$(\rho h)_e = \gamma \rho_{co} h_{co} + (1-\gamma) \rho_m C_{p_m} T \qquad \text{(D-4)}$$

where

ρ_{co} = the local coolant density.

h_{co} = the local coolant enthalpy.

ρ_m = the density of the porous matrix parent material.

C_{p_m} = the specific heat of the porous matrix parent material.

T = the local temperature.

Equation D-2 assumes that the coolant within a pore and the surrounding pore material are in thermal equilibrium. Assuming that purely laminar flow exists within the porous material, a one-dimensional analysis based on a spherical pore geometry yields the following equation for the local temperature differential within the porous matrix.

$$T_{pore} - T_{co} = 0.0625 D^2_{pore} (\dot{m})^2 \frac{C_{p_{co}}}{\gamma k_{co} k_e} (h_{co} - h_{c_i}) \qquad \text{(D-5)}$$

For the following typical set of reentry conditions,

Coolant:

Water

$h_c - h_{c_i}$ = 500 Btu/lb

$\dot{m}$ = 4 lb/ft^2-sec

Porous matrix:

316L stainless steel

$\gamma = 0.2$

$D_{pore} = 2.7\mu$

Equation D-5 indicates a structure-to-coolant temperature differential of 0.68 F.

D.2 HEATED SURFACE EQUATIONS

The ideal coolant flux and heat transfer at the heated surface are estimated using the equations in Appendix A.

D.3 NUMERICAL RESULTS

The resulting computer program has options for establishing the boundary conditions on both the inner and outer surfaces of the porous matrix. On the outer surface, a step change in heating may be imposed by a change in the heat transfer coefficient and/or the boundary layer recovery enthalpy. For the inner surface, either coolant flow rate or coolant cavity pressure may be maintained constant.

A series of calculations has been performed to determine the porous matrix response to step increases in heat transfer coefficient. Both a constant coolant flow rate condition and a constant inner pressure condition have been examined. For each case, the coolant flow conditions existing prior to the onset of the heating step are those required to establish thermal equilibrium with a liquid coolant film on the surface.

Figures D-1 and D-2 present surface temperature transients for porous 316L stainless steel for low and high surface pressure conditions as a function of the amplitude of the heating step. It is clear that for these conditions, maintaining a constant cooling flux during the transient results in a slower temperature rise than if internal coolant pressure is maintained constant. This is because coolant vaporization near the surface, after the onset of the heating step, increases back pressure, thus restricting the flow of coolant.

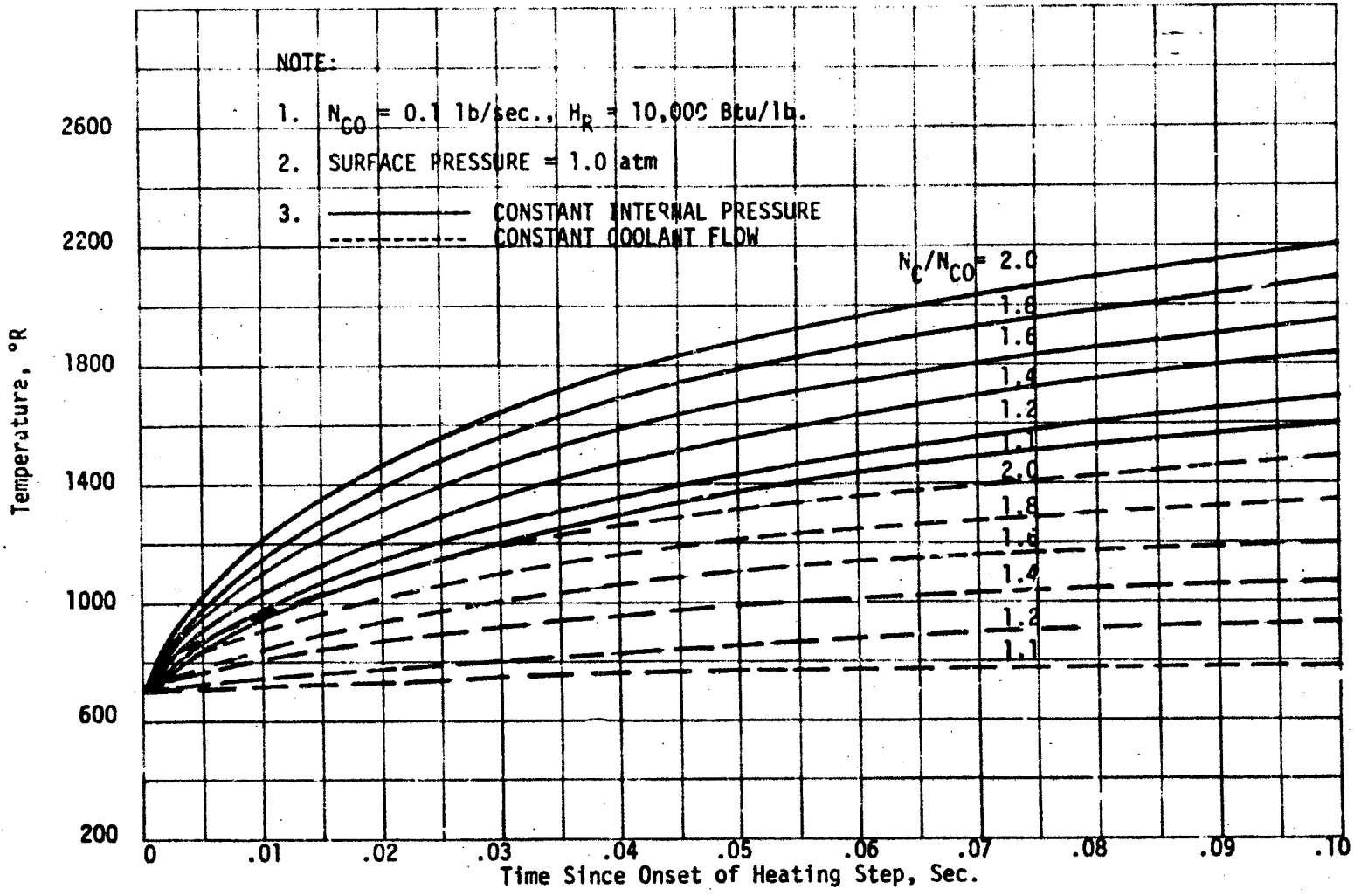


Figure D-1. Nosetip Surface Temperature Response, Low Surface Pressure

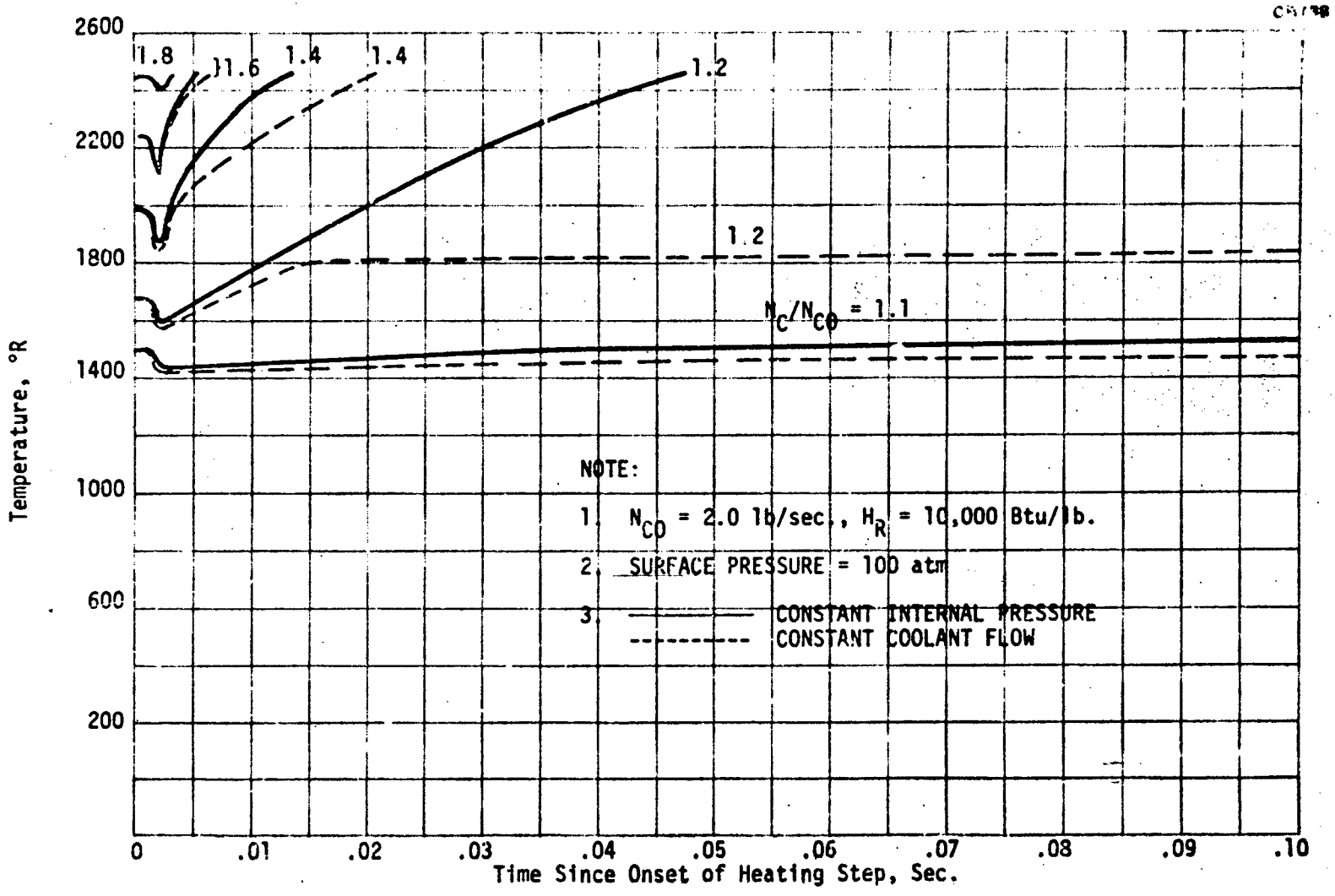


Figure D-2. Nosetip Surface Temperature Response, High Surface Pressure

The transients in general appear to be fairly long, and would tend to become longer for materials with increased thermal diffusivity, such as beryllium.

The S-3 trajectory was analyzed to see the effect of applying heating steps at any time during reentry. The nosetip location chosen was 34 deg from the stagnation point (essentially peak heating). Figure D-3 presents equilibrium surface temperatures that would be reached after the occurrence of the step. The maximum possible temperature corresponds to the assumed melting point of the nosetip material.

For the constant flow rate condition, even a 40-percent heating increase will not result in nosetip melt over the entire duration of the trajectory. For constant internal pressure, even a 10-percent heating increase will produce nosetip melt for at least a portion of reentry.

Figure D-4 presents the time interval after the onset of the heating step for the nosetip to begin melting. For even a 40-percent increase and a constant coolant pressure, a minimum of 48 msec is required. This should provide adequate time for a coolant flow control system to respond.

For use in determining nosetip degradation, Figure D-5 presents the initial melting rate once melting begins. These rates are significant and would probably rule out the use of any flow control system such as a gamma radiation sensor that relied on the detection of change in a thin surface layer. This is because the layer would need to be reusable.

In order to estimate the transient response of the nosetip in conjunction with a coolant flow control system, a series of quenching calculations were performed for which a 20-percent heating step was applied for a constant coolant pressure and then, upon the surface reaching the melt temperature, step changes in coolant pressure were applied while the heating step was still maintained.

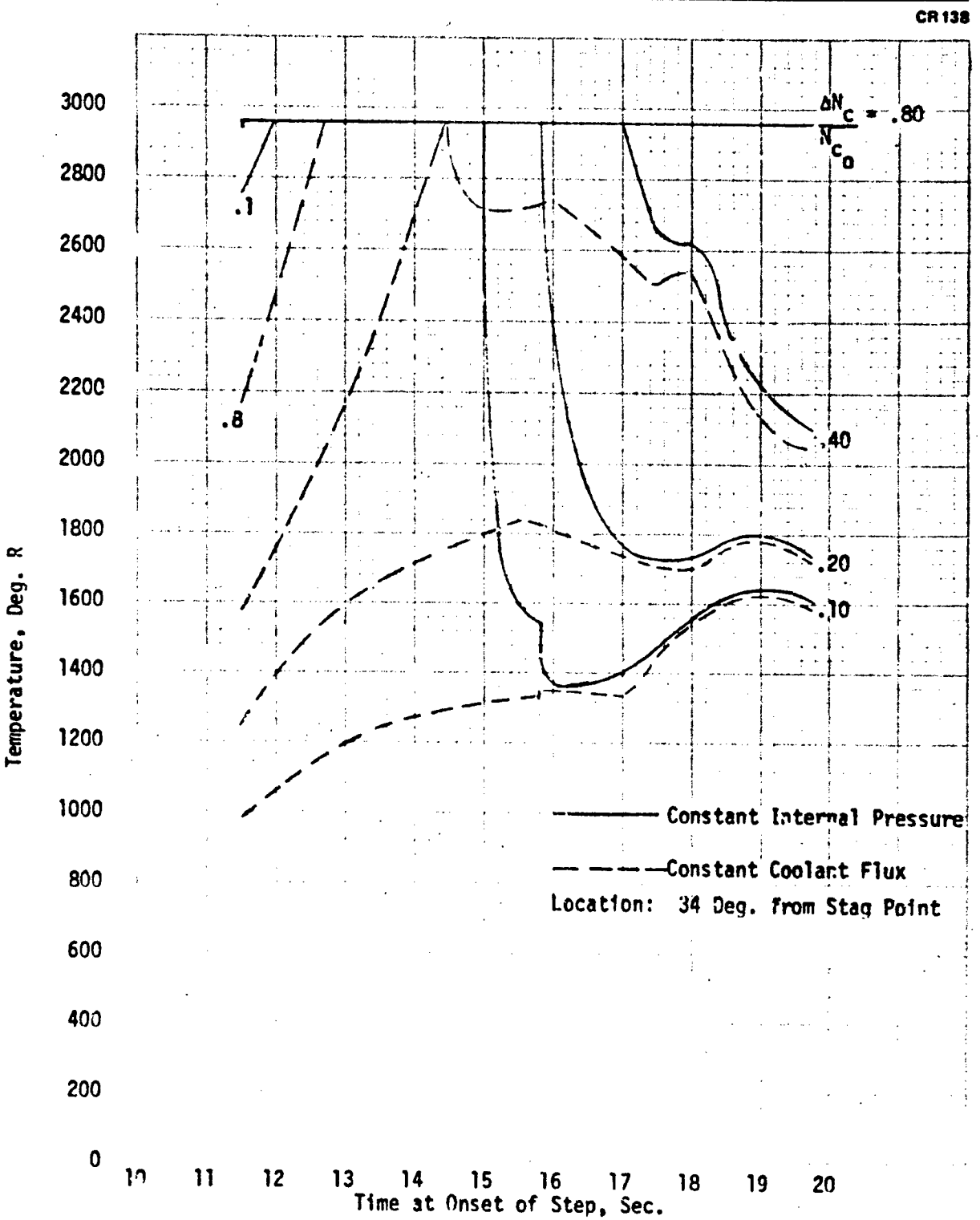


Figure D-3. Equilibrium Nosetip Surface Temperature After Onset of Heating Step, S-3 Trajectory

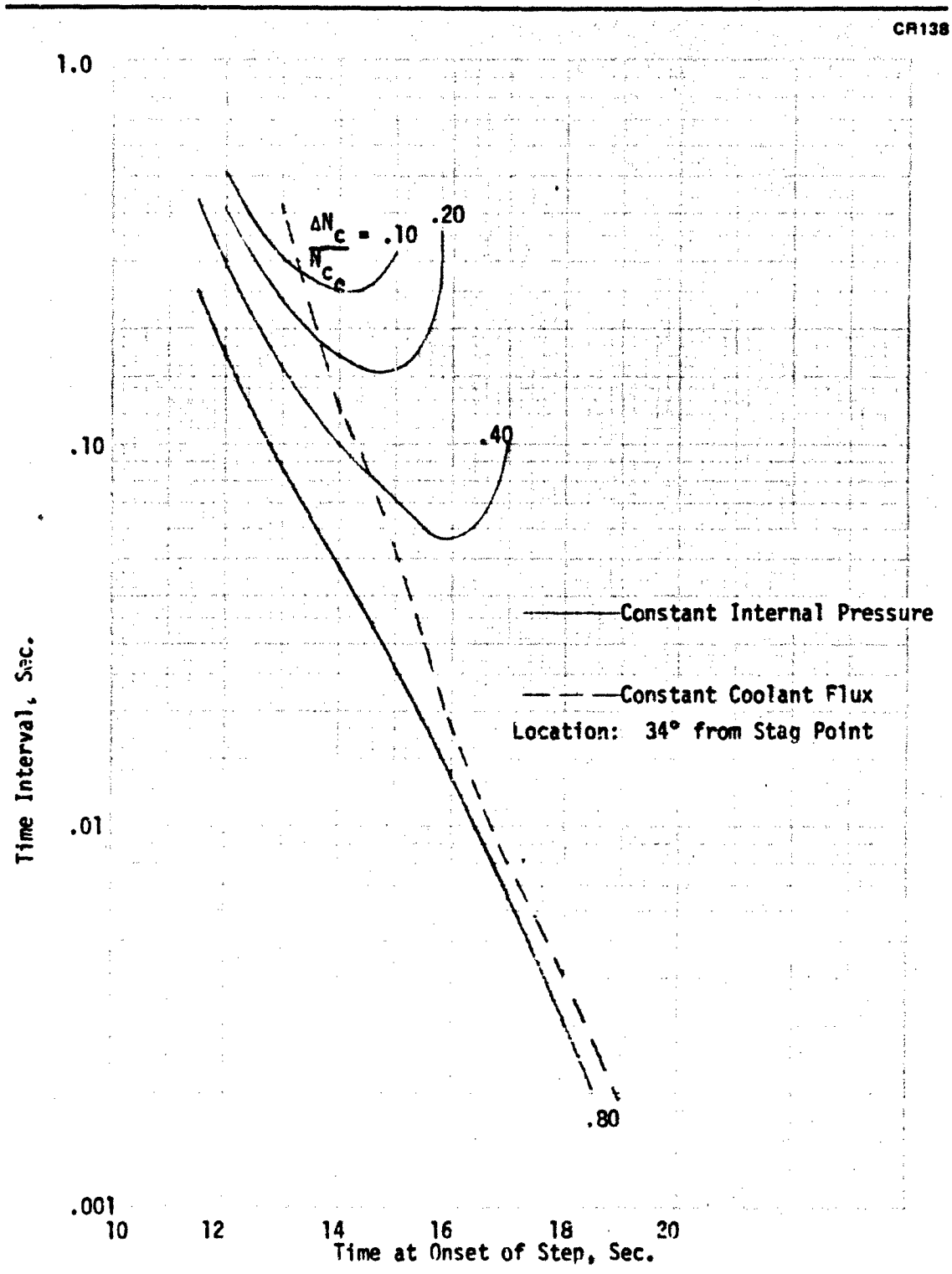


Figure D-4. Time Interval for Nosetip Surface to Melt After Onset of Heating Step, S-3 Trajectory

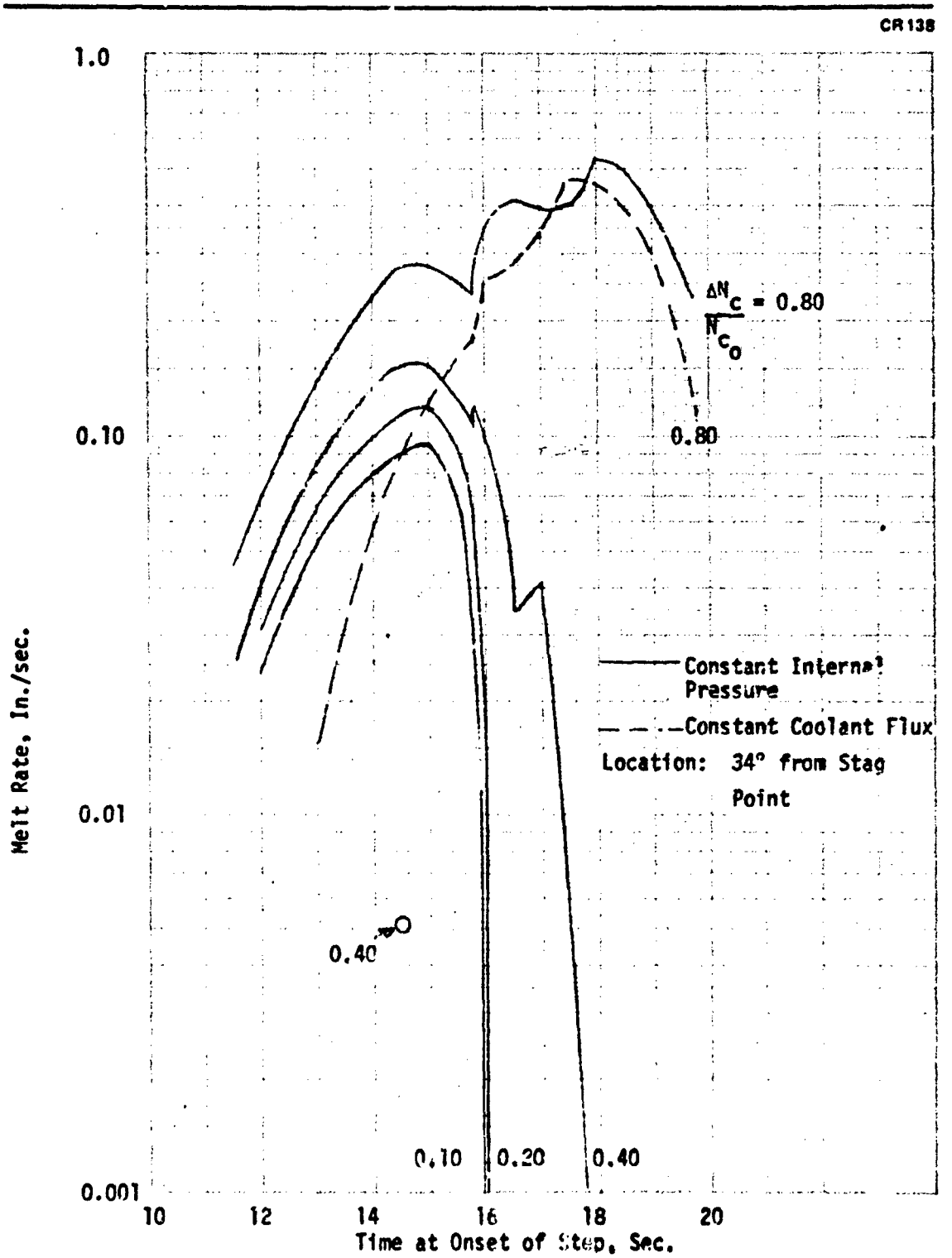


Figure D-5. Nosetip Initial Melt Rate After Onset of Heating Step, S-3 Trajectory

Figure D-6 presents the results of the calculations. The surface temperature immediately begins to decrease, reaches a minimum, and then eventually rises again to the melting temperature. The duration of this cycle is a direct function of the size of the coolant pressure increase. Figure D-7 presents required coolant pressure increase as a function of quench cycle duration. This type of information would be required to evaluate the performance capability of any coolant flow control system that relied on nosetip sensor input.

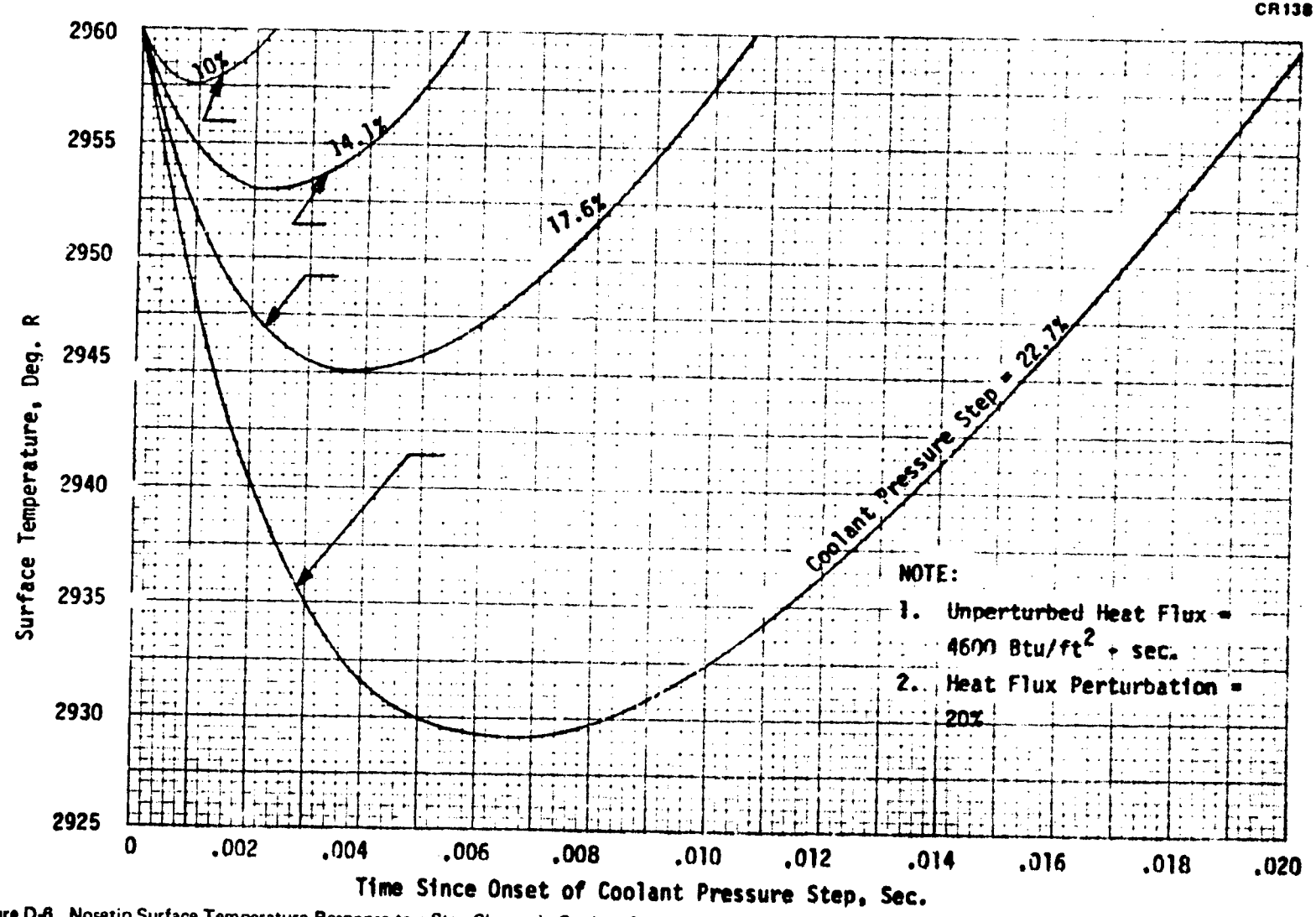


Figure D-8. Nosetip Surface Temperature Response to a Step Change in Coolant Supply Pressure

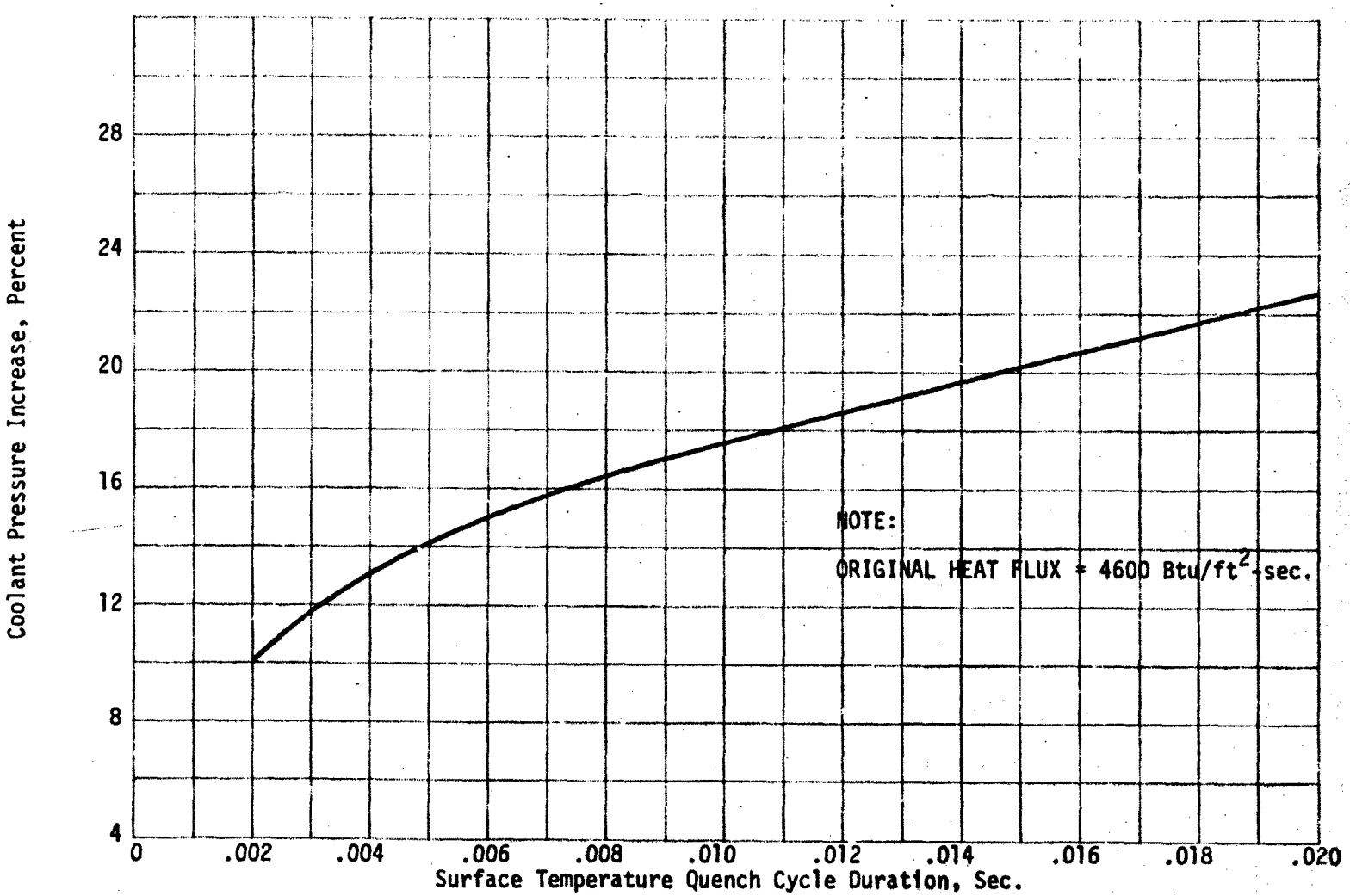


Figure D-7. Nosetip Surface Temperature Quench Cycle Time for a 20-Percent Increase in Heating

Appendix E
STRESS ANALYSIS

This appendix summarizes the calculations which were performed to verify the structural integrity of the recommended design. Analyses were accomplished for the wand, gas generator cover, reservoir wall, gas generator retainer thread, and substructure attachment A structural safety factor of 1.25 was applied to all loads.

E.1 WAND

Calculations were performed to verify that sufficient strength was available in the wand to prevent failure. Properties of the wand and wand material are shown in Table E-1. Two loading conditions, the S-3 and L-1(a) given in Figure 7-9, were considered for each of the two analysis points (A and B) shown in Figure E-1. The results for Point A are shown first.

Table E-1
COOLANT WAND PROPERTIES

Parameter	Value
Inside diameter	0.125 in.
Outside diameter	0.3 in.
Cross-sectional area	0.0585 in.^{2}
Moment of inertia	0.000386 in.^{4}
Ultimate tensile strength	260,000 psi

Wand compressive load due to P_A was computed using Equation E-1:

$$f_{com} = \frac{P_A}{A} = \frac{7,050}{0.0585} = 120,400 \text{ psi} \qquad \text{(E-1)}$$

CR135

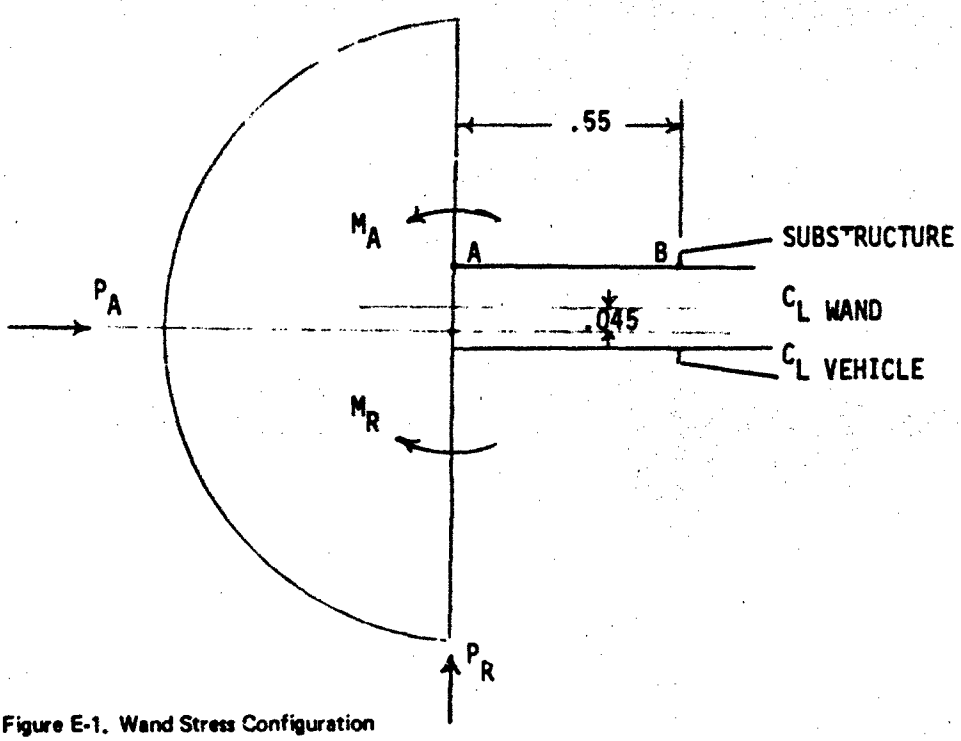


Figure E-1. Wand Stress Configuration

Bending stresses were computed with Equation E-2. Acceleration loads on the tip were neglected.

$$f_{be} = \frac{D/2\ M}{I} = \frac{(0.15)\ (356)}{0.000386} = 138,500 \text{ psi} \qquad \text{(E-2)}$$

where $M = 0.045\ P_A + M_A - M_R = 356$ in. -lb.

The total stress in the wand is the sum of these two. A value of 258,900 psi is obtained, which is just slightly lower than the allowable. Following an identical procedure for the other loading condition resulted in a total stress of 153,000 psi. It is obvious that the S-3 mission is more severe.

Calculations were also performed to evaluate the stress level at Point B in Figure E-1. Compressive stress was the same as shown in Equation E-1.

Bending stress calculations were modified slightly (Equation E-3) to include the moment introduced by the radial pressure force, P_R.

$$f_{be} = \frac{D/2\ M}{I} = \frac{(0.15)\ (180)}{0.000386} = 70,200 \text{ psi} \qquad \text{(E-3)}$$

where $M = 0.045\ P_A + M_A - M_R - 0.55\ P_R = 180$ in.-lb.

The total stress at this point is 190,600 psi, indicating that the most critical point on the wand is right at the nosetip-wand junction. A similar result was obtained for the L-1(a) condition, where a total stress of 93,800 psi was computed.

An analysis was performed to determine the minimum wand diameter which would be required if a beryllium wand were used. Assuming the heat shield could not carry any of the load, an outside diameter of 0.56 in. is needed. If the heat shield is included as a load-carrying member, this can be reduced. However, the diameter cannot be reduced to the 0.3-in. requirement dictated by the thermal protection system. It is obvious that downstream cooling effects must be considered for the design of a beryllium tip and wand.

E.2 GAS GENERATOR COVER AND RETAINER THREAD

The configuration analyzed for the gas generator cover and retainer thread is shown in Figure E-2. The design pressure, P, was computed to be 9,600 psi by multiplying the 7,000-psi operating pressure by the 1.25 safety factor and a factor of 1.1 to account for the acceleration loads. The total force acting on 1 in. of circumference is obtained as follows:

$$F_t = \frac{P\ (\text{area})}{\text{circum}} = \frac{P\ \frac{\pi}{4}\ 4.8^2}{\pi 4.8} = 11,500 \text{ lb/in.} \qquad \text{(E-4)}$$

The bending force at A is computed as shown in Equation E-5. The value obtained is less than the 190,000 psi allowable.

$$f_{be} = \frac{M\ t'2}{I} = \frac{(2,760)\ (0.15)}{0.00225} = 184,000 \text{ psi} \qquad \text{(E-5)}$$

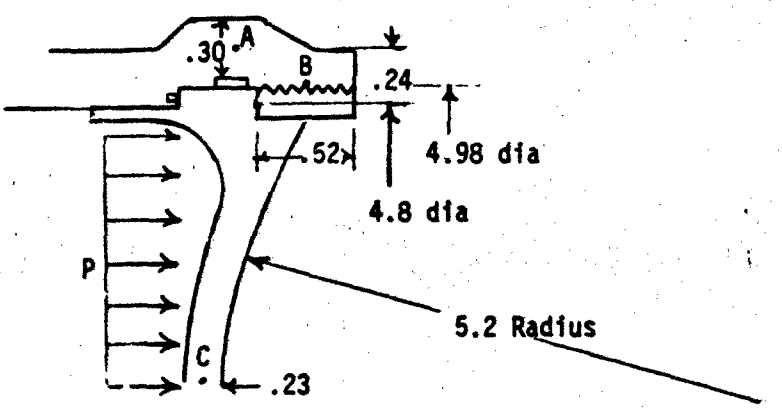


Figure E-2. Gas Generator Cover

where

$$M = 0.24F = 2,760 \text{ in.-lb/in.}$$

$$t = 0.30 \text{ in.}$$

$$I = \frac{1.0\,(0.3)^3}{12} = 0.00225 \text{ in.}^2$$

for the 17-4 reservoir material.

The stress at Point C was computed according to Case 5, page 261 of Reference E-1 (Equation E-6).

$$f = \frac{P\,(\text{radius})}{2t} = \frac{(9,600\,(5.2)}{(2)\,(0.23)} = 89,300 \text{ psi} \qquad \text{(E-6)}$$

A stress concentration factor of 2.5 was assumed to account for the change in section from a sphere to a plate. This results in a final stress of 223,000 psi, which is slightly below the allowable 250,000 psi for maraging steel.

The stress in the retainer thread (B of Figure E-2) was computed using Equation E-7. The allowable stress is

$$f_{th} = \frac{F_T}{A} = \frac{173,800}{4.00} = 43,500 \text{ psi} \qquad \text{(E-7)}$$

where

F_T = total force = $\frac{\pi}{4}(4.8)^2 (9,600) = 173,800$ lb.

A = shear area = $\pi \times 4.9 \times 0.52 \times \epsilon = 4.00$ in.^{2}

ϵ = efficiency = 0.5.

The allowable stress must be reduced to 55 percent of the maximum value for a thread. This results in an allowable of 137,000 psi, which is still much above the actual stress value.

E.3 RESERVOIR WALL

Calculations were performed at three points on the reservoir wall, as shown in Figure E-3. The reservoir wall thicknesses at Points B and C were computed with Equation E-8.

$$t_{in} = \frac{D_{in}}{2}\left(\frac{F_{tu} + P}{F_{tu} - P} - 1\right) \times SCF \qquad \text{(E-8)}$$

where

F_{tu} = ultimate tensile stress = 190,000 psi.

P = design pressure = 9,600 psi.

t = wall thickness.

D = diameter.

SCF = stress concentration factor for a junction of wall and end = 2.

The calculated thicknesses for B and C are 0.106 and 0.22 in.

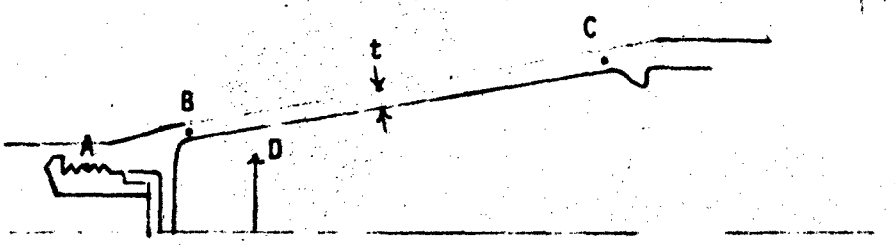


Figure E-3. Reservoir Wall

The stress in the thread at A is computed using Equation E-9.

$$f_{th} = \frac{F_T}{A} = \frac{28,100}{0.756} = 37,100 \text{ psi} \qquad \text{(E-9)}$$

where

$$F_T = \frac{\pi}{4} d_A^2 P = (0.785)(1.93)^2 (9,600) = 28,100 \text{ lb.}$$

$$A = \pi d_A \times \epsilon \times \text{thread length} = \pi (1.93)(0.5)(0.25) = 0.756 \text{ in.}^2$$

If the allowable stress is reduced to 55 percent of its original value, an allowable of 104,000 psi is obtained. This is approximately three times the actual.

E.4 SUBSTRUCTURE ATTACHMENT

Loading on the substructure attachment (Figure E-4) is due solely to acceleration loads. The peak acceleration of 90 g was assumed to act on the entire weight of the subsystem (16.13 lb). The 1.25 safety factor was also used, which results in a total load of 1,820 lb acting on the circumference

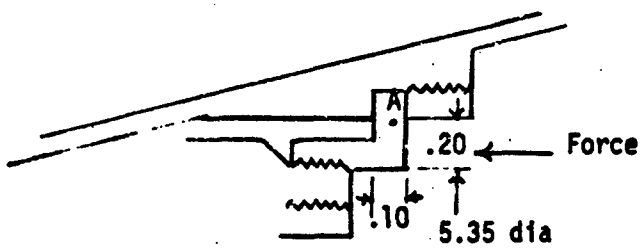


Figure E-4. Substructure Attachment

at A in Figure E-4. The stress at this point is computed according to Equation E-10.

$$f_{be} = \frac{M\,t/2}{I} = \frac{(364)\,(0.05)}{0.0014} = 13,000 \text{ psi} \qquad \text{(E-10)}$$

where

M = moment = 0.2 x 1,820 = 364.

t = thickness = 0.1.

I = moment of inertia = $\frac{\pi\,(5.35)\,(0.1)^3}{12}$ = 0.0014.

This component is made of beryllium, which has an allowable tensile strength of 50,000 psi. Therefore, the attachment mechanism as proposed is structurally sound.

E.5 REFERENCES

E-1. R. J. Roark. Formulas for Stress and Strain. McGraw Hill Book Company, Inc., 1954.